TECHNISCHE UNIVERSITÄT MÜNCHEN

Physik Department E21

Arbeitsgebiet stark korrelierte Elektronensysteme

Fluctuation-induced magnetic phase transitions in Fe and MnSi studied by neutron scattering

Dipl.-Phys. Univ. Jonas Kindervater

Vollständiger Abdruck der von der
Fakultät für Physik der Technischen Universität München
zur Erlangung des akademischen Grades eines

Doktors der Naturwissenschaften (Dr. rer. nat.)

genehmigten Dissertation.

Vorsitzender:		Univ.-Prof. Dr. Michael Knap
Prüfer der Dissertation:	1.	Univ.-Prof. Dr. Peter Böni
	2.	Univ.-Prof. Dr. Winfried Petry
	3.	apl. Prof. Dr. Christof Niedermayer, Universität Konstanz (nur schriftliche Beurteilung)

Die Dissertation wurde am 16.06.2015 an der Technischen Universität München eingereicht und durch die Fakultät für Physik am 05.10.2015 angenommen.

Abbreviations

CryoPAD	cryogenic polarization analysis device
Eq(s)	Equation(s)
FD	fluctuation-disordered
FL	fermi-liquid
FM	ferromagnetic
INSE	intensity modulated NSE
LMIEZE	longitudinal MIEZE
LNRSE	longitudinal NRSE
MIEZE	modulation of intensity with zero effort
MiniMuPAD	mini mu-metal polarization analysis device
MuPAD	mu-metal polarization analysis device
NRSE	neutron resonance spin echo
NSE	neutron spin echo
PM	paramagnetic
PO	partial order
QCP	quantum critical point
QPT	quantum phase transition
Ref(s)	Reference(s)
Sec(s)	Section(s)
TAS	triple axis spectrometer
TCP	tricritical point
TMIEZE	transversal MIEZE
TNRSE	transversal NRSE

Contents

Introduction

Fluctuations at phase transitions often stabilize new forms of complex electronic and magnetic order and are the heart of numerous important discoveries in modern solid state science, such as high-T_c superconductivity [1, 2], topological spin order [3] or the breakdown of the standard model to describe electrons in metals, namely - the Fermi liquid theory [4–6]. The understanding of these phenomena is directly linked to a precise examination of the relevant fluctuations, which can be realized with neutron scattering. Neutron scattering allows to directly measuring the correlation of the fluctuations in space and time.

To describe the transition from one phase to another phase, an order parameter can be introduced that is finite in the ordered and zero in the disordered phase. A distinction is drawn between phase transitions where the order parameter vanishes discontinuously, i.e. first-order transitions (cf. Fig. 0.1 (a)) and phase transitions where the order parameter vanishes continuously, i.e. second and higher order phase transitions (cf. Fig. 0.1 (e)). The discontinuous jump of the order parameter at first-order phase transitions is accompanied by latent heat while the system transits from one local minimum of the free energy landscape to another one (b)-(c). Fluctuations of the order parameter are usually irrelevant. In contrast, at second-order phase transitions strong fluctuations of the order parameter occur, due to the flat free energy landscape. The system evolves continuously from one minimum in the free energy to another one (f)-(h). Close to the transition, fluctuations extend over increasing length and time scales. The corresponding correlation lengths in space and time diverge according to universal scaling laws, depending only on the symmetry of the order parameter and not on the microscopic interactions [7]. A plethora of critical fluctuations may change a second-order phase transition to first-order. The theory for such fluctuation-induced first-order transitions was put forward by Brazovskii [9] and since then proposed for numerous different systems like liquid crystals [10], pion condensation in nuclear matter [11], spin-orbit coupled Bose-Einstein condensates [12]

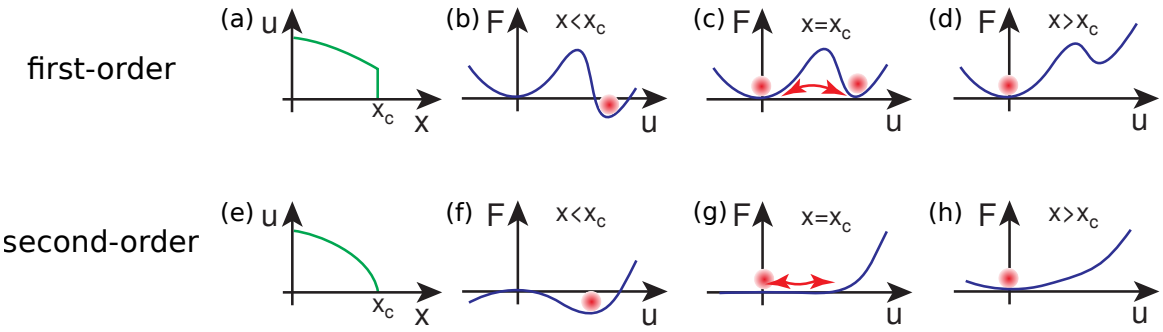

Figure 0.1.: Order parameter u and free energy F at a first (top row) and second (bottom row) order phase transition. At first-order or discontinuous phase transitions the order parameter u exhibits a step as function of the control parameter x (a) and the system jumps from one local minimum in the free energy to another local minimum (b)-(d). The order parameter at a second-order or continuous phase transition vanishes continuously (e) and the system experiences strong order parameter fluctuations due to the flat free energy landscape (f)-(h). The figure is taken from Ref. [8].

and Rayleigh-Bernard convection [13]. In a recent study the zero field transition from paramagnetism to helimagnetism in the cubic helimagnetic MnSi is explained within the framework of this theory [14, 15].

Particularly, phase transitions occurring at zero temperature are very interesting. In contrast to finite temperature phase transitions which are driven by thermal fluctuations, these quantum phase transitions (QPT) are driven by quantum fluctuations. Commonly, finite temperature phase transitions are suppressed by a non-thermal control parameter x, like hydrostatic pressure, magnetic field or doping, as shown in Fig. 0.2 (a) [20]. The influence of such zero temperature transitions can be felt in a characteristic V-shaped region of the x-T phase diagram, where quantum fluctuations govern the properties of the system, leading to novel physics. Continuous phase transitions that are suppressed to zero temperature are called quantum critical points (QCP) and the presence of a QCP is believed to be the key in understanding fundamental phenomena in physics, e.g. magnetically mediated superconductivity in $CePd_2Si_2$ (cf. Fig. 0.2 (b)) [17], UGe_2 (cf. Fig. 0.2 (c)) [21] or other materials [22, 23]. Also the breakdown of the Fermi liquid theory, the standard model to describe the conduction electrons in metals, in e.g. $NbFe_2$ [24, 25] or $YbRh_2Si_2$ (cf. Fig. 0.2 (d)) [19], is considered to be triggered by a QCP. In contrast to the preceding examples, MnSi exhibits an extended region of non-Fermi liquid behavior above the critical pressure where the magnetic order is suppressed [4, 26], accompanied by a non-trivial topology, i.e. a real space spin structure that cannot be continuously transformed into a ferromagnet [27].

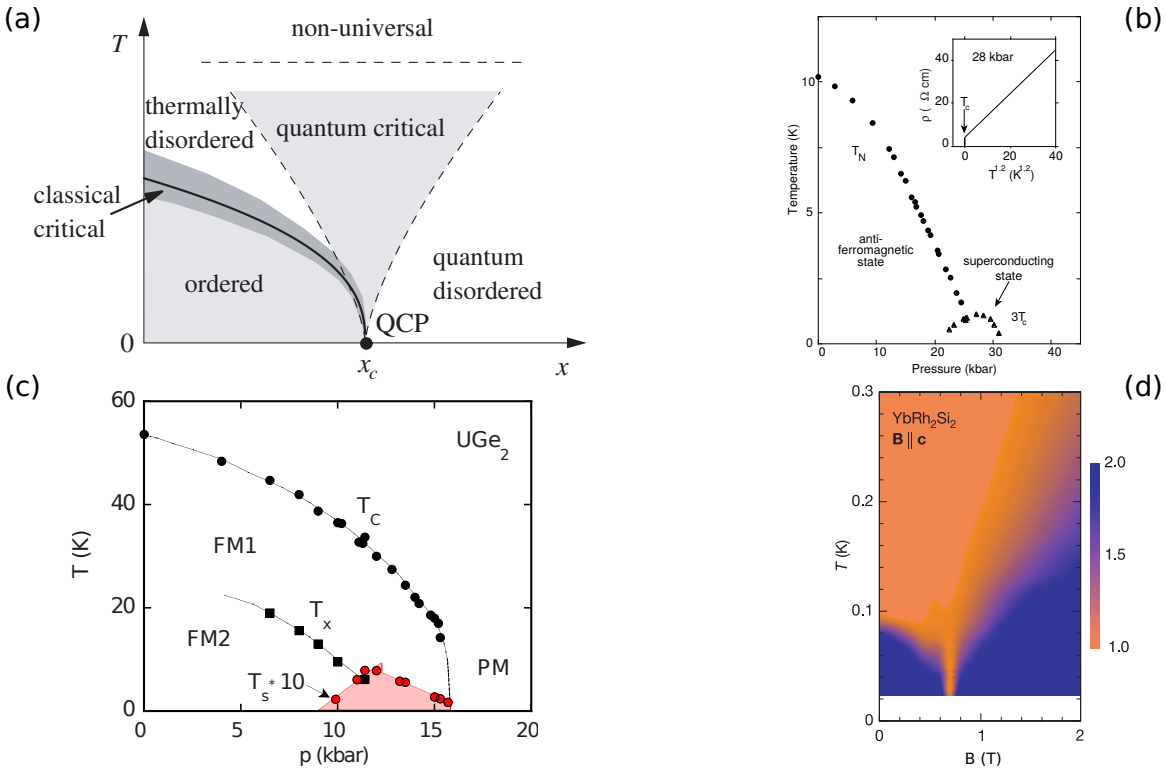

Figure 0.2.: Quantum phase transitions in different systems. Panel (a) shows a schematic phase diagram as function of temperature T and control parameter x, taken from Ref. [16]. (b) Emerging superconducting dome in $CePd_2Si_2$. The antiferromagnetic order is suppressed by pressure. The inset shows the drop of the resistivity at T_c. Figure is taken from Ref. [17]. (c) Coexistence of ferromagnetism an superconductivity in UGe_2. Figure taken from [18]. (d) Suppression of the antiferromagnetic order in $YbRh_2Si_2$ by a magnetic field along the crystalline c-axis. In the orange shaded V-shaped region non-Fermi liquid behavior is observed [19].

To directly measure the evolution and the fluctuations of the order parameter neutron scattering is a powerful tool. Diffraction allows measuring the correlation length of the fluctuations and inelastic techniques to address their life time. Critical slowing down as expected at continuous phase transitions makes an ultra-high energy resolution indispensable for such studies. Neutron spin echo (NSE) proposed by Mezei [28, 29] in 1972 uses the precession of the neutron spin to reach the highest energy resolution within the field of neutron spectrometry. In all spin echo techniques the energy resolution is decoupled from the width of the used wavelength band making high flux and high resolution available at the same time, being the perfect combination for such studies. The accessible time window spreads from ps to µs and hence from µeV to neV. Another variant of NSE is neutron resonance spin echo (NRSE) developed by Golub and Gähler [30–32], where resonant flips are employed to realize

the spin precession. The field geometry in NRSE allows to tilt the field boundaries and therefore to measure excitations with a finite dispersion [33]. Nevertheless, the main application for spin echo is in quasielastic scattering experiments, studying slow relaxation processes on large length scales. An example is the spin dynamics in spin glasses, where NSE was applied to numerous different systems to access the key parameters of the relaxation processes [34–37]. Another prototypical example is the study of second-order phase transitions. Spin echo allows proofing the validity of the present day understanding of critical phenomena on very large length and time scales [38]. Many of the most pressing scientific issues, as the magnetic systems discussed above, require measurements with the high resolution achievable with NSE spectroscopy, however, under more demanding conditions such as very large magnetic fields or strongly depolarizing samples. Modulation of IntEnsity with Zero Effort (MIEZE) [32, 39, 40] allows to overcome these restrictions as for example already shown for the combination of sub-μeV resolution with strong magnetic fields at the sample [41]. MIEZE will allow the investigation of e.g. quantum phase transitions in transverse Ising magnets [42] or field-induced Bose-Einstein condensation of magnons [43, 44] with spin echo resolution.

The scientific work presented in this thesis focuses on the investigation of the spatial and temporal evolution of fluctuations at the border to novel types of magnetic order. The thesis is organized in the following way.

Chapter 1 gives a short introduction into the fundamental concepts of neutron scattering and a description of the neutron scattering techniques employed within this thesis. The nuclear and magnetic scattering cross sections are explained, followed by a description of small angle neutron scattering (SANS), spherical neutron polarimetry (SNP), neutron spin echo (NSE), neutron resonance spin echo (NRSE) and modulation of intensity with zero effort (MIEZE).

Chapter 2 focuses on the different instrumental methods developed within this thesis. A new generation of the SNP device, MiniMuPAD, is introduced, that is optimized for small scattering angles. During the course of this thesis several aspects of the beamline RESEDA have been improved, a new resonant spin echo option namely -longitudinal NRSE- was setup, a new secondary spectrometer arm for SANS and MIEZE studies was built and first proof of principle experiments in very high magnetic fields were performed. At the end of the chapter a description of the measurement procedure and the treatment of the spin echo data is given.

Chapter 3 reports a comprehensive MIEZE study of the critical dynamics above and below the Curie temperature T_C in the archetypal ferromagnet iron. The critical fluctuations above the Curie point are in excellent agreement with scaling theory reported by Frey and Schwabl, considering a Heisenberg model taking dipolar interaction into account. In the ferromagnetic phase, well defined inelastic excitations are

observed in agreement with standard magnon theory. MIEZE proofs to be a very powerful technique to study critical fluctuations by combining large q-coverage and high energy resolution, while being insensitive to depolarizing effects at the sample position. This combination allows to go beyond the Heisenberg model and to investigate weaker interactions such as dipolar interactions, anisotropies, etc. The results proof that MIEZE and classical NSE give the very same results.

Chapter 4 is concerned with the cubic chiral helimagnets MnSi, $Mn_{1-x}Fe_xSi$ and $Mn_{1-x}Co_xSi$. After a short introduction to these non-centrosymmetric compounds the focus is on the critical spin-flip scattering at the paramagnetic to helimagnetic transition in MnSi. A SNP study shows that the spin resolved critical scattering at the phase transition is in very good agreement with a fluctuation-induced first-order transition in a so called Brazovskii scenario. SNP confirms a previously performed unpolarized SANS study and shows that there is no need for a more complex model to describe the transition. In the next part, the magnetic field evolution of the Brazovskii scenario in MnSi is investigated by a combination of SANS and MIEZE measurements. We find that the fluctuation-induced first-order transition changes to second-order at a tricritical point, proofing the validity of the Brazovskii scenario in MnSi. The last part of this chapter accounts for the suppression of the magnetic order by substitutional doping in $Mn_{1-x}Fe_xSi$ and $Mn_{1-x}Co_xSi$, addressed by a combination of SANS and NRSE measurements. The SANS measurements show an increase of the helical modulation vector and a reduction of the cubic anisotropy with increasing doping. Moreover an unconventional orientation of the helical domains is observed. We find a transition from an elastic to a fluctuating ground state in $Mn_{1-x}Fe_xSi$ ($x = 12\,\%$), accompanied by a topological Hall effect [45]. This observation may be understood as a new type of a topological spin liquid.

CHAPTER 1

Neutron Scattering and Neutron Scattering Techniques

In this chapter the fundamental equations describing the neutron scattering from - especially- magnetic samples are presented. Thereafter the experimental techniques used in this thesis are introduced. The magnetic structures and the corresponding fluctuations studied in this text have relatively large length scales, therefore all investigations took place at small scattering angles, employing the small angle neutron scattering (SANS) technique. SANS measurements give directly access to the energy integrated scattering function $S(q)$ and therefore allow to study the magnetic structure of the sample. More complex magnetic structures can be investigated by spherical neutron polarimetry (SNP). SNP measures the full spin dependent scattering cross section and allows analyzing magnetic structures that are untraceable with other techniques. Neutron spin echo techniques, in particular neutron spin echo (NSE), neutron resonance spin echo (NRSE) and modulation of intensity with zero effort (MIEZE) are used to study the lifetime of the magnetic fluctuations. These techniques measure the intermediate scattering function $S(q,\tau)$ directly in the time domain.

The chapter is organized as follows, at the beginning a short introduction to magnetic neutron scattering is given followed by a basic description of SANS, SNP, NSE, NRSE and MIEZE.

1.1. Neutron scattering

Neutron scattering is a very powerful technique, particularly in solid state physics, in order to study the structure and dynamics of the nuclear and magnetic structures of the sample. The strength of this technique is due to the specific characteristics

of the neutron and its interaction with matter. The most prominent properties, especially in contrast to widely complementary techniques like X-Ray scattering, can be summarized as follows:

- Neutrons are uncharged and therefore, hence able to easily penetrate the electron shell, as there is no Coulomb barrier to overcome. The penetration depth is very large allowing studying the bulk sample and not only the surface. Moreover, due to different nuclear interactions neutrons are able to distinguish between different isotopes of the same element. The strength of the interaction can be very high even for light elements like hydrogen, making it observable within a matrix of other elements.
- The energy of cold and thermal neutrons ranging from 0.1 meV to 100 meV is comparable to low energy excitations of the nuclear and magnetic system of interest, enabling not only to study the structure but also the excitations within the sample.
- The neutron exhibits a magnetic moment, allowing in a unique way to study the magnetic structure and excitations of the samples. In particular, when using polarized neutrons, magnetic structures can be resolved that are untraceable with other techniques. This can be used to study, for instance, the chirality of magnetic structures as in cubic helimagnets like MnSi.

In the following section the basic concepts of neutron scattering are introduced following the standard textbooks [46–48]. The basis of neutron scattering is to measure the probability that a neutron with wave vector $\mathbf{k}_i$ and spin state σ_i is scattered into a state with wave vector $\mathbf{k}_f$ and spin state σ_f while the sample changes its state from λ_i to λ_f. The probability can be evaluated in lowest order perturbation theory given by Fermi's Golden Rule. This probability can be described by the double differential scattering cross-section, when normalizing the probability to the incoming neutron flux and multiplying it by the number of final states of the neutron. The double differential scattering cross-section then reads

$$\frac{\mathrm{d}^2\sigma}{\mathrm{d}\Omega\mathrm{d}\omega} = \left(\frac{m_\mathrm{n}}{2\pi\hbar^2}\right)^2 \frac{k_f}{k_i} \sum_{\lambda_f,\sigma_f} \sum_{\lambda_i,\sigma_i} p_{\lambda_i} p_{\sigma_i} \left|\langle \mathbf{k}_f,\sigma_f,\lambda_f|\hat{U}|\mathbf{k}_i,\sigma_i,\lambda_i\rangle\right|^2 \cdot \delta(\hbar\omega + E_{\lambda_i} - E_{\lambda_f}). \quad (1.1)$$

Here m_n is the neutron mass, $\hbar$ the Planck constant divided by 2π, λ_f and λ_i are the final and initial state of the sample, p_{λ_i} and p_{σ_i} are the probability to find the sample in state λ_i and the neutron spin state to be σ_i. $\hat{U}$, is a potential describing the interaction between the neutron and the sample. The cross-section gives the number of neutrons scattered into a solid angle $\mathrm{d}\Omega$, with a energy transfer $\mathrm{d}\omega$. For the scattering process both energy and momentum are conserved. The energy transfer to the sample is given by

$$\hbar\omega = \frac{\hbar^2}{2m_\mathrm{n}}(\mathbf{k}_i^2 - \mathbf{k}_f^2) \quad (1.2)$$

and the momentum transfer by the scattering vector $\mathbf{Q}$

$$\hbar\mathbf{Q} = \hbar(\mathbf{k}_i - \mathbf{k}_f). \tag{1.3}$$

The interaction potential $\hat{U}$ depends on the specific scattering process, which can be nuclear or magnetic. The nuclear interaction potential is short range ($\propto 1/r^3$) while the magnetic interaction is not short range but weak, therefore Fermi's Golden Rule is valid in both cases.

1.1.1. Nuclear neutron scattering

The nuclear interaction of the neutron at position $\mathbf{r}$ with a nucleus at position $\mathbf{R}_j$ is described by the Fermi pseudo potential

$$\hat{U} = \frac{2\pi\hbar^2}{m_n} \sum_j b_j \delta(\mathbf{r} - \mathbf{R_j}). \tag{1.4}$$

The scattering length b_j depends on the specific nuclei and is of the order 10^{-12} cm. To further evaluate the scattering cross-section, we consider an unpolarized neutron beam and describe the incoming and outgoing neutrons by plane waves $|\mathbf{k}_i\rangle = e^{i\mathbf{k}_i\cdot\mathbf{r}}$, $|\mathbf{k}_f\rangle = e^{i\mathbf{k}_f\cdot\mathbf{r}}$. Introducing Heisenberg operators allows expressing the nuclear scattering cross-section for unpolarized neutrons by

$$\frac{\mathrm{d}^2\sigma}{\mathrm{d}\Omega\mathrm{d}\omega} = \frac{k_f}{k_i}\frac{1}{2\pi\hbar}\sum_{j,j'} b_j b_{j'} \int_{-\infty}^{\infty} \left\langle e^{-i\mathbf{Q}\hat{\mathbf{R}}_{j'}(0)} e^{-i\mathbf{Q}\hat{\mathbf{R}}_j(t)} \right\rangle e^{-i\omega t}\mathrm{d}t. \tag{1.5}$$

In this representation Eq. (1.5) contains the intermediate pair correlation function or intermediate scattering function

$$I(\mathbf{Q},t) = \frac{1}{N}\sum_{j,j'} \left\langle e^{-i\mathbf{Q}\hat{\mathbf{R}}_{j'}(0)} e^{-i\mathbf{Q}\hat{\mathbf{R}}_j(t)} \right\rangle, \tag{1.6}$$

which is the spatial Fourier transform of the van Hove correlation function [49]. The van Hove function describes the density-density correlation in the system. A time Fourier transform of the intermediate scattering function yields the dynamical structure factor $S(\mathbf{Q},\omega)$

$$S(\mathbf{Q},\omega) = \frac{1}{2\pi\hbar}\int I(\mathbf{Q},t) e^{-i\omega t}\mathrm{d}t. \tag{1.7}$$

Comparing Eq. (1.7) with equation (1.5) shows that the double differential scattering cross-section is proportional to the dynamical structure factor through a simple coupling constant. In nuclear scattering this constant is the square of the scattering length while in magnetic scattering it is $(\gamma_n r_0)^2$, where $r_0 = 2.8179 \cdot 10^{-15}$ m is the classical electron radius.

1.1.2. Magnetic neutron scattering

Magnetic neutron scattering to first order takes place due to the dipole-dipole interaction between the unpaired electron spins of the target with the magnetic moment of the neutron. The magnetic moment operator $\hat{\mu}_n$ of the neutron can be described by

$$\hat{\mu}_n = -\gamma_n \mu_N \hat{\sigma}, \tag{1.8}$$

where $\gamma_n = 1.913$ is a positive constant and $\mu_N = (e\hbar)/(2m_P)$ is the nuclear Bohr magneton, given by the elementary charge e and the proton mass m_P. $\hat{\sigma}$ is the Pauli spin operator described in more detail in Sec. 1.1.3. The interaction between the magnetic moment of the neutron and the local magnetic field $\mathbf{H}$ in the sample can be described by

$$\hat{U} = -\hat{\mu}_n \cdot \mathbf{H} \tag{1.9}$$

As described above we want to focus onto the interaction between the neutrons and the electrons of the sample. Therefore we have to evaluate the magnetic field generated by a single unpaired electron with velocity $\mathbf{v}_e$, which is given by

$$\mathbf{H} = \nabla \times \left(\frac{\boldsymbol{\mu}_e \times \mathbf{R}}{|\mathbf{R}|^3} \right) - \frac{e}{c} \frac{\mathbf{v}_e \times \mathbf{R}}{|\mathbf{R}|^3} \tag{1.10}$$

where the first term describes the magnetic field due to the magnetic moment $\boldsymbol{\mu}_e$ of the electron and the second term arises from the orbital motion. The magnetic moment operator $\hat{\boldsymbol{\mu}}_e = -2\mu_B \hat{\boldsymbol{s}}$ is given by the spin operator of th electron $\hat{\boldsymbol{s}}$ and the Bohr magneton $\mu_B = 9.274 \cdot 10^{-24}\,\mathrm{J/T}$. $\mathbf{R}$ is the distance between the electron and the point where the magnetic field is measured and $c = 2.998 \cdot 10^8\,\mathrm{m/s}$ is the speed of light. To evaluate the magnetic scattering cross-section one has to calculate the interaction potential. Therefore the magnetic field of a single electron given by Eq. (1.10) must be inserted into the equation for the scattering potential Eq. (1.9) and then into the general scattering cross-section equation (1.1). For a detailed evaluation we refer to Ref. [48]. The result is given by

$$\frac{\mathrm{d}^2\sigma}{\mathrm{d}\Omega \mathrm{d}\omega} = (\gamma_n r_0)^2 \frac{k_f}{k_i} F^2(\mathbf{Q}) e^{-2W(\mathbf{Q})} \sum_{\alpha,\beta} \left(\delta_{\alpha,\beta} - \frac{Q_\alpha Q_\beta}{Q^2} \right) S^{\alpha\beta}(\mathbf{Q},\omega),\ (\alpha,\beta = x,y,z), \tag{1.11}$$

where the magnetic scattering function $S^{\alpha\beta}(\mathbf{Q},\omega)$, the magnetic form factor $F(\mathbf{Q})$ and the Debye-Waller factor $e^{-2W(\boldsymbol{Q})}$ are introduced. The magnetic scattering cross-section has a much more complex structure compared to the nuclear cross-section Eq. (1.5). The former depends on the relative alignment between the scattering vector and the magnetic moments in the sample. Neutrons can only couple to magnetic moments which are perpendicular to $\mathbf{Q}$. The strength of the coupling is given by $(\gamma_n r_0)^2 \approx 10^{-25}\,\mathrm{cm}^2$ and therefore in the same order as the nuclear scattering.

All information about the magnetic structure of the sample is contained in the magnetic scattering function $S^{\alpha\beta}(\mathbf{Q},\omega)$ which can be evaluated to

$$S^{\alpha\beta}(\mathbf{Q},\omega) = \frac{1}{2\pi\hbar}\sum_{j,j'}\int_{-\infty}^{\infty} e^{i\mathbf{Q}(\mathbf{R}_j-\mathbf{R}_{j'})}\langle\hat{S}_j^{\alpha}(0)\hat{S}_{j'}^{\beta}(t)\rangle e^{-i\omega t}\mathrm{d}t \tag{1.12}$$

with the effective spin operator

$$\hat{S}_{j'}^{\alpha} = \frac{1}{2}g\hat{J}_j^{\alpha}. \tag{1.13}$$

The effective angular momentum operator $\hat{J}_j^{\alpha}$ combines the spin and orbital angular momentum (S and L), g is the Landé factor. The brackets $\langle\rangle$ denote the thermal average of the time dependent spin operators. $S^{\alpha\beta}(\mathbf{Q},\omega)$ correlates a magnetic moment j' at position $\mathbf{R}_{j'}$ and time $t=0$ with another magnetic moment j at position $\mathbf{R}_j$ and time t. It gives the probability, when finding j' with a specific value, to find j with another specific value. In this sense it is similar to the van Hove correlation function introduced for the density density correlations.

The correspondence to the van Hove correlation functions allows to connect the magnetic scattering function with the generalized susceptibility tensor $\chi^{\alpha\beta}(\mathbf{Q},\omega)$ using the fluctuation-dissipation theorem

$$S^{\alpha\beta}(\mathbf{Q},\omega) = \frac{N\hbar}{\pi}\left(1-e^{-\frac{\hbar\omega}{k_BT}}\right)^{-1}\mathrm{Im}\chi^{\alpha\beta}(\mathbf{Q},\omega), \tag{1.14}$$

with N being the total number of magnetic ions. This can be understood when considering the neutron to be a perturbing magnetic field $H^{\beta}(\mathbf{Q},\omega)$, and the scattered intensity is the response of the system $M^{\alpha}(\mathbf{Q},\omega)$

$$M^{\alpha}(\mathbf{Q},\omega) = \chi^{\alpha,\beta}(\mathbf{Q},\omega)H^{\beta}(\mathbf{Q},\omega). \tag{1.15}$$

1.1.3. Neutron beam polarization

The following section follows Ref. [50] and references therein.

Polarization of a neutron and of a neutron beam

The spin operator $\hat{\mathbf{S}} = (S_x,S_y,S_z)$ representing the observable of the neutron spin-$\frac{1}{2}$ has two eigenvalues $\pm\hbar/2$ with respect to an arbitrary quantization direction $\mathbf{e}$. The eigenvalue equation reads,

$$\hat{\mathbf{S}}|\boldsymbol{\chi}\rangle = \pm\frac{\hbar}{2}|\boldsymbol{\chi}\rangle, \tag{1.16}$$

with $|\boldsymbol{\chi}\rangle$ describing a pure spin state and $\hat{\mathbf{S}}$ being the spin operator. $\hat{\mathbf{S}}$ can be represented with the help of the Pauli Spin matrices

$$\sigma_x = \begin{pmatrix} 0 & 1 \\ 1 & 0 \end{pmatrix}, \qquad \sigma_y = \begin{pmatrix} 0 & -i \\ i & 0 \end{pmatrix}, \qquad \sigma_z = \begin{pmatrix} 1 & 0 \\ 0 & -1 \end{pmatrix} \tag{1.17}$$

which allow mapping of the two dimensional spin system on to the surface of a three dimensional sphere in real space. Enabling the Pauli Spin matrices the spin operator reads

$$\hat{\mathbf{S}} = \frac{\hbar}{2}\hat{\boldsymbol{\sigma}}, \tag{1.18}$$

with $\hat{\boldsymbol{\sigma}} = (\sigma_x,\sigma_y,\sigma_z)$. To describe the spin state a two component spinor can be used

$$\boldsymbol{\chi} = a\boldsymbol{\chi}_\uparrow + b\boldsymbol{\chi}_\downarrow = a\begin{pmatrix} 1 \\ 0 \end{pmatrix} + b\begin{pmatrix} 0 \\ 1 \end{pmatrix} \tag{1.19}$$

where $\boldsymbol{\chi}_\uparrow$ and $\boldsymbol{\chi}_\downarrow$ are the eigenvectors of the two dimensional Hilbert space. These eigenvectors can be imagined as spin up and down. To satisfy the normalization condition for $\boldsymbol{\chi}$ the coefficients a and b must fulfill

$$\boldsymbol{\chi}^\dagger\boldsymbol{\chi} = |a|^2 + |b|^2 = 1. \tag{1.20}$$

The polarization is defined as the expectation value of the spin operator $\langle\hat{\boldsymbol{\sigma}}\rangle$. Hence it reads

$$\boldsymbol{P} = \frac{2}{\hbar}\left\langle\hat{\boldsymbol{S}}\right\rangle = \langle\hat{\boldsymbol{\sigma}}\rangle\,. \tag{1.21}$$

For a single neutron as described in equation (1.19) fulfilling the normalization condition Eq. (1.20), the polarization will always be $|\boldsymbol{P}| \equiv 1$. In neutron scattering experiments there is not only one single neutron, but an ensemble of neutrons. To describe the spin state of the ensemble one introduces the density matrix formalism [51]. This formalism allows also to describe so called mixed states, which leads to a polarization $|\boldsymbol{P}| < 1$. The density matrix $\hat{\rho}$ for a two level system is defined by

$$\hat{\rho} = \boldsymbol{\chi}\boldsymbol{\chi}^\dagger = \begin{pmatrix} |a|^2 & ab^* \\ ba^* & |b|^2 \end{pmatrix}. \tag{1.22}$$

With the density matrix formalism the average of an arbitrary operator $\hat{O}$ can be calculated as the trace over the product of the density operator and $\hat{O}$, in detail $\langle\hat{O}\rangle = \mathrm{Tr}(\hat{\rho}\hat{O}) = \mathrm{Tr}(\hat{O}\hat{\rho})$. $\hat{\rho}$ can be expanded in terms of the unit matrix $\mathbb{1}_2$ and the Pauli matrices $\hat{\sigma}_i$ $(i = x,y,z)$. This allows to define $\hat{\rho}$ as

$$\hat{\rho} = \frac{1}{2}(\mathbb{1}_2 + \boldsymbol{P}\boldsymbol{\sigma}) \tag{1.23}$$

and hence the polarization is given by

$$\boldsymbol{P} = \begin{pmatrix} 2\mathrm{Re}(a^* b) \\ 2\mathrm{Im}(a^* b) \\ |a|^2 - |b|^2 \end{pmatrix} = \begin{pmatrix} \sin\theta\cos\Phi \\ \sin\theta\sin\Phi \\ \cos\theta \end{pmatrix}, \tag{1.24}$$

where θ and ϕ are the polar and azimuthal angles, respectively.

Larmor Precession

Larmor precession describes the precession of the neutron spin about an external magnetic field $\mathbf{B}$. The expectation value of the spin operator $\langle\hat{\boldsymbol{\sigma}}\rangle$ can be replaced in the classical picture by the vector $\boldsymbol{s}_n$. In the classical picture the spin $\boldsymbol{s}_n$ and the anti-parallel magnetic dipole moment $\boldsymbol{\mu}$ precess about the field direction $\mathbf{B}$. This motion is called Larmor precession and can be traced back to a torque which is exerted on the spin.

$$\mathbf{G} = \boldsymbol{\mu}_n \times \mathbf{B} = \gamma_L \boldsymbol{s}_n \times \mathbf{B} \tag{1.25}$$

From $\mathrm{d}L/\mathrm{d}t = M$ it follows that the time evolution of the spin in the external field is given by

$$\frac{\mathrm{d}\boldsymbol{s}}{\mathrm{d}t} = \gamma_L \boldsymbol{s}_N \times \mathbf{B}. \tag{1.26}$$

Applying an external field along the **z**-axis allows calculating the time evolution for each component of the spin

$$\frac{\mathrm{d}\boldsymbol{s}_x}{\mathrm{d}t} = \gamma_L s_y B, \quad \frac{\mathrm{d}\boldsymbol{s}_y}{\mathrm{d}t} = \gamma_L s_x B, \quad \frac{\mathrm{d}\boldsymbol{s}_z}{\mathrm{d}t} = 0. \tag{1.27}$$

The solutions of these differential equations are given by

$$s_x = s_x(0)\sin(\omega_L t + \phi_0), \quad s_y = s_y(0)\cos(\omega_L t + \phi_0), \quad s_z = s_z(0) \tag{1.28}$$

and directly show a rotation in the **xy**-plane perpendicular to the external magnetic field while the spin component s_z parallel to the field stays constant. The precession frequency is called Larmor frequency ω_L, namely

$$\omega_L = \gamma_L \cdot B. \tag{1.29}$$

Larmor precession can be used to manipulate and control the neutron spin direction. This is realized by applying fields of different strength B and length l along the flight pass of the neutron with wavelength λ. The precession angle depends on the time t the neutron stays in the field. With $\lambda = h/(m_n v)$ the precession angle is given by

$$\phi(\mathrm{rad}) = \omega_L \cdot t = 2\pi \cdot 2916 \cdot B(\mathrm{Gs})\frac{l(\mathrm{m})}{(v\frac{\mathrm{m}}{\mathrm{s}})} = 4.631 \cdot B(\mathrm{Gs})l(\mathrm{m})\lambda(\mathrm{Å}). \tag{1.30}$$

The preceding equation only describes the consequences of a constant magnetic field onto the spin. Special attention has to be drawn on regions where the field directions change and the neutron moves from an area of field $\boldsymbol{B}$ into a magnetic field $\boldsymbol{B}'$. The response depends on the transition frequency ω_H, with which $\boldsymbol{B}$ changes to $\boldsymbol{B}'$. One distinguishes between

Adiabatic transition: For slow changes of the field $\omega_L \gg \omega_H$ an adiabatic transition takes place. The neutron spin follows the direction of the changing field. Hence if the spin is aligned along $\boldsymbol{B}$ before the transition it will be aligned along $\boldsymbol{B}'$ afterwards (cf. Fig. 1.1 (a)).

Non-Adiabatic transition: In case of an abrupt field change $\omega_L \ll \omega_H$ a non-adiabatic transition takes place. This means the spin precesses in the beginning around $\boldsymbol{B}$ and after the transition about $\boldsymbol{B}'$ (cf. Fig. 1.1 b)).

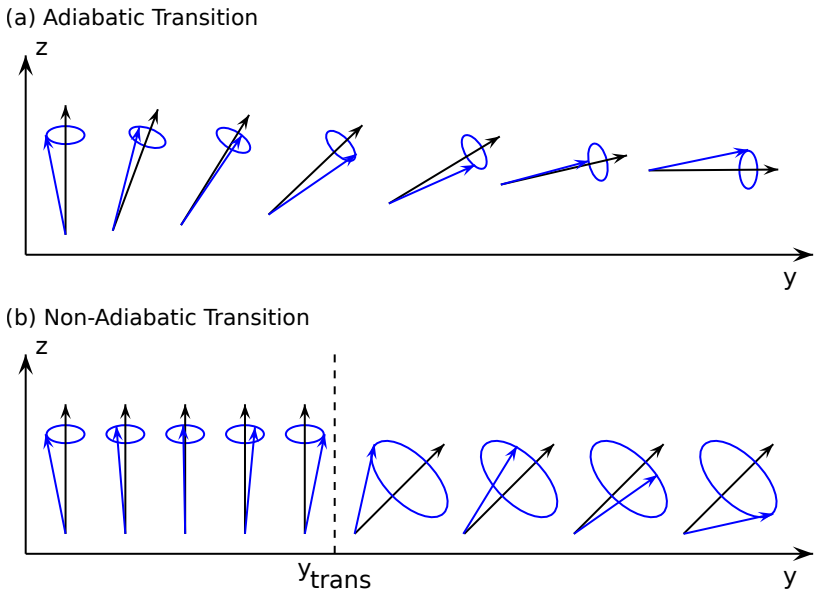

Figure 1.1.: Comparison between an adiabatic and a non-adiabatic field transition. The black arrows denote the magnetic field and the blue ones display the polarization. Figure (a) shows an adiabatic and figure (b) a non-adiabatic transition from a magnetic field originally aligned along the $\boldsymbol{z}$-axis onto the $\boldsymbol{y}$-axis. The non-adiabatic field change occurs at $\mathrm{y}_{\mathrm{trans}}$ in figure (b).

1.1.4. Polarized neutron scattering

In the previous sections 1.1.1 and 1.1.2 an unpolarized neutron beam was considered. To describe the scattering of a polarized neutron beam one has to account for the spin states of the incoming and outgoing neutrons σ_i and σ_f in equation (1.1). The

following section follows Ref. [50] and references therein.

Introducing Heisenberg operators allows to transform the time evolution of the sample states $|\lambda\rangle$ onto the operators. When also describing the neutrons by plane waves one can rewrite equation (1.1) as

$$\frac{\mathrm{d}^2\sigma}{\mathrm{d}\Omega\mathrm{d}\omega} = \left(\frac{m_\mathrm{n}}{2\pi\hbar^2}\right)^2 \frac{k_f}{k_i} \sum_{\sigma_i,\sigma_f} p_{\sigma_i} \langle\sigma_i|\hat{U}^\dagger_{\boldsymbol{Q}}(0)|\sigma_f\rangle\langle\sigma_f|\hat{U}_{\boldsymbol{Q}}(t)|\sigma_i\rangle \cdot \exp(-i\omega t). \tag{1.31}$$

Lovesey [48] has shown that the interaction potential of nuclear and magnetic scattering can be written in the form

$$\hat{U} = \hat{\beta} + \hat{\boldsymbol{\alpha}}\hat{\boldsymbol{\sigma}} \tag{1.32}$$

where $\hat{\beta}$ and $\hat{\boldsymbol{\alpha}}$ are operators having the dimension of length. They reflect the target system. $\hat{\beta}$ describes the spin independent and $\hat{\boldsymbol{\alpha}}$ the spin dependent part of the interaction potential. Hence evaluating the scattering cross-section for polarized neutrons it is sufficient to considering this general potential Eq. (1.32).

The crucial part is to calculate the average over all neutron spin states. This was first done in the 1960s by various groups [52–55], using the density matrix formalism. A detailed calculation is given in [48]. Here only some instructive steps are shown. The spin dependent part of equation (1.31) is

$$\sum_{\sigma_i} p_{\sigma_i} \sum_{\sigma_i'} \langle\sigma_i|\hat{U}^\dagger_{\boldsymbol{Q}}(0)|\sigma_f\rangle\langle\sigma_f|\hat{U}_{\boldsymbol{Q}}(t)|\sigma_i\rangle. \tag{1.33}$$

A diagonal density matrix $\hat{\rho}$ is given by

$$\hat{\rho} = \sum_\sigma p_\sigma |\sigma\rangle\langle\sigma| \tag{1.34}$$

and one can evaluate equation (1.33) in the following way

$$\sum_{\sigma_i} p_{\sigma_i} \sum_{\sigma_f} \langle\sigma_i|\hat{U}^\dagger(\boldsymbol{Q})|\sigma_f\rangle\langle\sigma_f|\hat{U}(\boldsymbol{Q})|\sigma_i\rangle = \mathrm{Tr}\hat{U}^\dagger\hat{U}\hat{\rho} = \mathrm{Tr}\hat{\rho}\hat{U}^\dagger\hat{U} \tag{1.35}$$

Now inserting the general interaction potential Eq. (1.32) and calculating the trace gives

$$\mathrm{Tr}\hat{\rho}\hat{V}^\dagger\hat{V} = \hat{\boldsymbol{\alpha}}^\dagger \cdot \hat{\boldsymbol{\alpha}} + \hat{\beta}^\dagger\hat{\beta} + \hat{\beta}^\dagger(\hat{\boldsymbol{\alpha}}\boldsymbol{P}) + (\hat{\boldsymbol{\alpha}}^\dagger\boldsymbol{P})\hat{\beta} + i\boldsymbol{P} \cdot (\hat{\boldsymbol{\alpha}}^\dagger \times \hat{\boldsymbol{\alpha}}). \tag{1.36}$$

In general the neutron spin state can also change during the scattering process. The interaction potential $\hat{V}$ transforms the initial polarization $\boldsymbol{P}$ to the final polarization

$\boldsymbol{P'}$. Thus the final polarization is given by

$$\boldsymbol{P'} = \frac{\mathrm{Tr}\hat{\rho}\hat{U}^\dagger\hat{\boldsymbol{\sigma}}\hat{U}}{\mathrm{Tr}\hat{\rho}\hat{U}^\dagger\hat{U}}. \tag{1.37}$$

Inserting the general potential Eq. (1.32) and calculating the $\mathrm{Tr}\hat{\rho}\hat{U}^\dagger\hat{\boldsymbol{\sigma}}\hat{U}$ gives

$$\begin{aligned}\mathrm{Tr}\hat{\rho}\hat{U}^\dagger\hat{\boldsymbol{\sigma}}\hat{U} =& \hat{\beta}^\dagger\hat{\boldsymbol{\alpha}} + \hat{\boldsymbol{\alpha}}^\dagger\hat{\beta} + \hat{\beta}^\dagger\hat{\beta}\boldsymbol{P} + \hat{\boldsymbol{\alpha}}^\dagger(\hat{\boldsymbol{\alpha}}\cdot\boldsymbol{P}) + (\hat{\boldsymbol{\alpha}}^\dagger\cdot\boldsymbol{P})\hat{\boldsymbol{\alpha}} - \boldsymbol{P}(\hat{\boldsymbol{\alpha}}^\dagger\cdot\hat{\boldsymbol{\alpha}}) \\ & - i\hat{\boldsymbol{\alpha}}^\dagger\times\hat{\boldsymbol{\alpha}} + i\hat{\beta}^\dagger(\hat{\boldsymbol{\alpha}}\times\boldsymbol{P}) + i(\boldsymbol{P}\times\hat{\boldsymbol{\alpha}}^\dagger)\hat{\beta}\end{aligned} \tag{1.38}$$

By a closer look to the nuclear and the magnetic interaction potential one can calculate the operators $\hat{\boldsymbol{\alpha}}$ and $\hat{\beta}$. In case of nuclear scattering only coherent scattering is considered and therefore the nuclear scattering potential (1.4) is spin independent and $\hat{\boldsymbol{\alpha}} = 0$. The spin independent part is given by

$$\hat{\beta} = \langle\boldsymbol{k'}|\hat{V}_N(\boldsymbol{r})|\boldsymbol{k}\rangle = N_{\boldsymbol{Q}}. \tag{1.39}$$

Magnetic scattering as described in section 1.1.2 is purely spin dependent leading to $\hat{\beta} = 0$ and

$$\hat{\boldsymbol{\alpha}} = \langle\boldsymbol{k'}|\hat{V}_M(\boldsymbol{r})|\boldsymbol{k}\rangle = (\gamma r_0)\hat{\boldsymbol{\sigma}}\cdot\boldsymbol{M}_{\perp\boldsymbol{Q}}. \tag{1.40}$$

The complete potential which will be considered here is

$$V(\boldsymbol{Q}) = N_{\boldsymbol{Q}} + (\gamma r_0)\hat{\boldsymbol{\sigma}}\cdot\boldsymbol{M}_{\perp\boldsymbol{Q}}. \tag{1.41}$$

Inserting Eq. (1.39), (1.40) and (1.36), (1.33) in (1.35) gives the double differential scattering cross-section

$$\begin{aligned}\frac{d^2\sigma}{d\Omega dE'} =& \frac{k'}{k}\frac{1}{2\pi\hbar}\int \mathrm{d}t\,[\\ & \left\langle N_{\boldsymbol{Q}}N_{\boldsymbol{Q}}^\dagger\right\rangle && \text{pure nuclear contribution} \\ & + (\gamma r_0)^2\left\langle M_{\perp\boldsymbol{Q}}M_{\perp\boldsymbol{Q}}^\dagger\right\rangle && \text{pure magnetic contribution} \\ & + (\gamma r_0)\boldsymbol{P}\left[\left\langle N_{\boldsymbol{Q}}^\dagger M_{\perp\boldsymbol{Q}}\right\rangle + \left\langle M_{\perp\boldsymbol{Q}}^\dagger N_{\boldsymbol{Q}}\right\rangle\right] && \text{nuclear-magnetic interference} \\ & - i(\gamma r_0)\boldsymbol{P}\left\langle M_{\perp\boldsymbol{Q}}\times M_{\perp\boldsymbol{Q}}^\dagger\right\rangle && \text{chiral magnetic contribution} \\ &]\exp(i\omega t).\end{aligned} \tag{1.42}$$

The change of the initial polarization $\boldsymbol{P}$ to the polarization after scattering $\boldsymbol{P'}$ is given by Eq. (1.37). Inserting Eq. (1.39), (1.40) in (1.36), (1.38) and then everything

in equation (1.37) gives

$$\begin{aligned}\boldsymbol{P'}\frac{d^2\sigma}{d\Omega dE'} =& \frac{k'}{k}\frac{1}{2\pi\hbar}\int \mathrm{d}t\,[\,\boldsymbol{P}\left\langle N_{\boldsymbol{Q}}N_{\boldsymbol{Q}}^{\dagger}\right\rangle - (\gamma r_0)^2\boldsymbol{P}\left\langle M_{\perp\boldsymbol{Q}}M_{\perp\boldsymbol{Q}}^{\dagger}\right\rangle \\ &+ (\gamma r_0)^2\left\langle (\boldsymbol{P}M_{\perp\boldsymbol{Q}}^{\dagger})M_{\perp\boldsymbol{Q}}\right\rangle + (\gamma r_0)^2\left\langle M_{\perp\boldsymbol{Q}}^{\dagger}(\boldsymbol{P}M_{\perp\boldsymbol{Q}})\right\rangle \\ &+ (\gamma r_0)\left(\left\langle N_{\boldsymbol{Q}}^{\dagger}M_{\perp\boldsymbol{Q}}\right\rangle + \left\langle M_{\perp\boldsymbol{Q}}^{\dagger}N_{\boldsymbol{Q}}\right\rangle\right) \\ &+ i(\gamma r_0)\boldsymbol{P}\times\left(\left\langle M_{\perp\boldsymbol{Q}}^{\dagger}N_{\boldsymbol{Q}}\right\rangle - \left\langle N_{\boldsymbol{Q}}^{\dagger}M_{\perp\boldsymbol{Q}}\right\rangle\right) \\ &+ i(\gamma r_0)^2\left\langle M_{\perp\boldsymbol{Q}}\times M_{\perp\boldsymbol{Q}}^{\dagger}\right\rangle\,]\exp(-i\omega t). \end{aligned} \tag{1.43}$$

Equations (1.42) and (1.43) are called the Blume-Maleyev equations [53, 55]. The first describes the energy transfer and the direction of the scattered neutrons while the second describes the polarization of the scattered beam. These equations can be rewritten in a tensor form as it is shown in [56, 57]. Considering a frame of reference where $\boldsymbol{Q}$ is parallel to the $\boldsymbol{x}$-axis. With the abbreviations given in table 1.1 the scattering cross-section (1.42) can be rewritten.

$$\sigma \equiv \frac{d^2\sigma}{d\Omega dE'} \equiv N + M^y + M^z - P^xC + P^yR^y + P^zR^z \tag{1.44}$$

The first term N is the pure nuclear contribution from eq. (1.42). M^y and M^z describe the pure magnetic scattering. These contributions are polarization independent and still present if an unpolarized beam is used. The term C which is linear in P_x describes the chiral magnetic contribution. There are two independent interactions present in the sample, therefore scattered neutrons from these two interactions can interfere leading to the nuclear-magnetic interference described by R^y and R^z.

Introducing the polarization tensor $\overline{\boldsymbol{P}}$ and the polarization created in the scattering process $\boldsymbol{P''}$ allows to formulate the expression for the scattered polarization $\boldsymbol{P'}$ with respect to the incident polarization $\boldsymbol{P}$ in a tensor equation.

$$\boldsymbol{P'} = \overline{\boldsymbol{P}}\boldsymbol{P} + \boldsymbol{P''} \tag{1.45}$$

The polarization tensor $\overline{\boldsymbol{P}}$ and the created polarization $\boldsymbol{P''}$ are given by

$$\sigma\overline{\boldsymbol{P}} = \begin{pmatrix} (N - M^y - M^z) & -iI^z & iI^y \\ iI^z & (N + M^y - M^z) & M_{\mathrm{mix}} \\ -iI^y & M_{\mathrm{mix}} & (N - M^y + M^z) \end{pmatrix}, \quad \sigma\boldsymbol{P''} = \begin{pmatrix} C \\ R^y \\ R^z \end{pmatrix}. \tag{1.46}$$

This formalism describes how additional information about the magnetic structure of some sample can be extracted from a scattering experiment. Therefore one has

Table 1.1.: Description of the terms contained in 1.42 and 1.43 after [57]

term	correlation functions	description
N	$\frac{k'}{k}\left\langle N_{\boldsymbol{Q}} N^{\dagger}_{\boldsymbol{Q}}\right\rangle_{\omega}$	Nuclear contribution
$M^{y/z}$	$r_0^2\frac{k'}{k}\left\langle M^{y/z}_{\perp\boldsymbol{Q}} M^{\dagger y/z}_{\perp\boldsymbol{Q}}\right\rangle_{\omega}$	$y-$ and $z-$components of the magnetic contribution
$R^{y/z}$	$r_0\frac{k'}{k}\left\langle N^{\dagger}_{\boldsymbol{Q}} M^{y/z}_{\perp\boldsymbol{Q}}\right\rangle_{\omega} + \left\langle M^{\dagger y/z}_{\perp\boldsymbol{Q}} N_{\boldsymbol{Q}}\right\rangle_{\omega}$	Real parts of the nuclear-magnetic interference term
$I^{y/z}$	$r_0\frac{k'}{k}\left\langle N^{\dagger}_{\boldsymbol{Q}} M^{y/z}_{\perp\boldsymbol{Q}}\right\rangle_{\omega} - \left\langle M^{\dagger y/z}_{\perp\boldsymbol{Q}} N_{\boldsymbol{Q}}\right\rangle_{\omega}$	Imaginary parts of the nuclear-magnetic interference term
C	$ir_0^2\frac{k'}{k}\left(\left\langle M^{y}_{\perp\boldsymbol{Q}} M^{\dagger z}_{\perp\boldsymbol{Q}}\right\rangle_{\omega} + \left\langle M^{z}_{\perp\boldsymbol{Q}} M^{\dagger y}_{\perp\boldsymbol{Q}}\right\rangle_{\omega}\right)$	Chiral contribution
M_{mix}	$r_0^2\frac{k'}{k}\left(\left\langle M^{y}_{\perp\boldsymbol{Q}} M^{\dagger z}_{\perp\boldsymbol{Q}}\right\rangle_{\omega} + \left\langle M^{z}_{\perp\boldsymbol{Q}} M^{\dagger y}_{\perp\boldsymbol{Q}}\right\rangle_{\omega}\right)$	Mixed magnetic contribution or magnetic-magnetic interference term

to measure the polarization of the scattered beam. Such an experiment will allow to measure the polarization matrix $\check{P}$ of the sample. $\check{P}$ connects the formalism introduced by Blume and Maleyev with the experiment. The polarization matrix $\check{P}$ is defined using equation (1.45) by

$$\check{P}_{ij} = (P_j \overline{P}_{ji} + P_i'')/|\boldsymbol{P}|, \tag{1.47}$$

with $i,j = x,y,z$. The index i describes the direction of the outgoing polarization and the index j the direction of the incoming polarization. In order to measure $\check{P}$ one has to perform a polarization analysis experiment. This will be explained in Sec. 1.3.1.

1.2. Small angle neutron scattering

Small angle Neutron Scattering (SANS) is used to study large magnetic or nuclear structures ranging from 50 to 2000 Å. A schematic drawing of a typical SANS instrument is shown in Fig. 1.2. The white neutron beam provided by the neutron source enters the instrument from the left, where the mechanical velocity selector selects a wavelength band from the cold spectrum. The wavelength band has typically a width of $\Delta\lambda/\lambda = 0.05 - 0.20$. In a SANS instrument the divergence of the neutron beam is adjusted by the length of the collimation L_1 with typical length of 2-20 m. After the collimation the neutron beam hits the sample and scatters into the detector vessel. The detector is positioned at a distance L_2 (typical 2-20 m) from the sample. A SANS detector is typically two dimensional. Both collimation and detector vessel are evacuated in order to reduce absorption and scattering from air.

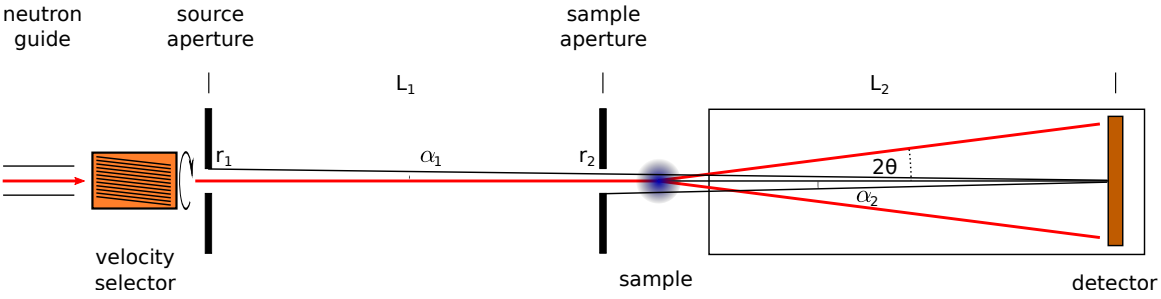

Figure 1.2.: Sketch of a typical small angle neutron scattering setup. The wavelength distribution can be adjusted by the mechanical velocity selector. Afterwards the neutron beam enters the collimation were the divergence of the beam is adjusted by two apertures, i.e. the source and the sample aperture. After the sample the neutron beam enters the detector vessel.

1.2.1. Resolution function for small angle scattering

In a real experiment not only scattering with a scattering vector q contributes to the measured signal but also scattering in a finite range around $\bar{q}$. In the following text we want to describe how to calculate the finite resolution of a SANS instrument due to a finite wavelength spread and the collimation of the neutron beam. We follow the description by Pedersen *et al.* [58]. The resolution can be described by the resolution function $R(q,\bar{q})$, where $\bar{q}$ is the mean scattering vector. $R(q,\bar{q})$ enters the expression of the measured intensity $I(\bar{q})$ through

$$I(\bar{q}) = \int \frac{\mathrm{d}\sigma(q)}{\mathrm{d}\omega} \cdot R(q,\bar{q})\mathrm{d}q. \tag{1.48}$$

For our discussion all contributions to the resolution function $R(q,\bar{q})$ are assumed to have a Gaussian shape.

As described above the wavelength of a SANS instrument is typically defined by a mechanical velocity selector, which gives a triangular shaped wavelength distribution. For simplicity, this is approximated by a Gaussian distribution, with the full width at half maximum (FWHM) $\sigma_\lambda = \Delta\lambda/(2\sqrt{2\ln 2})$. The FWHM of the q distribution due to the wavelength spread σ_w is then given by

$$\sigma_w = \bar{q}\frac{\Delta\lambda}{\bar{\lambda}}\frac{1}{2\sqrt{2\ln 2}}. \tag{1.49}$$

For the experimental resolution due to finite collimation, we consider the setup as shown in figure 1.2. The collimation is defined by to apertures, the source aperture at the beginning of the instrument and the defining aperture in front of the sample. Both are considered to be of a circular shape with radius r_1 and r_2. The distance

between the source aperture and the defining aperture is L_1 and the later and the detector is L_2. We consider that both L_1 and L_2 are large compared to the radii r_1 and r_2. The half angular extent from one point of the detector to the source aperture is $\alpha_1 = r_1/(L_1 + L_2)$ and to the sample aperture $\alpha_2 = r_2/L_2$.

One can distinguish two cases, first scattering at $\bar{q} \approx 0$. In this case the scattering is given by a delta function $\delta(q)$, hence the resolution function $R(q,\bar{q})$ is given by the direct beam profile. Second, we consider the case for scattering with $\bar{q} \neq 0$. The angular distribution perpendicular to the scattering plane is given by

$$\Delta\beta_1 = \frac{2r_1}{L_1} - \frac{1}{2}\frac{r_2^2}{r_1}\frac{\cos^4 2\bar{\theta}}{L_2^2 L_1} \qquad \text{for } \alpha_1 \leq \alpha_2 \quad (1.50)$$

$$\Delta\beta_1 = 2r_2\left(\frac{1}{L_1} + \frac{\cos^2 2\bar{\theta}}{L_2}\right) - \frac{1}{2}\frac{r_1^2}{r_2}\frac{L_2}{L_1}\frac{1}{\cos^2 2\theta(L_1 + L_2/\cos^2 2\theta)} \qquad \text{for } \alpha_1 < \alpha_2. \quad (1.51)$$

The distribution in the scattering plane is given by

$$\Delta\beta_2 = \frac{2r_1}{L_1} - \frac{1}{2}\frac{r_2^2}{r_1}\frac{\cos^2 2\bar{\theta}}{L_2^2 L_1}\left(L_1 + \frac{L_2}{\cos 2\bar{\theta}}\right)^2 \qquad \text{for } \alpha_1 \geq \alpha_2 \quad (1.52)$$

$$\Delta\beta_2 = 2r_2\left(\frac{1}{L_1} + \frac{\cos 2\bar{\theta}}{L_2}\right) - \frac{1}{2}\frac{r_1^2}{r_2}\frac{L_2}{L_1}\frac{1}{\cos 2\theta(L_1 + L_2/\cos 2\theta)} \qquad \text{for } \alpha_1 < \alpha_2 \quad (1.53)$$

With the angular distributions one can calculate the FWHM of the q distribution for both in plane and out of plane scattering

$$\sigma_{C1} = \bar{k}\cos\bar{\theta}\frac{\Delta\beta_1}{2\sqrt{2\ln 2}} \quad (1.54)$$

$$\sigma_{C2} = \bar{k}\frac{\Delta\beta_2}{2\sqrt{2\ln 2}}. \quad (1.55)$$

The resolution function due to finite collimation is given by the product of the in plane and out of plane q distributions

$$R_C(q,\bar{q}) = \frac{1}{2\pi\sigma_{C1}\sigma_{C2}}\exp\left[-\frac{1}{2}\left(\frac{(q_1 - \bar{q})^2}{\sigma_{C1}^2} + \frac{q_2^2}{\sigma_{C2}^2}\right)\right]. \quad (1.56)$$

The prefactor normalizes the resolution function to unity when integrating the two dimensional q space.

1.3. Spherical Neutron Polarimetry

1.3.1. Polarization Analysis

In a polarization analysis experiment the neutron beam polarization of the incoming and outgoing beam is well defined. The first experiments making use of polarized neutrons were performed Nathans *et al.* [59] in 1959 to identify the magnetic structure of nickel and iron. For this experiment the beam was either polarized up or down. Ten years later the setup was improved by Moon and Riste [60] to the so called longitudinal polarization analysis (Fig. 1.3 (a)). Using two spin flippers before and after the sample allows to distinguish between spin flip and non-spin flip scattering and therefore to separate magnetic and nuclear scattering by aligning the incoming polarization parallel to $\boldsymbol{Q}$. In this configuration all magnetic scattering is spin flip. Separation of spin flip and non-spin flip scattering also allows distinguishing coherent and incoherent scattering. For the XYZ-method the spin-flippers around the sample are replaced by field regions in which the field direction is adiabatically changed to any direction (Fig. 1.3 (b)). All techniques discussed above utilize a guide field at the sample position to maintain the polarization. Polarization components that are not aligned parallel to this guide field are depolarized and cannot be measured. These techniques only allow measuring the main diagonal of the polarization matrix Eq. (1.47).

A full polarization analysis also accessing the off diagonal elements of the polarization matrix can only be realized by a zero field region at the sample. In this so called Spherical Neutron Polarimetry (SNP) [61] (Fig. 1.3 (c)) the manipulation of the incoming P_{in} and outgoing P_{out} polarization takes place before and after the zero-field region and the transition from guide field to zero field and back to guide field is non-adiabatic.

1.3.2. Devices for Spherical Neutron Polarimetry

There are three different types of devices capable to perform a full SNP measurement, CryoPAD, MuPAD and MiniMuPAD. CryoPAD (CRYOgenic Polarization Analysis Device) was the first SNP device invented by Tasset *et al.* in 1989 [61, 62]. The zero field at the sample is here realized by double cryogenic Meissner shielding made of niobium and an additional MuMetal shielding. In the meantime a third generation CryoPAD [63] with an accuracy of better than 0.5° exists. In Fig. 1.4 (a) a schematic drawing of CryoPAD is shown.

An alternative device for spherical polarization analysis is the so called MuPAD (MU-Metal Polarization Analysis Device). MuPAD was presented in 2004 by Janoschek *et al.* [64]. In contrast to CryoPAD, MuPAD uses only a double mu-metal shielding to maintain the zero field region between the up and downstream polarization ma-

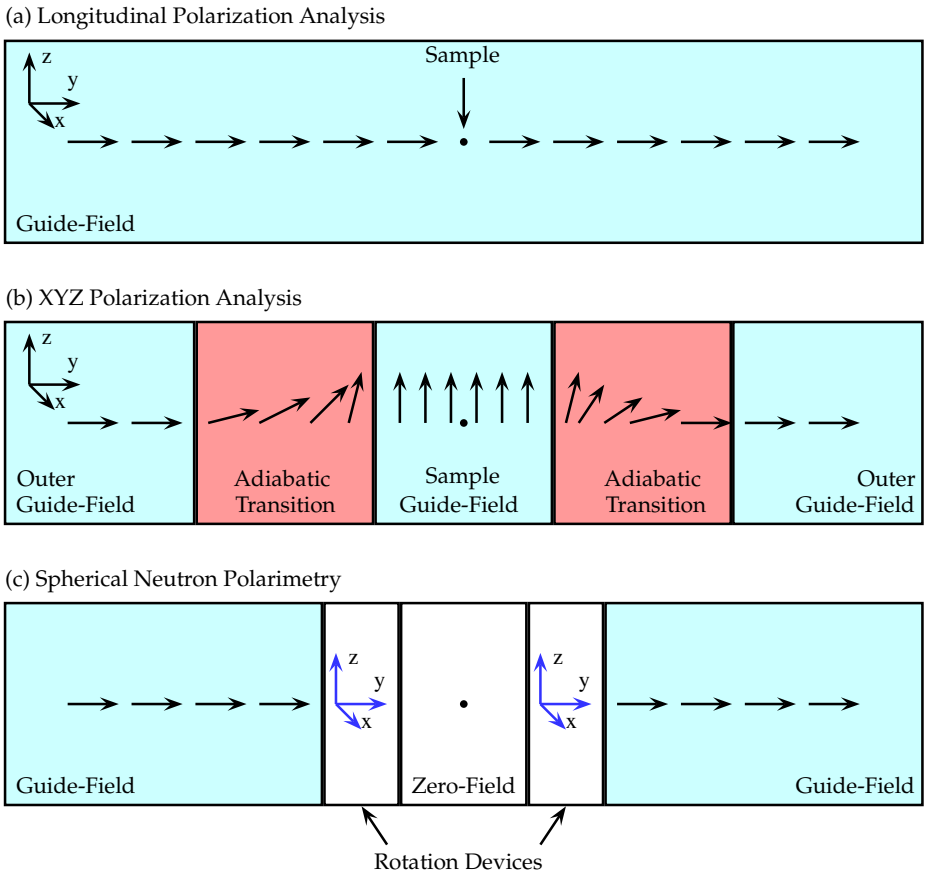

Figure 1.3.: The black arrows denote the guide field direction. Figure (a) shows a setup for longitudinal polarization analysis. The guide-field is in one direction through the whole setup. Figure (b) displays the XYZ-method. In this method one can align the guide-field at the sample position along any direction. The guide field in the rest of the setup is constant. The change from the outer guide field to the field at the sample is conducted in an adiabatic transition. Figure (c) displays an SNP setup. The guide field ends non-adiabatically at some rotation device where the spin is aligned in the desired direction (indicated by the blue reference frame). At the sample region is no magnetic field. Behind the sample the spin performs a non-adiabatic transition from zero-field into the rotation device. Here the polarization is aligned from any arbitrary direction onto the guide field of the instrument. The figure is taken from [50].

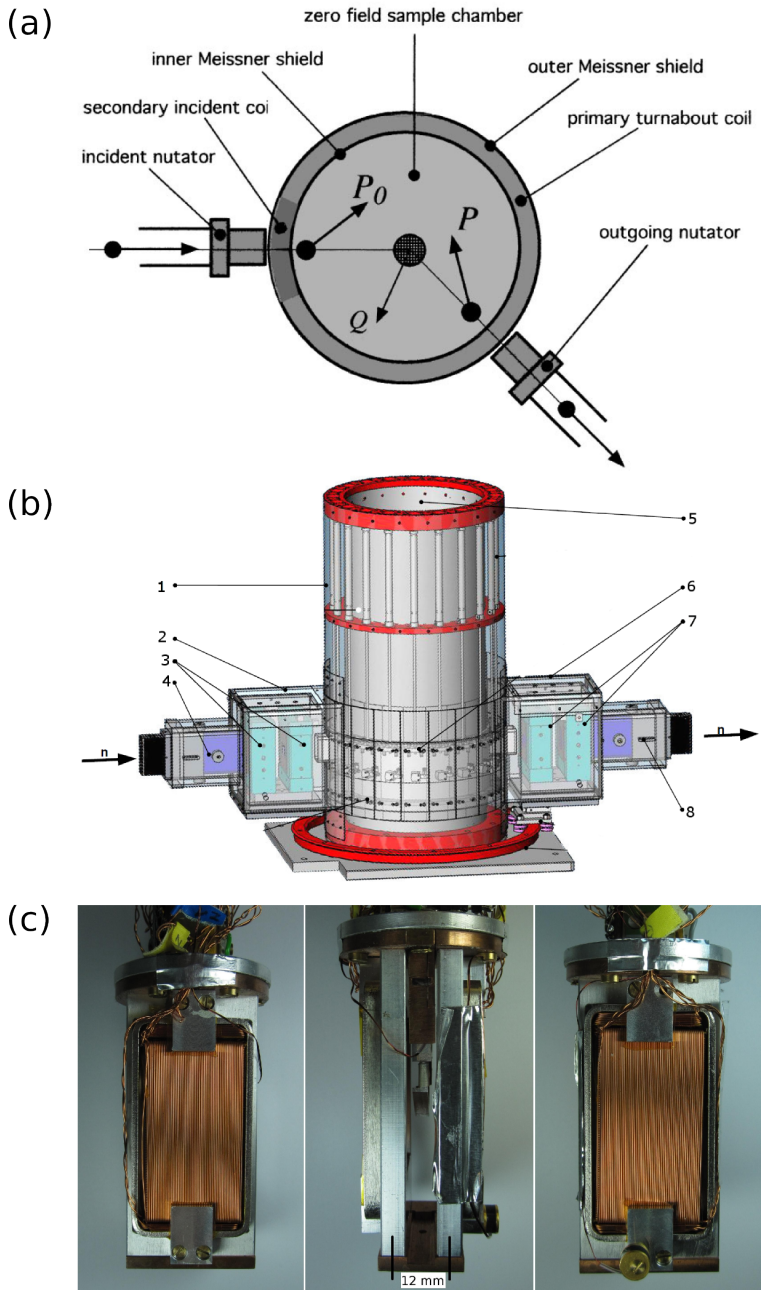

Figure 1.4.: Different Spherical Neutron Polarimetry (SNP) devices. (a) Schematic drawing of CryoPAD taken from [62]. The figure shows the field geometry and the important components to manipulate the neutron spin polarization. (b) Technical drawing of MuPAD taken from [57]. (1) Mu-Metal, (2) primary immobile arm, (3) precession coils to manipulate the incoming polarization, (4) coupling coil for incoming beam, (5) opening for inserting the cryostat, (6) secondary movable arm, (7) precession coils to manipulate the outgoing polarization and (8) the outgoing coupling coil. (c) Picture of the MiniMuPAD, with front view (left), side view (center) and back view.

nipulation components. The shielding reduces the external fields to less than 1 mG. The polarization is coupled in and out of the shielded regions by coupling coils. An overview of the main components of MuPAD is shown in Fig. 1.4 (b). MuPAD is about 1.5 m long from the beginning of the primary arm to the end of the secondary arm.

CryoPAD and MuPAD exhibit some disadvantages concerning mechanical handling and the effort for operation. The long flight paths of MuPAD and CryoPAD require a lot of effort to control the polarization direction and allow only a small divergence of the beam. To overcome these problems we have invented a very small and compact device, the so called MiniMuPAD (MINI MU-Metal Polarization Analysis Device) [15, 50]. The MiniMuPAD is shown in Fig. 1.4 (c). It is only 48 mm in diameter and is designed to be mounted within the cryostat. There is no extra magnetic shielding to realize a zero field region at the sample position. Parasitic rotations are suppressed by the Mu-Metal yokes around the precession coils and the fact, that the distance between the coils is only about 12 mm. Hence, a neutron with a wavelength of 1 Å precesses only about 1° in a field of 0.03 mT as for example the earth's magnetic field. MiniMuPAD allows full SNP measurements with an accuracy better than 3°.

1.4. Neutron Spin Echo Techniques

Neutron Spin Echo (NSE) proposed in 1972 by Mezei [28, 29] measures the neutron velocity difference before and after the scattering process by comparing the Larmor precession phase of the neutron spin in exactly predefined magnetic field integrals. NSE reaches the highest energy resolution of all neutron spectroscopy techniques. Since 1972 several other Larmor techniques were reported, increasing the field of application. In 1987 Golub and Gähler developed Neutron Resonance Spin Echo (NRSE) [30] were the constant field regions of NSE are replaced by a combination of a constant and an oscillating field. The magnetic field geometry in NRSE allows manipulating the neutron spin phase across the beam cross section, to perform Larmor diffraction or phonon focusing. Nevertheless, all these techniques do not allow depolarizing conditions at the sample position, like strong magnetic fields or depolarizing samples. Modulation of IntEnsity with Zero Effort (MIEZE) [32, 39, 40] overcomes this problem. In MIEZE all neutron spin manipulation is performed in front of the sample, making the technique insensitive for beam depolarization at the sample.

In the following sections NSE, NRSE and MIEZE are introduced following Ref. [65].

1.4.1. Neutron Spin Echo (NSE)

Fig. 1.5 (a) shows a schematic depiction of a NSE spectrometer. The neutron beam travels along the y-axis entering the spectrometer from the left hand side. First the beam passes the polarizer were it is polarized along the z-axis. After the polarizer the beam travels along the first precession region of distance L_1 and magnetic field B_0^1, the sample region and the second precession region of distance L_2 and magnetic field B_0^2. Before the beam reaches the detector it is analyzed along the z-axis.

Let us consider a single neutron with velocity v_1 traveling through the spectrometer. The neutron performs Larmor precession in the magnetic field and accumulates a spin phase ϕ_1. According to equation (1.29) and (1.30) ϕ_1 is given by

$$\phi_1 = \gamma B_0^1 \cdot t_1 = \gamma B_0^1 \cdot \frac{L_1}{v_1}. \tag{1.57}$$

After the scattering process at the sample the neutron has the velocity v_2 and the spin phase ϕ_2 accumulated in the second precession region is given by

$$\phi_2 = \gamma B_0^2 \cdot t_2 = \gamma B_0^2 \cdot \frac{L_2}{v_2}. \tag{1.58}$$

The total spin phase ϕ is

$$\phi = \phi_1 + \phi_2 = \gamma \left(\frac{B_1 L_1}{v_1} + \frac{B_2 L_2}{v_2} \right) = \gamma B L \left(\frac{1}{v_1} - \frac{1}{v_2} \right) \tag{1.59}$$

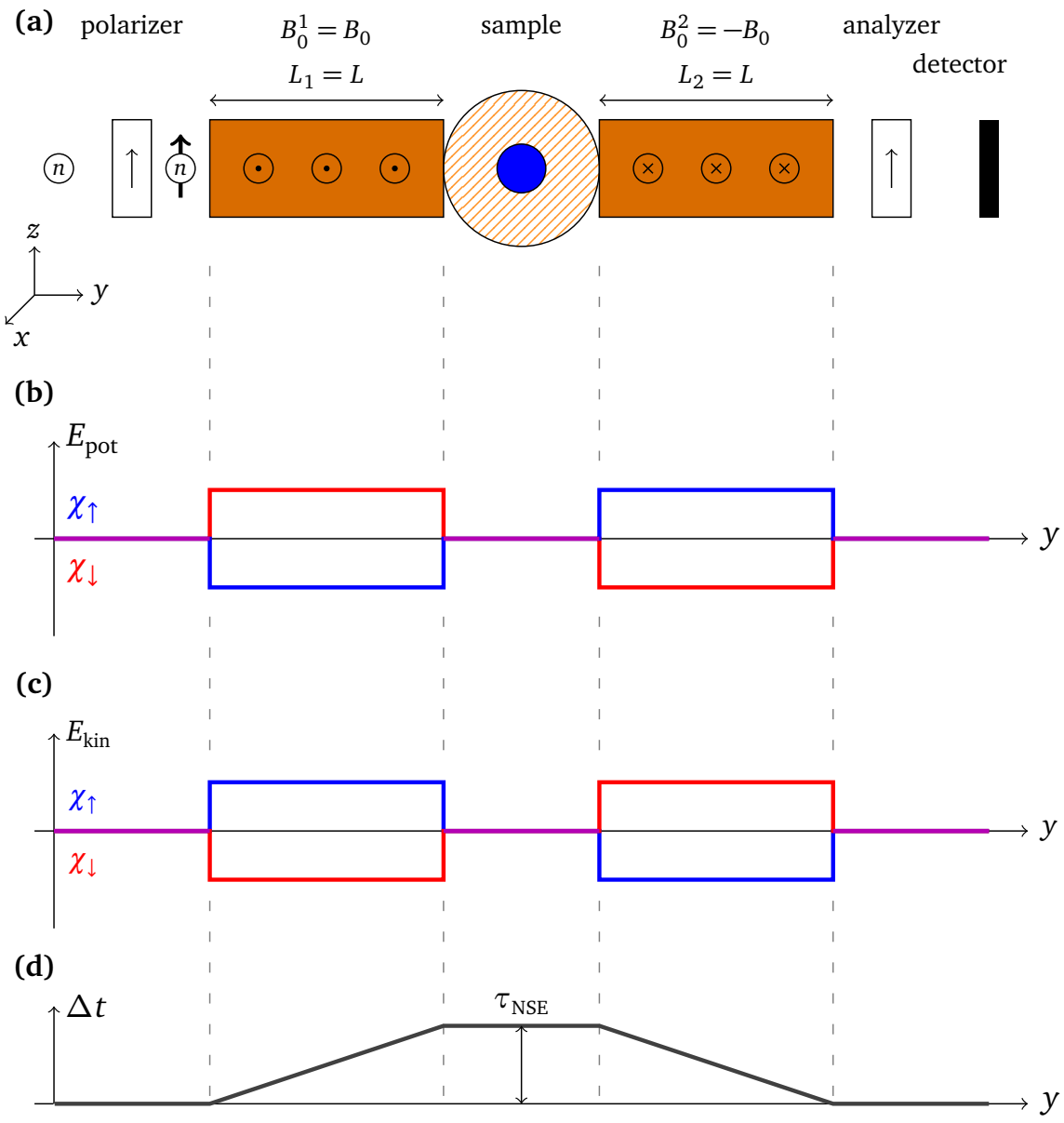

Figure 1.5.: (a) Schematic drawing of a NSE spectrometer. The neutron beam travels along the y-axis passing the polarizer, the first precession field B_0^1, the second precession field B_0^2 and the analyzer until it reaches the detector. (b) and (c) show the potential and kinetic energy of the eigenstates $\chi_\uparrow$ and $\chi_\downarrow$ as function of the neutron flight path. In (d) the flight time difference Δt of the eigenstates $\chi_\uparrow$ and $\chi_\downarrow$ as function of the neutron flight path. The spin echo time τ_{NSE} is given by the flight time difference Δt at the sample position. Figure taken from Ref. [66].

where in the last step we considered that $L_1 = L_2$ and $B_1 = -B_2$. In a quasielastic scattering process the energy transfer between sample and neutron is small and hence the velocity change, therefore one can define $v_2 = v_1 + \delta v$ with $\delta v \ll v_1$. This allows to rewrite Eq. (1.59)

$$\phi = \gamma BL \left(\frac{1}{v_1} - \frac{1}{v_1 + \delta v} \right) = \gamma BL \left(\frac{\delta v}{v_1^2 + v_1 \delta v} \right) \approx \gamma BL \frac{\delta v}{v_1^2}. \tag{1.60}$$

The energy transfer due to the scattering process is given by

$$\begin{aligned} \hbar\omega = \frac{m_n}{2}((v_1 + \delta v)^2 - v_1^2) &= \frac{m_n}{2}(2v_1\delta v + \delta v^2) \\ &\approx \frac{m_n}{2}(2v_1\delta v) \\ &= m_n v_1 \delta v. \end{aligned} \tag{1.61}$$

Now one can rewrite the total spin phase in terms of the transfered energy

$$\phi = \gamma BL \frac{\hbar\omega}{m_n v_1^3} = \left(\frac{\gamma\hbar BL}{m_n v_1^3} \right) \omega = \tau_{NSE}\omega. \tag{1.62}$$

In this expression the spin echo time τ_{NSE} is defined by

$$\tau_{NSE} = \left(\frac{\gamma\hbar BL}{m_n v_1^3} \right), \tag{1.63}$$

which is a measure for the resolution of the spin echo spectrometer. In order to reach high resolution, which means large τ_{NSE} one needs large magnetic field integrals BL and it is advantageous to use a large neutron wavelength.

The polarization of the neutron beam in the z direction is given by the average over all spin phases ϕ present in the beam $P =< \sigma_z >=< \cos\phi >$ (compare with Eq. (1.21)). The spin phase depends on the energy transfer $\hbar\omega$ and the probability that a neutron is scattered with this energy transfer is given by $S(q,\omega)\mathrm{d}\omega$, therefore the polarization is given by

$$P =< \sigma_x >=< \cos\phi >= \int S(q,\omega) \cos\omega\tau_{NSE} \mathrm{d}\omega, \tag{1.64}$$

which is nothing else then the intermediate scattering function $I(q,\tau_{NSE})$.

Besides the classical description NSE can also be described in a semi-classical picture. For the semi-classical picture we choose the quantization axis to be along x. The initial neutron polarization is considered to be along the z direction, being an eigenstate of $< \sigma_z >$, given by $\boldsymbol{\chi}^z_\uparrow$. As the quantization axis is chosen to be along x i.e. as defined by the field direction, the initial spin state can be described in eigenstates

of $< \sigma_x >$ by

$$\boldsymbol{\chi}^z_\uparrow = \frac{1}{\sqrt{2}}(\boldsymbol{\chi}^x_\uparrow + \boldsymbol{\chi}^x_\downarrow) = \frac{1}{\sqrt{2}} \begin{pmatrix} 1 \\ 1 \end{pmatrix}^x . \tag{1.65}$$

The semi-classical description considers the classical trajectories of the quantum mechanical eigenstates to explain the neutron spin echo principle. The up eigenstate $\chi_\uparrow$ has a magnetic moment opposite to the constant magnetic field B_0 and $\chi_\downarrow$ a magnetic moment parallel to B_0. This leads to different potential energies in the precession field regions as shown in figure 1.5 (b). The potential energy is given by

$$E^{\uparrow/\downarrow}_{\text{pot}} = \pm \mu B. \tag{1.66}$$

For the spin up state $\chi_\uparrow$ the potential energy is decreased while the potential energy of the down sate $\chi_\downarrow$ is increased while entering the magnetic field regions. At the same time the total energy is conserved as the magnetic field in the precession regions is constant in time. Therefore the kinetic energy for each of the spin states has to change accordingly in order to conserve the total energy. The kinetic energy is shown in figure 1.5 (c) and the change of kinetic energy for the up and down state is given by

$$E^{\uparrow/\downarrow}_{\text{kin}} = E_{\text{ges}} \mp E^{\uparrow/\downarrow}_{\text{pot}} = E_{\text{ges}} \left(1 \mp \frac{E^{\uparrow/\downarrow}_{\text{pot}}}{E_{\text{ges}}} \right). \tag{1.67}$$

These different kinetic energies for each spin state can be translated to different velocities and associated with different times $t^{\uparrow/\downarrow}$ needed to travel the precession regions. The traveling time is given by

$$t^{\uparrow/\downarrow} = \frac{L}{v^{\uparrow/\downarrow}} = \frac{L}{v_0} \mp \frac{\hbar \gamma B_z L}{2 m v_0^3} = t_0 \mp \frac{\tau_{NSE}}{2}. \tag{1.68}$$

This expression shows that the delay between both spin states after the first precession region is the spin echo time τ_{NSE}

$$t^\downarrow - t^\uparrow = \tau_{NSE}. \tag{1.69}$$

The time delay Δt is also shown in figure 1.5 (d).

1.4.2. Neutron Resonance Spin Echo (NRSE)

Neutron resonance spin echo (NRSE) is a variant of the NSE where the precession field regions are replaced by two resonant spin flipper coils separated by a distance L. A schematic drawing of a NRSE spectrometer is shown in Fig. 1.6 (a). The resonant spin flipper coils, called NRSE coils, consist of a constant B_0 and a rotating magnetic field B_{rf}. The B_0 field points along the x axis, perpendicular to the precession plane x,y while B_{rf} is in the precession plane, rotating with frequency ω. We consider the neutron beam again being initially polarized along the z axis. The magnetic field

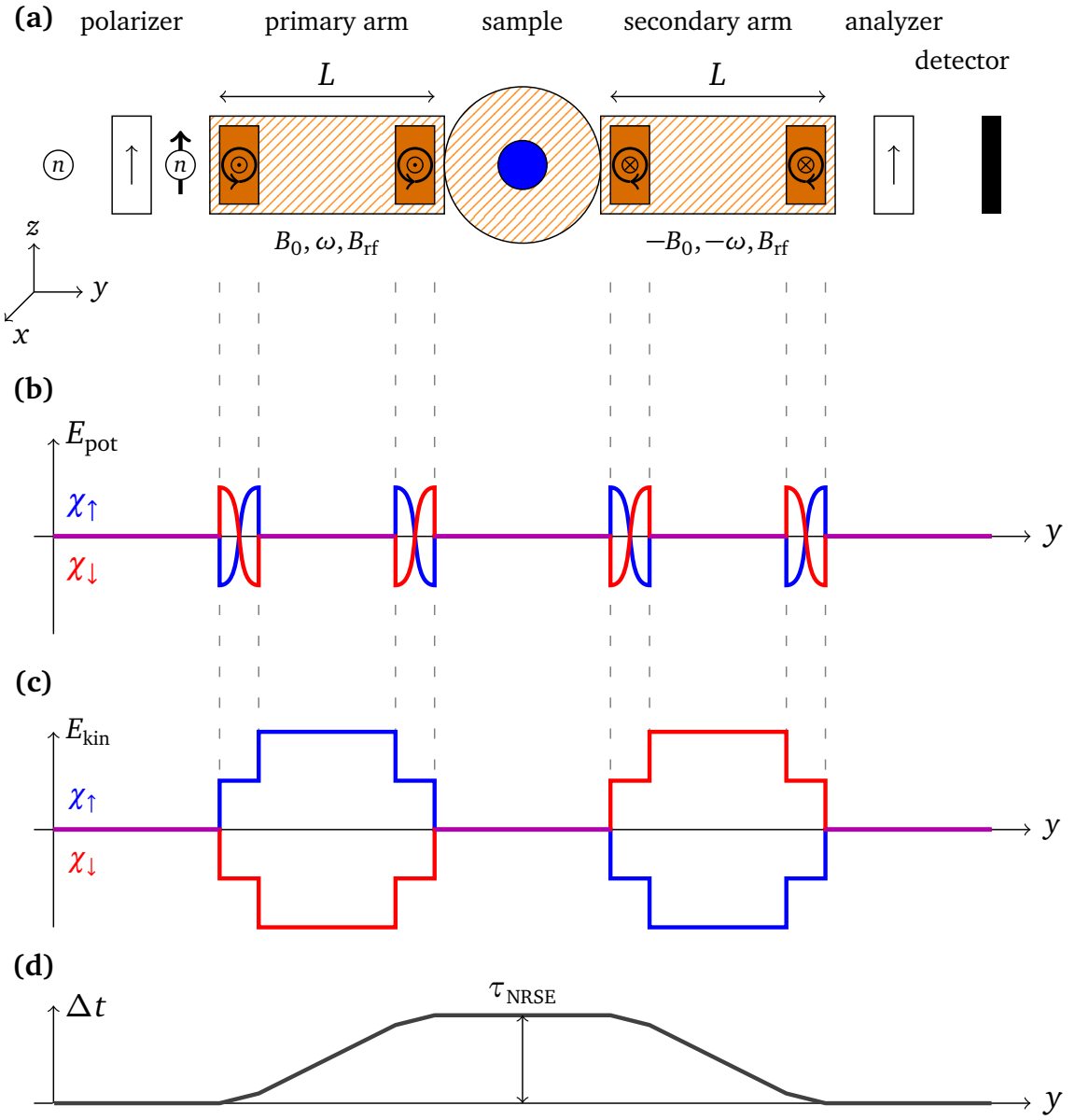

Figure 1.6.: (a) Schematic drawing of a NRSE spectrometer. The neutron beam enters the spectrometer from the left side and passes the polarizer, the two precession regions, and the analyzer until it reaches the detector. In contrast to NSE the precession regions consist of two resonant spin flippers at the beginning and the end. In panel (b) and (c) the kinetic and potential energy of the eigenstates $\chi_\uparrow$ and $\chi_\downarrow$ as function of the neutron flight path are shown. Panel (d) displays the flight time difference Δt of the eigenstates $\chi_\uparrow$ and $\chi_\downarrow$ as function of the neutron flight path. The spin echo time τ_{NSE} is given by the flight time difference Δt at the sample position. Taken from Ref. [66].

produced by the NRSE coil can be described by

$$\boldsymbol{B} = \begin{pmatrix} B_{rf}\cos(\omega t) \\ B_{rf}\sin(\omega t) \\ B_0 \end{pmatrix}. \tag{1.70}$$

When the neutrons enter the NRSE coil, they start to precess about B_0. The effect of the rotating field on the neutron spin can be understood in a coordinate frame precessing with the spin. If the NRSE coil is at resonance, which means that the Larmor frequency of the neutron precessing about B_0 is the same as the frequency of the rotating field $\gamma B_0 = \omega_L = \omega$, there is no x component of the magnetic field left in the rotating coordinate frame. The neutron now only experiences the constant field B_{rf} and the spin precesses about this field. Amplitude of the rotating field and flight time inside the RF field, determines the precession angle and is adjusted for a 'π-flip' to $\pi = \gamma B_{\mathrm{rf}} \cdot t = \gamma B_{\mathrm{rf}} \cdot l/v$, where l is the length of the rf-coil and v the neutron velocity. Considering a neutron with spin along y-axis entering the NRSE-coil when the rotating field is along the z-axis, then the effect of such a 'π-flip' is to change the spin to the $-y$ axis. Back in the laboratory reference frame one can describe the effect of a 'π-flip' on a neutron with a general spin orientation in the precession plane given by the angle ϕ_0 to the z-axis by the resulting angle ϕ. This resulting angle, given in terms of the spin phase ϕ, depends on the phase of the rf-field ϕ_1 and the time spent in the rf-field. It is given by

$$\phi = \phi_0 + 2(\phi_1 - \phi_0) + \omega t = 2\phi_1 + \omega t - \phi_0 = 2\omega t + \omega\frac{l}{v}. \tag{1.71}$$

To determine the phase accumulated at the sample position one has to consider two of these flippers with a distance L between each other. Therefore one has to insert the phase accumulated after the first NRSE-coil as initial phase ϕ_0 for the second NRSE-coil. The phase after the primary spectrometer arm then reads

$$\phi_A = 2\phi_2 + \omega t - (2\phi_1 + \omega t - \phi_0) = \phi_0 + 2(\phi_2 - \phi_1) \tag{1.72}$$

and the phase change or precession angle is only given by the difference of the phases of the oscillating field

$$\Delta\phi = 2(\phi_2 - \phi_1). \tag{1.73}$$

These phases are locked and therefore ϕ_2 is given by the neutron flight time in the precession region between the NRSE-coils. Thus, one can express the phase difference by

$$\Delta\phi = 2(\phi_2 - \omega\frac{L}{v}) - 2\phi_1 = \omega\frac{L}{v} = 2\frac{\gamma B_0 L}{v}. \tag{1.74}$$

Comparing with Eq. (1.57) shows that traveling through the precession region consisting of two NRSE coils with constant fields B_0 in distance L gives twice the precession angle than traveling through a magnetic field region of length L and field strength

B_0, as in classical NSE. Therefore the description of NRSE is analogous to the case of NSE when considering the double field integral and the spin echo time for the case of NRSE can be written as

$$\tau_{NRSE} = \frac{2\hbar\gamma B_0 L}{mv^3} = \frac{2\hbar\omega L}{mv^3} = 2\tau_{NSE} \tag{1.75}$$

1.4.3. Modulation of Intensity with Zero Effort (MIEZE)

Modulation of intensity with zero effort (MIEZE) is resonant spin echo technique. The MIEZE setup, shown in Fig. 1.7 (a), consists of two NRSE coils (A and B) at the beginning and the end of the primary precession region. In contrast to NRSE these coils are run at different frequencies ω^A and ω^B and corresponding static fields B_0^A and B_0^B, while still performing a 'π-flip'. The distance between the resonant coils is given by L_1, the distance between sample and detector by L_2 and the distance between the last NRSE-coil and the sample is given by L_S. The neutron precession angle before coil A is $\phi_A = 0$ and after the coil given by

$$\phi_{A'} = 2\omega_A t_A - \phi_A = 2\omega_A t_A, \tag{1.76}$$

where t_A is the time of arrival at the coil. The precession angle after the second coil is then given by

$$\phi_{B'} = 2\omega_B t_B - \phi_B = 2\omega_B(t_A + \frac{L_1}{v}) - 2\omega_A t_A = 2(\omega_B - \omega_A)t_A + 2\frac{\omega_B L_1}{v}. \tag{1.77}$$

The spin phase after the second coil depends on both the time of arrival at coil A and the velocity of each neutron, therefore a physical meaning of $\phi_{B'}$ is not obvious. However, by measuring $\phi_{B'}$ at a certain point C at a distance L_2 all velocity dependent phase factors cancel out as mentioned before, and an oscillating signal is observed. The time of arrival at C is given by

$$t_C = t_A + \frac{L_1 + L_2}{v}. \tag{1.78}$$

And $\phi_{B'} = \phi_C$ can be expressed by t_C as

$$\begin{aligned}\phi_C &= 2(\omega_B - \omega_A)\left(t_C - \frac{L_1 + L_2}{v}\right) + 2\frac{\omega_B L_1}{v} \\ &= 2(\omega_B - \omega_A)t_C + \frac{2}{v}\left(\omega_B L_1 - (\omega_B - \omega_A)(L_1 + L_2)\right).\end{aligned} \tag{1.79}$$

By choosing

$$\omega_B L_1 = (\omega_B - \omega_A)(L_1 + L_2) \tag{1.80}$$

all velocity dependent phase factors cancel out and an oscillating signal is observed when placing a spin analyzer somewhere between the second coil and the detector.

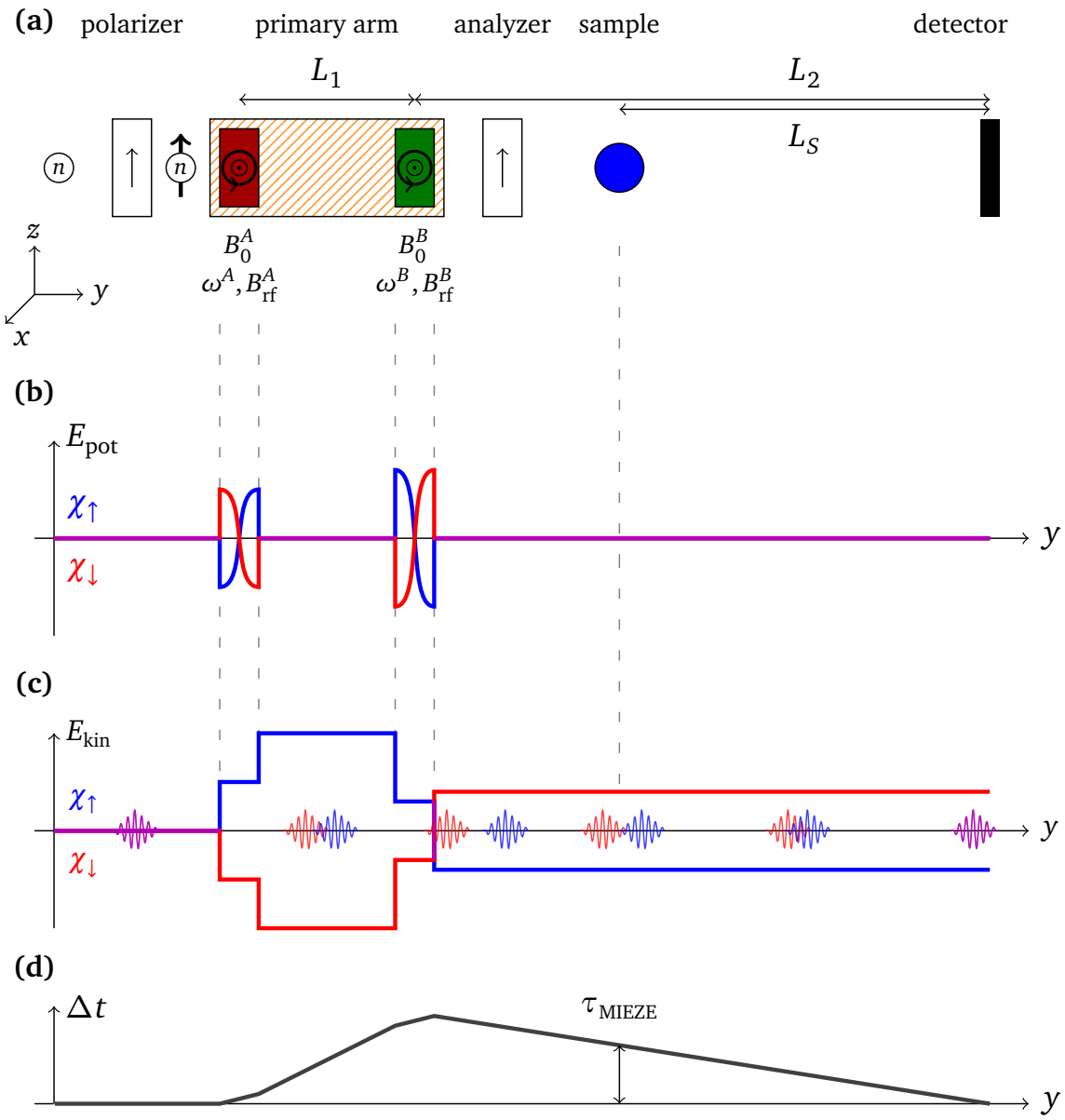

Figure 1.7.: (a) Schematic drawing of a MIEZE spectrometer. The neutron beam enters the spectrometer from the left side and passes the polarizer, the precession region and the analyzer until it reaches the detector. Panel (b) and (c) show the kinetic and potential energy of the eigenstates $\chi_\uparrow$ and $\chi_\downarrow$ as function of the neutron flight path. In panel (d) the flight time difference Δt of the eigenstates $\chi_\uparrow$ and $\chi_\downarrow$ as function of the neutron flight path are shown. The spin echo time τ_{MIEZE} is given by the flight time difference Δt at the sample position. Taken from Ref. [66].

The spin phase at position C is then given by

$$\phi_C = 2(\omega_B - \omega_A)t_C \tag{1.81}$$

To measure the phase ϕ_C, one has to measure the intensity transmitted through the analyzer. It is given by the cosine projection of the polarization on the analyzer axis. Hence, the evolution of the spin phase in time is translated by the analyzer into a intensity oscillation in time and can be written as

$$I_C(t) = \frac{I_0}{2}\left(\cos 2(\omega_B - \omega_A)t + 1\right) = I_0 \cos^2(\omega_B - \omega_A)t. \tag{1.82}$$

The distance d_π on which the phase of the oscillating signal described by Eq. (1.82) changes by π is

$$d_\pi = \frac{\pi}{\omega_B - \omega_A} \cdot v. \tag{1.83}$$

In order to observe the oscillation in time the effective distance d_{eff}, on which neutrons are converted in the detector, has to be much smaller than d_π.

For a monochromatic beam the oscillation Eq. (1.82) is not suppressed by an envelope and can be measured everywhere behind the analyzer. In case of a finite wavelength distribution $f(v)$ with a mean width Δv, the intensity at a distance Δ away from the focus point can be expressed by

$$I_C(t_C) = \frac{I_0}{2}\int \mathrm{d}v f(v)\left(\cos\left(2(\omega_B - \omega_A)\left(t_C + \frac{\Delta}{v}\right)\right) + 1\right). \tag{1.84}$$

For an estimate of the mean width $\bar{\Delta}$ of the envelope one assumes that $2(\omega_B - \omega_A)\Delta/v \approx \pi$. Then the mean width is in first order given by

$$\bar{\Delta} = \frac{\pi v}{\frac{\Delta v}{v} 2(\omega_B - \omega_A)}. \tag{1.85}$$

Now a sample described by the scattering law $S(\omega)$ behind the second NRSE coil at a distance L_S to the detector is introduced (figure 1.7). We assume quasi elastic scattering with small energy transfers ($\hbar\omega \ll \frac{1}{2}mv^2$). The small energy transfer results in a change of the arrival time at the detector given by

$$\Delta t = \frac{\hbar\omega L_s}{mv^3}, \tag{1.86}$$

thus reducing the contrast of the intensity oscillation. Compared to Eq. (1.82) one obtains

$$I_C(t_C) = \frac{I_0}{2}\int \left(\cos 2(\omega_B - \omega_A)\left(t_C + \frac{\hbar\omega L_s}{mv^3}\right) + 1\right) S(\omega)\mathrm{d}\omega. \tag{1.87}$$

The symmetry of $S(\omega)$ allows to rewrite Eq. (1.87) by

$$I_C(t_C) = \frac{I_0}{2} \int \left(\cos 2(\omega_B - \omega_A) t_C + \cos 2(\omega_B - \omega_A) \frac{\hbar \omega L_s}{m v^3} + 1 \right) S(\omega) \mathrm{d}\omega \qquad (1.88)$$

and therefore, as in the case of spin echo, to separate the instrumental and the sample part. All information about the sample is contained in the the MIEZE contrast C in the amplitude of the oscillation

$$C = \int S(q,\omega) \cos(\omega \tau_{MIEZE}) \mathrm{d}\omega. \qquad (1.89)$$

Again one can define a characteristic time measuring the resolution of the spectrometer, the MIEZE time τ_{MIEZE} which is given by

$$\tau_{MIEZE} = \frac{h}{m} \cdot \frac{L_S(\omega_B - \omega_A)}{v^3} = \frac{m^2}{\pi h^2} \cdot L_S(\omega_B - \omega_A) \lambda^3. \qquad (1.90)$$

In MIEZE, the contrast C takes the role of the polarization P in NSE or NRSE.

CHAPTER 2

Experimental Methods

The measurements presented in this thesis were performed at two distinct SANS instruments: SANS-1 @ Heinz Maier-Leibnitz Zentrum (MLZ) in Garching, Germany and SANS-II @ Paul Scherrer Institut (PSI) in Villigen, Switzerland. All studies with polarized neutrons, especially spin echo measurements and additional SANS measurements were carried out at the neutron resonance spin echo spectrometer RESEDA @ MLZ. RESEDA is not a distinct SANS instrument, therefore different modifications were realized to improve the capability of performing experiments with small scattering angles. Furthermore, the RESEDA setup was improved to realize MIEZE measurements in a standardized way. A new NRSE technique called longitudinal NRSE was implemented to increase the dynamic range and the resolution of RESEDA. The spherical neutron polarimetry device MiniMuPAD was improved to achieve higher resolution and less background.

The chapter starts with a description of the new MiniMuPAD, followed by a discussion of the improvements realized at RESEDA and closes with a description of the data treatment in spin echo.

2.1. Spherical Neutron Polarimetry with MiniMuPAD

The MiniMuPAD (Mini Mu-Metal Polarization Analysis Device), introduced in Sec. 1.3.2 is a very small setup capable to perform full spherical neutron polarimetry (SNP). Compared to the existing devices CryoPAD and MuPAD the complete MiniMuPAD setup is very compact. MiniMuPAD was constructed to be used as an inset in a standard top-loading Closed Cycle Cryostat (CCR) as used for experiments at the

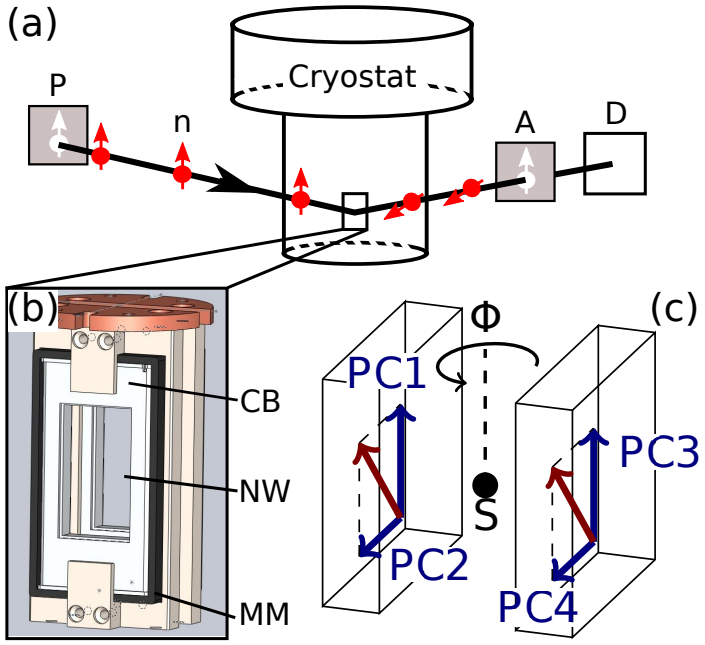

Figure 2.1.: Schematic depiction of the miniaturized spherical neutron polarimetry device MiniMuPAD. (a) Schematic overview of the complete setup with cryostat, polarizer (P), analyzer (A), and detector (D). (b) Close-up view of the SNP device, as composed of the coil bodies (CB) with their neutron window (NW). The coils are surrounded by a μ-metal yoke (MM). (c) Orientation of the precession coils (blue arrows), the resulting local magnetic field (red arrow), and sample (S). The picture is taken from Ref. [15].

MLZ. The design allows a very simple implementation of a SNP measurement option at different polarized instruments and especially at imaging beam lines where small distances between sample and detector are crucial in order to reach a high spatial resolution.

2.1.1. First generation MiniMuPAD

The MiniMuPAD has a maximum diameter of 48 mm and was designed to be inserted directly into a cryostat with an internal diameter of 50 mm. Fig 2.1 (a) gives an overview of the setup. The polarized neutron beam can reach the MiniMuPAD and the sample mounted inside, either through a zero field region or in a weak guide field. For the spin manipulation two precession coils before (PC1 and PC2) and two after the sample (PC3 and PC4) are used. The coils produce magnetic fields as indicated by the blue arrows in Fig. 2.1 (c), perpendicular to the neutron beam. PC1, PC2 and respectively PC3, PC4 are wound directly on top of each other. In this configuration each coil assembly can produce a magnetic field of arbitrary strength and direction

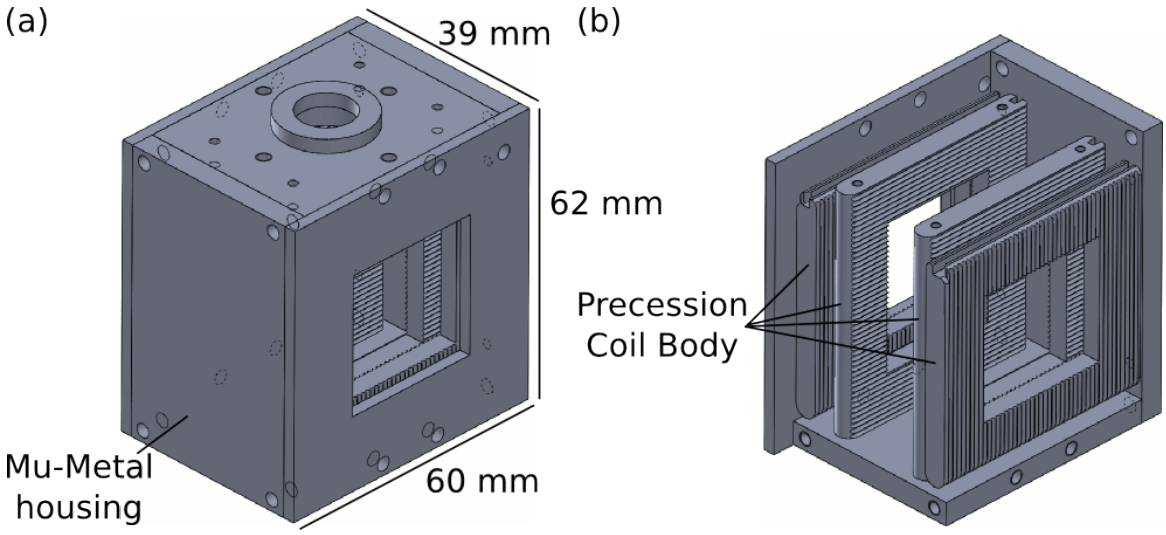

Figure 2.2.: Construction drawing of the second generation MiniMuPAD. In panel (a) the MiniMuPAD with closed Mu-Metal housing is shown. The setup is 62 mm high and the width is 60 mm. In beam direction the MuMetal box extends over 39 mm. Panel (b) shows the bodies of the precession coils.

in the plane perpendicular to the neutron beam. Such a field allows to rotate the incoming and outgoing polarization towards any direction [50]. Each of these two coil sets is surrounded by a μ-metal yoke (cf. (MM) in Fig. 2.1 (b)), to shortcut the magnetic fields of the coils and hence imitate infinite long coils. The sample region is shielded from external stray fields or the earth magnetic field by the μ-metal yokes. A distance of only 12 mm between incoming and outgoing precession devices combined with shielding, allows to perform polarization analysis with an accuracy of better than 3°.

2.1.2. Second generation MiniMuPAD

The design and simulation of the second generation MiniMuPAD was started during the course of the Bachelor thesis of F. Haslbeck [67]. A newly available closed cycle cryostat with a 80 mm diameter sample tube allowed to increase the size of the setup to a maximum diameter of 78 mm. The basic concept focused on the optimization of the setup towards SANS and imaging experiments. To increase the accuracy of the spin alignment a full MuMetal housing was designed as shown in Fig. 2.2 (a) and (b). The geometry of the MuMetal shielding is optimized by means of finite element simulations using COMSOL [68]. In contrast to the first MiniMuPAD, the precession coils are separated to allow an easier adjustment of the SNP measurement. All coils are made of bare aluminum wire to reduce background from small angle scattering and increase the transmission. We expect a reduction of the small angle scattering background by factor of ten when comparing to the results presented later in Fig. 2.5

for the rf-coils of the NRSE setup. The sample can be rotated between the precession coils about the vertical axis in the available sample space of 50 mm × 50 mm × 10 mm. A neutron beam of maximum 26 mm × 27 mm can pass the setup.

2.1.3. Outlook

The third generation MiniMuPAD is planned to carry out SNP experiments under large scattering angles $0 \leq 2\theta \leq 100°$. The most crucial part for this setup is the design of the curved precession coils as they cannot easily be wound. A first approach uses spark erosion to produce these coils.

2.2. Improvements of RESEDA

The **RE**sonance **S**pin **E**cho for **D**iverse **A**pplications beamline RESEDA [69] is located in the neutron guide hall west of the Heinz Maier-Leibnitz Zentrum (MLZ). The neutron guide NL5-S provides the instrument with a cold wavelength spectrum ranging from 3 to 10 Å. A tiltable mechanical velocity selector allows adjusting the width of the triangular wavelength distribution from 10 to 20 %. The original setup of RESEDA consists of one primary and two secondary double MuMetal shielded spectrometer arms, which allow to study two scattering vectors at once, up to $q_{max} = 2.5\,\text{Å}^{-1}$. For the quasielastic measurements NSE and transversal NRSE are employed, covering a dynamic range of 0.001 to 5 ns. The constant B_0-field used in the transversal NRSE setup is aligned vertical, i.e. perpendicular to the neutron beam direction as originally proposed by Golub and Gähler. Recently, a so-called longitudinal NRSE option was made available at RESEDA [41, 70] were the B_0-field is applied parallel to the neutron beam. This new technique increases the dynamic range at RESEDA by at least three orders of magnitude.

2.2.1. Improvements of the longitudinal NRSE setup

The working principle of longitudinal NRSE was first demonstrated by W. Häußler *et al.* by combining a NSE and a longitudinal NRSE spectrometer arm at IN11 (ILL) [71, 72]. A first complete LNRSE spectrometer was realized at RESEDA as shown in Fig. 2.3. The fundamental difference to transversal NRSE is the alignment of the B_0 field along the beam direction, reproducing the very same field configuration as in classical NSE instruments. In this field configuration well established correction elements from NSE, e.g. Fresnel and Pythagoras coils, can be used. These correction elements allow to correcting for depolarizing effects due to field inhomogeneity and beam divergence.

One of the biggest advantages compared to transversal NRSE and especially NSE is the fact that non-divergent neutron beams do not require any correction for de-

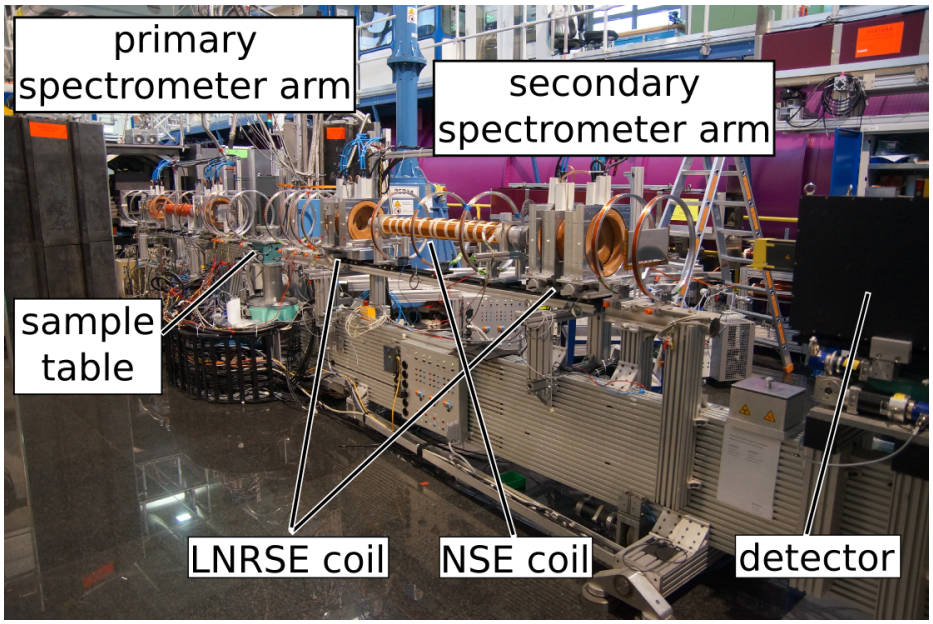

Figure 2.3.: Longitudinal NRSE setup as realized at RESEDA. The neutrons path the spectrometer arm from left to right. Primary and secondary spectrometer arm are identically. Each arm consists of two longitudinal NRSE coils with solenoids in between. A longitudinal guide field is sustained by several large copper coils. The analyzer is placed in the detector housing on the right.

polarizing effects originating from field inhomogeneity. The correction for divergent beams is smaller than in NSE. Non-divergent neutrons passing a solenoid accumulate different field integrals $J(r)$ depending on the distance r to the symmetry axis of the solenoid. To first order, the field integral is given by

$$J(r) \approx B_0 L \left(1 + \frac{r^2}{2RL}\right) \tag{2.1}$$

where B_0 is the magnetic field strength at the symmetry axis of the solenoid, L its length and R the radius. The largest differences in J for neutrons with different r are accumulated at the entrance and exit of the solenoid. The difference between LNRSE in NSE is that in LNRSE all neutrons experience a π flip at the center of the solenoid. The solenoids are designed symmetrically with respect to the center, hence the field integral accumulated on each side are the same for non-divergent neutrons. Due to the π-flip in the center the inhomogeneity subtract each other in the accumulated Larmor phase.

This self-correction allowed in the first test experiments already to measure a spin echo at an effective field integral of $J_{\text{eff}} = 240\,\text{mT m}$ without any correction elements. Today's state of the art spin echo spectrometers, e.g. IN15, IN11 and JNSE, are operated at about twice the field integral. The longitudinal field geometry allows to implement longitudinal guide fields between the NRSE coils, to conserve the precession plane, hence there is no need for magnetic shielding. Furthermore, the method of field integral subtraction can be applied [73] to reach infinitively small spin echo times. This method is very important, as the resonant flip coils cannot be operated at very small frequencies, without loss of polarization. LNRSE and TNRSE can be used in MIEZE mode.

2.2.2. Improvements of the SANS setup

For MIEZE studies it is very important to improve measurements under small scattering angles. The setup at RESEDA was improved in terms of the beam collimation and the small angle scattering background. To perform SANS and MIEZE measurements a new secondary spectrometer arm has been constructed which allows to change the sample to detector distance L_2 as introduced in Fig. 1.2, from 0.5 to 5 m. The new arm is shown in Fig. 2.4 can also support the standard transversal NRSE modules. Another step was to define the collimation, therefore new slits in front of the spectrometer arm have been mounted: two pinholes with a diameter of $d = 5\,\text{mm}, 10\,\text{mm}$ and a slit with $10\,\text{mm} \cdot 40\,\text{mm}$. The sample aperture can be adjusted by different slits directly in front of the sample. In contrast to a dedicated SANS instrument the length of the collimation is fixed at RESEDA as the precession region is required for the quasielastic measurements. The collimation has a length of about 4 m.

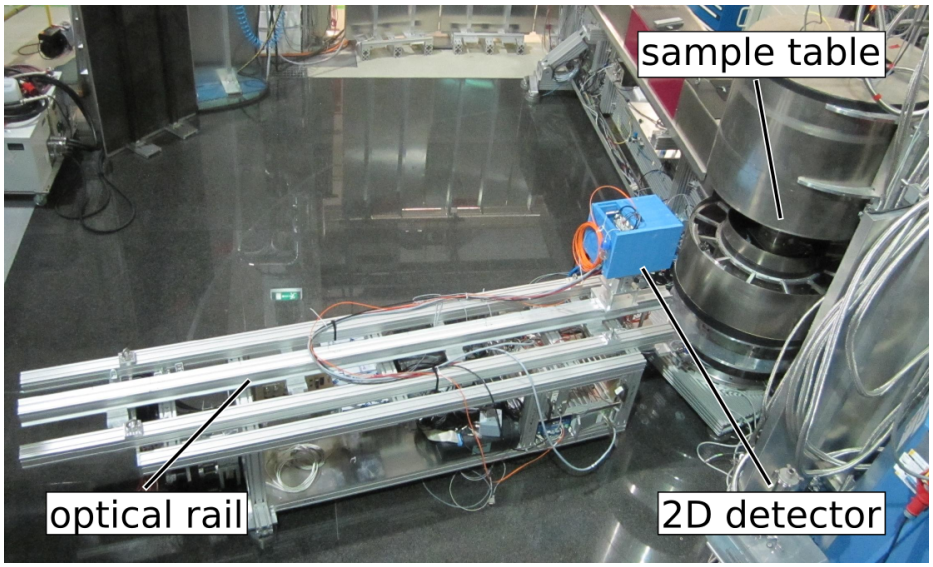

Figure 2.4.: New modular spectrometer arm at RESEDA with MIEZE/SANS option mounted. The two dimensional CASCADE detector is placed in the blue box next to the sample position. A optical rail in the center of the arm allows to change the sample to detector distance and to mount flight tubes. The whole arm can be moved on air pads to allow large scattering angles $0 \leq 2\theta \leq 50°$.

A very important improvement was the reduction of parasitic background scattering in the small angle regime. Therefore a flight tube was installed in the primary spectrometer arm between the NRSE coils. Within this flight tube a slit system comprised of cadmium pinholes with a diameter of $d = 50\,\text{mm}$ at a distance of 300 mm from each other is mounted. These pinholes remove neutrons from the beam which do not hit the sample position. Absorbing these neutrons furthermost from the sample as possible reduces the possibility that they may lead to a background signal. To ensure the absorption the inside of the tube is covered with cadmium and boron.

Besides the small angle scattering background generated from air scattering, the contribution due to material in the beam is very important. While in a dedicated SANS instrument the amount of material in the beam (i.e neutron windows) is reduced as much as possible, in case of RESEDA there are essential components like the NRSE coils which have to be in the beam. The influence of the different components strongly depends on the utilized material and position in the spectrometer. Background from components at the beginning of the precession region is already blocked in the collimation, while the background from those components directly placed in front of the sample, i.e. second NRSE coil, MEZEI flipper and for MIEZE spin analyzer cannot be absorbed easily. To quantify the contribution of these components to the background, a small angle scattering study of different coils used at RESEDA was

Table 2.1.: Parmeters of the different coils tested at SANS-1.

abbr.	coil	transmission	description	used in
N1	TNRSE coil	0.933 ± 0.002	new design, anodized aluminum, Kapton foil	TNRSE
N2	TNRSE coil	0.864 ± 0.002	new design, aluminum coated with Paramicron, Kapton foil	TNRSE
A1	TNRSE coil	0.958 ± 0.002	old design, uncoated aluminum, Kapton foil	TNRSE
CC	coupling coil	0.965 ± 0.002	coated aluminum	TNRSE
RF	rf-coil	1.001 ± 0.002	uncoated aluminum	both
RFA	rf-coill	0.992 ± 0.002	anodized aluminum	both
MF	Mezei flipper	0.966 ± 0.002	anodized aluminum	LNRSE
SC	Fresnel coil	0.901 ± 0.002	anodized aluminum, Kapton foil	LNRSE

performed at SANS-1 @ MLZ. The study covers a q-range from $0.01\,\text{Å}^{-1} \leq q \leq 0.1\,\text{Å}^{-1}$ using neutrons with a wavelength of $\lambda = 6\,\text{Å}$. In Tab. 2.2.2 a summary of all studied coils and their transmission is given. Figure 2.5 shows the radial q dependence of the scattering intensity. The intensities given are in absolute units per coil and pixel.

The scattering is very large in the regime up to about $0.03\,\text{Å}^{-1}$, while towards larger q-values the scattering is governed by isotropic incoherent scattering and reduced by a factor of 100. Concerning the small angle scattering longitudinal and transversal NRSE differ in the point that the B_0 coils of the former are not penetrated by the neutron beam while in the later the windings are directly in the beam. Therefore different TNRSE coils have been studied, especially the newest design, which also allows large tilt angles. These coils N1 and N2 differ in their coating. The B_0 coil with anodized windings produces a factor of two less background for $q < 0.03\,\text{Å}^{-1}$ than the coils with Paramicron coating. In case of the rf-coil the difference is even larger, by using pure aluminum in contrast to anodized aluminum the scattering is reduced by a factor 100. In a first step all rf-coils were replaced by coils wound from pure aluminum wire.

In the longitudinal NRSE setup especially the Fresnel coils are important for very high resolution. The Fresnel coils produce very strong small angle scattering background. It is very important to improve these coils or even to make them dispensable by means of better main coils.

Another important improvement was the implementation of a data structure to handle SANS measurements and software tools to treat these data. The software package covers functions to allow an easy evaluation of radial q-scans or scans of other typical parameters, i.e. temperature, field, or rocking angle in multi-dimensional

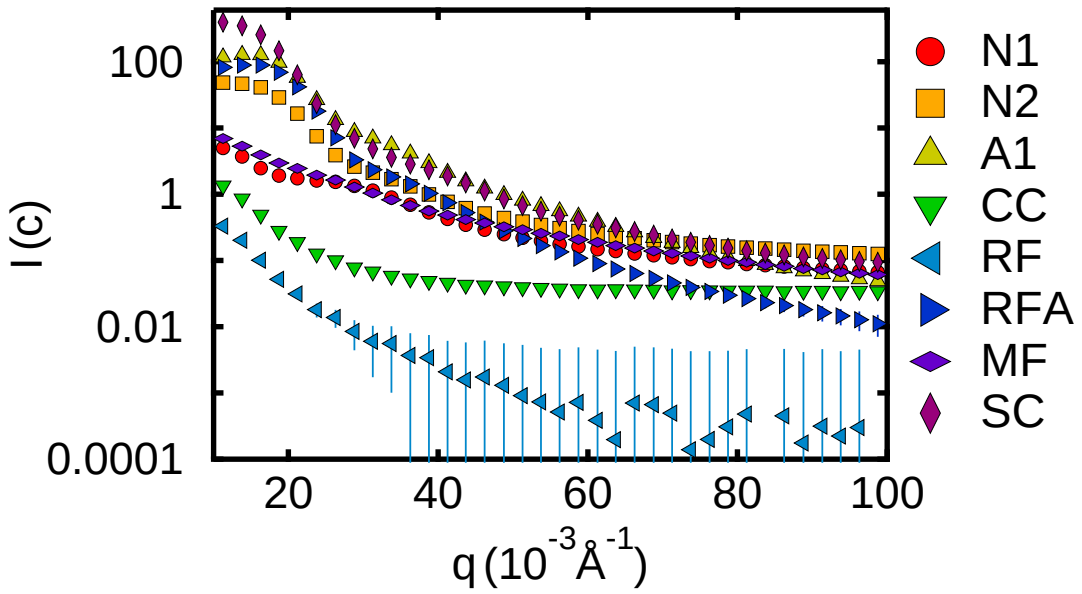

Figure 2.5.: Radial q dependence of the small angle scattering from different coils. The intensity is normalized to water and given as counts per pixel and coil. N1 anodized new NRSE coil, N2 coated with paramicron new NRSE coil, A1 anodized old NRSE coil, CC coupling coil made of coated aluminum wire, RF rf-coil made of pure aluminum wire, RFA anodized aluminum wire, MF Mezei flipper, SC Fresnel coil.

regions of interest.

2.2.3. Improvements of the MIEZE setup

The main difference for the equipment between a NRSE and a MIEZE setup is that for MIEZE a detector with a high time resolution (better than $\Delta t = 1000\,\mathrm{ns}$) is needed. At RESEDA a position sensitive CASCADE detector [74, 75] with an active area of $200 \times 200\,\mathrm{mm}$ is used for the MIEZE measurements. In this detector six foils coated with boron convert the neutrons. The thickness of the boron layers varies between 0.8 and 1.5 µm and their distance is of the order of 4.4 mm. The electronic time resolution is $\Delta t = 50\,\mathrm{ns}$. Besides the time resolution which is even much better than demanded also the thickness of the layers is important. Considering Eq. (1.83) the effective thickness d_{eff} of the converting layer should be smaller than $d_{\mathrm{eff}} \ll 0.4\,\mathrm{mm}$ for a neutron wavelength of $\lambda = 8\,\text{Å}$ and a MIEZE frequency of $\omega_{MIEZE} = (\omega_B - \omega_A) = 2\pi \cdot 600\,\mathrm{kHz}$, otherwise the MIEZE contrast cannot be observed.

The CASCADE detector allows to record a MIEZE signal on each foil separately

which increases the efficiency when combining all foils to about 70 % (λ dependent) of that of a standard ^{3}He-based detector. For the combination of the MIEZE contrast from different foils one has to consider that the MIEZE signal on different foils has different phases. Furthermore the wavelength distribution at RESEDA with a width between $\Delta\lambda/\lambda = 0.1$ and 0.2 reduces the spatial extent of the MIEZE group as described in Eq. (1.85). Considering a typical spin echo time with $\omega_{MIEZE} = (\omega_B - \omega_A) = 2\pi \cdot 0.6\,\mathrm{kHz}$ and a wavelength spectrum centered at $\lambda = 8\,\text{Å}$ with a width $\Delta\lambda = 0.1 - 0.2$ the spatial extent varies from 2 mm to 1 mm. The spatial extent of the MIEZE group is much smaller than the distance between the foils and therefore will not allow measuring the MIEZE signal on all foils at the same time.

In MIEZE all spin precession is carried out in the primary spectrometer arm, therefore no spin manipulating device has to be supported by the secondary spectrometer arm. The only crucial requirement is the precise positioning in distance and orientation of the detector with respect to the second NRSE coil. A central optical rail on the new modular SANS arm allows a precise and reproducible positioning of the detector. The distance between the second NRSE coil and the detector, L_2, can be adjusted by better than 1 mm. A vertical translation stage allows adjusting the detector in height. The possibility to tilt and rotate the detector is planned.

Misalignments of the detector may result in flight path differences and therefore phase differences of the MIEZE signal. These phase differences can reduce the contrast when integrating over too large detector regions. Fig. 2.6 shows the phase of the MIEZE signal for each pixel on the detector. The data were measured by placing a standard graphite sample at the sample position and evaluating the MIEZE signal for each pixel separately. A perfectly aligned detector will show circular rings. The width of these rings decreases with increasing MIEZE frequency. The asymmetry of the phase map presented in Fig. 2.6 may origin from different effects: (1) misalignment of the detector, (2) sample shape and (3) a curvature of the detecting foil in the detector.

As for the SANS measurements the software package available at RESEDA was extended by a tool for the visualization of the MIEZE data. The MIEZE panel allows to display the data with respect to all four dimensions of a typical MIEZE data set: detector or pixel, foil, τ_{MIEZE} and time channel.

For future studies the MIEZE option at RESEDA has to be improved to carry out measurements with a fixed phase of the MIEZE echo at all spin echo times. A fixed MIEZE phase following follow the change of the phase due to the scattering process at the sample and to improve the statistic and accuracy of measurements with low contrast or count rate. In the latter case one can impose the phase for the fit of the MIEZE echo. Fitting with a fixed phase significantly increases the accuracy of the resulting contrast. To implement a phase fixation all four frequency generators

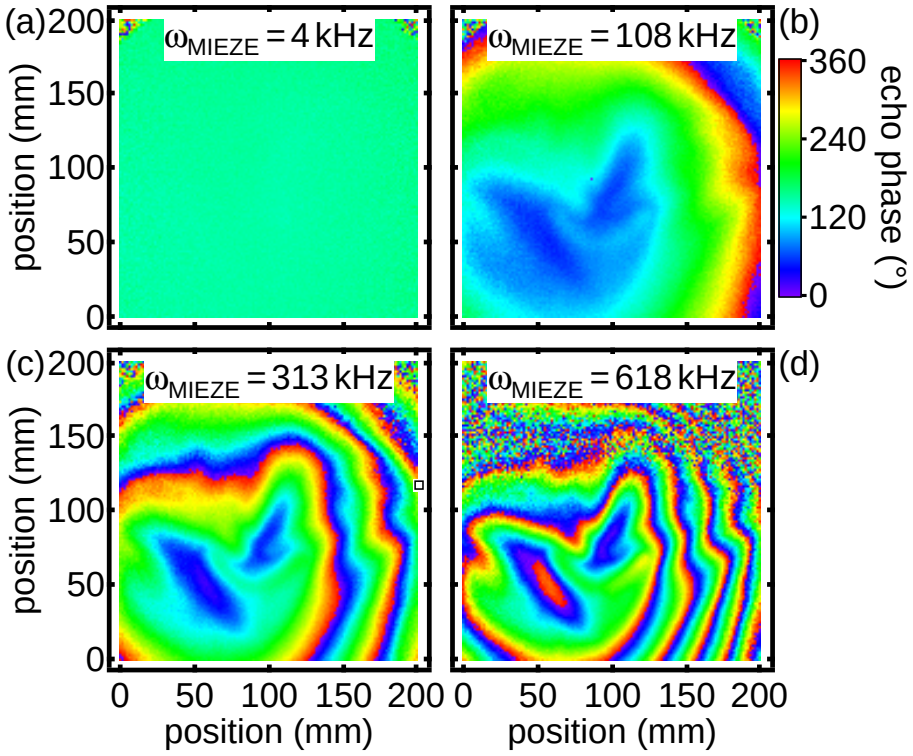

Figure 2.6.: Typical phase map of a MIEZE measurement recorded at different MIEZE frequencies: (a) 4 kHz, (b) 108 kHz, (c) 313 kHz and (d) 618 kHz.

have to be synchronized and operated in sync mode. The control software has to be changed in order to send a burst signal before each MIEZE count.

2.2.4. MIEZE measurements in strong magnetic fields

As discussed in section 1.4 an outstanding advantage of the MIEZE technique with respect to classical NSE is the possibility to perform measurements under depolarizing conditions at the sample position, as for example strong magnetic fields. In case of the magnetic systems studied within this thesis magnetic fields are very important to tune their properties. A lot of effort was put to realize high resolution MIEZE measurements with strong magnetic fields. First proof of principle experiments [41] were performed using a cryogen free 5 T magnet optimized for small angle scattering with an active stray field compensation. This magnet can be used with magnetic fields parallel and perpendicular to the neutron beam. It was combined with the transversal MIEZE setup as shown in Fig. 2.7 (a). The second magnet used was a 17 T helium cooled superconducting magnet [76] without stray field compensation. This magnet only allows applying the magnetic field parallel to the neutron beam and it was combined with the longitudinal MIEZE setup as shown in Fig. 2.7 (b).

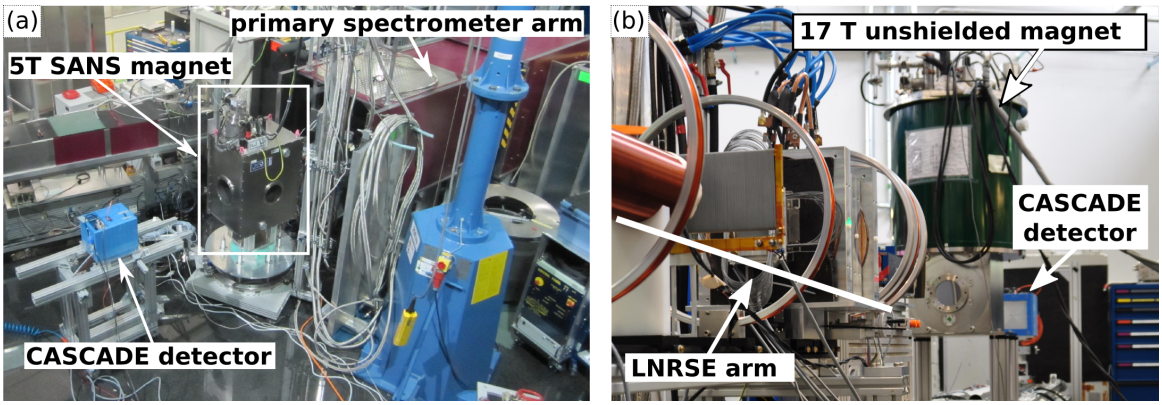

Figure 2.7.: MIEZE and magnetic field setup at RESEDA. (a) TMIEZE setup as combined with an actively shielded 5 T SANS magnet from the MLZ sample environment group. (b) LMIEZE setup combined with the Birmingham 17 T magnet [76].

First results from measurements in the direct beam with the 5 T magnet are shown in Fig. 2.8 with parallel (a) and perpendicular magnetic field (b). The distance between both coils is $L_1 = 2.641\,\mathrm{m}$ and the distance between the second coil and the detector $L_2 = 3.08\,\mathrm{m}$. The sample detector position was $L_{SD} = 1.38\,\mathrm{m}$ and the neutron wavelength was set to $\lambda = 8.33\,\text{Å}$. A solenoid around the spin analyzer was used for the longitudinal sample field to compensate the remaining stray fields which disturb the coupling of the neutron spin at the exit of the mu-metal shielding. In both geometries, with parallel and perpendicular field no reduction of the resolution between zero field and the maximum field of 5 T is observed. The MIEZE contrast remains at the value observed in zero field.

The results of the measurements with the 17 T magnet, in combination with the longitudinal MIEZE setup are shown in Fig. 2.8 (c). These measurements were performed using a neutron wavelength of 10.5 Å. The distance between the LNRSE coils was set to $L_1 = 1.925\,\mathrm{m}$, the distance between last coil and detector was set to $L_2 = 5.000\,\mathrm{m}$ and the sample to detector distance to $L_{SD} = 2.6\,\mathrm{m}$. The MIEZE contrast shown in Fig. 2.8 (c) at the highest MIEZE time is well above the commonly defined resolution limit of $1/e$. Extrapolating towards this limit suggests a resolution of about 20 ns. To reach these high MIEZE times frequencies slightly above 1 MHz and effective magnetic fields of $B_0 \approx 70\,\mathrm{mT}$ were applied in the LNRSE coils.

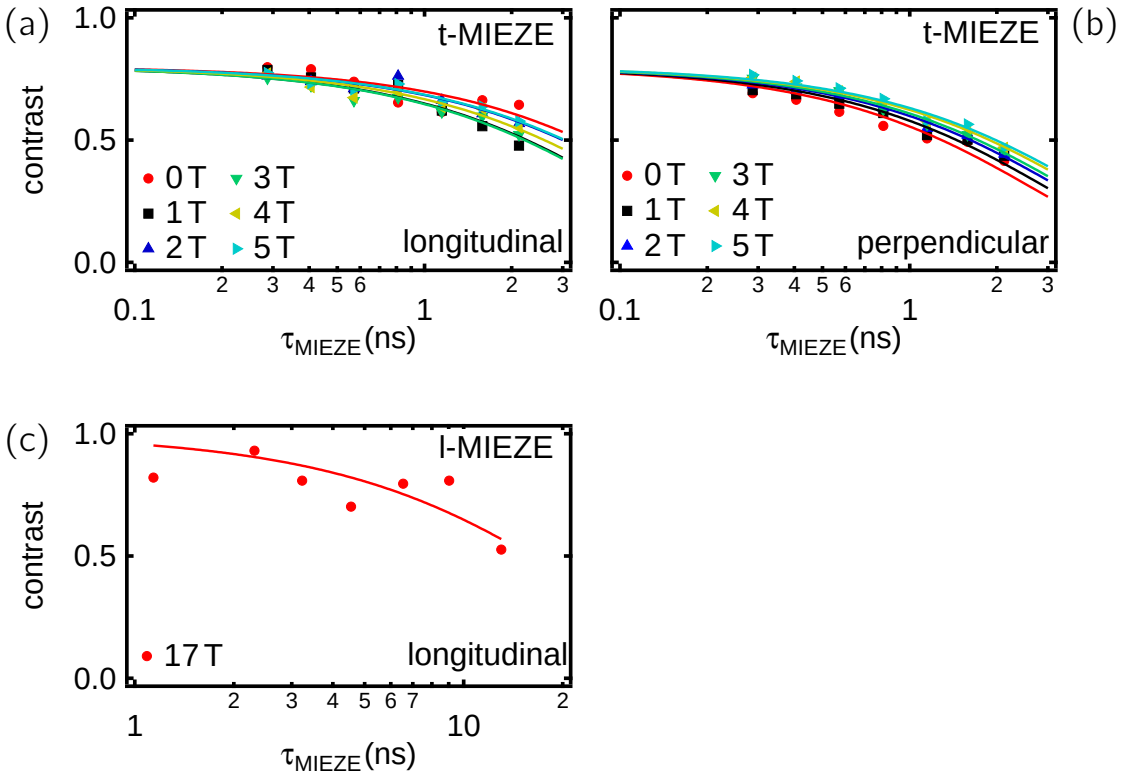

Figure 2.8.: MIEZE resolution with magnetic field at the sample. Typical data as recorded with a 5 T SANS magnet, where the field was applied perpendicular (a) and parallel (b) to the neutron beam. (c) Data recorded at 17 T applied longitudinal to the neutron beam using the Birmingham SANS magnet [76].

2.3. Measuring and normalizing $S(q,\tau)$ data sets

In the following section the reduction of spin echo data is discussed. At the beginning a description of how the polarization or contrast is measured is given. Here it is important to note that magnetic samples may lead to a more complex measurement routine. In the next step different procedures to normalize the polarization or contrast are described to obtain $S(q,\tau)/S(q,0)$. The normalized intermediate scattering function can be applied to a physical model after the instrumental resolution is considered. Furthermore a description is given how different data sets can be combined or background can be subtracted and how to combine data on a position sensitive detector.

2.3.1. Recording $S(q,\tau)$

The central task of recording a $S(q,\tau)$ data set is to quantify either the polarization P as in NSE and NRSE or the contrast C as for MIEZE. It is not possible to measure polarization or contrast directly but the projection of the polarization/contrast onto an analyzer axis. For the rest of this section polarization and contrast are used synonymously. The intensity at the exit of the analyzer is connected to the polarization by

$$I = \frac{I_0}{2}\left(1 + P \cdot \cos(\phi(\Delta J))\right), \tag{2.2}$$

and can be recorded as a function of the additional spin phase ϕ, introduced through a field integral ΔJ. The additional field integral ΔJ is given by the field integrals in the primary J_1 and secondary J_2 spectrometer arms through $\Delta J = J_2 - J_1$. The intensity as function of the additional field integral is called spin echo group and can be recorded in case of NSE/NRSE by an asymmetric scan of the field integral in one spectrometer arm, while in MIEZE the frequency in one NRSE coil of the primary spectrometer arm is changed. The so called spin echo point is the point where $\Delta J = 0$. Using Eq. (1.64) and considering the effect of the wavelength distribution of the incoming neutron beam $f(\lambda)$ on the polarization the spin echo group reads

$$I(\tau,\Delta J) = \frac{I_0}{2}\left(1 + \underbrace{\int \mathrm{d}\lambda f(\lambda)\cdot\cos(\phi(\Delta J))}_{\text{envelope and spin echo}} \times \underbrace{\int \mathrm{d}\omega S(q,\omega)\cos(\omega\tau)}_{\text{sample physics}}\right). \tag{2.3}$$

The integration over the wavelength distribution describes the envelope of the spin echo group and the oscillation frequency is given by the the cosine of the additional field integral. The physics of the sample is given by the second integral by defining the amplitude of the oscillation i.e. the polarization. To discuss the effect of the wavelength distribution we consider a purely elastic scattering process by setting the second integral to unity. A monochromatic neutron beam results in a spin echo

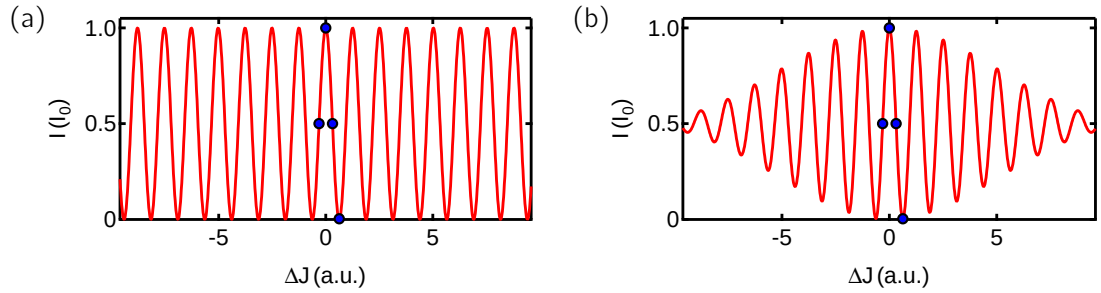

Figure 2.9.: Spin echo group for a monochromatic (a) and triangular shaped (b) wavelength distribution. The triangular distribution is centered at $\lambda = 5\,\text{Å}$ with a width of $\Delta\lambda/\lambda = 0.1$. The blue markers in both panels indicate the points, separated by a phase of $\pi/2$, at which the intensities in the 4-point-method is measured.

group with no reduction of the amplitude as shown in Fig. 2.9 (a). At RESEDA a mechanical wavelength selector is used to select a certain wavelength λ with a wavelength distribution $\Delta\lambda/\lambda = 0.1 - 0.2$. The transmitted wavelength distribution has a triangular shape with a full width at half maximum $\Delta\lambda$. Considering a triangular shaped wavelength distribution the spin echo group is given by

$$I(\Delta J) = \frac{I_0}{2}\left(1 + \cos(\phi^*(\Delta J)\lambda_0)\frac{\sin^2(\frac{1}{2}\phi^*(\Delta J)\Delta\lambda)}{(\frac{1}{2}\phi^*(\Delta J)\Delta\lambda)^2}\right) \tag{2.4}$$

with $\phi^*(\Delta J) = \phi(\Delta J)/\lambda_0$. Figure 2.9 (b) shows a spin echo group with a typical width of the wavelength distribution $\Delta\lambda/\lambda = 0.1$. Eq. (2.4) shows that with increasing width of the wavelength distribution the width of the spin echo group is reduced. To get access to the physics of the sample one has to precisely determine the amplitude of the oscillation. The amplitude is observed by measuring several points on the spin echo group and fitting a cosine to these points. In a standard measurement it is not necessary and efficient to measure the full spin echo group as shown in Fig. 2.9. When considering statistical errors and the reduction of the amplitude due to the wavelength distribution for large ΔJ it is most efficient to use the so called 4-point-method [77]. In this method four points separated by $\pi/2$ are measured starting with $\phi(\Delta J) = -\pi/2$ as shown by the blue circles in Fig. 2.9. The frequency of the oscillation is defined by the mean wavelength λ_0 and instrumental parameters and therefore precisely known. This gives a reliable result on both the amplitude and the phase of the spin echo group.

The determination of the echo amplitude is getting more difficult when magnetic structures are studied which have polarizing effects as for example MnSi [77] or $Ba_2CuGe_2O_7$ [78]. In these cases the 4-point-method may not give accurate results. Scattering from the helical order of MnSi polarizes the neutron beam, as will be

discussed in Sec. 4.2. This changes the spin echo group in two ways: firstly the maximum reachable polarization is only 50 % of the initial polarization and secondly the presence of a spin rotation group may interfere with the spin echo group. After passing through the primary spectrometer arm, the polychromatic neutron beam is completely depolarized. The sample repolarizes the beam and with gradually increasing the field integral in the secondary spectrometer arm J_2 the so called spin rotation is recorded at the detector. When further increasing J_2 the spin echo group occurs at the spin echo point $J_1 = J_2$. Fig. 2.10 (a) shows the spin rotation and spin echo group in MnSi where the blue curve is a fit to the data. The spin rotation group does not depend on the spin echo time and does not contain information of the spin dynamics. For small spin echo times the spin echo and the spin rotation group may overlap resulting in a beating of the signal. In this case it is not possible to extract a meaningful amplitude of the spin echo group by means of the 4-point-method. To overcome this problem several points have to be measured and the fit parameters for the spin rotation group have to be fixed for all τ.

An even more complex situation occurs when several magnetic peaks overlap due to a coarse q resolution. This is the case for $Ba_2CuGe_2O_7$ which has a cyclodial antiferromagnetic ground state below $\approx 3\,\mathrm{K}$. The projection of this structure with respect to the scattering vector Q has a helical contribution and therefore polarizes the beam. In the ground state two pairs of incomensurate satellite reflections at $(1 \pm \xi, \mp\xi, 0)$ and $(1 \mp \xi, \pm\xi, 0)$ with $\xi = 0.0273$ are observed. The small incumensarability may not allow to separate all reflections in q space. The slightly different q of the overlapping cycloidal domains results in slightly different oscillation frequencies and therefore in a beating of both the spin rotation and spin echo group as shown in Fig. 2.10 (b). For more details see Ref. [78]. This complex structure of the spin echo group does not allow using the 4-point-method.

2.3.2. Normalizing $S(q,\tau)$

The expression "normalization" describes how the intermediate scattering function $S(q,\tau)/S(q,0)$ is determined from the spin echo group as shown in Fig. 2.9. From the fit to the echo group the amplitude A, the average count rate y_0 and the echo phase ϕ_0 are obtained. Here we discuss three different methods to evaluate $S(q,\tau)/S(q,0)$.

The first procedure directly identifies the amplitude of the echo with the normalized intermediate scattering function $S(q,\tau)/S(q,0) = A(\tau)$. For this approach the average count rate has to be the same for all spin echo times. This method has the smallest statistical uncertainty and is often used to obtain a first overview of the data and check their consistency.

In the second methods $S(q,\tau)/S(q,0)$ is defined as the polarization of the echo, i.e. the amplitude divided by the average count rate $S(q,\tau)/S(q,0) = A(\tau)/y_0(\tau)$. The

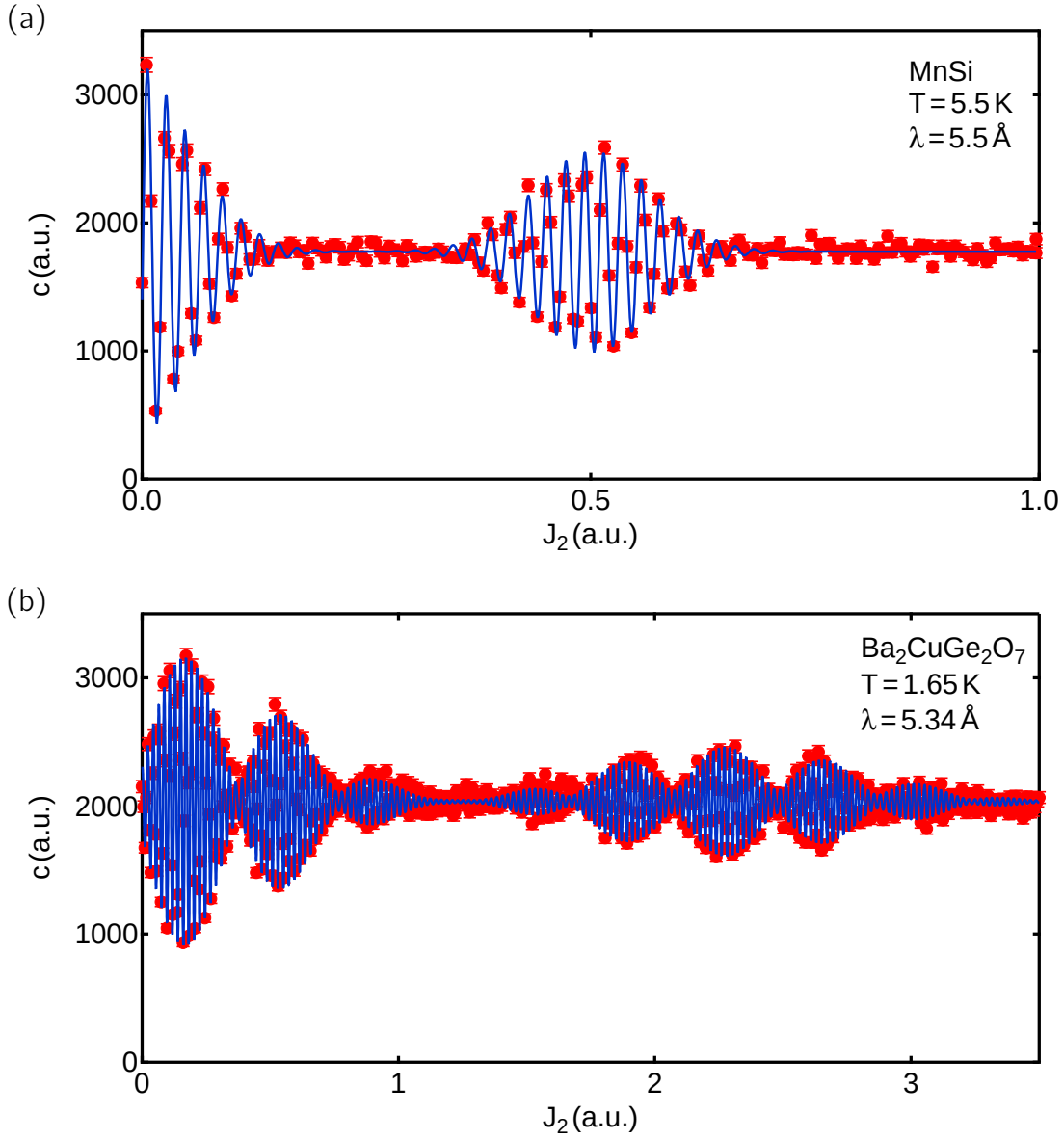

Figure 2.10.: (a) Spin rotation and spin echo group in MnSi taken from [77]. (b) Spin rotation and spin echo group of the cycloidal structure in $Ba_2CuGe_2O_7$ taken from [78]. The blue curves are fits to the data.

polarization gives the most reliable results and is the normalization which is used for all spin echo data discussed in this thesis.

The third procedure is also based on the polarization of the echo but all data are additionally divided by the polarization at $\tau = 0$. This procedure can be used when the initial polarization of the measurement is different to the resolution. Po-

larizing samples may lead to the half polarization in the echo, as discussed in the previous section. The intermediate scattering function is given by $S(q,\tau)/S(q,0) = (A(\tau)/y_0(\tau))/(A(0)/y_0(0))$.

2.3.3. Correcting for instrumental resolution

The next step to extract $S(q,\tau)/S(q,0)$ from the measured data after the normalization, as described in Sec. 2.3.2, is to correct for the instrumental resolution. The instrumental resolution is the polarization or contrast observed when measuring an elastic scatterer. A typical resolution curve recorded with the longitudinal MIEZE setup is shown in Fig. 2.11 (a) (red circles). At large τ the resolution decreases due to inhomogeneity in the precession field. The small dip at 0.1 ns is due to imperfect tuning. In order to correct for these decreases and to obtain only the decay introduced by the sample, the data (green boxes in panel (a)) have to be divided by the resolution. The result is shown in panel (b).

Several effects influence the shape of the resolution curve. The reduction of contrast and polarization at large spin echo times may be due to field inhomogeneity in the B_0 field of the resonant flip coils, divergence of the neutron beam, the phase front in the beam cross section and in MIEZE the shape of the sample. The loss for the small spin echo times may be due to fail of the rotating wave approximation [79] at small frequencies. Therefore it is very important to perform the resolution measurement under the same conditions as the measurements with the sample i.e. same wavelength, slits and tuning of the spectrometer.

2.3.4. Summation and subtraction of data sets

The summation and subtraction of different data sets becomes important when different spin echo measurements are added due to low statistics or a background measurement needs to be subtracted. There are in general two ways to add or subtract spin echo data sets. Both methods can be applied to NSE, NRSE and MIEZE

The first method combines the raw counts and the spin echo is fitted to the data after the summation. This approach is only possible if for both data sets the phase of the spin echo is the same for each spin echo time τ. If this is not the case the combination may destroy the cosine signal.

The second strategy to combine spin echo data sets is to first fit the spin echo data to the raw counts and then afterwards combine the echo amplitude and the average count rate according to the monitor count rate or measurement time of each data set. This method is stable even if the phase of the spin echo signal varies between data sets. It can only be applied if the statistic for each data set is already sufficient enough to allow a reasonable fit to the spin echo.

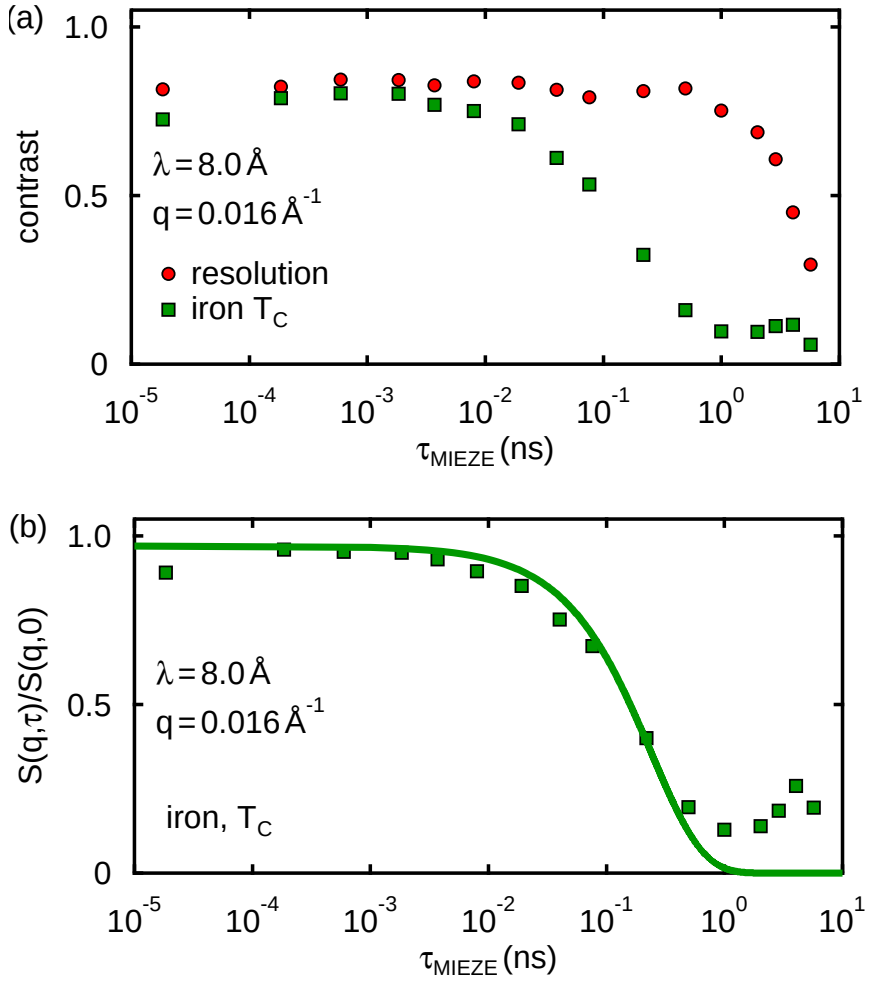

Figure 2.11.: Resolution correction of spin echo data. Panel (a) shows the resolution curve measured with a graphite sample (red circles) and the critical scattering from iron at T_C (green squares). The data are measured with the longitudinal MIEZE setup at RESEDA. Panel (b) shows the data from iron shown in panel (a) after correcting for the resolution.

2.3.5. Grouping regions when using a position sensitive detector

For MIEZE measurements a position sensitive detector, e.g the CASCADE detector as described in Sec. 2.2.3, can be employed to cover large q-regions. The study of dynamic processes over large scattering vectors is very important at for example second order phase transitions (compare Ch. 3) the q-dependence of the linewidth Γ gives important informations about the critical behavior. To employ the full detector area similar aspects as in the previous Sec. 2.3.4 have to be considered: (1) the count rate in each pixel or region of interest has to be large enough to allow a reliable fit to the spin echo group. (2) When combining several pixels to one region of interest the phase of the spin echo should not vary to much, otherwise a fit will give zero contrast. To account for these effects two types of "grouping" routines are implemented

pregrouping here the count rate of all pixels in one region of interest (or mask) are summed, the spin echo is then fitted to the sum

postgrouping the spin echo is fitted in each pixel separately; all amplitudes and averages of those pixels belonging to one region of interest or mask are summed.

Both routines can be combined to increase the statistics by first *pregrouping* the whole detector in a certain array, e.g. 5×5 pixels or 10×10 pixels, and afterwards *postgroup* the detector according to the desired q regions. It is important to note that the size of the MIEZE group depends on the MIEZE frequency and therefore changes within one MIEZE run as can be seen in Fig. 2.6.

2.4. Wavelength determination using resonance spin echo

The spin echo time in all neutron spin echo techniques directly depends on the third power of the mean neutron wavelength; therefore a precise determination is important. Resonant spin echo techniques like NRSE and longitudinal MIEZE allow a very accurate determination of λ by measuring the change of rf-frequency required for a certain change in spin phase. For this measurement the spectrometer has to be set to the spin echo point, meaning the phase accumulated in the primary spectrometer arm ϕ_A has to be exactly the opposite of the phase accumulated in the secondary spectrometer arm ϕ_B, i.e $\phi_A = \phi_B$. In NRSE this is realized by operating both spectrometer arms at the same frequency but with opposite B_0-fields. For the MIEZE setup the spin echo has to be realized within only the primary spectrometer arm. Longitudinal MIEZE allows to use the resonant flip coils as in NRSE for the forth precession ϕ_A and the field integral subtraction coil for the back precession ϕ_B. In contrast to MIEZE measurements the resonant flip coils have to be operated at the same frequency and the field integral subtraction coil between the NRSE coils is used

as in standard NSE. The neutron spin phase change introduced by both resonant coils (compare Eq. (1.74)) is described by

$$\phi_A = \frac{m_n}{h} n \omega_A L \lambda \tag{2.5}$$

for both setups NRSE and longitudinal MIEZE. The parameter n is 2 for a π-flip and standard NRSE coils and $n = 4$ for bootstrap coils ($n = 1$ for $\pi/2$ without bootstrap). The phase change depends on the distance L between the NRSE coils, their rf-frequency ω_A, the neutron wavelength and on the fundamental constants i.e. mass of the neutron m_n and Planck constant h. ϕ_A can be increased to $\phi_A^{2\pi} = 2\pi + \phi_A$ by increasing ω_A to $\omega_A^{2\pi}$. The phase change of 2π is given by

$$2\pi = \phi_A^{2\pi} - \phi_A = \frac{m_n}{h} n L \lambda (\omega_A^{2\pi} - \omega_A) = \frac{m_n}{h} n L \lambda \Delta\omega_A. \tag{2.6}$$

This allows to determine the wavelength through

$$\lambda = \frac{2\pi h}{m_n L n \Delta\omega_A}. \tag{2.7}$$

Besides fundamental constants the wavelength determination depends only on the measurement of the rf-coil distance L and the frequency needed for a phase change of 2π $\Delta\omega_A$. The error in measuring L is of the order of $\sigma_L \approx 0.001\,\mathrm{m}$ for typical distances of $L \approx 2\,\mathrm{m}$ and the error of the frequency measurement $\sigma_{\Delta\omega_A} \approx 1 \cdot 10^{-7}\,1/\mathrm{s}$. With the given errors of the fundamental constants this allows to determine the neutron wavelength at RESEDA with an accuracy of $\sigma_\lambda \approx 10^{-4}\,\text{Å}$.

CHAPTER 3

Critical fluctuations at the Curie point in Iron

Iron is the archetypal ferromagnet and a model system to study fundamental phenomena like continuous phase transitions. This chapter reports a comprehensive study of the critical dynamics around the transition from ferro- to paramagnetism in iron, employing the spin echo technique MIEZE. The results show that not only the exchange interaction but also the dipolar interaction is needed to explain the critical dynamics in iron. All measurements were performed at the beamline RESEDA at MLZ using the longitudinal MIEZE option.

3.1. Introduction to the critical dynamics of dipolar ferromagnets

The important tools to describe the critical dynamics at continuous phase transitions are dynamical scaling theory [80, 81], mode coupling theory [82, 83] and renormalization group theory [84]. Dynamical scaling theory directly predicts the inverse lifetime of the critical fluctuations to assume the form $\Gamma = Aq^z$, with the critical dynamic exponent z and a constant A [85]. However, applying these concepts to the archetypal example of a second-order phase transition, the transition from paramagnetism to ferromagnetism, only considering a simple Heisenberg model sometimes fails. In isotropic bulk ferromagnets like EuO, EuS, Ni, and Fe the transition cannot be explained by only accounting for the exchange interaction. These systems exhibit a distinct mismatch in Γ between theory and experimental results at small momentum transfers. A deviation between theory and experiment may be overcome by not only considering the short range isotropic ferromagnetic exchange interaction but also the long-range dipolar interaction. The Anisotropic dipole-dipole interaction plays an important role for almost all ferromagnets, as it lifts the degeneracy between eigenmodes

propagating longitudinal and transversal to their wave vector [86]. Large correlated patches of spins cause an anisotropic demagnetization effect. The dipole-dipole interaction can be understood as a feed-back effect of the critical fluctuations for the long wavelength limit.

Historically, the dipolar interaction was first treated as a very weak perturbation of the simple Heisenberg Hamiltonian. The dynamic critical exponent of a three-dimensional Heisenberg ferromagnet is $z = 5/2$, while the dipolar interaction leads to $z = 2$ [85]. A crossover from isotropic fluctuations to fluctuations influenced by the dipolar interactions was expected by theory, when approaching T_C from the paramagnetic phase. Evidence for such crossover was found in hyperfine interaction experiments [87].

Nevertheless, the crossover of the critical exponent could not be observed in neutron scattering experiments. All neutron scattering studies find a critical exponent of $z = 5/2$. A spin echo study by Mezei *et al.* [38, 88, 89], extending to significantly lower q and higher energy resolution than preceding studies, gave also no evidence for a crossover and at the same time shows a clear deviation from the scaling function described by P. Résibois and C. Piette [90], which considers only the exchange interaction. The experimental results show a clear deviation of the temperature dependence that cannot be explained.

Finally, E. Frey and F. Schwabl have investigated these problems by computing the scaling functions for ferromagnets including the dipolar interaction in mode coupling theory [91–93]. They found the cross over in the dynamical critical exponent for the transverse linewidth from $z = 2.5$ to 2 to take place at smaller wave vectors than expected and hence was not identified by neutron scattering.

The discussion of critical behavior in dipolar ferromagnets starts with an effective Hamiltonian as introduced by Frey [94]. The Hamiltonian including short range isotropic exchange and long range dipolar interactions reads

$$H = \sum_q \left[-J_0 + Jq^2a^2 + Jg\frac{q^\alpha q^\beta}{q^2} \right] S^\alpha_{-\mathbf{q}} S^\beta_{\mathbf{q}}, \tag{3.1}$$

with the lattice constant a, the exchange constant $2J$ and the Fourier-transform of the spin operator given by

$$S^\alpha_{\mathbf{q}} = \frac{1}{\sqrt{N}} \sum_l S^\alpha_l e^{i\mathbf{q}\cdot\mathbf{x}_l}. \tag{3.2}$$

The dimensionless parameter g is the ratio of the dipolar energy $(g_L\mu_B)^2/a^3$ and the

exchange energy $2J$, multiplied by a constant factor $4\pi b^2$

$$g = 4\pi b^2 \frac{(g_L \mu_B)^2/a^3}{2J} \propto \frac{\text{Dipolar Energy}}{\text{Exchange Energy}} \tag{3.3}$$

with the Landè factor g_L, the Bohr magneton μ_B and b depending on the lattice structure: $b = 1$ (sc), $\sqrt{2}$ (bcc) and 2 (fcc). The dipolar interaction is expected to be much smaller than the exchange interaction and therefore $g \ll 1$ [84]. The dipolar interaction introduces an anisotropy to the spin fluctuations with respect to their wave vector $\boldsymbol{q}$ and therefore lifts the degeneracy between the magnetization modes propagating longitudinal to the spin direction $\boldsymbol{S} \parallel \boldsymbol{q}$ and transversal to the spin direction $\boldsymbol{S} \perp \boldsymbol{q}$. This effect becomes important in the region $q^2 + \kappa^2 \leq q_D^2$, where $\kappa = 1/\xi$ is the inverse correlation length and $\kappa = \kappa_0 \left((T - T_\mathrm{C})/T_\mathrm{C}\right)^\nu$ with $\kappa_0 = 1.22\,\text{Å}^{-1}$[95] and $\nu = 0.627$ for an isotropic 3d Heisenberg magnet [96, 97]. The dipolar wavenumber q_D measures the strength of the dipolar interaction and is given by $g = (q_D a)^2$. The strength of the dipolar interaction q_D can be inferred, e.g., from the internal susceptibility at $q = 0$ $\chi_t(0,T) = (q_D/\kappa(T))^2$ [86]. The susceptibilities for the transversal and longitudinal magnetization modes are given by

$$\chi_t = (\boldsymbol{q},T) = \frac{\Psi}{\kappa^2(T) + q^2} \text{ and } \chi_l = (\boldsymbol{q},T) = \frac{\Psi}{\kappa^2(T) + q^2 + q_D^2}, \tag{3.4}$$

respectively, where Ψ is a non-universal static amplitude

$$\Psi = \frac{(g_L \mu_B)^2}{2Ja^2}. \tag{3.5}$$

Frey and Schwabl calculated the Heisenberg equation of motion for the two transversal and one longitudinal modes [91] and developed a mode coupling theory. They were able to calculate the two dimensional scaling function $\gamma^\alpha(x,y)$ ($\alpha = \perp$, $\parallel$) as function of the scaling variables $x = \kappa/q$ and $y = q_D/q$. The linewidth of the critical fluctuations in dipolar ferromagnets obeys the scaling law

$$\Gamma^\alpha(q,\kappa,g) = A q^z \gamma^\alpha(x,y), \tag{3.6}$$

with $z = 5/2$. A is a non-universal parameter which is related to the stiffness of the spin waves. Fig. 3.1 shows the scaling function for the longitudinal and transverse fluctuations as function of the single scaling variable $x = \kappa/q$. $\gamma^\alpha(x)$ is shown for different values

$$\varphi = \tan^{-1}\left(\frac{q_D}{\kappa}\right) = \frac{N\pi}{40} \tag{3.7}$$

with $N = 0,1,2,...,19$. The temperature dependence of N is introduced by the temperature dependence of κ. Hence, increasing temperature corresponds to smaller N. The curve with $N = 1$ is indistinguishable from $N = 0$, which is the scaling function calculated by P. Résibois and C. Piette [90] for isotropic ferromagnets without dipolar

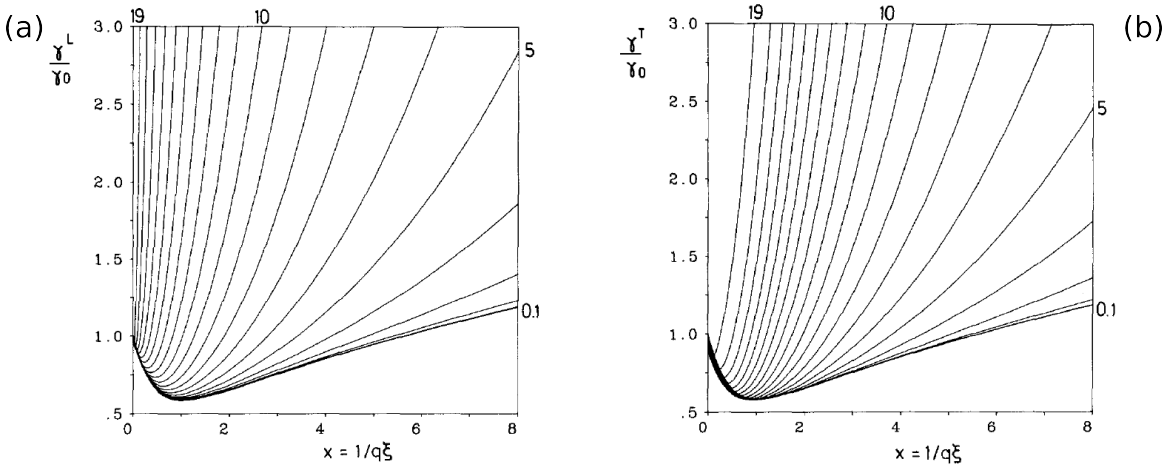

Figure 3.1.: Longitudinal γ^L (a) and transversal γ^T (b) scaling function versus $x = 1/q\xi = \kappa/q$ calculated within the mode-coupling theory by E. Frey and F. Schwabl [91, 93, 94]. The different curves correspond to different temperatures with $\varphi = N\pi/40$.

interactions.

3.2. Experimental setup and sample

The spin echo measurements presented in this chapter were performed at neutron wavelengths $\lambda = 8.0\,\text{Å}$ and $\lambda = 5.4\,\text{Å}$, respectively, with the longitudinal MIEZE option at the beam line RESEDA (MLZ) as described in Sec. 2.2.1. The first and second longitudinal NRSE coil were placed at a distance of $L_1 = 1.926\,\text{m}$, the distances between the second coil and the detector was set to $L_2 = 3.818\,\text{m}$ and between sample and detector to $L_{\text{SD}} = 2.525\,\text{m}$, respectively. In this configuration a dynamic range from $1.6 \times 10^{-5}\,\text{ns}$ to 5 ns was covered.

To reach the Curie temperature of iron $T_{\text{C}} = 1043\,\text{K}$ [98], the sample was heated using a high temperature furnace (HTF-01), with a resistive Nb double cylinder heating element. The Eurotherm temperature controller allowed to measure with a temperature stability of $\Delta T \approx 0.05\,\text{K}$. Temperature stability and hysteresis effects were verified by several temperature scans.

The sample investigated in this study is a bcc iron single crystal of cylindrical shape with a diameter of 9 mm and a height of 25 mm. A $\langle 110 \rangle$ axis is aligned approximately 10° of the cylinder axis of the crystal. For the measurements the cylinder axis was mounted vertical. The sample is the same as reported in previous studies in Brookhaven [95].

3.3. Experimental results

Here we present the experimental results of the MIEZE measurements performed at the beamline RESEDA. MIEZE is ideally suited to study the critical fluctuations above and below the Curie point in iron, as its resolution is unaffected by the depolarization of the neutron beam in the ferromagnetic phase. At the beginning of this section a temperature scan of the critical scattering intensity is presented. The second part focuses on the MIEZE measurements above and below the Curie temperature.

3.3.1. Temperature scan

The temperature dependence of the critical small angle scattering was used to identify the Curie temperature T_C. Fig. 3.2 (a) shows the scattered intensity evaluated in different q regions and panel (b) the transmission through the sample. A sharp peak in the scattered intensity and a sharp minimum in the transmission at $T_C = 1023.2\,\mathrm{K}$ defines the Curie temperature with an accuracy of 0.2 K. The offset of about 20 K to the values reported in the literature of 1043 K (compare Tab. A.1) may originate in a temperature gradient between sample and thermometer. A temperature gradient in the sample is not present as the peak signature is very narrow, i.e. $\Delta T = 0.2\,\mathrm{K}$. Furthermore, temperature scans with increasing and decreasing temperature do not show any hysteresis. The distinct suppression of the transmission at T_C is a vivid example for the phenomenon of critical opalescence. Magnetic fluctuations on all time- and energy-scales are present in the sample and tremendously increase the scattering cross section, making the sample almost in-transparent for neutrons. The scattering intensity has a maximum at a temperature $T^* < T_C$ in the ferromagnetic phase. This peak shifts to higher temperatures with increasing scattering vector and may be due to scattering from the shrinking ferromagnetic domains when approaching the Curie point. A similar effect has been observed in EuO as reported in Ref. [99].

3.3.2. Quasielastic measurements

In this section the focus is on the determination of the linewidth of the critical fluctuations. The MIEZE measurements are performed in a small angle scatting geometry. This geometry allows to study the fluctuations around $Q = 0$, therefore only transversal fluctuations can be measured. Longitudinal fluctuations can be accessed only around Bragg peaks with h,k,$l \neq 0$.

The quasielastic measurements were performed at several temperatures in the range $T_C - 10\,\mathrm{K}$ to $T_C + 30\,\mathrm{K}$. The combination of the MIEZE technique with the area sensitive CASCADE detector allowed covering a q-range of $0.009\,\text{Å}^{-1} \leq q \leq 0.043\,\text{Å}^{-1}$ at $\lambda = 8.0\,\text{Å}$ and $0.013\,\text{Å}^{-1} \leq q \leq 0.068\,\text{Å}^{-1}$ at $\lambda = 5.4\,\text{Å}$ with one experimental setting, respectively.

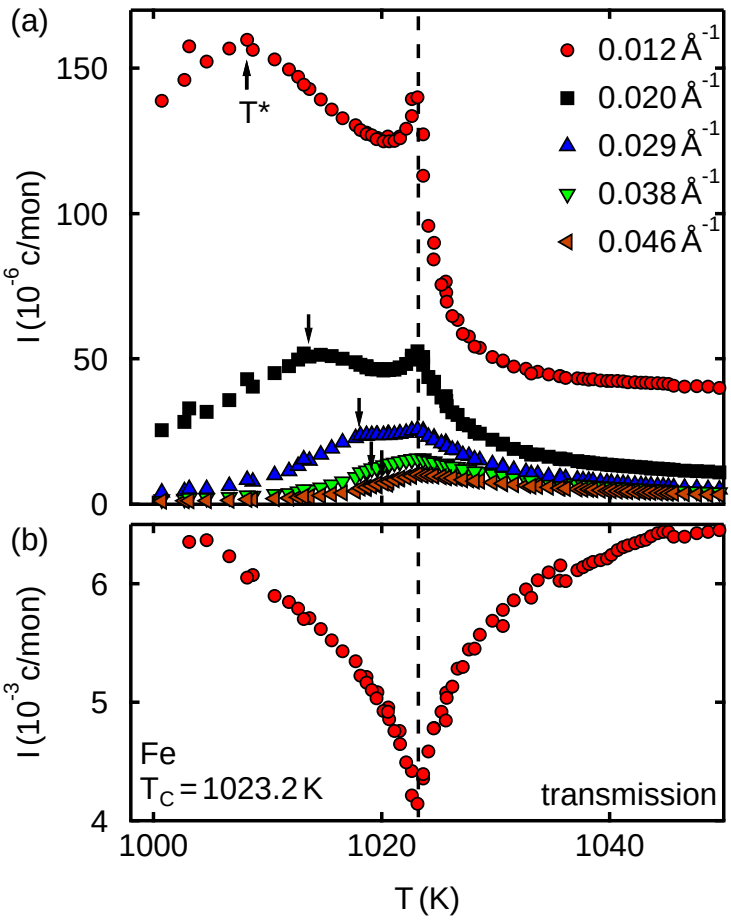

Figure 3.2.: Temperature dependence of the critical scattering around the Curie temperature T_C. (a) Scattering intensity as function of temperature evaluated in different q regions. The Curie temperature T_C is marked by the dashed line. (b) Transmission through the iron sample as function of temperature. The Curie temperature T_C is defined by the sharp minimum of the transmission and the maximum of the critical scattering.

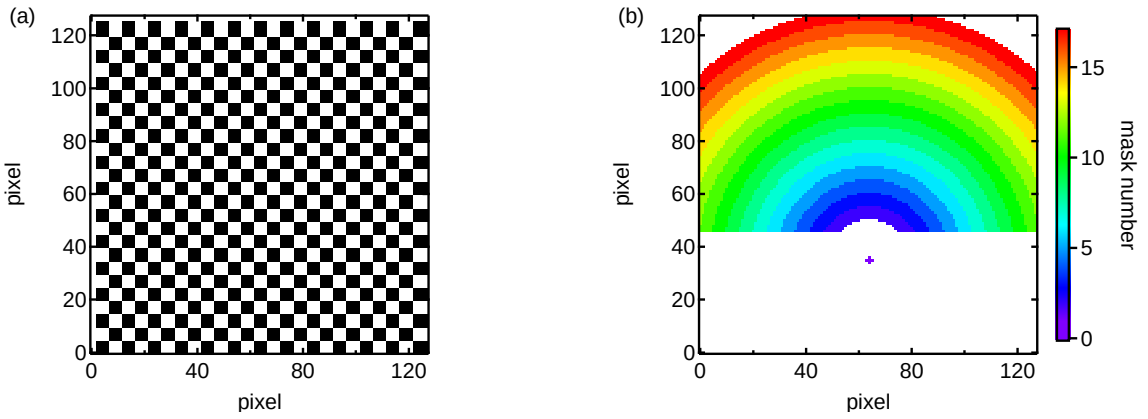

Figure 3.3.: Pregrouping and postgrouping masks as used for the measurement of the fluctuations in Fe. In panel (a) the pregrouping mask is shown. The $128 \cdot 128$ pixels of the detector are combined in regions with a size of $5 \cdot 5$ pixels. The postgrouping, shown in panel (b) consists of circles centered on the direct beam with a width of 5 pixels. The white regions are not evaluated due to background from the spin analyzer.

The data reduction to extract the normalized intermediate scattering function $S(q,\tau)/S(q,0)$ was carried out according to Sec. 2.3.5: First the detector was *pregrouped* in arrays of $5 \cdot 5$ pixels. The *pregrouping* mask is shown in Fig. 3.3 (a). For each of these masks the counts in the corresponding array of pixels is summed. The MIEZE echo is than fitted to this sum. The fit results, i.e. echo amplitude and the average count rate, are than in a second step combined according to the *postgrouping* mask shown in Fig. 3.3 (b). This *postgrouping* mask defines circular regions with a width of 5 pixels around the direct beam and therefore regions of constant q or more precisely of constant 2θ. This procedure of *pre-* and *post-* grouping allows to extract the intermediate scattering function $S(q,\tau)$ with sufficient statistics, while still keeping a high MIEZE contrast.

All measurements from the iron sample were normalized to a standard graphite sample, with the same shape as the iron sample and the same slits as for the iron measurement. The normalized intermediate scattering function $S(q,\tau)/S(q,0)$ measured at the Curie temperature T_C, $T_C+4\,\mathrm{K}$ and $T_C+10\,\mathrm{K}$ using a neutron wavelength of 5.4 Å and 8.0 Å are shown in Fig. 3.4 and Fig. 3.5, respectively. The characteristic decay time of the fluctuations decreases with increasing scattering vectors and increasing temperature, as expected. Large arrays of spins fluctuate slower than small regions and the fluctuations become stronger when approaching the transition. At small scattering vectors a strong background contamination is visible as the data do not decay to zero. In the direct beam at $q = 0$ for $\lambda = 5.4\,\text{Å}$ (cf. Fig. 3.4) $S(q,\tau)/S(q,0)$ is slightly larger than one. The very large count rate in the direct beam on the detector

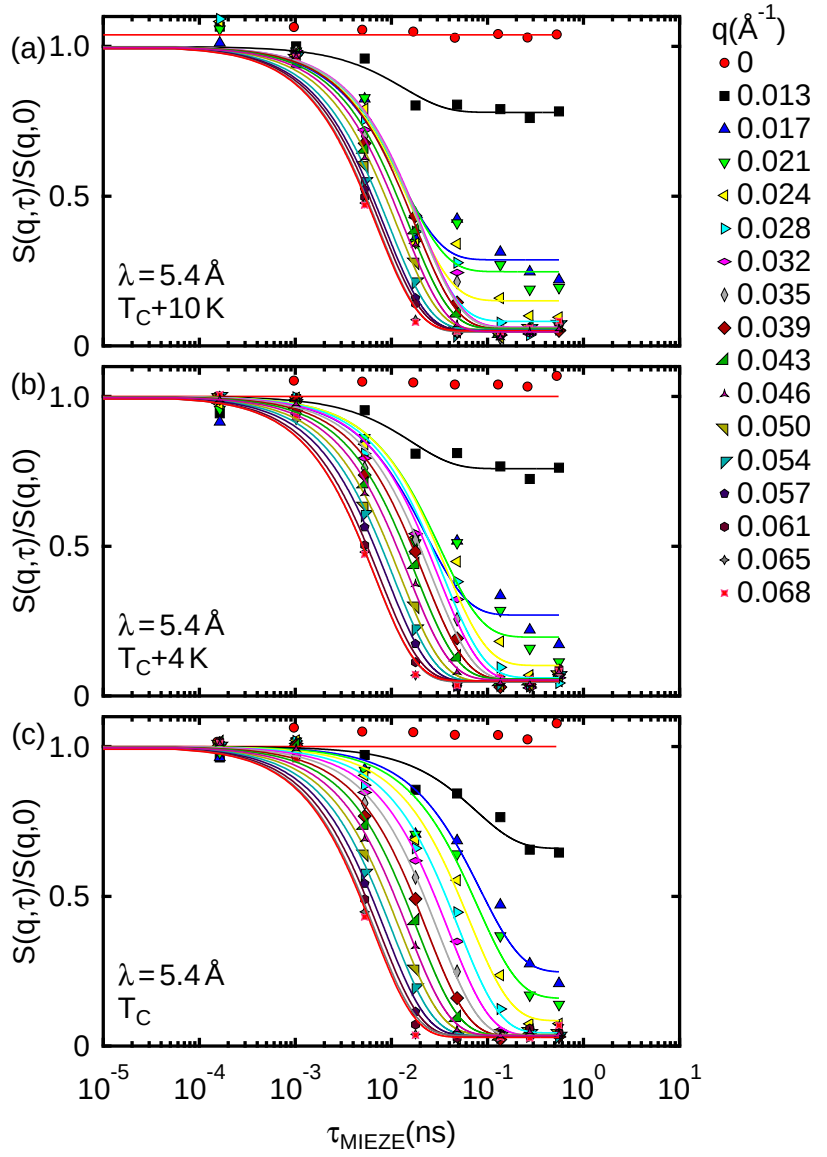

Figure 3.4.: Normalized MIEZE contrast in iron for measurements at (a) $T_C + 10\,K$, (b) $T_C + 4\,K$ and (c) T_C. Data were recorded using neutrons with a mean wavelength of $\lambda = 5.3\,Å$.

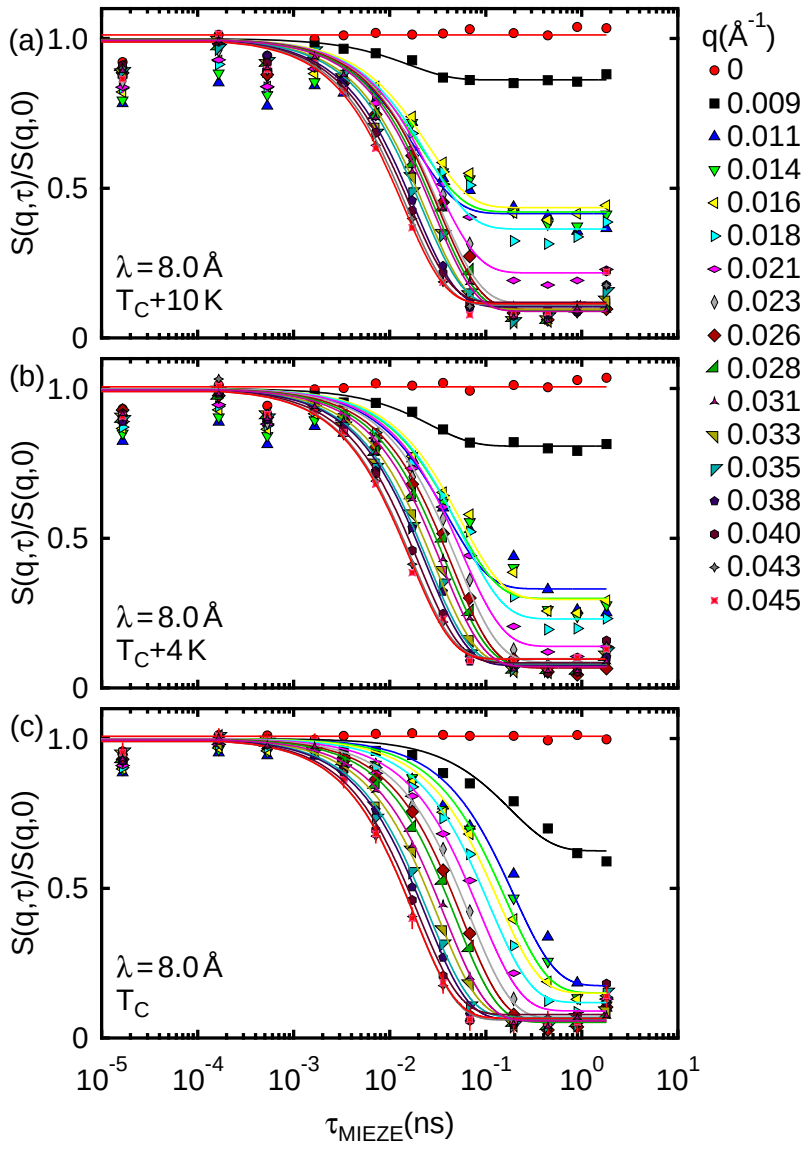

Figure 3.5.: Normalized MIEZE contrast in iron for measurements at (a) $T_C + 10\,K$, (b) $T_C + 4\,K$ and (c) T_C. Data were recorded using neutrons with a mean wavelength of $\lambda = 8.0\,Å$.

may be the reason for this unphysical effect. At $\lambda = 8.0\,\text{Å}$, were the neutron flux is smaller by a factor of twelve with respect to $\lambda = 5.4\,\text{Å}$, $S(q,\tau)/S(q,0) = 1$ in the direct beam. The normalized scattering functions for all other data discussed in this chapter are shown in the appendix Sec. A.

Critical fluctuations above T_C are assumed to have a Lorentzian line shape as reported in Ref. [100], hence all data are fitted with a single exponential decay of the form

$$\frac{S(q,\tau)}{S(q,0)} = A \cdot \exp\left[-\frac{\Gamma\tau}{\hbar}\right] + (1 - A), \tag{3.8}$$

where $A \leq 1$ is a q dependent parameter and allows to account for an elastic background i.e. the direct beam. The fit results are shown as solid lines in Figs. 3.4, 3.5 for a few selected temperatures and for all other temperatures in Appendix A.

Linewidth of the critical fluctuations above the Curie point

In Fig. 3.6 the q-dependence of the linewidth Γ is shown for different temperatures $T = T_\text{C}$ (a), $T_\text{C} + 1\,\text{K}$ (b), $T_\text{C} + 2\,\text{K}$ (c), $T_\text{C} + 4\,\text{K}$ (d), $T_\text{C} + 10\,\text{K}$ (e), $T_\text{C} + 30\,\text{K}$ (f). The blue triangles are measured with a neutron wavelength of 5.4 Å and the green squares with 8.0 Å, respectively. For all temperatures an increase of Γ with increasing scattering vector is observed. At larger scattering vectors the statistical errors increase, due to significantly smaller count rates. In panel (a) the results from the MIEZE measurement are directly compared with results from classical neutron spin echo [38] (black circles), both techniques are in excellent agreement with each other. The solid lines represent curves with $\Gamma = Aq^{2.5}$, with $A = 140\,\text{meVÅ}^{5/2}$ (red curve) and $A = 119\,\text{meVÅ}^{5/2}$ (orange curve). While the former value results from triple axis (TAS) measurements taken from Ref. [100], the latter is a fit to our MIEZE data. The small difference may be due to the precise experimental configuration, the quality of the data and the assumptions concerning the line shape. Very close to T_C the line shape may be non-Lorentzian. In case of the TAS measurement "real" q scans while in the MIEZE measurement 2θ scans are performed. Obviously, there are very strong deviations for $T > T_\text{C}$ between the solid line and the data. Especially at small scattering vectors q the difference is large being a first indication for the influence of the dipolar interaction.

The dynamical scaling hypothesis Eq. (3.6) allows to extract the dynamical scaling function for different temperatures by calculating

$$\gamma^T(x) = \frac{\Gamma(T)}{\Gamma(T_\text{C})} = \frac{\Gamma(T)}{Aq^{2.5}}. \tag{3.9}$$

Fig. 3.7 shows the scaling functions calculated for different temperatures using $A = 119\,\text{meVÅ}^{5/2}$ and the data shown in Fig. 3.6. The solid lines are from the theory of

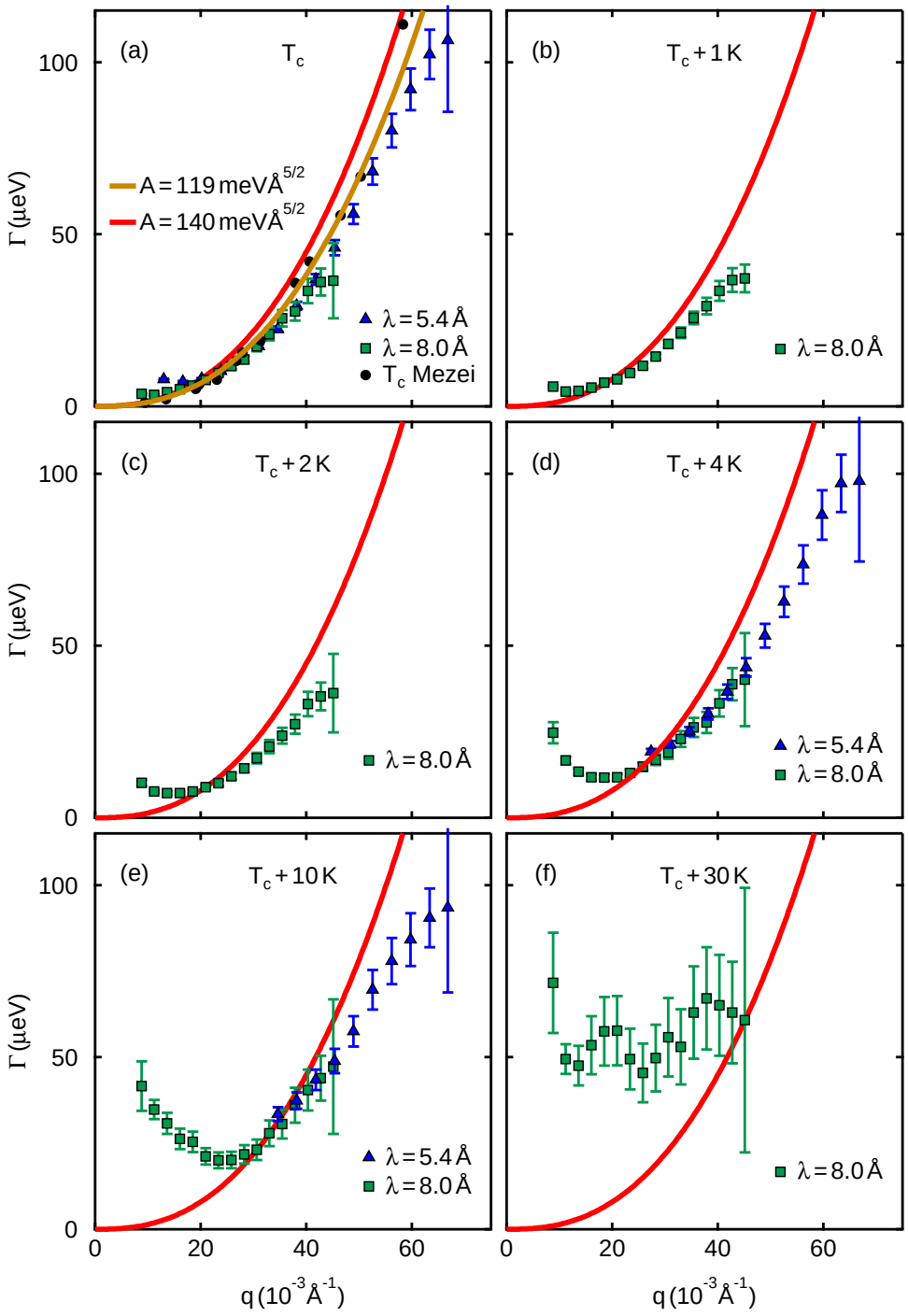

Figure 3.6.: Linewidth of the critical fluctuations in iron as function of the scattering vector q, measured for different temperatures $T = T_C$ (a), $T = T_C + 1\,\mathrm{K}$ (b), $T = T_C + 2\,\mathrm{K}$ (c), $T = T_C + 4\,\mathrm{K}$ (d), $T = T_C + 10\,\mathrm{K}$ (e), $T = T_C + 30\,\mathrm{K}$ (f). The blue triangles are measured at $\lambda = 5.4\,\text{Å}$ and the green squares at $\lambda = 8.0\,\text{Å}$. The black circles in panel (a) are the results reported by Mezei *et al.* [38]. The solid lines represents $Aq^{5/2}$ with $A = 140\,\mathrm{meV\text{Å}}^{5/2}$ [100] (red curve) and $A = 119\,\mathrm{meV\text{Å}}^{5/2}$ (orange curve).

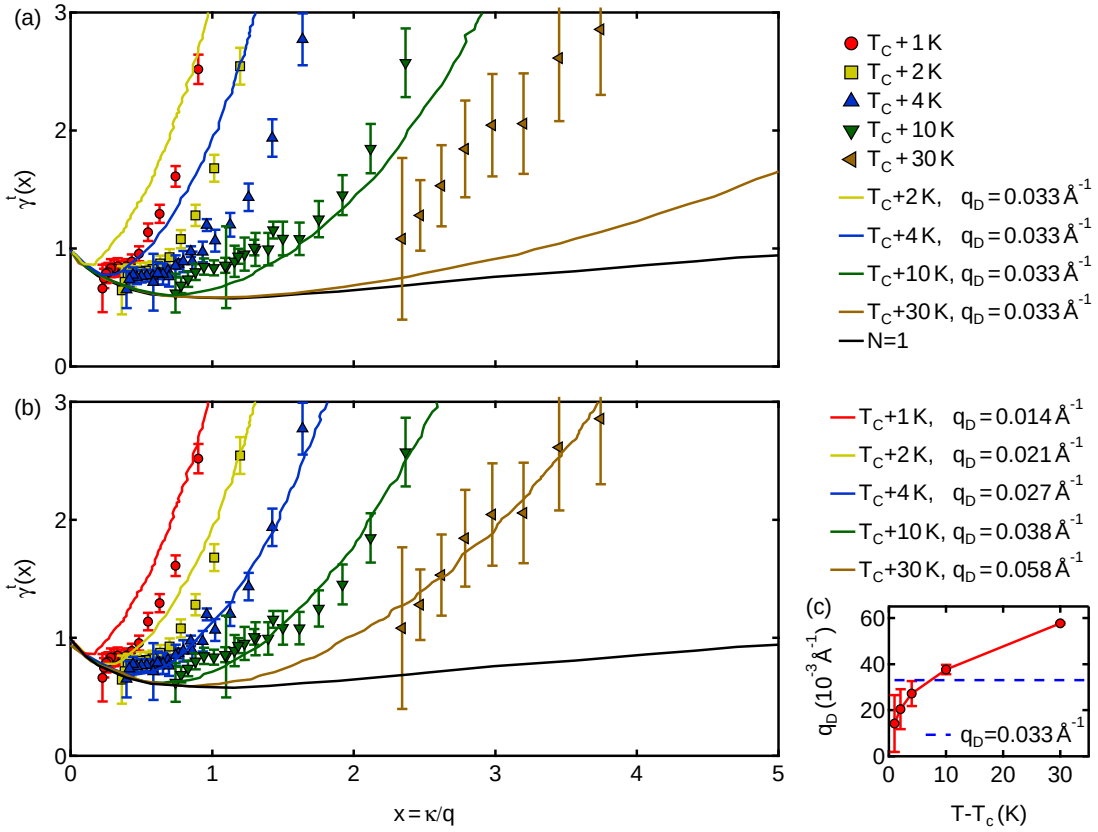

Figure 3.7.: Scaling function of the critical fluctuations calculated from the linewidth shown in Fig. 3.6 using Eq. (3.9) with $A = 119\,\mathrm{meV\AA}^{5/2}$. The solid lines are the scaling functions calculated within the theory by E. Frey and F. Schwabl [91, 93, 94]. Panel (a) shows the scaling function as calculated for a constant $q_D = 0.033\,\mathrm{\AA}^{-1}$. In panel (b) q_D is adjusted to fit scaling function and experimental results. Panel (c) shows the temperature dependence of q_D as used in panel (b). The error bars reflect the fact that the determination of N using Eq. (3.7) is associated with an increasing error when approaching T_C.

Frey and Schwabl taken from Fig. 3.1. In panel (a) the theoretical scaling functions were selected according to Eq. (3.7) with $q_D = 0.033\,\text{Å}^{-1}$ [101]. The experimental and theoretical scaling functions obey the same dependence from x, decreasing to a minimum in the range $0 < x < 1$ and increasing for larger x. Also the trend as function of temperature is the same. Nevertheless, the agreement between theory and experimental results is not very good for both low and high temperatures. In order to quantify the deviation between theory and experimental results we have adjusted q_D in Eq. (3.7) in order to match experimental data and theoretical scaling function. Fig. 3.1 (b) shows the scaling function selected such that they fit the experimental data. The according dipolar wave numbers q_D are shown in panel (c) as function of temperature. The blue dashed line reflects the literature value $q_D = 0.033\,\text{Å}^{-1}$ from Ref. [101]. For $T_\text{C} < T < T_\text{C} + 8\,\text{K}$ q_D is slightly smaller than reported in literature, while above T_C+8 K q_D is significantly larger. It has to be noted that in Fig. 3.1 scaling functions are only pictured for integer values of N and the temperature dependence of N becomes very steep when approaching T_C, hence the uncertainty of q_D increases. The strong deviation towards smaller q_D is most likely an artifact, while the larger Q_D can be understood as a stronger damping of the transversal fluctuations and may be explained by the influence of the conduction electrons. Similar deviations of the damping have also been found in nickel as reported in Ref. [102, 103].

Inelastic excitations below the Curie point

MIEZE allows to extend the study of the critical fluctuations in iron below the Curie temperature in the region were the neutron beam is completely depolarized due to the ferromagnetic domains. In conventional NSE this is not easily possible. However, NSE can be altered in order to study under depolarizing conditions by adding two additional spin analyzers before and behind the sample. This variant of NSE is called Intensity Modulation NSE (INSE) and has been reported by B. Farago and F. Mezei [104]. In a first test measurement with INSE B. Farago *et al.* have studied the magnon dynamics in iron. Fig. 3.8 compares the results of the INSE and our MIEZE data. Panel (a) displays the normalized intermediate scattering functions as measured with INSE and MIEZE. Close to the transition at $T_\text{C} - 1\,\text{K}$ a decay is observed, that is very similar to a single exponential. Both the results of Farago *et al.* and ours are in excellent agreement with each other. At smaller temperatures $T_\text{C} - 3\,\text{K}$ and $T_\text{C} - 10\,\text{K}$ the shape of the curve changes to an oscillation damped by an exponential decay. However, the negative intermediate scattering function as reported by Farago *et al.* cannot be observed with MIEZE due to a technical aspect that is described at the end of Sec. 2.2.3. All MIEZE data shown in Fig. 3.8 (a) are the absolute value of $S(q,\tau)/S(q,0)$. The last two data points at $T_\text{C} - 10\,\text{K}$ are put to negative values by hand, while the open points reflect the original data. All data sets can be fitted by

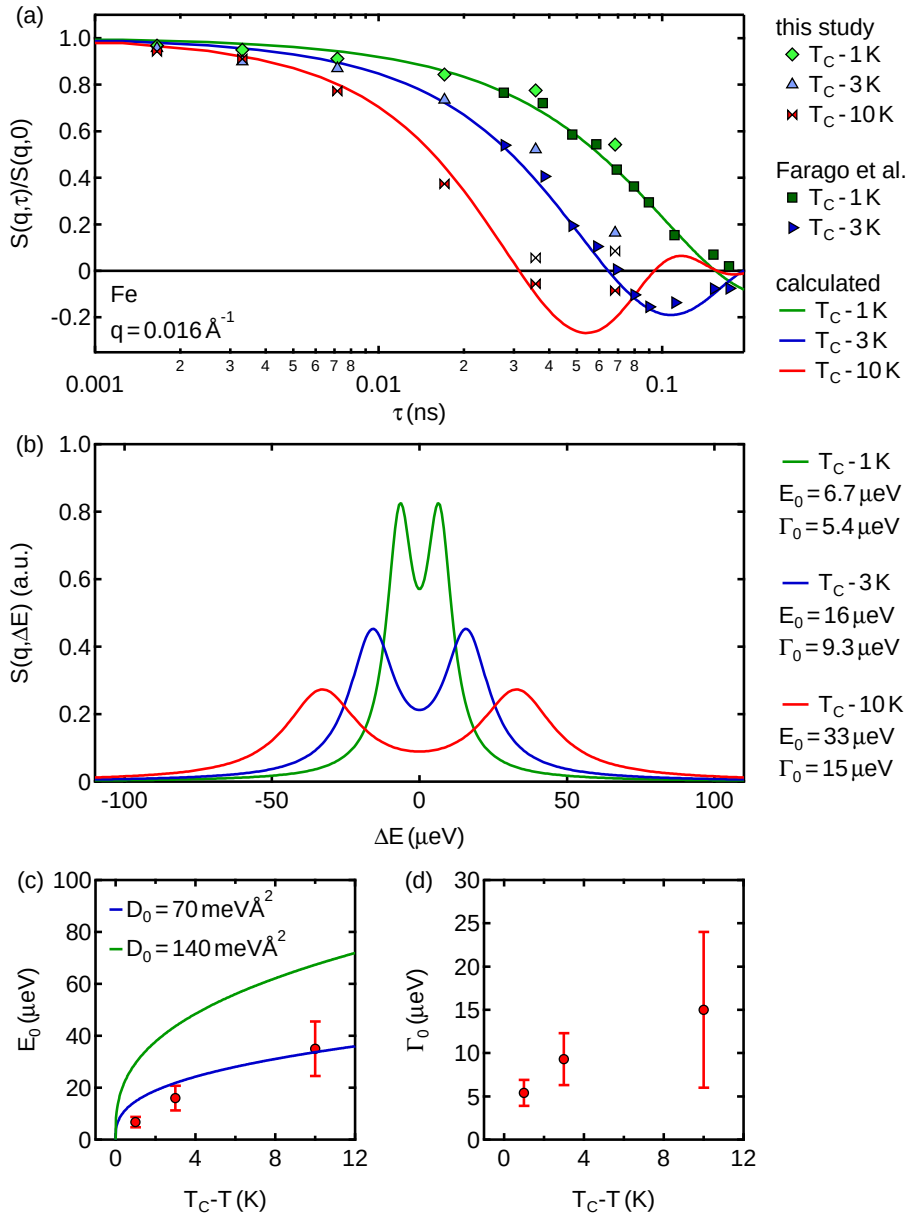

Figure 3.8.: Scattering function of iron in the time and energy space recorded in the ferromagnetic phase i.e. for $T < T_C$. In panel (a) the normalized intermediate scattering function at a scattering vector of $q = 0.016\,\text{Å}^{-1}$ is shown. Results by Farago *et al.*, using a variant of classical NSE so-called Intensity Modulation NSE [104], are directly compared to the results of our MIEZE study. The solid lines represent the Fourier transform of two Lorentzians centered at $\pm E_0$ with a width of Γ_0. Panel (b) shows the Fourier transform of the solid lines from panel (a). In panel (c) and (d) the temperature dependence of E_0 and Γ_0 are displayed, respectively. The solid lines in panel (c) are curves of the form $E_0 = D_0\left((T_C - T)/(T_C)\right)^{0.36}$.

the Fourier transform of two Lorentzians centered at $\pm E_0$ assuming the form

$$S(q,\Delta E) = S_0 \left(\frac{1}{(E - E_0)^2 + \Gamma_0^2} + \frac{1}{(E + E_0)^2 + \Gamma_0^2} \right), \tag{3.10}$$

with a width Γ_0. The solid lines in panel (a) are the results of the fits and panel (b) shows the Fourier transform. For $T_C - 10\,\mathrm{K}$ to few data points are available allowing no precise fit. Nevertheless, we observe distinct inelastic excitations with a finite energy in the range $6.7\,\mu\mathrm{eV} \leq E_0 \leq 33\,\mu\mathrm{eV}$ as shown in panel (c). In standard magnon theory the temperature dependence of the magnon energy is given by $E_0 = D_0((T_C - T)/T_C)^{0.36}$ [105, 106]. The solid lines reflect curves with the literature value $D_0 = 140\,\mathrm{meV\,\AA^2}$ (green curve) and $D_0 = 70\,\mathrm{meV\,\AA^2}$ (blue curve) fitting the data, respectively. The mismatch between theory and experimental results may be explained by the q resolution (FWHM $\sigma_q = 0.004\,\mathrm{\AA^{-1}}$ following Sec. 1.2.1) in combination with the varying spectral weight in the region of interest on the detector. Within the selected mask the intensity decreases with $1/(q^2 + \kappa^2)$, hence smaller q values are over estimated than larger q resulting in smaller energies E_0. Panel (d) shows the temperature dependence of the magnon width Γ_0. The error bars do not allow any predictions.

3.4. Discussion

Iron is one of the archetypal systems for the investigation of static and dynamic properties at second-order phase transitions. Our diffraction and MIEZE data directly show how the fluctuations become stronger in time and space when approaching the transition from the paramagnetic phase, resulting in a textbook example of critical opalescence. At T_C where fluctuations emerge on all length and time scales, the transmission decreases by a factor ≈ 2.

The temperature and q dependence of the lifetime of the critical fluctuations above T_C proof to be in good agreement with previous studies [38], showing clear deviation from a simple Heisenberg model treating the dipolar interaction only as weak perturbation [90]. Our results are in much better agreement with the theory put forward by Frey and Schwabl [91–93], based on a Hamiltonian comprised of exchange and dipolar interaction. The data resemble the shape of the scaling function proposed by Frey and Schwabl and the strength of the dipolar interaction q_D is in the same order of magnitude as reported in literature [101]. Nevertheless, our results do not agree with a temperature independent q_D. We observe a stronger damping of the transversal fluctuations. The mismatch may be explained by the influence of the conduction electrons Similar effects have been observed in nickel [102]. The conduction electrons are delocalized, consequently more dominant on larger regions, i.e. at small q. Compared to localized electrons the delocalized electrons are correlated, hence stronger damped.

Below T_C we find distinct inelastic excitations, i.e. magnons. The MIEZE methods proofs to give the same results as observed with INSE [104], even though the amount of points measured do not allow a rigorous determination of the magnon energy and width from only the MIEZE data. Nevertheless, the temperature dependence of the magnon energy extracted from combining the INSE and the MIEZE data is in agreement with standard magnon theory. Even though our first results are very promising, a precise determination of the shape of the intermediate scattering function below T_C using only the MIEZE method will be addressed in a future study.

Our data show that MIEZE yields the same results as classical NSE or more complex methods like INSE. This study demonstrates the advantage of the MIEZE technique for studies requiring high energy resolution in the small angle scattering regime. The combination of the MIEZE technique with a large position sensitive detector allows to study very efficiently quasi elastic dynamics over large q regions and is ideally suited to study critical dynamics. In particular, the possibility to perform measurements with depolarizing samples or depolarizing sample environments opens up the field for the investigation of field induced QPTs or the study of melting and reorientation transitions in the flux line lattice of superconductors.

CHAPTER 4

Cubic chiral Dzyaloshinskii-Moriya helimagnets

This chapter discusses the magnetic ground state and the dynamics in the cubic chiral Dzyaloshinskii-Moriya helimagnets MnSi, $Mn_{1-x}Fe_xSi$ and $Mn_{1-x}Co_xSi$, studied by means of SANS and spin echo spectroscopy. At the beginning a short introduction to the helimagnets, their magnetic phase diagram and the most important properties of the different magnetic phases is given. Further, polarized neutron scattering at the paramagnetic to helimagnetic transitions in zero magnetic field is reported, followed by a combined unpolarized SANS and MIEZE study of the evolution of the transition to the tricritical point in finite field and temperature. In the last part of this chapter the suppression of the helical order by means of iron and cobalt doping is discussed.

4.1. Introduction

Cubic chiral Dzyaloshinskii-Moriya helimagnets are a fascinating class of materials as they exhibit a very general and fascinating magnetic phase diagram (cf. Fig. 4.1). This class of materials includes metals such as MnSi, $Mn_{1-x}Fe_xSi$, $Mn_{1-x}Co_xSi$, semiconductors like $Fe_{1-x}Co_xSi$ and insulators as Cu_2OSeO_3. All these materials crystallize in the $P2_13$ (B20) space group, lacking inversion symmetry. Although the most prominent member of this group, MnSi, has been studied for decades, great scientific interest was recently generated by the discovery of a topologically non trivial spin structure, i.e. a so called skyrmion lattice [3].

4.1.1. Magnetic phase diagram

All chiral helimagnets share a common magnetic phase diagram (see Fig. 4.1), when scaling the magnetic field axis with the critical field H_{c2} and the temperature axis

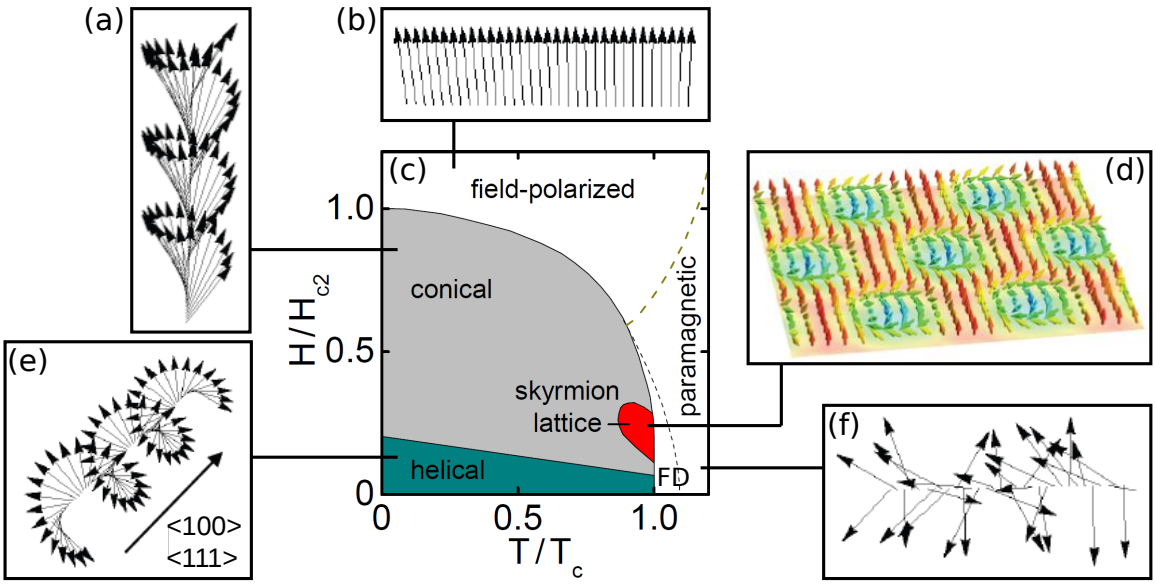

Figure 4.1.: Generalized magnetic phase diagram (c) of the cubic chiral Dzyaloshinskii-Moriya helimagnets as function of relative temperature T/T_c and relative magnetic field H/H_{c2}. The dashed lines are cross over lines from the paramagnetic phase into the fluctuation disordered (FD) and the field-polarized regime, respectively. The different panels depict the real space arrangement of the spins: helical phase (e), conical phase (a), field polarized ferromagnet (b), Skyrmion lattice (d) and paramagnetic phase (f). Figure taken from Ref. [107].

with the transition temperature T_c, respectively. The magnetic phase diagram can be explained by a hierarchy of energy scales [108] comprising of decreasing strength: (i) Ferromagnetic exchange interaction, aligning the magnetic moments parallel to each other. The lack of inversion symmetry gives rise to a (ii) Dzyaloshinskii-Moriya spin-orbit interaction which favors an orthogonal alignment of the magnetic moments. Combining these two gives rise to a long wavelength homochiral helix with a wavelength $\lambda_{\text{hel}} = 180$ Å for MnSi. Finally, (iii) a cubic magnetic anisotropy due to higher-order spin-orbit coupling aligns the helices along certain crystal directions [111] or [100], depending on the material. Theoretically the magnetic phase diagram and the transition between the different phases can be explained by a Ginzburg-Landau theory. The key elements of this Ginzburg-Landau theory presented below follow the supplementary material of Ref. [14]: Classically, the free energy functional is given by $\mathcal{F} = \int d^3x f$, with the free energy density f. The free energy density for chiral helimagnets can be separated in $f = f_0 + f_{\text{cub}}$ where f_0 has full rotational symmetry in zero external magnetic field and is given by [109, 110]

$$f_0 = \frac{1}{2}\boldsymbol{\phi}(r - J\nabla^2)\boldsymbol{\phi} + D\boldsymbol{\phi}(\nabla \times \boldsymbol{\phi}) + \frac{u}{4!}(\boldsymbol{\phi}^2)^2 - \mu_0\mu\boldsymbol{\phi}\mathbf{H}. \tag{4.1}$$

The three component dimensionless order parameter $\boldsymbol{\phi}$ represents the direction of the magnetization $\boldsymbol{M} = \mu\boldsymbol{\phi}$, with $\mu = \mu_B$/f.u.. J is the exchange stiffness and u the interaction parameter. D represents the Dzyaloshinskii-Moriya interaction and the last term the Zeemann energy. The terms of second and higher order in spin orbit coupling are summarized in f_{cub}. This term breaks the rotational symmetry for $\boldsymbol{H} = 0$ due to cubic anisotropies. It is given by

$$f_{\text{cub}} = \frac{J_{\text{cub}}}{2}\left[(\partial_x\phi_x)^2 + (\partial_y\phi_y)^2 + (\partial_z\phi_z)^2\right] + ..., \tag{4.2}$$

where the strength is given by J_{cub}. In zero field, this term forces the helices to point either along $\langle 111\rangle$ or $\langle 100\rangle$. The general ansatz minimizing the free energy density is a single conical helix. It can be written as

$$\boldsymbol{\phi}(\boldsymbol{r}) = \hat{\phi}_0\phi_0 + \Psi_{\text{hel}}\hat{e}^- e^{i\boldsymbol{k}_{\text{hel}}\boldsymbol{r}} + \Psi^*_{\text{hel}}\hat{e}^+ e^{-i\boldsymbol{k}_{\text{hel}}\boldsymbol{r}}, \tag{4.3}$$

with the homogeneous magnetization ϕ_0 and the complex amplitude of the helix Ψ_{hel}, with pitch vector $\boldsymbol{k}_{\text{hel}}$. The direction is given by $\hat{e}^{\pm} = (\hat{e}_1 \pm \hat{e}_2)/\sqrt{2}$, where the unit vectors $\hat{e}_i$ and the pitch vector $\boldsymbol{k}_{\text{hel}}$ generate a dreibein $\hat{e}_1 \times \hat{e}_2 = \hat{\boldsymbol{k}}_{\text{hel}}$.

This Ginzburg-Landau free energy describes the *helical* (Fig. 4.1 (e)) ground state in zero field and below T_c where the helices are aligned along the easy axis $\langle 111\rangle$ or $\langle 100\rangle$. When increasing the magnetic field above H_{c1}, the helices align along the magnetic field and the system enters the *conical* (a) phase where the magnetic moments of the helices bend more and more towards the field direction with increasing field. At H_{c2} the field polarized *ferromagnetic* (b) phase is reached. At high temperatures the system is in the *paramagnetic* (f) phase and completely disordered. However, in a small temperature and field region below T_c the so called A-phase emerges which was identified as topologically non trivial spin structure consisting of *skyrmions* (f) stabilized by thermal Gaussian fluctuations. The skyrmion lattice is discussed in the following section.

4.1.2. Skyrmion lattice

The skyrmion lattice is a topologically non trivial spin structure consisting of whirls in the magnetization which are stabilized in a small phase pocket below T_c. First referred to as A-phase [112] (c.f. red area in Fig. 4.1). Skyrmions were proposed by the nuclear physicist Tony Skyrme as a particle-like solution in a nonlinear field theory for interacting pions [113–115]. MnSi is the first bulk solid state system where skyrmions could be identified in 2009 [3]. Since then, skyrmion lattices, have been found in various materials ranging from pure metals [3, 116], to semiconductors [117, 118], and insulators [119, 120] as a generic feature of all B20 helimagnets. Besides the B20 compounds skyrmions also have been found on surfaces [121] and in thin films [122, 123].

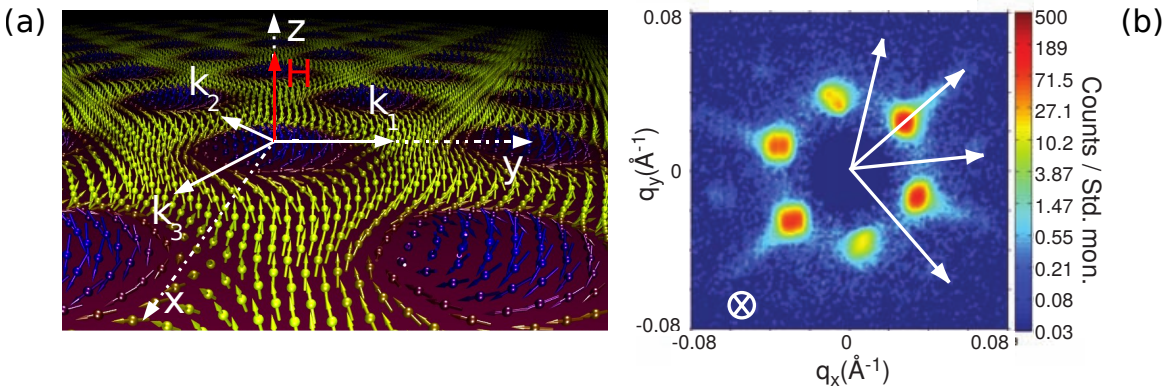

Figure 4.2.: (a) Real space image of the skyrmion lattice. Figure from [111]. The image shows a plane perpendicular to the magnetic field H. (b) Typical SANS pattern of a skyrmion lattice. The magnetic field is applied parallel to the neutron beam (taken from Ref. [3]).

The skyrmions arrange themselves in a hexagonal lattice. A skyrmion in B20 compounds can be characterized by a superposition of three helices $\boldsymbol{k}^i_{\mathrm{hel}}$, in the plane perpendicular to the magnetic field, with a fixed phase relation, 120° between the helices and a superimposed ferromagnetic component. Fig. 4.2 (a) shows a real space image of a skyrmion lattice. Along the magnetic field skyrmions form tubes similar to the flux line lattices in type-II superconductors. Each of the skyrmions carries one quantum of emergent magnetic flux.

Experimentally, the skyrmion lattice in MnSi was identified by SANS measurements [3] and measurements of the topological Hall effect [124–126]. The SANS pattern is quite similar to those of flux line lattices and has a characteristic six-fold symmetry as can be seen in Fig. 4.2 (b). The weak particle like character of the skyrmion could be proofed by a careful SANS study employing so called Renninger scans.

The non-trivial topology of the skyrmions gives rise to an additional signal to the Hall effect [124–126] called topological Hall-effect appearing on top of the anomalous Hall effect. Each spin of electrons traveling through the skyrmion lattice follows adiabatically the magnetic structure. Thus, the electrons collect a geometrical phase, i.e. the Berry phase, leading to their sideway deflection and hence to an additional contribution to the Hall-effect. The size of the topological Hall signal allows determining the density and winding number of the skyrmion lattice.

Very efficient gyromagnetic coupling between electrons and the magnetic structure allows manipulating the skyrmion lattice by an electric current. To completely unpin the skyrmion lattice only ultra-low current densities are needed $1 \times 10^6\,\mathrm{A\,m^{-2}}$ [127, 128] in contrast to the high densities ($1 \times 10^{12}\,\mathrm{A\,m^{-2}}$) required to move ferro-

magnetic domain walls, making skyrmions very interesting for spintronic applications, e.g. data storage devices with high bit density [129]. Nevertheless, the precise temperature dependence of the Skyrmion dynamics and the dynamics of the creation and annihilation [130] have to be understood in order to adopt Skyrmions for applications.

4.1.3. Paramagnetic to chiral transition in MnSi at zero magnetic field

The paramagnetic to helimagnetic transition in MnSi has been the subject of heated scientific discussions in recent years. There were several proposals for explaining the phase transition. The transition is expected to be of second-order on a mean field level as discussed by Grigoriev *et al.* [131, 132]. Nevertheless, specific heat measurements revealed a first-order character of the transition [133–135]. However, the precise character of the first-order transition has a subtle dependence on the strength of the cubic anisotropy. The same hierarchy of energy scales that is discussed above as basis for the magnetic phase diagram is expected to be reflected in the fluctuation spectrum when approaching the helimagnetic order from high temperature. For high temperatures $T \gg T_c$, essentially ferromagnetic fluctuations at $Q = 0$ are present. At a certain temperature, when the correlation length ξ reaches the order of the Dzyaloshinskii-Moriya interaction ξ_{DM}, isotropic chiral fluctuations develop on a sphere at finite $Q = k_{\mathrm{hel}}$ in reciprocal space. When cooling down further the cubic anisotropy, ξ_{cub} forces the chiral fluctuations along the easy axis of the system. These different fluctuating regimes are depicted in Fig. 4.3 (a). To distinguish between the three models separated by two cross overs we introduce the so called Ginzburg length ξ_{Gi} [136]. The Ginzburg length describes the length scale at which fluctuations have an important role and therefore lead to the breakdown of the mean field scenario. The three models introduced in Fig. 4.3 (a) are:

(i) Wilson-Fisher-scenario $\xi_{\mathrm{cub}} \gg \xi_{\mathrm{DM}} \gg \xi_{\mathrm{Gi}}$: The transition takes place from essential ferromagnetic fluctuations directly into the helimagnetic regime. This can be described by a Wilson Fisher renormalization fixed point approach [7].

(ii) Brazovskii-scenario $\xi_{\mathrm{cub}} \gg \xi_{\mathrm{Gi}} \gg \xi_{\mathrm{DM}}$: The helical isotropic distributed fluctuations are strongly interacting and drive the transition to first-order [9].

(iii) Bak-Jensen-scenario $\xi_{\mathrm{Gi}} \gg \xi_{\mathrm{cub}} \gg \xi_{\mathrm{DM}}$: In this scenario the isotropic chiral fluctuations, are only weakly interacting and evolve to anisotropic chiral fluctuations along the anisotropy direction of the system as described in Ref. [109].

Brazovskii scenario in MnSi

Janoschek *et al.* [14] could show that in MnSi the Brazovskii scenario of a fluctuation-induced first-order transition is realized. As discussed above it is essential to determine the precise relation between the relevant length scales in the system at the transition:

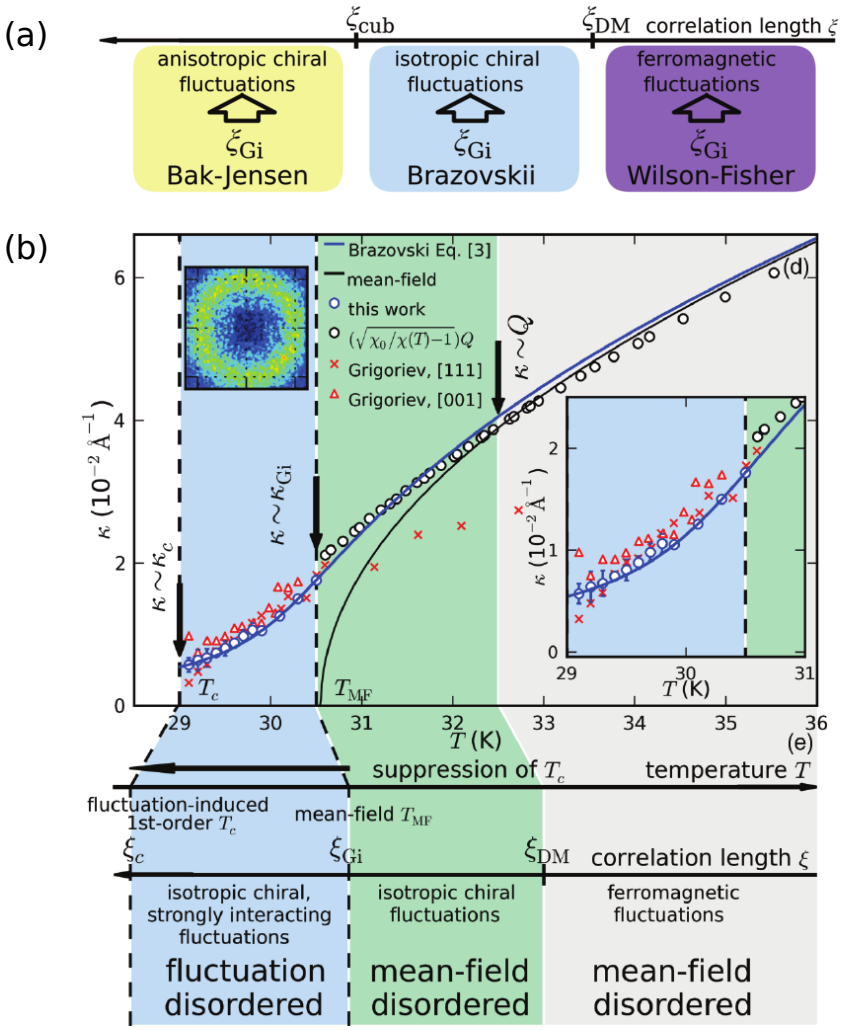

Figure 4.3.: Helimagnetic transition in MnSi. (a) Two crossovers in the fluctuation spectrum separate the three models discussed in the text describing the transition as first-order transition. Panel (b) depicts the inverse correlation length as function of temperature. Below 30.5 K the data are extracted from SANS and above 30.5 K from susceptibility measurements. The solid black line reflects the high temperature behavior while the blue line describes the renormalization of κ within the Brazovskii scenario. Figures are taken from Ref. [14].

The chiral Dzyaloshinskii-Moriya length $\xi_{\mathrm{DM}} = 1/k_{\mathrm{hel}}$, the cubic anisotropy length $\xi_{\mathrm{cub}} = 1/(\alpha_{\mathrm{cub}} k_{\mathrm{hel}})$ and the Ginzburg length which is given by the correlation length at the transition $\xi_{\mathrm{Gi}} = \xi(T_{\mathrm{c}})$. Janoschek *et al.* extracted these length scales from energy integrated SANS measurements. The scattering cross section for chiral helimagnets based on the free energy as mentioned above has been first derived by Grigoriev *et al.* [131]. The double Lorentzian profile is given by

$$\frac{\mathrm{d}\sigma}{\mathrm{d}\Omega} = A \frac{k_B T}{\left(q + k_{\mathrm{hel}}\right)^2 + \kappa^2} \times \frac{k_{\mathrm{hel}}^2 + q^2 + \kappa^2}{\left(q - k_{\mathrm{hel}}\right)^2 + \kappa^2 + \alpha_{cub}^2 k_{\mathrm{hel}}^2 (\hat{q}_x^4 + \hat{q}_y^4 + \hat{q}_z^4 - 1/3)}. \tag{4.4}$$

Here, k_B is the Boltzmann constant, A a proportionality constant depending on, e.g., the sample size and the neutron flux, T the temperature, k_{hel} the helical wave vector, $q = |\boldsymbol{q}|$ the magnitude of the scattering vector, κ the inverse correlation length, and α_{cub} the strength of the cubic anisotropy. α_{cub} can be directly connected to the Ginzburg-Landau ansatz in Eq. (4.2) by $\alpha_{\mathrm{cub}} = |J_{\mathrm{cub}}|/(2J)$. Its sign determines whether the helical domains align along $\langle 111 \rangle$ ($\alpha_{\mathrm{cub}} < 0$) or along $\langle 100 \rangle$ ($\alpha_{\mathrm{cub}} > 0$). The cross section describes the scattering intensity arising from the critical fluctuations for $T > T_{\mathrm{c}}$. The intensity accumulates on a sphere in reciprocal space with radius k_{hel} and shallow maxima along the $\langle 111 \rangle$ directions (for $\alpha_{\mathrm{cub}} < 0$) due to the cubic invariant $(\hat{q}_x^4 + \hat{q}_y^4 + \hat{q}_z^4 - 1/3)$, with $\hat{q} = \boldsymbol{q}/q$. Janoschek *et al.* employed simultaneous fits to the radial intensity distribution along several crystal directions to extract the temperature dependence of the inverse correlation length κ and the cubic anisotropy α_{cub}. The results for κ are shown in Fig. 4.3 (b) (blue circles) together with the temperature dependence expected for a mean-field transition (black solid line). The interaction between the strong chiral fluctuations leads to a non-analyticity in the free energy, renormalizing κ. According to this renormalization, the inverse correlation length in the Brazovskii scenario behaves as

$$\kappa(T) = \kappa_{\mathrm{Gi}} \sqrt{\frac{\left[\tau + \left(1 - \tau^3 + \sqrt{1 - 2\tau^3}\right)^{1/3}\right]^2}{2^{1/3}\left(1 - \tau^3 + \sqrt{1 - 2\tau^3}\right)^{1/3}}}, \tag{4.5}$$

with $\tau = (2^{1/3}/3)\kappa_{\mathrm{MF}}^2/\kappa_{\mathrm{Gi}}^2 = (T - T_{\mathrm{MF}})/T_0$. T_{MF} is the mean-field transition temperature. The temperature dependence described by Eq. (4.5) (blue solid line in Fig. 4.3 (b)) is perfectly recovered by the experimentally observed κ values.

Skyrmion liquid phase at the transition to helical order

A completely different scenario describing the formation of a skyrmion liquid phase in zero magnetic field between the paramagnetic and the helimagnetic phase was proposed by Rößler *et al.* [137]. However, this model is based on an additional phenomenological parameter, going beyond the minimal model comprised of the three energy scales only. This scenario implies a second phase transition at $T_{\mathrm{sk}} > T_{\mathrm{c}}$. The

formation of a skyrmion phase in a bulk sample at zero magnetic field is of tremendous interest, as it would open up new field for applications in spintronics.

In order to reveal the potential zero field skyrmion phase, Pappas and coworkers [138, 139] have investigated the so-called chiral fraction η of the magnetic intensity observed above T_c, which provides a measure of a chiral magnetic structure ordering predominantly in one of two possible chiral domains. The most important aspect in their argumentation is the observation of a chiral fraction $\eta \approx 1$ up to $T_c + 1\,\mathrm{K}$. Their data presented in Fig. 4.4 show the homochirality of the system below T_c and a smooth decay of η starting at $T_c + 1\,\mathrm{K}$.

However, η measures to what extent a system is homochiral, but there is no connection to the topological winding number or the phase relation of the underlying multi-q structure. Both are the defining properties of the new skyrmion structure found in MnSi under applied magnetic field.

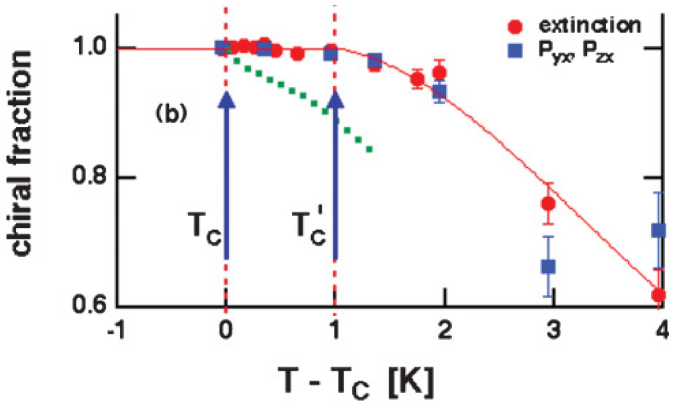

Figure 4.4.: Temperature dependence of the chiral fraction η as measured by Pappas *et al.* [139]. The chiral fraction η shows a completely chiral phase up to $T' = T_c + 1\,\mathrm{K}$.

4.1.4. Paramagnetic to chiral transition in MnSi at finite magnetic field

In the previous section it was argued, that the zero field transition from paramagnetism to helical order is a fluctuation-induced first-order transition. In contrast, the transition from the conical to the field polarized ferromagnetic phase at low temperatures is of second-order. Therefore, the character of the transition has to change from first- to second-order when following the transition line with increasing magnetic field. In a comprehensive study of the specific heat, Bauer *et al.* [140] could show that this is realized in a tricritical point at $\mu_0 H_{\mathrm{TCP}}^{\mathrm{int}} = 340\,\mathrm{mT}$ and $T_{\mathrm{TCP}} = 28.5\,\mathrm{K}$.

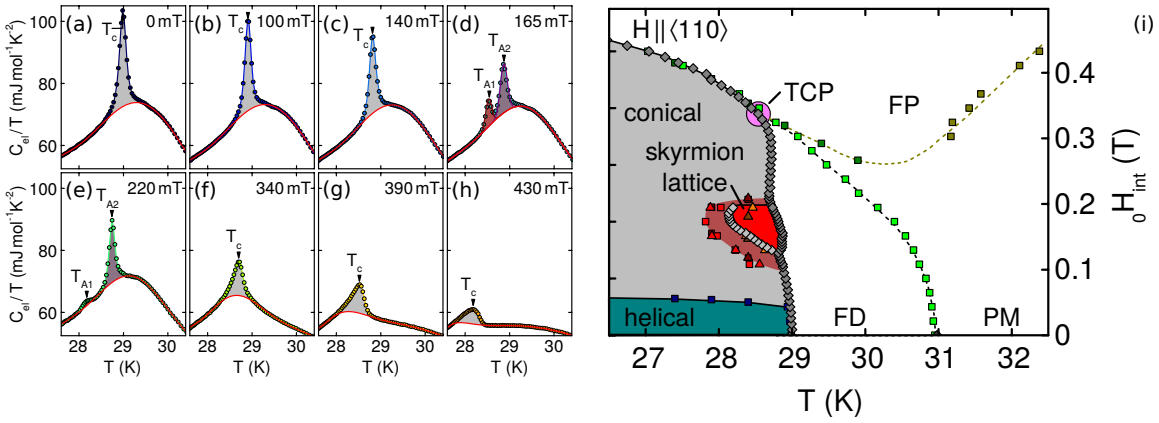

Figure 4.5.: Specific heat of MnSi as function of temperature for different magnetic fields from zero field (a) to 430 mT (h). The magnetic field is applied along the ⟨110⟩ direction. Panel (i) displays the magnetic phase diagram inferred from the specific heat data. Both the cross over line from the fluctuation disordered (FD) to the paramagnetic phase (PM) and the cross over line from the field polarized (FP) to the PM phase end in the tricritical point (TCP). All figures are taken from Ref. [140].

Typical specific heat data are shown in Fig. 4.5 (a) to (h). At zero field (panel (a)) a sharp symmetric first-order peak is visible on top of a broad shoulder. This sharp peak is associated with the helimagnetic transition temperature T_c and has a characteristic latent heat due to a weakly broadened first-order transition. The shoulder can be explained in terms of a Vollhardt invariance [141] at the temperature T_2. T_2 may be identified as the cross-over between ferromagnetic and isotropic chiral fluctuations as discussed above. At the magnetic field were $T_c = T_2$ the form of the specific heat peak changes to an asymmetric mean field like lambda anomaly (Fig. 4.5 (f)). This identifies the tricritical point (TCP) as also shown in the magnetic phase diagram in Fig. 4.5 (i).

This study not only allowed to identify the tricritical point but also to precisely identify the skyrmion lattice as a thermodynamic phase. Both, the transition into and out of the skyrmion phase shows peaks in the temperature dependent specific heat (c.f. 4.5 (d) and (e)) at T_{A1} and T_{A2}, respectively, clearly marking the lower and the upper boundary of the skyrmion phase.

4.1.5. Suppression of magnetic order by hydrostatic pressure and substitutional doping

Hydrostatic pressure suppresses the helical order in MnSi as can be seen in the pressure versus temperature phase diagram shown in Fig. 4.6 (a). While suppressing the

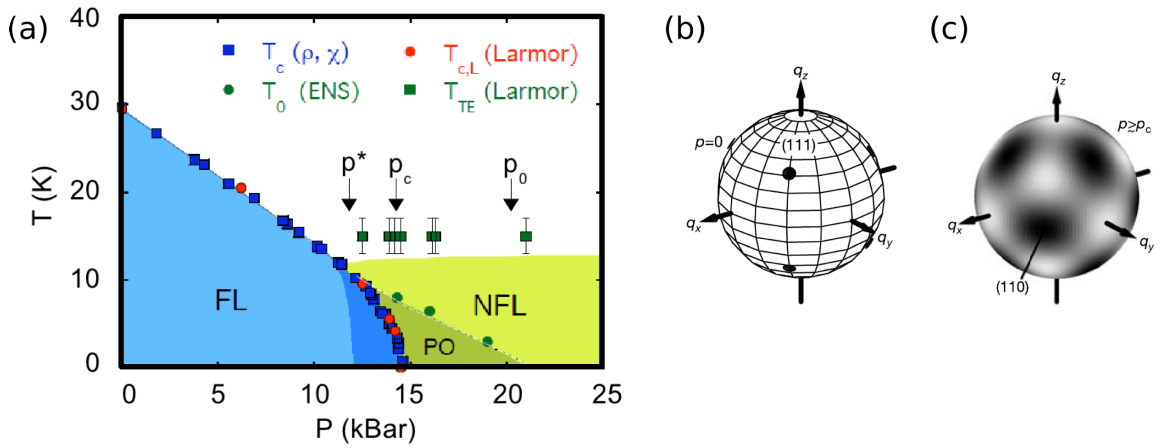

Figure 4.6.: Influence of hydrostatic pressure on the magnetic phase diagram of MnSi. Panel (a) shows the temperature-pressure phase diagram of MnSi, taken from [142]. The transition temperature T_c is inferred from resistivity ρ and ac susceptibility χ data from Ref. [143] (blue squares). T_0 is based on energy integrated SANS data from Ref. [144]. $T_{c,L}$ and T_{TE} are from Larmor diffraction data [142]. The light blue area indicates the region of Fermi liquid behavior and the dark blue region a regime of phase segregation seen in μSR [145]. In the green shaded region non-Fermi liquid behavior is observed. The dark green area is the region where the partial magnetic order occurs. The scattering distribution shows sharp peaks along the $\langle 111 \rangle$ below the critical pressure p_c (panel (b)) and broad maxima along the $\langle 110 \rangle$ directions (panel (c)) in the partial order above p_c [144].

helical transition temperature T_c, the characteristic magnetic fields B_{c1} and B_{c2} do not change. T_c vanishes at a critical pressure $p_c = 14.6\,\text{kbar}$ [146, 147]. At $p^* = 12\,\text{kbar}$ and $T^* = 12\,\text{K}$, the character of the transition changes to clear first-order, as inferred from the metamagnetic transition under applied magnetic field [148–150]. In the ordered phase (light blue shaded area) the electrons can be described by the standard model for metals, the Fermi liquid (FL) theory. The helical modulation is quite long compared to inter atomic distances, hence, by adding spin fluctuations to the Ginzburg-Landau theory, the ordered phase can be described as a weakly spin-polarized ferromagnet [151, 152]. The dark blue area shows a phase separation in the range between p^* and p_c, revealed by NMR [153] and μSR [145] measurements. Above p_c and below $T^* \approx 12\,\text{K}$ (light green shaded area), an extended non-Fermi liquid (NFL) regime is observed, that expresses itself in, e.g. an unusual temperature dependence of the resistivity. In contrast to the T^2 dependence expected from Fermi liquid theory, a $T^{3/2}$ dependence of the resistivity is observed down to mK and up to at least three times p_c [4, 26, 154, 155]. Below p_c the scattering intensity assumes sharp maxima along the $\langle 111 \rangle$ (c.f. Fig. 4.6 (b)) and for $p > p_c$ broad maxima along the crystalline $\langle 110 \rangle$ direction as shown in panel (c). The latter is referred to as partial order (PO) [144] and is shown as dark green area in panel (a). The scattering intensity in the PO has the same wave number ($\approx 0.035\,\text{Å}^{-1}$) as the helical intensity below p_c. Hence, helices or at least chiral fluctuations survive above p_c, however, the orientation cannot be explained within the Ginzburg Landau theory introduced in Sec. 4.1.1, as the $\langle 110 \rangle$ direction is not stable for the considered cubic anisotropy.

The temperature T_0 below which the partial order is observed can be called a freezing temperature. Below this temperature the fluctuations become slow enough to be measurable with energy integrated neutron scattering (SANS) [144] and NMR [156] measurements, suggesting a static structure on time scales between $10^{-10}\,\text{s}$ and $10^{-11}\,\text{s}$ [145]. The pressure were T_0 extrapolates to zero is called $p_0 = 21\,\text{kbar}$. A neutron Larmor diffraction study [142] of the thermal expansion revealed that neither at p_c nor at p_0 the sign of the Grüneisen parameter changes, which would indicate a first-order quantum phase transition. Recently, in a comprehensive study of the topological Hall effect, Ritz *et al.* [27, 157] could show that with increasing pressure the topological Hall effect increases by a factor of 10 in finite field. Furthermore, above p_c the topological Hall signal can even be observed at zero field extending in the complete non-Fermi liquid regime. Consequently, topological non trivial skyrmion like structures or fluctuations may be the reason for the non-Fermi liquid behavior in MnSi under hydrostatic pressure.

Besides hydrostatic pressure also the substitution of manganese atoms by iron or cobalt suppresses the magnetic order in MnSi. Substitutional doping, also referred to as "chemical pressure" decreases the lattice constant and may change the number of valance electrons per unit cell. Both effects change the electronic band structure and therefore the density of states at the Fermi level. Doping increases the disorder in the

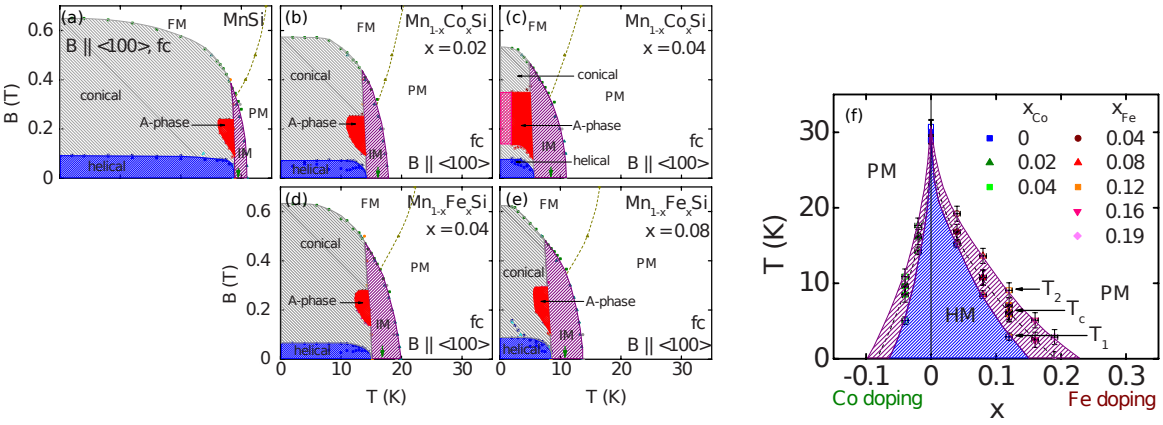

Figure 4.7.: Influence of iron and cobalt doping onto the magnetic H-T phase diagram of MnSi (a). Panels (b) and (c) depict the magnetic phase diagram of $Mn_{1-x}Co_xSi$ for $x = 0.02$ and $x = 0.04$, respectively. The magnetic phase diagram of $Mn_{1-x}Fe_xSi$ $x = 0.04$ and $x = 0.08$ are shown in panels (d) and (e), respectively. The doping versus temperature phase diagram for iron doping (to the right) and cobalt doping (to the left) is displayed in panel (f). All figures taken from Ref. [159].

system leading to unexpected changes of the physical properties. Nevertheless, the effect of disorder seems to be small in $Mn_{1-x}Fe_xSi$ and $Mn_{1-x}Co_xSi$ as the magnetic phase diagram shown in Fig. 4.7 stays essentially the same [158–160].

The number of valance electrons per formula unit increases by one respectively two when doping with iron or cobalt. Cobalt doping has twice the effect of iron doping as can be seen in the magnetic phase diagrams shown in Fig. 4.7 (a) to (e). The suppression of T_c is the same in $Mn_{1-x}Fe_xSi$ and $Mn_{1-x}Co_xSi$ crystals when the amount of iron doped into the host crystal is twice the amount of cobalt $x_{Fe} = 2x_{Co}$. Substitutional doping does not change the critical fields H_{c1} and H_{c2}. The helical wave number k_{hel} significantly increases with doping as will be discussed in more detail in Sec. 4.4.1. Nevertheless, the increase of k_{hel} is also reflected in an increase of the Skyrmion density giving rise to a large topological Hall effect $\sim 50\,n\Omega\,cm$ [45]. Measurements of the magnetization, specific heat and susceptibility reported in Ref. [159] suggest that with the suppression of T_c to zero an underlying ferromagnetic quantum critical point at $x_c^{Fe} \approx 0.192$ and $x_c^{Co} \approx 0.084$ occurs (see Fig. 4.7 (f)). In contrast to pure MnSi under hydrostatic pressure, the first-order character of the Brazovskii transition in $Mn_{1-x}Fe_xSi$ and $Mn_{1-x}Co_xSi$ smears out more and more when approaching the critical concentration [159]. A neutron scattering study referred to this phenomenon as chiral criticality [161].

In conclusion, the effects on the physical properties of MnSi introduced by hydrostatic pressure and doping are very similar and a combined discussion may give new

insight to answer open questions as for example the precise nature of the partial order.

4.1.6. SANS measurements on chiral magnets

All measurements described in this chapter are performed on helical magnets as described in the previous sections in the small angle scattering regime. There are two scattering geometries which allow to observe the different magnetic phases introduced in Sec. 4.1.1.

- $\boldsymbol{B} \perp \boldsymbol{n}$: In this geometry (Fig. 4.8 (a)) both the conical and the Skyrmion phase can be observed. While the conical peaks occur on the horizontal axis the Skyrmion peaks occur along the z-axis.
- $\boldsymbol{B} \parallel \boldsymbol{n}$: This geometry is shown in Fig. 4.8 (b). It allows to observe the sixfold geometry of the Skyrmion crystal on the detector.

In Fig. 4.8 also the rocking angle ω is introduced as a rotation of the sample together with the magnetic field about the z-axis. The azimuthal angle α is defined as angle between a point on the detector and the z-axis, also indicated on the detector image in Fig. 4.8.

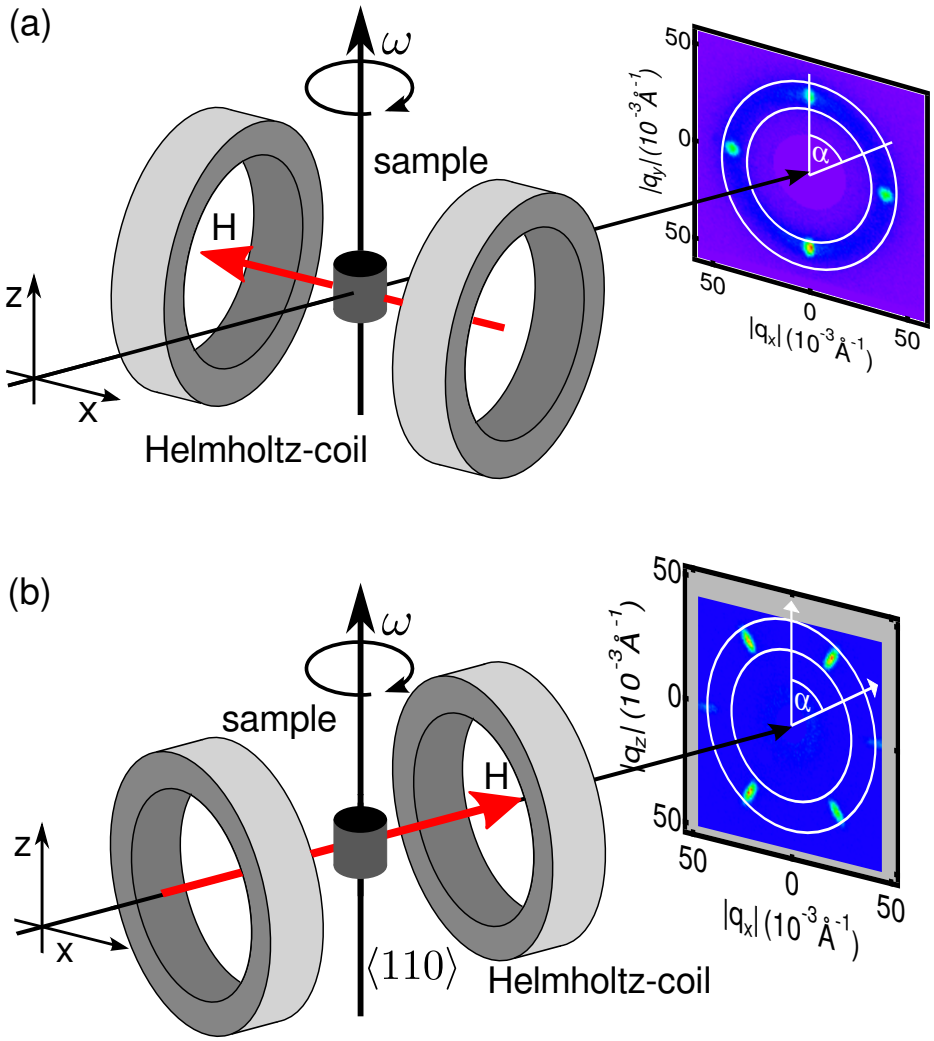

Figure 4.8.: Orientation of magnetic field with respect to the neutron beam. In panel (a) the field is aligned horizontally, perpendicular to the neutron beam. This orientation allows accessing the conical order on the horizontal axis and the Skyrmion crystal on the vertical axis. In (b) the magnetic field is aligned parallel to the neutron beam, which allows observing the sixfold symmetry of the Skyrmion crystal. The rocking angle ω is defined as a rotation of the sample and the magnetic field about the z-axis. α as defined on the detector gives the azimuthal angle.

4.2. Critical spin-flip scattering at the helimagnetic transition of MnSi

In order to clarify whether the proposed Brazovskii scenario (see Sec. 4.1.3) describing the transition within the minimal model can also explain the scattering of polarized neutrons, we re-investigated the critical spin-flip scattering and the chiral fraction η above T_c. Therefore, a new compact spherical neutron polarimetry device called MiniMuPAD was designed and built. The construction of the first MiniMuPAD and the measurements of the data presented in this section were already performed within my diploma thesis [50], whereas the analysis was part of this thesis. The analysis shows that the critical scattering at the helimagnetic transition of MnSi is in very good agreement with the Brazovskii scenario. This section follows our publication [15].

4.2.1. Experimental setup and sample

For a detailed description of MiniMuPAD see Sec. 2.1 and Ref. [15, 50]. The MiniMuPAD was used at the beamline RESEDA using neutrons with a wavelength of $\lambda = 4.5\,\text{Å}$ and a spread of $\Delta\lambda/\lambda = 0.16$. The neutron beam was polarized using a cavity and analyzed using a bender with an efficiency of 95% and 98%, respectively. A position sensitive CASCADE detector with an active area of $200\,\text{mm} \cdot 200\,\text{mm}$ was positioned at a distance of 1596 mm from the sample. The MnSi single crystal used for this study is the one that has already been investigated in Ref. [14]. The sample was oriented by X-ray Laue diffraction and aligned such that two $\langle 111 \rangle$ directions were orthogonal to the neutron beam with one axis being horizontal. These domains are denoted by $\mathbf{k}_1 \parallel [1\bar{1}\bar{1}]$ and $\mathbf{k}_2 \parallel [1\bar{1}1]$. The neutron beam was aligned along the [110] as shown in Fig. 4.9 (a). The detector in combination with the possibility to rotate the sample about an angle Φ as described in Fig. 2.1 allowed to track several points on the sphere with $|\mathbf{Q}| = k_{\text{hel}}$ going well above previous studies [138].

4.2.2. Experimental results

For a physically transparent theoretical account of the critical spin-flip scattering and also to proof the working principal of the MiniMuPAD, we start with the spin-resolved energy-integrated neutron scattering cross section $\sigma_{\hat{e}_{out},\hat{e}_{in}}(\mathbf{Q}) = \frac{\mathrm{d}\sigma}{\mathrm{d}\Omega}$, with momentum transfer $\mathbf{Q}$, as motivated in Sec. 1.1.4. This cross section describes the transition of the neutron spin eigenstate $\hat{e}_{in}$ to $\hat{e}_{out}$ with $\vec{\sigma}|\hat{e}_\alpha\rangle = e_\alpha|\hat{e}_\alpha\rangle$ and $\alpha = x,y,z$. In general, the scattering cross section is comprised of a purely nuclear and purely magnetic contribution, as well as an interference term between nuclear and magnetic scattering [55, 162]. For the measurement shown in Fig. 4.9 no spin analyzer was placed behind the sample. Instead the sample itself was used as spin analyzer and only the incoming polarization was rotated in the (k_1,k_2)-plane by the precession coils of the MiniMuPAD. The results can be described by the spin-polarization dependent

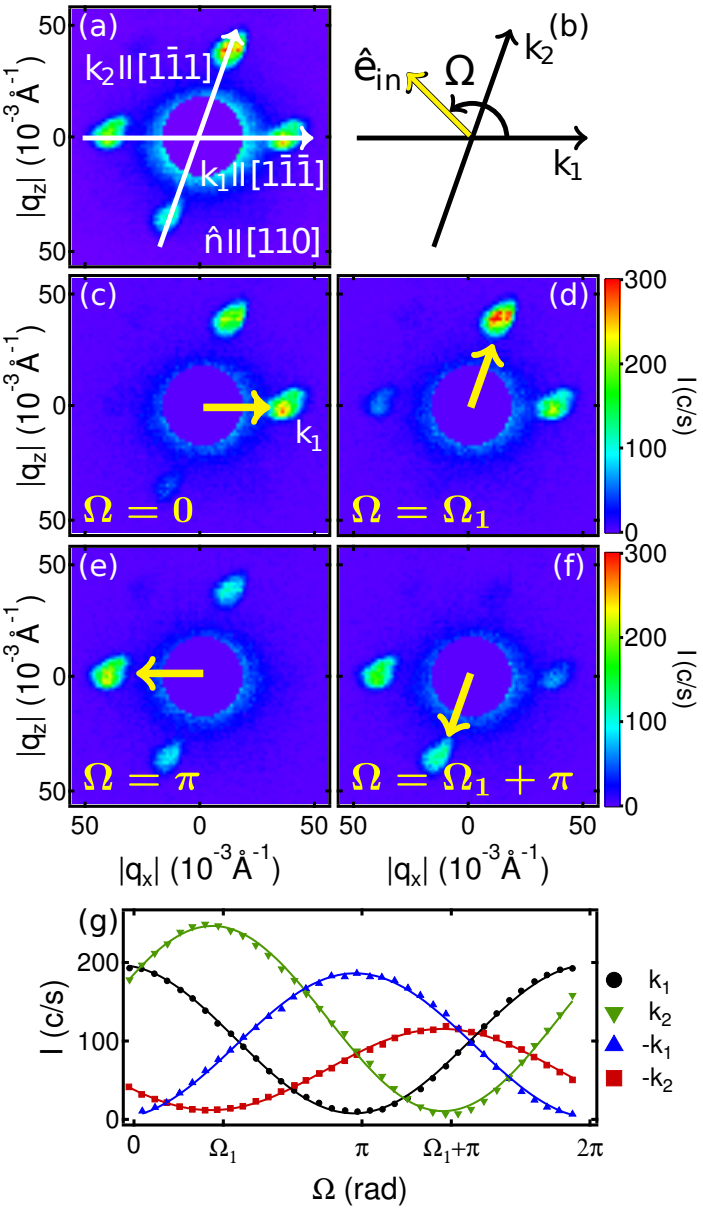

Figure 4.9.: The spin-selective Bragg scattering of the helimagnetic order in MnSi is used to show the operating principle of the MiniMuPAD. In panel (a) a unpolarized scattering pattern is shown, by summing all incoming polarization directions. (b) Sketch defining then angle between $\boldsymbol{k}_1$ and the incoming polarization direction $\hat{e}_{\mathrm{in}}$. (c) through (f) scattering patterns for different orientations of the incoming polarization. Figure is reproduced from [15].

scattering cross-section

$$\sigma(\mathbf{Q},\hat{e}_{in}) = \sum_{\tau=\pm1} \sigma_{\tau\hat{e}_{out},\hat{e}_{in}}(\mathbf{Q}). \tag{4.6}$$

The magnetic contribution to the magnetic part of this cross section can be separated into a symmetric and an antisymmetric part

$$\sigma_{mag}(\mathbf{Q},\hat{e}_{in}) = \sigma^{S}_{mag}(\mathbf{Q}) + (\hat{Q}\hat{e}_{in})\sigma^{A}_{mag}(\mathbf{Q}), \tag{4.7}$$

the antisymmetric part is weighted with the scalar product $\hat{Q}\hat{e}_{in}$, with $\hat{Q} = \mathbf{Q}/Q$. As measure for the chirality of the magnetic system one can now define the chiral fraction η by

$$\eta(\mathbf{Q}) = \frac{\sigma^{A}_{mag}(\mathbf{Q})}{\sigma^{S}_{mag}(\mathbf{Q})}. \tag{4.8}$$

In zero magnetic field Eq. (4.3) can be simplified and the magnetization in the helical order of MnSi can be described by $\vec{M}(\mathbf{r}) = M_{hel}(\hat{e}_1 \cos \mathbf{k}_{\rm hel}\mathbf{r} + \hat{e}_2 \sin \mathbf{k}_{\rm hel}\mathbf{r})$, with the helical modulation vector $\mathbf{k}_{\rm hel}$, and the orthonormal unit vectors $\hat{e}_i\hat{e}_j = \delta_{ij}$ $(i,j = 1,2)$, being orthogonal to $\mathbf{k}_{\rm hel}$. A left handed helix is then given by $\hat{e}_1 \times \hat{e}_2 = -\hat{k}_{\rm hel}$. The magnetic Bragg scattering from a helix has an equal contribution of the symmetric and antisymmetric part $\sigma_{mag}(\mathbf{Q})|_{\rm Bragg} = \pm\sigma_{mag}(\mathbf{Q})|_{\rm Bragg}$. The sign defines the handedness of the helix. For the left handed helimagnetic ground state of MnSi one therefore expects a scattering cross section of the form

$$\sigma_{mag}(\mathbf{Q} = \mathbf{k}_{\rm hel},\hat{e}_{in}) \propto 1 + (\hat{k}_{\rm hel}\hat{e}_{in}) = 2\cos^2(\delta\Omega/2), \tag{4.9}$$

where $\delta\Omega$ is the angle between the incoming polarization and the helical domain $\mathbf{k}_{\rm hel}$, as also defined in Fig. 4.9 (b).

This sinusoidal dependence can be measured by rotating the incoming polarization in the plane perpendicular to the incoming neutron beam, while using no spin analyzer. The results of such a measurement are shown in Fig. 4.9, where panel (a) shows an integrated scattering pattern over all incoming polarization directions. The angle Ω defines the orientation of the incoming neutron beam with respect to $\mathbf{k}_1$ as shown in panel (b). Figures (c) through (f) show scattering patterns for $\Omega = 0$, $\cos^{-1}(1/3)$, π and $\cos^{-1}(1/3) + \pi$. These angles correspond to the helical domains aligned along the $\langle 111 \rangle$ directions of the crystal. In Fig. 4.9 (g) the integrated intensity on all four helical spots ($\mathbf{k}_1$, $\mathbf{k}_2$, $-\mathbf{k}_1$ and $-\mathbf{k}_2$) as function of Ω are shown. The data are perfectly fitted by Eq. (4.9). The difference in the amplitude of the oscillation may come from a small misalignments of the $\mathbf{k}_2$ axis with respect to the SNP device. See also Fig. 4.9 (a).

By means of an additional spin analyzer behind the sample the critical spin-flip

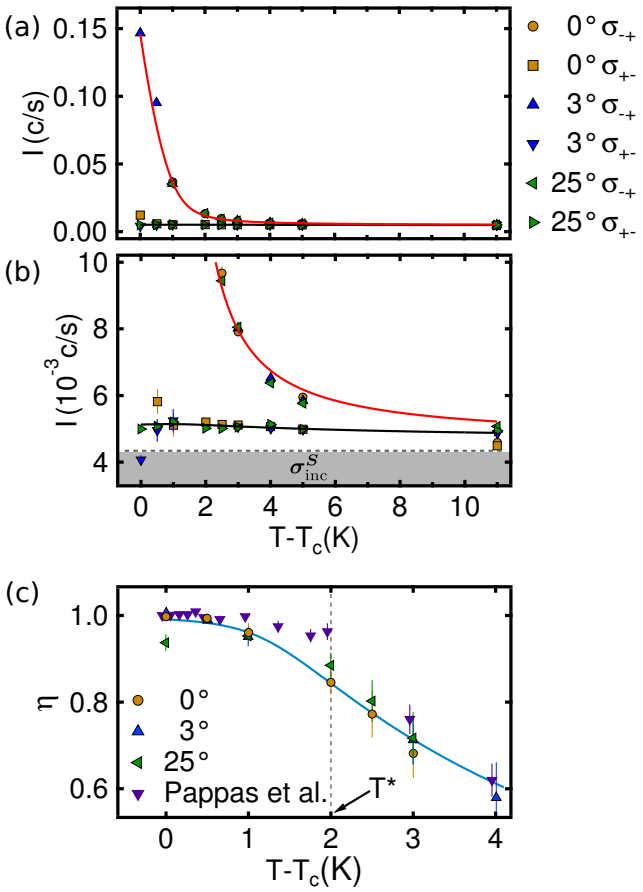

Figure 4.10.: (a) Temperature dependence of the spin-flip scattering cross section of MnSi $\sigma^{\parallel}_{\pm,\mp}(\mathbf{Q})$ close to the critical temperature $T > T_c$. The spin-flip scattering has been measured with different orientations on the sphere with $|\mathbf{Q}| = k_{\mathrm{hel}}$, defined by the angle $\Phi = 0°, 3°, 25°$. For $\Phi = 0°$, $\hat{Q} \parallel [1\bar{1}\bar{1}]$ all other orientations are defined by an anticlockwise rotation about the [112] axis, compare also Fig. 2.1 (c). The data measured for $\Phi = 25°$ were corrected for transmission. (b) Same data but on a different intensity scale. The gray shaded area is the fitted incoherent spin-flip background $\sigma^{S}_{\mathrm{inc}}$. (c) the chiral fraction η as function of temperature calculated with Eq. (4.11) from the spin-flip data. The solid lines are fits to the Brazovskii theory, predicting a turning point of $\eta(T)$ at T^*. Figure from Ref. [15].

scattering can be accessed. For this study the polarization of the incoming and outgoing neutrons was aligned parallel and antiparallel to the transferred momentum $\mathbf{Q}$. The cross section reads $\sigma_{\tau_{out}\hat{Q},\tau_{in}\hat{Q}}(\mathbf{Q})$ with $\tau_{out}, \tau_{in} = 1, -1$ being the up $\uparrow$ and down $\downarrow$ state of the neutrons with respect to $\hat{Q}$. According to the theory for chiral magnets [131] and as an extension of Eq. (4.4) one expects the spin-flip scattering to assume the form

$$\sigma^S_{mag}(\mathbf{Q}) \mp \sigma^A_{mag}(\mathbf{Q}) = \frac{Ak_BT}{(|\mathbf{Q}| \pm k_{\rm hel})^2 + \kappa^2(T)} \tag{4.10}$$

for $T > T_{\rm c}$. Here, k_B is the Boltzmann constant and $\kappa(T)$ the temperature dependent inverse correlation length as shown in Fig. 4.3 (b). The inverse correlation length provides the connection to the different scenarios described in Sec. 4.1.3. In case of the Brazovskii scenario, $\kappa(T)$ renormalizes as shown in Eq. (4.5), due to the strong interaction of the chiral paramagnons. In Fig. 4.10 (a) and (b) the critical spin flip scattering $\sigma^{\parallel}_{\pm\mp}(\mathbf{Q})$ measured on a sphere with a radius of the helical modulation vector $\mathbf{k}_{\rm hel}$ is shown as function of temperature. Approaching $T_{\rm c}$, the chiral magnetic intensity indeed develops isotropically on the sphere as can be seen in panel (b). $\sigma^{\parallel}_{-+}$ has a very strong temperature dependence above $T_{\rm c}$, while the channel $\sigma^{\parallel}_{+-}$ is barely temperature dependent as it is suppressed by an additional factor $4k^2_{\rm hel}$ in the denominator of Eq. (4.10). The solid lines in Fig. 4.10 (a) and (b) are fits to the data using Eq. (4.10). For this fit we used the published results for $\kappa(T)$ [14], also shown in Fig. 4.3 (b). Hence, only two free parameters, namely the magnitude A and a $\mathbf{Q}$-independent incoherent background σ^S_{inc} shown as dashed line in Fig. 4.3 (b). Fitting all data sets simultaneously gives a remarkably good agreement with both cross sections for $\pm k_{\rm hel}$.

The chiral fraction η can be extracted from the critical spin-flip scattering when subtracting the fitted background σ^S_{inc} by

$$\eta(\mathbf{Q}) = \frac{\sigma^A_{mag}(|\mathbf{Q}| = k_{\rm hel})}{\sigma^B_{mag}(|\mathbf{Q}| = k_{\rm hel})} = \frac{1}{1 + \kappa^2(T)/(2k^2_{\rm hel})}. \tag{4.11}$$

Fig. 4.10 (c) shows the results of this study compared with those of Pappas *et al.* [138]. It is essential to note that the experimental values depend sensitively on σ^S_{inc} (likewise the error bars of η). Within the error bars, however, the chiral fraction is in very good agreement with the Brazovskii theory of $\kappa(T)$. In particular, $\eta(T)$ displays a characteristic point of inflection at a temperature $T^* - T_{\rm c} \approx 2\,{\rm K}$. It is finally instructive to note that $\eta(T)$ reported by Pappas *et al.* [138, 139] differs substantially up to $\approx 2\,{\rm K}$ above $T_{\rm c}$ as shown in Fig. 4.10 (c). Based on the information given in Refs. [138, 139] we strongly suspect that this difference is due to an overestimation of σ^S_{inc}.

4.2.3. Discussion

In conclusion, we have investigated the critical spin-flip scattering with an emphasis on the chiral fraction η close to the helimagnetic transition in MnSi. For our study we have developed a miniaturized, low-cost SNP device, that allows an easy implementation of polarization analysis up to scattering angles of $2\theta = 15°$ at different beamlines. Considering carefully the importance of incoherent scattering yielding background we find excellent quantitative agreement of the temperature dependence of the chiral fraction η at various sample orientations with the Brazovskii scenario of a fluctuation-induced first order transition. Our study [15] provides a quantitative connection of η with elastic neutron scattering as well as the magnetization, susceptibility, and specific heat discussed in Ref. [14], completing a remarkably comprehensive account in a minimal model, introduced in Sec. 4.1.1, that does not require any additional phenomenological parameters such as those needed in a recent proposal [137] for the prediction of skyrmion formation at zero magnetic field in bulk chiral magnets.

4.3. Evolution of the helimagnetic transition in MnSi with magnetic field

In the previous section, the helimagnetic transition in MnSi in zero magnetic field was identified as fluctuation-induced first-order transition that can be described within a Brazovskii scenario. The transition from the conical to the field induced ferromagnetic phase at low temperatures is of second-order. Consequently, the phase transition has to change from first- to second-order somewhere on the transition line. In a recent thermodynamic study, Bauer *et al.* [140] could show that this change takes place at a tricritical point at $\mu_0 H_{\mathrm{TCP}}^{\mathrm{int}} = 340\,\mathrm{mT}$ and $T_{\mathrm{TCP}} = 28.5\,\mathrm{K}$ as discussed in Sec. 4.1.4.

The helimagnetic transition is driven to first-order, because the chiral fluctuations at finite q have a large phase space available, leading to strong interactions. A magnetic field applied to the sample reduces the available phase space by forcing the chiral fluctuations to develop along the field direction. Therefore, the first-order Brazovskii transition is suppressed and evolves towards a second-order transition.

In this section, we first report a SANS study to determine the correlation length of the chiral fluctuations in reciprocal space. Secondly, a MIEZE study accessing the quasi elastic linewidth of the fluctuations at the transition is discussed. The results precisely identify the temperature and field were the transition changes from first to second-order and give additional evidence for the Brazovskii scenario in MnSi.

4.3.1. Correlation length of the magnetic fluctuations

The discussion of the magnetic field evolution starts with the SANS measurements performed at SANS-1 (MLZ). In the following section the SANS experiments and their evaluation are reported.

Experimental setup and sample

The measurements have been performed at SANS-1 (MLZ), investigating the magnetic correlation length at the helimagnetic transition. For the experiment, neutrons with a wavelength of $\lambda = 5.5\,\text{Å}$, coarsely monochromatized $\Delta\lambda/\lambda = 0.10$ by a mechanical velocity selector were used. The collimation of the initial beam was set to 12 m with a pinhole of 20 mm diameter at the entrance of the collimation section and a 4 mm pinhole in front of the sample. The detector was positioned 10.2 m behind the sample. To access the complete (B,T)-phase diagram a superconducting magnet, optimized for small angle scattering, combined with a closed cycle cryostat were used. The magnet allows for in-plane fields up to 5 T and is the same as described in Sec. 2.2.4 and shown in Fig. 2.7 (a). A minimal temperature of 4 K was available with the cryostat. The sample was mounted on a sample stick, which allowed for rotation about the vertical $\langle 110 \rangle$ axis of the sample. A spherical shaped MnSi single crystal

(OFZ 59) with a ⟨110⟩ direction oriented vertically was used as sample. The diameter of the sphere is 6 mm and a ⟨111⟩ axis was aligned horizontally, perpendicular to the neutron beam and parallel to the magnetic field. Hence, neutron beam and magnetic field resembles the perpendicular geometry as described in Sec. 4.1.6. Considering the sample shape and the measured susceptibility as described in Ref. [163] the internal field applied to the sample is given by $H_{\mathrm{int}} = 0.90 \cdot H_{\mathrm{ext}}$. All magnetic fields in this section are given as internal fields.

Experimental results

In Fig. 4.11 typical SANS patterns for temperatures below (left column) and above (middle column) the helical transition temperature T_{c} are shown. From bottom to top the magnetic field increases, starting at zero field up to $\mu_0 H^{\mathrm{int}} = 432\,\mathrm{mT} > \mu_0 H^{\mathrm{int}}_{\mathrm{TCP}}$. Each scattering pattern shows the sum of a rocking scan about $\omega \pm 3°$. In zero magnetic field and below the transition temperature, helical peaks appear along the horizontally oriented crystalline ⟨111⟩ axis (cf. Fig. 4.11 (s)). With increasing field at the same position conical peaks appear as can be seen in panels (a), (d), (g), (j), (m) and (p). Above T_{c} and in zero magnetic field, the critical scattering accumulates on an isotropic sphere as described within the Brazovskii scenario [14] (Fig. 4.11 (t)). In Fig. 4.12 the intensity on the ring with $q = |\mathbf{k}_{\mathrm{hel}}|$ is shown versus the azimuthal angle α. The intensity is flat as function of α, with small peaks along the ⟨111⟩ direction. The small peaks at $\alpha = 0°$ and $\alpha = 180°$ correspond to a small cubic anisotropy of $\alpha_{\mathrm{cub}} \approx (-0.04 \pm 0.01)\,\text{Å}^{-1}$, as will be discussed in the following sections. Besides this small anisotropy the region above T_{c} shows an isotropic sphere of critical intensity, that is observed as a ring on the SANS detector.

Increasing the magnetic field forces the magnetic fluctuations above T_{c} to align more and more along the horizontal field direction. Up to $\mu_0 H^{\mathrm{int}} = 135\,\mathrm{mT}$ (cf. Fig. 4.11 (n),(q)) the fluctuations are still symmetric with respect to $Q = 0$, showing small remnants of the skyrmion phase along the vertical ⟨110⟩ direction. Above 135 mT (cf. panel (k)) the fluctuations do not accumulate on a full ring anymore but on spherical segments along the magnetic field. The symmetry of the fluctuations about $q = 0$ changes completely when crossing the tricritical point in Fig. 4.11 (h). Above $\mu_0 H^{\mathrm{int}}_{\mathrm{TCP}}$, the center of mass of the fluctuations is not anymore a ring around $Q = 0$ but $\mathbf{q} = \pm\mathbf{k}_{\mathrm{hel}}$.

The Brazovskii fluctuations are also visible in the temperature dependence of the scattering intensity. In the right column of Fig. 4.11 the intensity is evaluated as function of temperature on the *peaks* (red filled circles) and on the *ring* (black filled boxes). The latter region is a ring with radius k_{hel}, excluding the positions where the helical peaks occur below T_{c}. When approaching the transition in zero field (cf. panel (u)) from high temperatures the intensity on both ring and peak increase until at

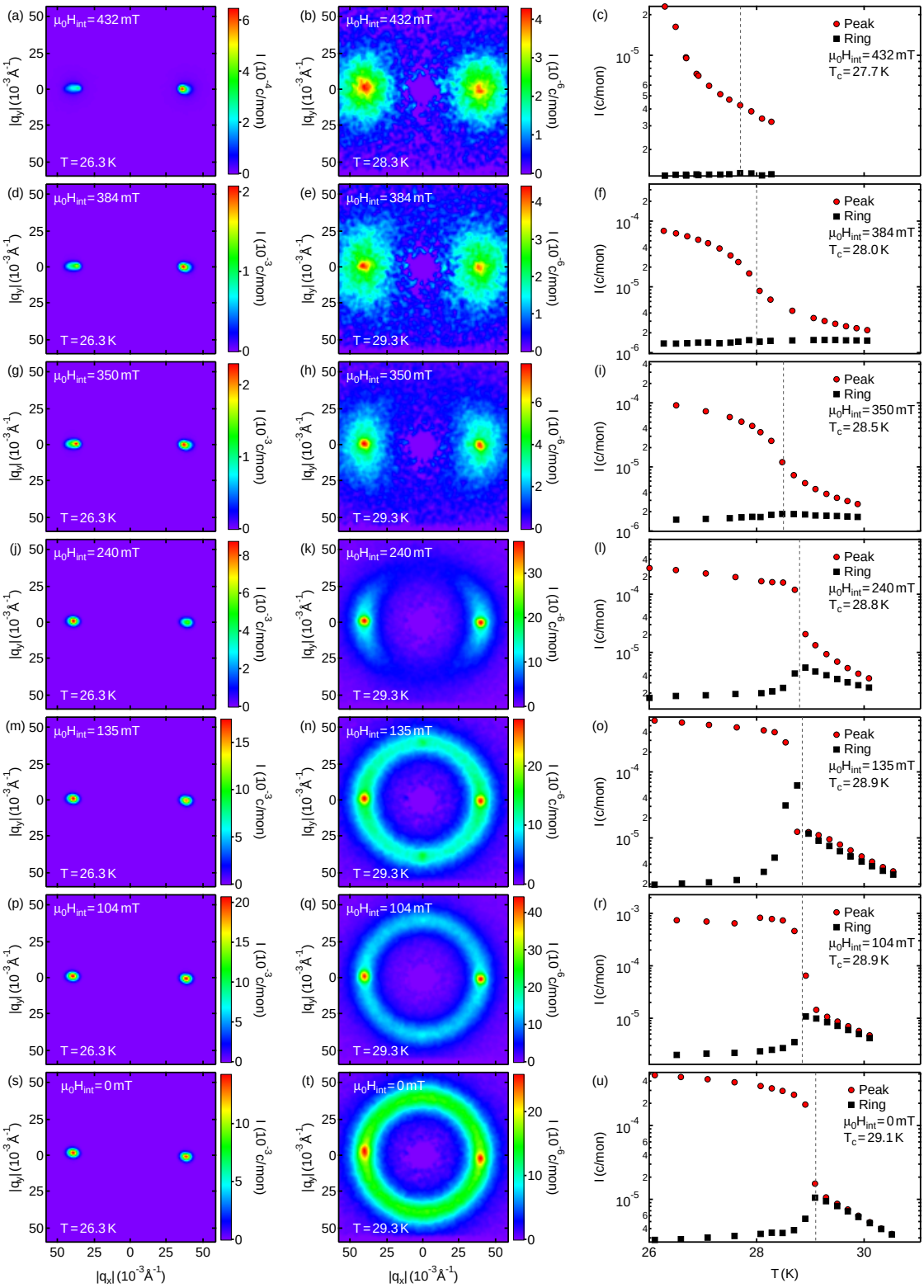

Figure 4.11.: Typical SANS patterns measured below (left column) and above (middle column) the helical transition temperature T_c. (right column) Temperature dependence of the intensity evaluated on the helical peak and a ring with $Q = k_{hel}$. From bottom to top the magnetic field is increased from zero to $B > B_{TCP}$.

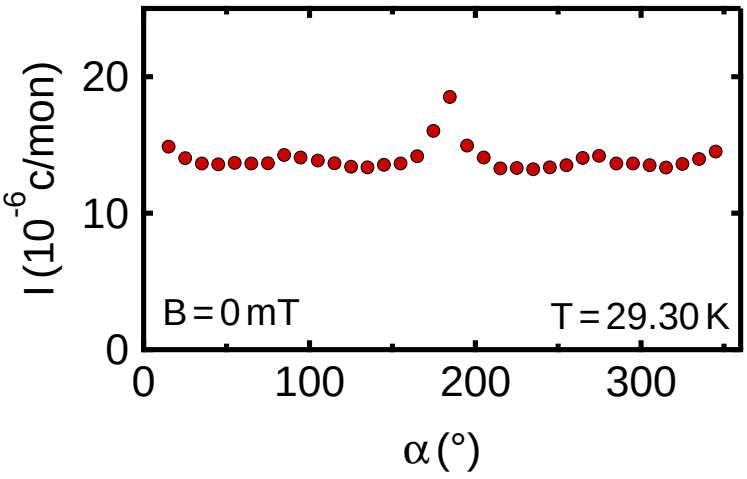

Figure 4.12.: Intensity as function of the azimuthal angle α evaluated on ring with a radius corresponding to the helical modulation vector $Q = 0.04\,\text{Å}^{-1}$. The data were measured at zero magnetic field and $T = 29.3\,\text{K}$ are taken from Fig. 4.11 (t). The peaks at $\alpha = 0°$ and 180° correspond to the higher intensity on the horizontal line in in Fig. 4.11 (t).

T_c the peak intensity increases very strongly within a very small temperature region $\Delta T \approx 0.15\,\text{K}$ while the ring intensity decreases to the background level. This behavior is present up to 135 mT, where the intensity on the ring also exhibits a sudden increase at T_c. This peak is due to the fact that this field corresponds to the skyrmion phase and two structural skyrmion peaks scatter into the selected *ring* region. At 240 mT the ring is not isotropically populated anymore and varies with the azimuthal angle α. The intensities on ring and the peak do not anymore increase with the same rate.

The transition temperature T_c is defined as the point where the derivative of the peak intensity versus temperature curve is minimized. With this definition T_c is at the same position as the sharp peak on top of the broad shoulder in the specific heat and the peak in the susceptibility. In the right column of Fig. 4.11 T_c is indicated by the dashed line. T_c shifts with increasing field slightly towards smaller temperature. The shift from zero field $T_c = 29.1\,\text{K}$ to the tricritical point by -0.5 K is in excellent agreement with Ref. [140]. Moreover, the sharp first-order feature in the intensity smears out when increasing the magnetic field.

Two dimensional fit to the SANS data

For a more quantitative analysis, the scattering patterns were fitted using the scattering cross section for chiral helimagnets given in Eq. (4.4). Eq. (4.4) is valid for chiral magnets above the transition temperature T_c, where the length of the chiral

modulation vector is given by k_{hel}. The cubic invariant results in an easy axis of the chiral fluctuations along the $\langle 111 \rangle$ crystalline directions for $\alpha_{cub} < 0$ or along the $\langle 100 \rangle$ directions for $\alpha_{cub} > 0$. $|\alpha_{cub}|$ characterizes the strength of the anisotropy. The correlation length of the magnetic fluctuations is given by κ. The scattering cross section Eq. (4.4) only holds for zero magnetic field but it can be extended to also describe the magnetic fluctuations in an external magnetic field. Therefore, the inverse correlation length κ has to be split in one that is parallel to the magnetic field $\kappa_{\parallel}$ and one which is perpendicular to the magnetic field $\kappa_{\perp}$. This extended formula evaluated by M. Garst is given in the appendix through Eqs. (B.1), (B.2) and (B.3). The extended scattering cross section also covers the dipolar interaction χ_{int}. By defining $\chi_{int} = 0$ and $\kappa = \kappa_{\parallel} = \kappa_{\perp}$ the zero field formula (4.4) is recovered.

To extract the correlation length at the transition as a function of field and temperature the complete two dimensional SANS patterns were fitted. In contrast, to the study of Janoschek *et al.* [14] where the intensity as function of q for certain crystalline directions was fitted.

The fit to the zero field data allows to directly comparing the fitting procedure and the actual data with the results of Janoschek *et al.* In Fig. 4.13 the results of the fit are shown. All fits give a normalized χ^2 of about 0.95. The red data result from a fit with freely varying α_{cub} and κ, while the amplitude A is fixed to the mean value of all temperatures. A fixation of α_{cub} to $\alpha_{cub} = 0.04\,\text{Å}^{-1}$ results in the green data. The length of the helical wave vector k_{hel}, shown in panel (a), increases with temperature by about 10 % from $0.036(5)\,\text{Å}^{-1}$ at T_{c} to 30.52 K, being slightly stronger than reported in Ref. [14]. For the cubic anisotropy α_{cub} (cf. Fig. 4.13 (b)) very weak temperature dependence, as expected within the Brazovskii theory, is observed. The mean value of $\alpha_{\mathrm{cub}} = -0.04(1)\,\text{Å}^{-1}$ is about twice the value reported by Janoschek *et al.*, which may be due to the better resolution of our measurement. Nevertheless, the influence of the temperature dependence onto the inverse correlation length is negligible as shown in Fig. 4.13 (c). Both, κ resulting from fits with free α_{cub} and fixed α_{cub} are in very good agreement with each other and more importantly with the calculated temperature dependence of κ from the Brazovskii theory (black solid line).

In a next step the field dependence of the correlation length is determined by fitting the extended scattering cross-section Eq. (B.1) to the data measured in applied magnetic field. For these fits the dipolar interaction was neglected ($\chi_{\mathrm{int}} = 0$) and the cubic anisotropy was fixed at $-0.041(1)\,\text{Å}^{-1}$. As discussed above, under applied magnetic field two inverse correlation lengths describe the critical scattering $\kappa_{\parallel}$ and $\kappa_{\perp}$. For the measurements discussed here the magnetic field was aligned along the [111] crystalline direction. As the measurements discussed here were performed with the magnetic field aligned along the [111] crystalline direction, both, α_{cub} and $\kappa_{\parallel}$ change the anisotropy of the scattering pattern in this direction. Hence, α_{cub} is fixed to the zero field value to sustain reasonable results for $\kappa_{\parallel}$.

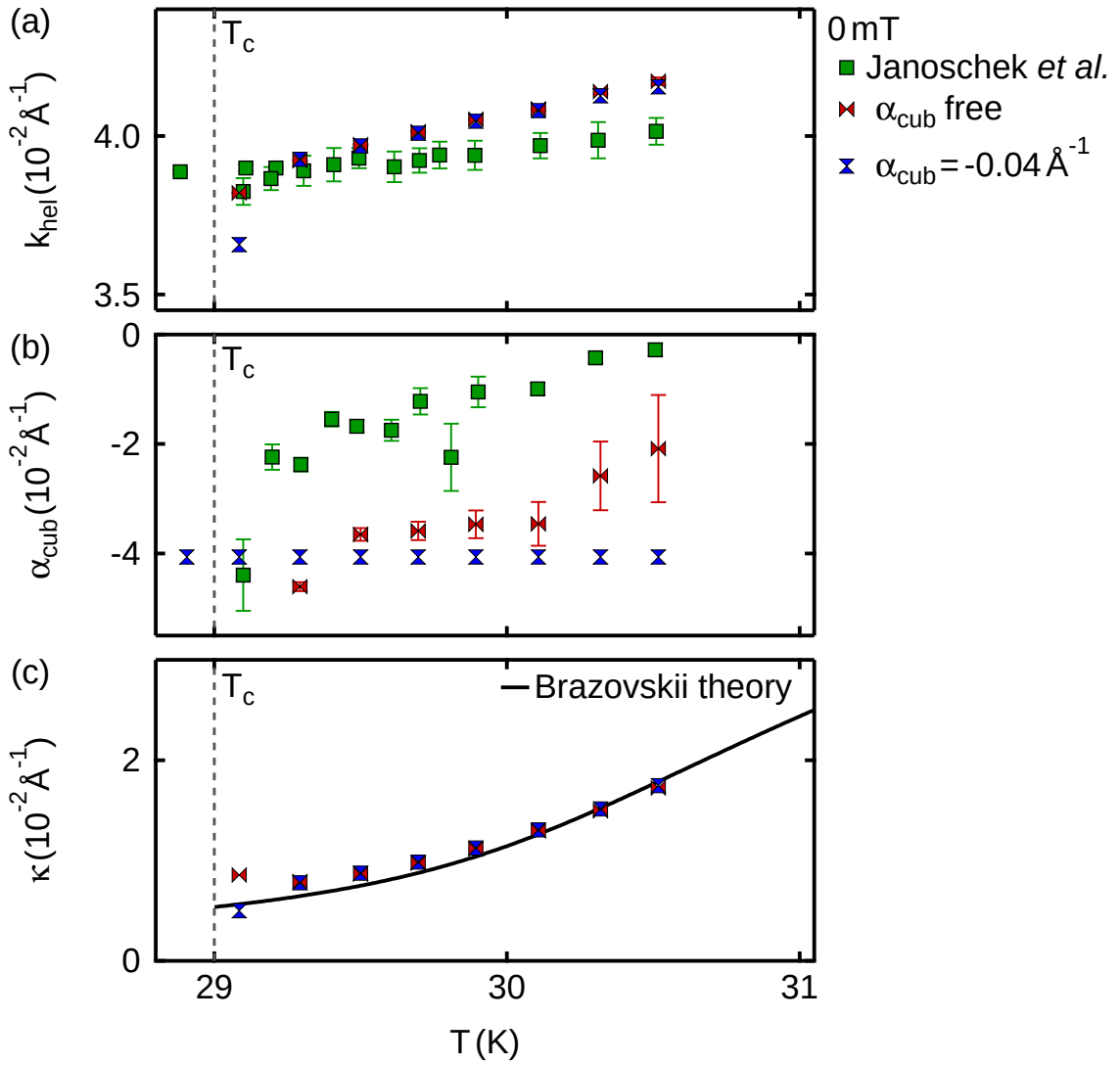

Figure 4.13.: Comparison of the fit results as obtained for the zero field data for a freely variable α_{cub} (red data), α_{cub} fixed to -0.04 Å^{-1} (blue data) and the results published by Janoschek *et al.* [14] (green squares). In (a) the helical pitch k_{hel}, (b) the cubic anisotropy α_{cub} and (c) the inverse correlation length κ is shown versus temperature.

The outcomes of the fits are shown in Fig. 4.14. In the left column the inverse correlation length parallel $\kappa_{\parallel}$ (green squares) and perpendicular $\kappa_{\perp}$ (red circles) to the magnetic field are shown for internal magnetic fields from 0 to 432 mT. On the right hand side the temperature dependence of the helical wave vector k_{hel} is shown. The zero field data (k) and (l) are the same as shown in Fig. 4.13, but on a different temperature scale. The blue dashed lines are the intensity on the peak position as function of temperature, in order to identify the transition temperature T_{c}. At $\mu_0 H_{\mathrm{Int}} = 104\,\mathrm{mT}$ the skyrmion phase is crossed in the temperature scan, resulting in a dip of the intensity below T_{c} (cf. gray shaded area in Fig. 4.14 (i) and (j)). The inverse correlation length $\kappa_{\parallel}$ and $\kappa_{\perp}$ increase with temperature up to $\mu_0 H_{\mathrm{Int}} = 350\,\mathrm{mT}$, where the slope of $\kappa_{\parallel}$ and $\kappa_{\perp}$ becomes opposite to each other. From $\mu_0 H_{\mathrm{Int}} = 350\,\mathrm{mT}$ on $\kappa_{\parallel}$ decreases with temperature (cf. Fig. 4.14 (c) and (a)). The difference between $\kappa_{\parallel}$ and $\kappa_{\perp}$ increases with increasing magnetic field, while at 104 mT (cf. Fig. 4.14 (k)) both inverse correlation lengths are still quite similar. In zero field κ and in finite field $\kappa_{\perp}$ do not become zero at T_{c}. Above $\mu_0 H_{\mathrm{int}}^{\mathrm{TCP}}$ $\kappa_{\perp}$ seems to decrease continuously to zero.

The helical pitch k_{hel} shown on the right hand side in Fig. 4.14 increases with temperature. The zero field data are in good agreement with those published in Ref. [14] as shown in Fig. 4.13 (c). The field dependence is marginal. There is a very small overall reduction of k_{hel} with increasing field.

Inverse Correlation length calculated from Brazovskii theory

As described in the Appendix B.2 $\kappa_{\parallel}$ and $\kappa_{\perp}$ can be determined in the Brazovskii theory introduced in Sec. 4.1.3. The temperature and magnetic field dependence can be calculated by solving the implicit equations (B.13) and (B.15). The field dependence is introduced by the magnetization of the sample. Fig. 4.15 shows the magnetization of MnSi with the field aligned along the [111] crystalline axis. The field is given as internal field $\mu_0 H_{\mathrm{int}}$. In the theory described in App. B.2 the magnetization is given by ϕ_0 in units of μ_{B}/f.u..

In the left column of Fig. 4.14 the calculated inverse correlation lengths are shown as solid lines. The oscillations are numerical artifacts from solving the system of equations. In the calculation the dimensionless fit parameter $\tilde{u}$ is introduced. $\tilde{u}$ represents a energy density and is given in units of $(1/Jk_{\mathrm{hel}})$. The parameter is expected to be temperature and field independent. Up to 240 mT calculated and measured inverse correlation lengths are in quite good agreement, with $\tilde{u} = 5964$. From 350 mT on the calculations do not resemble the measurements. The trend can be recovered by changing the fit parameter to $\tilde{u} = 13419$.

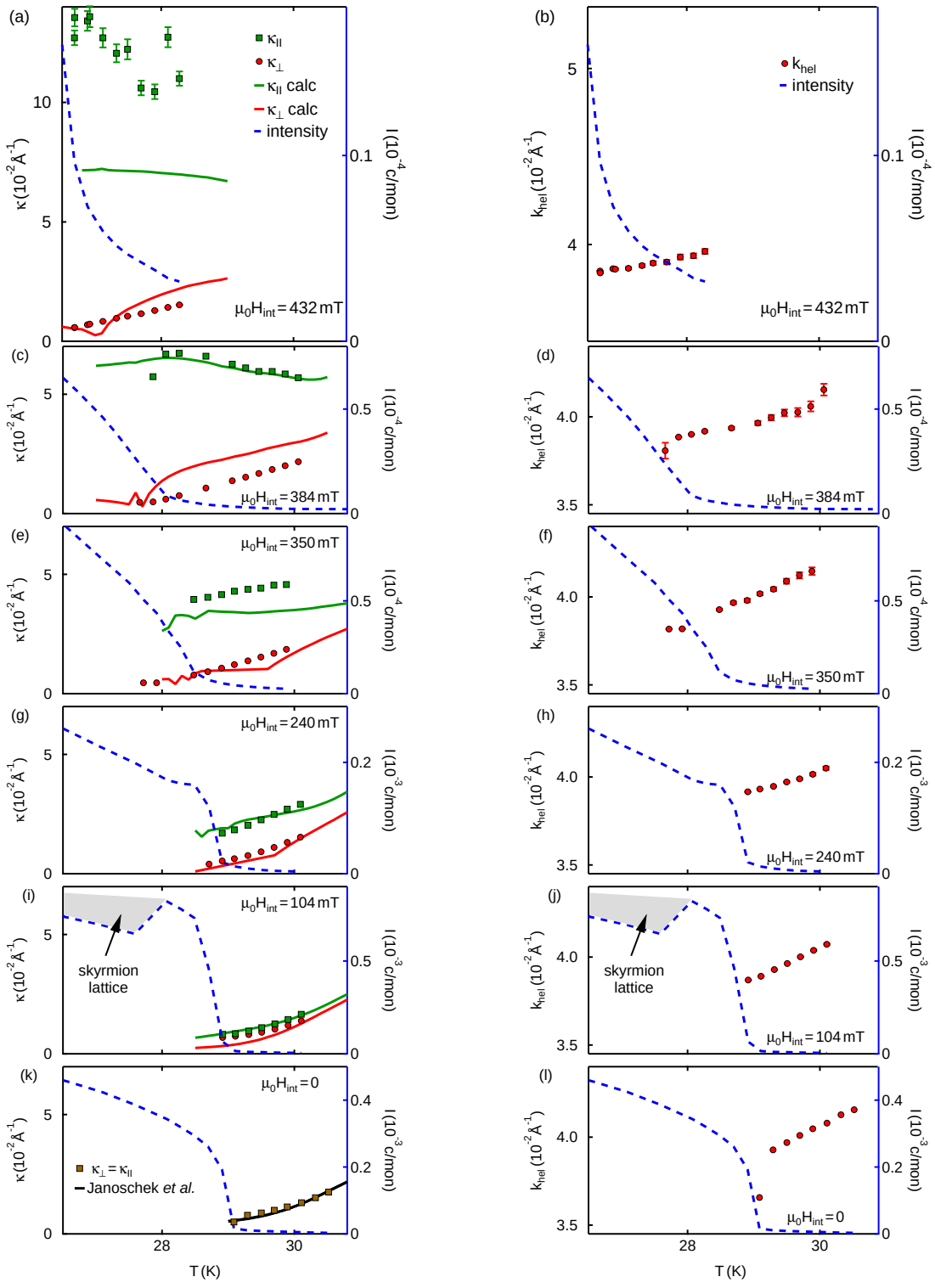

Figure 4.14.: Temperature dependence of the perpendicular $\kappa_\perp$, parallel $\kappa_\parallel$ inverse correlation length (left column), and the helical pitch $k_{\rm hel}$ (right column) for various magnetic field in MnSi. The data points are inferred from fits to the scattering patterns with the anisotropy parameter fixed to $\alpha_{\rm cub} = -0.04(1)$ Å^{-1}. The solid lines are calculated within the Brazovskii theory and the blue dashed line is the intensity on the peak position.

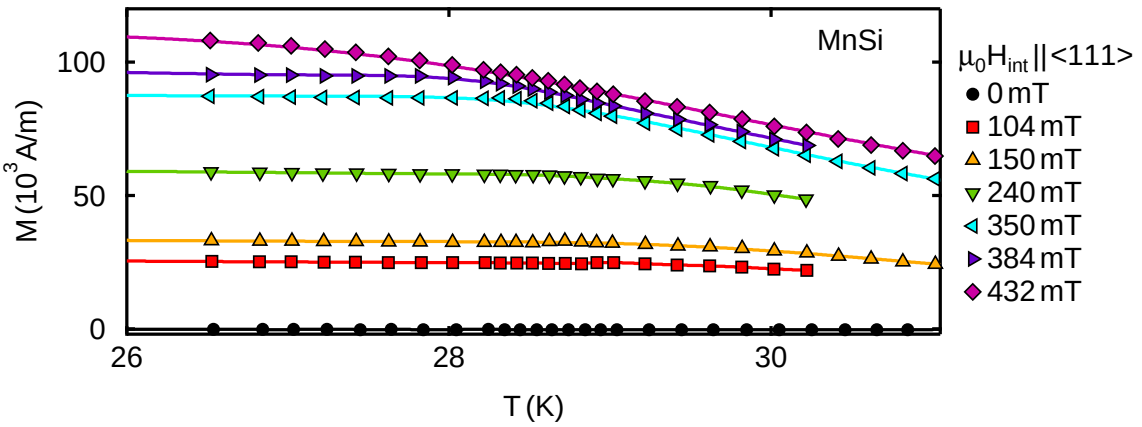

Figure 4.15.: Magnetization of MnSi as function of temperature for various magnetic fields, measured by A. Bauer in a Physical Property Measurement System (PPMS) from Quantum Design. The data are recorded with the field aligned along the [111] axis of the crystal. Solid lines are guides to the eye.

4.3.2. Quasielastic linewidth of the magnetic fluctuations

In the following sections the quasielastic measurements of the fluctuations at the paramagnetic transition as function of temperature and magnetic field are discussed.

Experimental setup and sample

The temperature dependence of the quasi elastic linewidth was determined by means of MIEZE measurements at the instrument RESEDA (MLZ) using the transverse NRSE option with μ-metal shielding, covering a dynamic range of 0.4 ns to 3.5 ns. As spin analyzer a 5V cavity before the sample was mounted. The beam collimation was defined by a $30 \times 30\,\mathrm{mm}^2$ slit at the beginning of the spectrometer and a $10 \times 10\,\mathrm{mm}^2$ slit in front of the sample. Magnetic fields up to 400 mT were applied using the normal conducting magnet "Garfield" designed by T. Reimann. The magnetic field was aligned perpendicular (vertical) to the neutron beam resembling the *transverse* field geometry as described in Sec. 4.1.6. In this geometry the conical peaks occur on the vertical axis above and below the direct beam on the detector. To reach temperatures down to 3.5 K a standard closed cycle cryostat was employed. The cylindrical shaped (diameter 10 mm, height 30 mm) MnSi single crystal (OFZ 128-3) with a crystalline $\langle 111 \rangle$ direction parallel to the cylinder axis was mounted to a sample stick, that allowed for rotations about the vertical cylinder axis. To allow a direct comparison between the SANS study presented in Sec. 4.3.1 and the results discussed here all magnetic fields are given as internal fields. Considering the sample shape and the measured susceptibility as described in Ref. [163] the internal field applied to the

sample is given by $H_{\rm int} = 0.96 \cdot H_{\rm ext}$.

The instrumental resolution and especially the effect of path length differences that may occur in the sample was corrected with a resolution measurement on the helical, respectively, conical peaks at 4 K while background was measured at 40 K. Fig. B.1 shows the resulting absolute value of the normalized intermediate scattering functions for all studied temperatures and magnetic fields. For this discussion the data were fitted with a single exponential decay of the form

$$\frac{S(q,\tau)}{S(q,0)} = A \cdot \exp\left[-\frac{\Gamma\tau}{\hbar}\right] + (1 - A), \tag{4.12}$$

with $A = 1$. This approach assumes one exponential decay process. As can be seen in Fig. B.1 this simple model does not perfectly fit the data. A more complex analysis will be discussed elsewhere.

Experimental results

Fig. 4.16 summarizes the results of the MIEZE measurements. The quasielastic linewidth is shown as function of temperature for five different magnetic fields in the range $0 \leq \mu_0 H_{\rm int} \leq 384\,{\rm mT}$, measured on the helical/conical peaks $q = k_{\rm hel}$. All MIEZE measurements were performed after zero field cooling to 10 K and then heating of the sample in applied magnetic field. For each field the integrated intensity is shown (blue open squares). At 104 mT the sample passes the skyrmion phase near $T = 28.5\,{\rm K}$, leading to a kink. This kink reflects a transfer of spectral weight from the conical to the Skyrmion peaks.

$T_{\rm c}$ is identified in the same way as for the SANS measurements discussed in Sec. 4.3.1, by the derivative of the intensity versus temperature curve. As for the SANS data $T_{\rm c}$ shifts by -0.5 K from zero field $T_{\rm c} = 28.9\,{\rm K}$ to the tricritical point $T_{\rm c} = 28.3\,{\rm K}$. The offset off 0.2 K between $T_{\rm c}$ measured with SANS-1 and with RESEDA is small and may arise from a different temperature gradient between sample and thermometer. At SANS-1 a different cryostat with a longer sample tube was used to fit into the magnet.

$T_{\rm c}$ is not only reflected in the temperature dependence of the intensity but also in the temperature dependence of the linewidth Γ. At $T_{\rm c}$ Γ increases, showing a finite lifetime of the chiral fluctuations. The increase of Γ shifts to smaller temperatures with increasing field, as observed for $T_{\rm c}$ in the intensity. In zero field and up to 240 mT, a step in Γ is present that vanishes to a monotonic increase above $\mu_0 H_{\rm int}^{\rm TCP} = 340\,{\rm mT}$. At $\mu_0 H_{\rm int}^{\rm TCP} = 384\,{\rm mT}$ the increase of Γ seems to already start below $T_{\rm c}$.

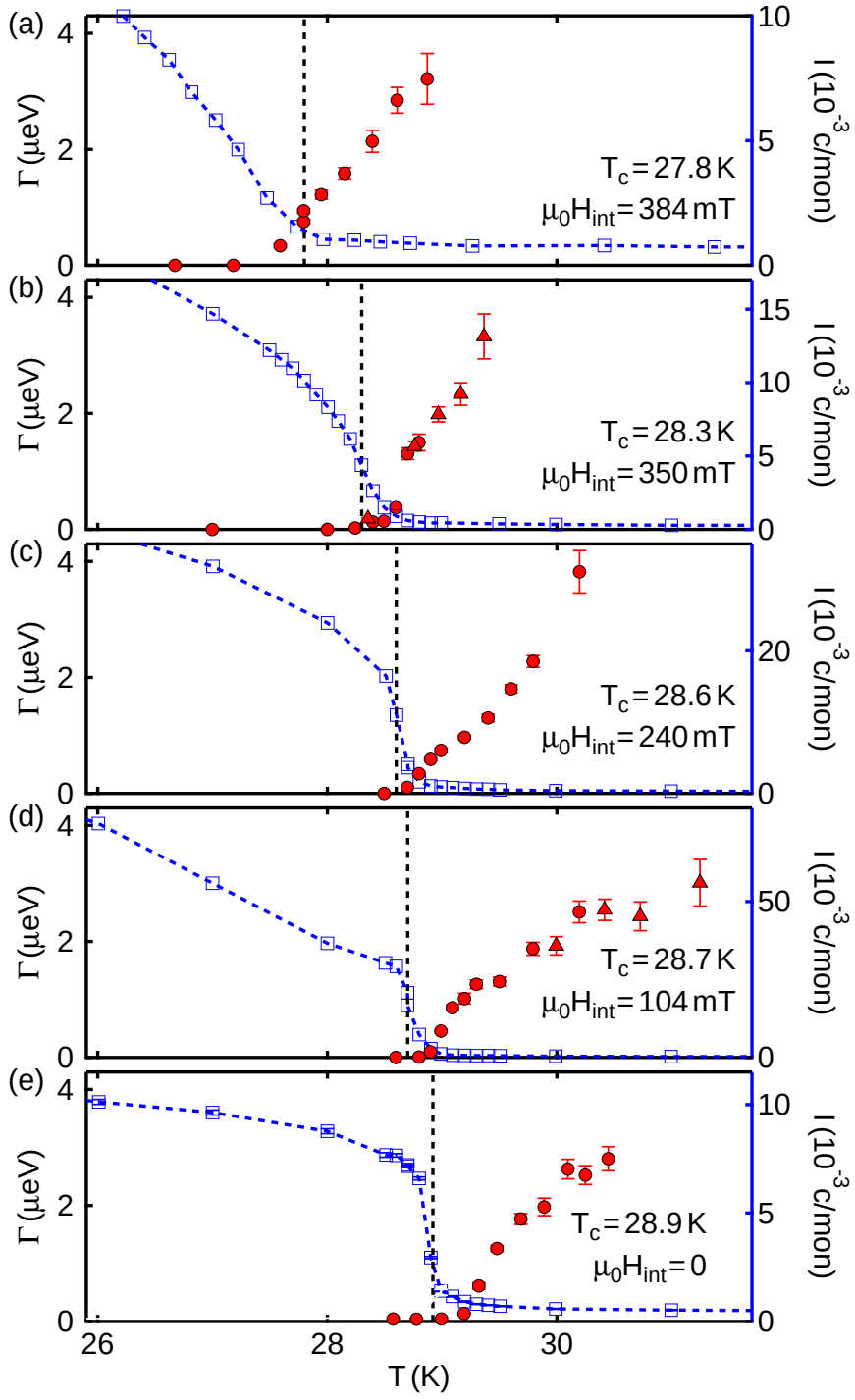

Figure 4.16.: Quasielastic linewidth (red data) of the chiral fluctuations measured as function of temperature for various vertical magnetic fields in the range $0 \leq \mu_0 H_{\mathrm{int}} \leq 384\,\mathrm{mT}$. The blue dashed line displays the intensity, evaluated at the same q position and the black dashed line indicates T_{c}. The linewidth Γ results from a fit assuming a single exponential decay.

4.3.3. Discussion

Our combined SANS and MIEZE study shows the evolution of the paramagnetic to helimagnetic transition in MnSi from a first-order in zero field to a second-order transition for $H_{\mathrm{int}} \geq H_{\mathrm{int}}^{\mathrm{TCP}}$ in agreement with previously performed specific heat measurements [140]. The temperature and field dependence of both the relevant correlation length $\kappa_{\perp}$, $\kappa_{\parallel}$ and the quasi elastic linewidth Γ are in very good agreement with the Brazovskii scenario of a fluctuation-induced first-order transition that breaks down at the tricritical point, as expected.

The scattering patterns above T_{c} vividly show the symmetry change of the fluctuation spectrum from isotropic chiral fluctuations on a sphere, to circular segments, to isotropic fluctuations around the conical peak positions at $\boldsymbol{q} = \pm\boldsymbol{k}_{\mathrm{hel}}$. In zero field the fluctuations accumulate on a two dimensional surface in reciprocal space while for $H \geq H_{\mathrm{int}}^{\mathrm{TCP}}$ only two points in reciprocal space are populated. The steep drop in the intensity at T_{c} evolves to a monotone decrease for $H_{\mathrm{int}} \geq H_{\mathrm{int}}^{\mathrm{TCP}}$ and the transition temperatures slightly decreases with increasing field from $T_{\mathrm{c}} = 29.00(5)\,\mathrm{K}$ in zero field to $28.50(5)\,\mathrm{K}$ at $350\,\mathrm{mT}$.

The zero field data show that the analysis by fitting the full scattering pattern gives reliable results and the direct comparison to the previously published data by Janoschek *et al.* [14] shows a remarkably good agreement, although both studies were performed at different instruments and with different samples. The stronger cubic anisotropy α_{cub} observed in this study may be explained by the significantly higher q resolution of the measurements at SANS-1. Nevertheless, the exact temperature dependence of α_{cub} has only a very small influence on the temperature dependence of the inverse correlation length κ. This small influence justifies fixing $\alpha_{\mathrm{cub}} = 0.041(1)\,\mathrm{\AA}^{-1}$ for the fits of the data measured under applied magnetic field.

Comparing the field and temperature dependence of the measured inverse correlation length with the inverse correlation length calculated within the Brazovskii scenario gives a very good agreement for magnetic fields below $H_{\mathrm{int}}^{\mathrm{TCP}}$. At the tricritical point the simple model with only a single fit parameter, i.e $\tilde{u}$, does not hold anymore. The Brazovskii theory presented in Sec. B.2 only considers the most important renormalization effects. Close to the tricritical point and in the region of the second-order transition higher order corrections to the free energy have to be considered to describe $\kappa_{\perp}$ and $\kappa_{\parallel}$.

The temperature dependence of the quasielastic linewidth Γ confirms the reduction of T_{c} as observed from the intensity. The first-order like step in Γ vanishes with increasing field. For magnetic fields larger then $\mu_0 H_{\mathrm{int}}^{\mathrm{TCP}}$ the linewidth Γ increases monotonically, as expected for a second-order transition.

The tricritical point in MnSi, originally identified by specific heat measurements [140], is explicitly observed with neutron scattering. At the tricritical point the symmetry of the chiral fluctuations change, resulting in a reduction of the available phase space. Hence, the strong interactions between the fluctuations are suppressed and the fluctuation-induced first-order transition changes to a second-order transition. The application of the Brazovskii theory allows to predict the temperature and field dependence of the inverse correlation length $\kappa_\perp$ and $\kappa_\parallel$ when approaching the tricritical point. This study provides another proof for the validity of the Brazovskii scenario in MnSi.

4.4. Suppression of magnetic order in $Mn_{1-x}Fe_xSi$ and $Mn_{1-x}Co_xSi$

The magnetism in MnSi may be suppressed by substitutional doping of iron or cobalt atoms on the manganese sites, as discussed in Sec. 4.1.5. In this section, a comprehensive study of single crystals of $Mn_{1-x}Fe_xSi$ and $Mn_{1-x}Co_xSi$ by SANS and transversal NRSE measurements is reported.

The following discussion consists of two parts. First, SANS measurements characterizing the magnetic ground state in zero magnetic field are reported. Second, the focus is on the temperature dependence of the scattering intensity and the temperature dependence of the lifetime of the magnetic fluctuations at the transition into the helical phase in zero field.

4.4.1. Investigation of the magnetic ground state

Experimental setup and samples

In a first step the magnetic ground state of all samples was studied by means of SANS measurements. The experiments were carried out at the instruments RESEDA at the Heinz Maier-Leibnitz Zentrum (MLZ) in Garching, Germany and at SANS-II at PSI, Villigen, Switzerland. T. Adams performed a preliminary study focusing on the Skyrmion phase at the beamline MIRA (MLZ) [164]. The measurements at SANS-II were performed together with S. Ernst in the framework of his Bachelor thesis [165]. At MLZ a standard pulse tube cooler was utilized reaching temperatures down to 3.5 K. For temperatures down to 0.5 K a He-3 and down to 50 mK a dilution-insert was used, respectively. The measurements at SANS-II were carried out with a 11 T cryomagnet with dilution insert reaching temperatures down to 50 mK. All key parameters of the experiments at the different beamlines are summarized in Tab. 4.4.1.

We studied single crystals of pure MnSi, $Mn_{1-x}Co_xSi$ ($x = 0.02$ and $x = 0.04$) and $Mn_{1-x}Fe_xSi$ ($x = 0.02, 0.04, 0.06, 0.08, 0.10, 0.12$ and 0.16). A characterization by means of magnetization, ac susceptibility and specific heat measurements of most of these samples is reported in Ref. [159]. Two single crystals, $Mn_{1-x}Fe_xSi$ $x = 0.06$ and $x = 0.10$, were additionally grown as described in Ref. [159]. All samples under study possess a cylindrical shape and were oriented by x-ray Laue diffraction, such that a crystalline $\langle 110 \rangle$ direction was aligned perpendicular to the scattering plane. The rotation about this vertical axis defines the rocking angle ω (see Fig. 4.8).

Magnetic ground state

The influence of iron doping on the scattering pattern in zero magnetic field is shown in Fig. 4.17. For $x \leq 0.08$ data is recorded at a temperature of ≈ 3.5 K, $x = 0.10$

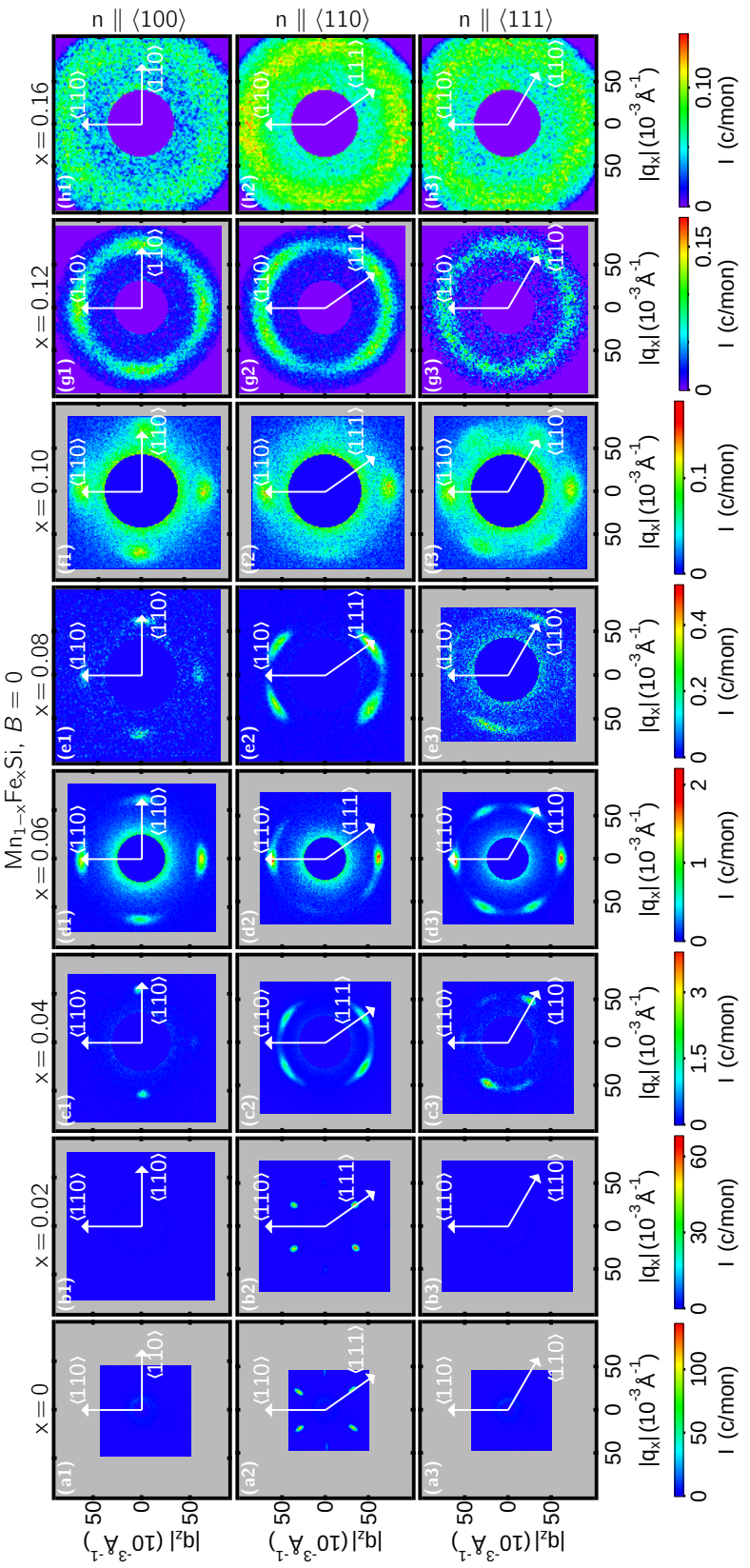

Figure 4.17.: Scattering pattern of $Mn_{1-x}Fe_xSi$ for various iron concentrations and crystal orientations ($\langle 100\rangle$ in (a1)-(h1), $\langle 110\rangle$ in (a2)-(h2) and $\langle 111\rangle$ in (a3)-(h3) $\langle 100\rangle$) measured in zero magnetic field at temperatures $T \approx 3.5\,\mathrm{K}$ ($0 \leq x \leq 0.08$), $0.5\,\mathrm{K}$ ($x = 0.10$) and $0.05\,\mathrm{K}$ ($0.12 \leq x \leq 0.16$).

Figure 4.18.: Azimuthal intensity distribution of $Mn_{1-x}Fe_xSi$ for various iron concentrations and crystal orientations measured in zero magnetic field evaluated from the scattering pattern shown in Fig. 4.17. The intensities are normalized to the Bragg peak intensity I_P.

Table 4.1.: Instrumental parameters at the different beamlines used for this study. (1) @ MLZ, (2) @ PSI, (3) normal conducting magnet in Helmholtz geometry, (4) superconducting cryomagnet MA11.

instrument	λ (Å)	$\Delta\lambda/\lambda$	detector	$B_{\max}$ (T)	$T_{\min}$ (K)	samples
RESEDA$^{(1)}$	5.42	0.10	CASCADE	$0.4^{(3)}$	0.05	$x_{\mathrm{Fe}} = 0,\ 0.02,\ 0.04,$ 0.06, 0.08, 0.10, 0.12; $x_{\mathrm{Co}} = 0.02,\ 0.04$
SANS-II$^{(2)}$	4.76	0.10	He-3 PSD	$11^{(4)}$	0.05	$x_{\mathrm{Fe}} = 0.12,\ 0.16$

was measured at 0.5 K and $0.12 \leq x \leq 0.16$ at 0.05 K. The iron concentration increases from left to right. In the top row (a1) - (h1), the samples are oriented with $n \parallel \langle 100 \rangle$, in central row (a2) - (h2) with $n \parallel \langle 110 \rangle$ and in the bottom row (a3) - (h3) all samples are aligned with $n \parallel \langle 111 \rangle$. Fig. 4.18 shows the corresponding azimuthal intensity distributions, evaluated on a ring with radius $q = k_{\mathrm{hel}}$ and width Δq. The radial width Δq was selected according to the radial width of the peak or ring. All intensities are plotted as function of the azimuthal angle α. α is measured clockwise from the vertical $\langle 110 \rangle$ axis as depicted on the detector in Fig. 4.8. The intensities are normalized to the peak intensity I_P of each sample.

In the first column of Fig. 4.17, panels (a1) to (a3), the results for pure MnSi are shown. MnSi shows a well-defined scattering pattern with helical Bragg spots along the $\langle 111 \rangle$ directions. The rocking width of the helical Bragg spots is very narrow $\Delta\omega = 1.3(8)^\circ$. Nevertheless, panel (a2) shows four helical peaks being only observable as all panels in Fig. 4.17 show the sum of a rocking scan of $\omega \pm 3^\circ$. At $q_z = 0$ along q_x weak spots occur due to double scattering. The azimuthal width $\Delta\alpha$, the radial width Δq and the rocking width $\Delta\omega$ of the helical peaks are limited by the instrumental resolution, the sample size and the slit in front of the sample. Increasing the iron content broadens the helical Bragg spots in azimuthal and radial q direction. Up to an iron concentration of $x = 0.12$ clear helical peaks are visible. The sample with $x = 0.16$ shows a ring with broad peaks of a slightly higher intensity. All samples clearly show a helical structure resulting from the interplay of exchange and Dzyaloshinskii-Moriya interaction. The strongest effect of the substitutional doping on the magnetic ground state, visible in the low temperature scattering patterns, is a change of the strength of the cubic anisotropy. The broadening of the peaks is primarily visible in an increase of the azimuthal width $\Delta\alpha$, while the radial width Δq stays relatively constant up to $x = 0.08$. This can also be seen from the azimuthal intensity distributions in Fig. 4.18. At $x = 0.12$ iron doping peaks are still visible. In addition to these peaks a ring of scattering intensity emerges. This diffuse scattering is obviously concentrated on a ring or sphere with $q = k_{\mathrm{hel}}$, however, it is not isotropically distributed, suggesting that the ring of diffuse scattering originates either from

unpinned helices or isotropic chiral fluctuations, similar to those observed in pure MnSi above T_c for $H = 0$. Nevertheless, the energy integrated SANS measurements presented here do not allow to distinguish between static randomly aligned helices or isotropic chiral fluctuations.

The scattering patterns for cobalt doped samples are shown in Fig. 4.19, for the neutron beam parallel to ⟨100⟩ (top row) and ⟨110⟩ (bottom row). Increasing doping leads to the same behavior as discussed above for iron, however for half the concentrations ($x_{Co} = 2x_{Fe}$). The azimuthal width strongly increases while the radial width stays relatively constant.

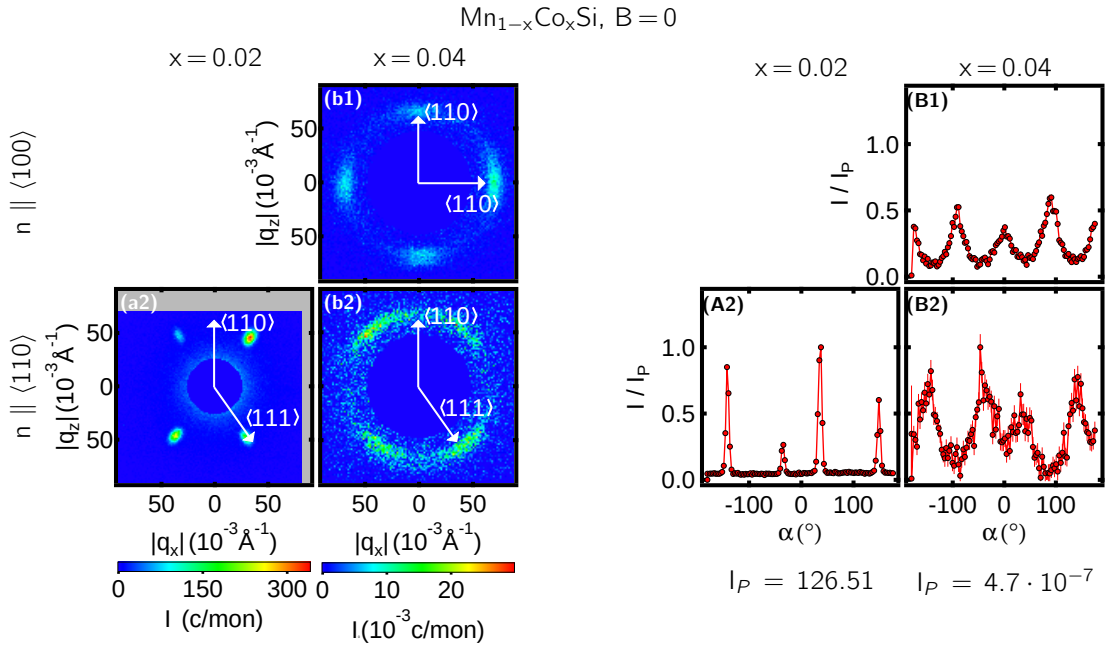

Figure 4.19.: SANS patterns and azimuthal intensity distribution of the magnetic ground state of $Mn_{1-x}Co_xSi$ for $x = 0.02$ and $x = 0.04$. The figures show data measured with the neutron beam along [100] and [110] in zero magnetic field.

Magnetic anisotropy

In the previous section the strength of the magnetic anisotropy was discussed, here we focus on the direction of the anisotropy. The Ginzburg Landau ansatz as presented in Sec. 4.1.1 and especially with the contribution to the free energy presented in Eq. (4.2) only allows for alignments of the helices along the ⟨111⟩ or ⟨100⟩ directions. The ⟨110⟩ direction results in a saddle point of the free energy, hence, is not stable.

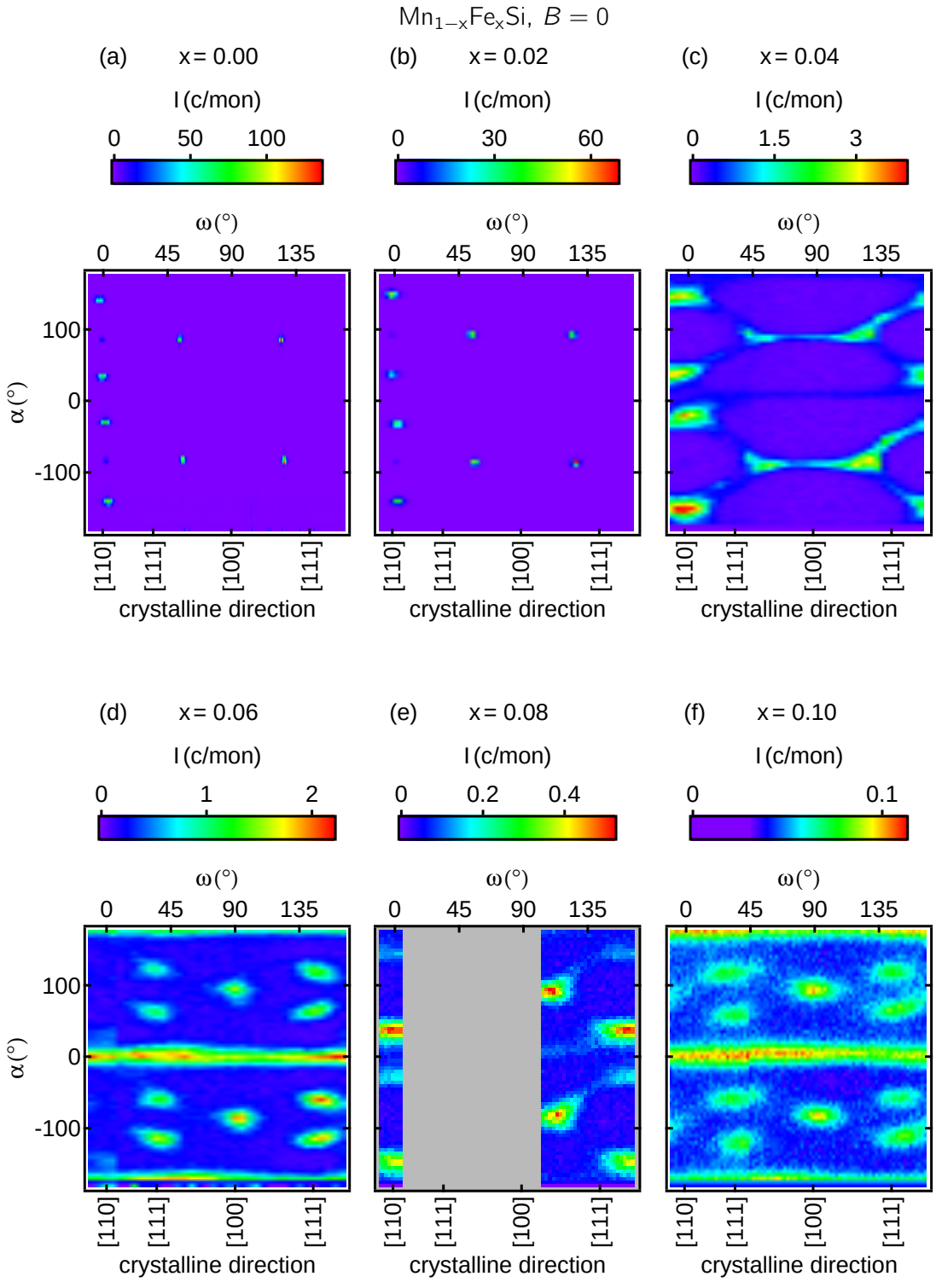

Figure 4.20.: Rocking map as function of azimuthal angle α and rocking angle ω of $Mn_{1-x}Fe_xSi$ for different iron concentrations. While (a)-(c) and (e) show a helical order which is aligned along the $\langle 111 \rangle$ direction, in (d) and (f) the pinning of the helical order is clearly along $\langle 110 \rangle$.

In case of pure MnSi the easy axis is the ⟨111⟩ direction, as also discussed above and visible in the rocking map shown in Fig. 4.20 (a). Fig. 4.20 shows a mapping of the intensity from the sphere with radius $|\boldsymbol{k}_{\mathrm{hel}}|$ onto a plane as function of the rocking angle ω and azimuthal angle α for different iron concentrations. $\omega = 0$ corresponds to an alignment of the neutron beam along the crystalline [110] direction and α is measured clockwise with respect to the vertical [110] direction. In MnSi (a), a clear ⟨111⟩ anisotropy is visible as only peaks along this direction appear. The same holds for $x = 0.02$ (b). At $x = 0.04$ (c) the first hint for a change of the anisotropy direction becomes visible as weak intensity along the ⟨110⟩ direction in Fig. 4.17 (c1), (c3) and Fig. 4.20 (c) appears. A ⟨110⟩ anisotropy forms at an iron concentration of $x = 0.06$ with distinct peaks along the ⟨110⟩-crystal axis. The ⟨110⟩ anisotropy changes back to an ⟨111⟩ anisotropy at $x = 0.08$, with remnants of ⟨110⟩ intensity (e3). At $x = 0.10$ the anisotropy direction is again ⟨110⟩. For higher iron concentrations (i.e. $x = 0.12$ and $x = 0.16$) the determination of the anisotropy direction becomes difficult as the diffuse ring becomes stronger than the helical peaks. Nevertheless, fitting the scattering patterns with the scattering cross section Eq. (4.4) as done in Sec. 4.3.1, allows to determine the sign of α_{cub} and therefore to decide whether the anisotropy is along ⟨100⟩ ($\alpha_{\mathrm{cub}} > 0$) or along ⟨111⟩ ($\alpha_{\mathrm{cub}} < 0$). These two samples have been studied together with S. Ernst at SANS-II (PSI) and are discussed in more detail in his Bachelor thesis Ref. [165]. The fits reveal that the $Mn_{1-x}Fe_xSi$ sample with $x = 0.12$ has a ⟨111⟩ anisotropy while the sample with $x = 0.16$ observes a very weak ⟨100⟩ anisotropy.

As discussed above both $Mn_{1-x}Co_xSi$ samples under study show unambiguously a anisotropy in ⟨111⟩ direction.

Helical pitch

The pitch of the helical modulation vector k_{hel} increases with increasing iron and cobalt concentration as can be seen in Fig. 4.21 where the scattering intensity is plotted as function of radial $\boldsymbol{q}$, evaluated in a sector covering the helical peak. Panel (a) shows the results for iron and (b) for cobalt doping. The peak position shifts from $0.036\,\text{Å}^{-1}$ for pure MnSi to $0.088\,\text{Å}^{-1}$ at $x = 0.16$ iron doping. The increase of k_{hel} corresponds to a reduction of the helix length by more than a factor of two, from 173 Å to 71 Å. Cobalt doping has twice the effect as iron doping because twice as many electrons are added to the crystal per unit cell, as discussed in the introduction. This can be explicitly seen in Fig. 4.22, where both the helical wave vector k_{hel} and the length of the helical modulation λ_{hel} is plotted versus iron and cobalt doping. The iron axis is scaled by a factor of two compared to the cobalt axis. Both, the data for $Mn_{1-x}Fe_xSi$ (red circles) and the data for $Mn_{1-x}Co_xSi$ (green squares) are in very good agreement when considering that cobalt doping increases the electron concentration twice as much as iron doping.

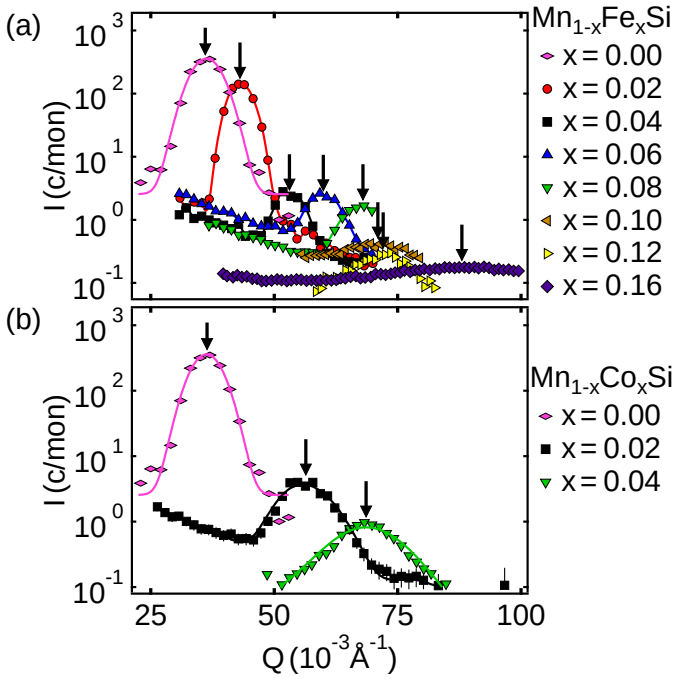

Figure 4.21.: Panels (a) and (b) show the radial q-dependence of the neutron scattering intensity for $Mn_{1-x}Fe_xSi$ and $Mn_{1-x}Co_xSi$ in the helical order, respectively. The pitch of the helical order increases with increasing iron and cobalt concentration.

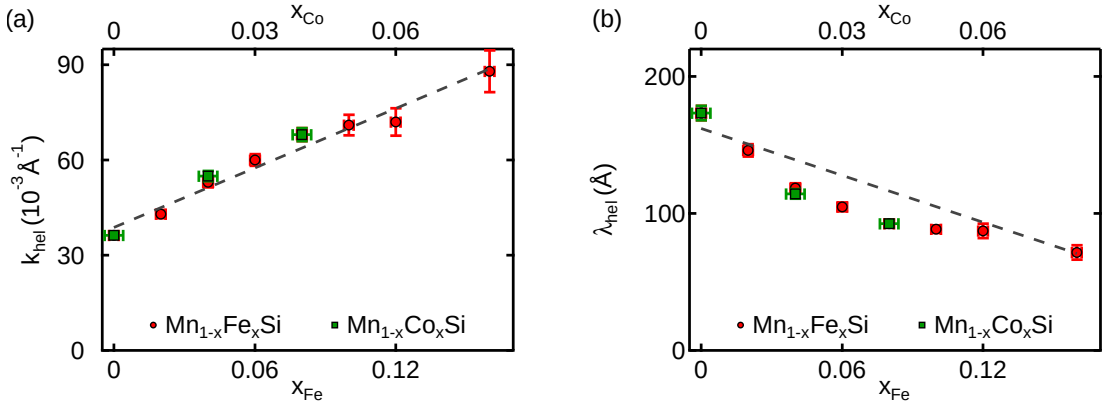

Figure 4.22.: Iron and cobalt dependence of the helical modulation vector k_{hel} (a) and length of the helix $\lambda_t extrmhel$ in $Mn_{1-x}Fe_xSi$ and $Mn_{1-x}Co_xSi$. The dashed lines are guides to the eye.

4.4.2. Stability of magnetic order

Experimental setup and sample

All quasi-elastic measurements were performed at RESEDA (MLZ) using the standard transverse NRSE setup with double μ-metal shielded spectrometer arms covering a dynamic range from 0.2 ns to 2 ns. The sample environment was the same as described in Sec. 4.4.1. In contrast to the SANS measurements a single 3-He counter was used as detector. The collimation in the primary spectrometer arm was the same but at the beginning of the secondary arm slits were added to reduce the background signal. The measurements presented here are performed on the helical Bragg spot. All samples were oriented with a helical satellite peak in the scattering plane.

Experimental results

The temperature dependence of the energy integrated intensity from the magnetic satellites of all $Mn_{1-x}Fe_xSi$ samples under study is shown on the left hand side of Fig. 4.23. To allow a comparison between the different samples the intensities are normalized to the intensity of pure MnSi by considering the magnetic moment at base temperature taken from Ref. [159]. As discussed in Sec. 4.3.1, T_c is determined as the minimum of the derivative of the temperature dependence of the scattering intensity. The black dashed line indicates T_c. Below T_c a kink occurs, indicated by the black arrow in Fig. 4.23, that becomes more pronounced with increasing iron concentration and may origin in a reorientations of helical domains. For pure MnSi, shown in panel (a), the intensity at 3.5 K is about ten times larger than at the kink. In contrast, the sample with $x = 0.10$ (k) does not show any temperature dependence of the intensity for temperatures below the kink. For the sample with the highest iron concentration under study $x = 0.12$ shown in panel (m) a definition of T_c is very difficult, as there is no sharp feature in the temperature dependence of the scattering intensity. The derivative identifies T_c at $T_c = (5 \pm 1)$ K.

The results of the quasi elastic NRSE measurements are summarized on the right hand side of Fig 4.23. All data were measured while heating the sample in zero magnetic field. A comparison between a graphite measurement and a low temperature measurements on the $Mn_{1-x}Fe_xSi$ and $Mn_{1-x}Co_xSi$ samples revealed that they are identical for $0 \leq x \leq 0.10$. However, the intensity of the low temperature measurements on the $Mn_{1-x}Fe_xSi$ and $Mn_{1-x}Co_xSi$ is larger than the intensity from resolution sample, hence the former were selected as resolution. For $Mn_{1-x}Fe_xSi$ $x = 0.12$ a deviation to the graphite measurement was observed down to the lowest available temperature 50 mK, beeing the first hint for the absence of static order in this sample. To consider the resolution we selected the low temperature measurement from the sample with $x = 0.10$. In Fig. B.2 and B.3 shown the appendix all normalized intermediate scattering functions are depicted.

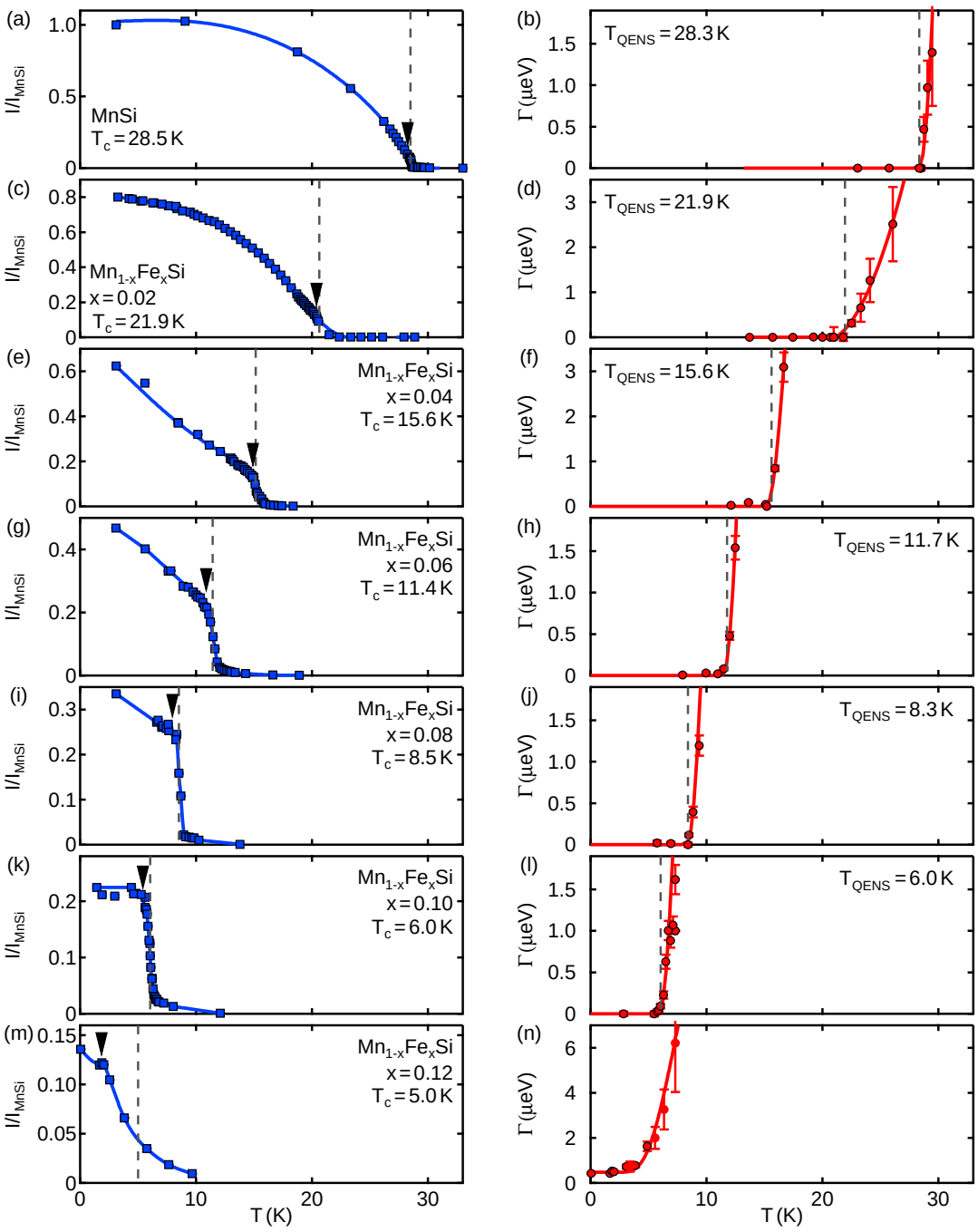

Figure 4.23.: Suppression of the helical order in $Mn_{1-x}Fe_xSi$ ($0 \leq x \leq 0.12$) as observed in the scattering intensity and the linewidth Γ of the fluctuations. The left column shows the intensity as function of temperature. T_c is indicated by the black dashed line. The black arrow slightly below T_c points at a characteristic kink present for all iron concentrations. On the right hand site the quasielastic line width Γ as function of temperature is shown. The black dashed line indicates the temperature T_{QENS} where $\Gamma = 0$. All data are measured on the position of the helical Bragg peak. The solid lines are guides to the eye.

The quasielastic line width Γ is extracted by a fit to $S(q,\tau)/S(q,0)$ considering a single exponential decay of the form

$$\frac{S(q,\tau)}{S(q,0)} = A \cdot \exp\left[-\frac{\Gamma\tau}{\hbar}\right] + (1 - A), \tag{4.13}$$

with $A = 1$ and $y_0 = 0$. The line width Γ versus temperature is shown on the right hand side in Fig. 4.23. All samples in the range ($0 \leq x \leq 10$) show a characteristic temperature dependence of Γ. At low temperatures in the helical phase, Γ is resolution limited, i.e. $\Gamma = 0$, at a temperature T_{QENS} Γ exhibits a sudden increase. T_{QENS} is indicated by the black dashed line. For increasing iron concentration T_{QENS} decreases as observed for T_{c}. $Mn_{1-x}Fe_xSi$, $x = 0.02$ (cf. Fig. 4.23 (d)) exhibits a weaker increase of Γ, due to a strong background contamination. The collimation of the neutron beam was not adjusted properly in this special measurement. In contrast to all other samples, Γ remains finite in the full temperature range under study for the sample with $x = 0.12$ (cf. Fig. 4.23 (n)). No static magnetic order is observed down to 50 mK in this sample.

In conclusion, the measurements reported in this section allow to extract two characteristic temperatures T_{c} and T_{QENS}. T_{c} is defined by the minimum of the derivative of the intensity versus temperature data and resembles the sharp peak on the shoulder in the specific heat data as shown for MnSi in Fig. 4.5 (a). T_{QENS} defines the temperature were the chiral fluctuations become static indicated by a resolution limited Γ. Another characteristic temperature T_2 is defined by the Vollhardt invariance in the specific. At $T_2$the cross over from the chiral fluctuating to ferromagnetic fluctuating regime takes place, as discussed in Sec. 4.1.4. Fig 4.24 summarizes the evolution of these temperatures with increasing iron concentration. The data for T_{c}, T_{QENS} are from this study while those for T_2 are from Ref. [159]. In the green shaded area a static helical order is observed. The blue shaded region indicates a phase of predominant isotropic chiral fluctuations, which become ferromagnetic above the cross over line defined at T_2.

All characteristic parameters of the helical order k_{hel}, λ_{hel}, $\Delta\omega$, $\Delta\alpha$ and the characteristic temperatures T_{c} and T_{QENS} for both $Mn_{1-x}Fe_xSi$ and $Mn_{1-x}Co_xSi$ are summarized in Tab. 4.2.

4.4.3. Discussion

Substitutional doping of iron and cobalt atoms into MnSi, similar to hydrostatic pressure, decreases the lattice constant but in addition, also increases the amount of electrons per formula unit. Thus directly affecting the electronic structure. The increase of the number of electrons per formula unit dominates the influence onto the magnetic structure, as a cobalt doping of x_{Co} corresponds precisely to the effect of

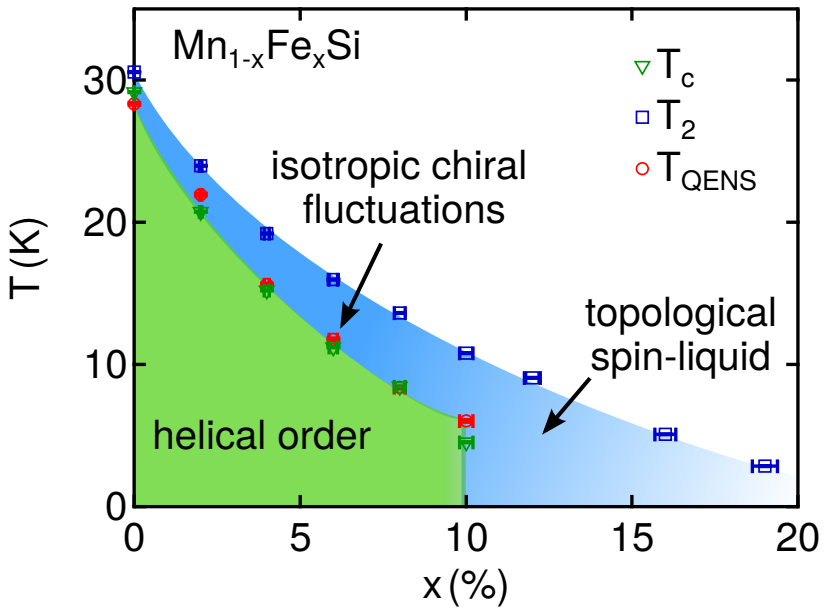

Figure 4.24.: Doping versus temperature phase diagram of $Mn_{1-x}Fe_xSi$ inferred from SANS (T_c), spin echo (T_{QENS}) and specific heat measurements (T_2). The data for T_2 are taken from ref. [159]). In the green shaded area a static helical order is observed, while the blue shaded region shows chiral fluctuations. Above T_2 ferromagnetic fluctuations are observed.

$2x_{Fe}$ iron doping in various properties, e.g. T_c and k_{hel}. The effect of disorder seems to be weak, at least up to an iron concentration of $x = 0.10$, as the incoherent background in the scattering patterns is rather small up to this concentration.

Less obvious is the influence on the magnetic anisotropy α_{cub}. α_{cub} decreases with increasing doping. Additionally, an unexpected orientation of the helical domains in the crystalline $\langle 110 \rangle$ direction occurs for $x = 0.06$ and 0.10. Peaks along the $\langle 110 \rangle$ direction are very similar to the *partial magnetic order* under hydrostatic pressure in pure MnSi. However, the minimal model for chiral helimagnets as introduced in Sec. 4.1.1 does not explain the alignment of helices along the $\langle 110 \rangle$ direction. The free energy cannot be minimized for helical domains pointing along this direction, as all higher order terms to f_{cub} result in saddle points. In the minimal model there is no explanation for a state with several helical domains pointing along $\langle 110 \rangle$. Beyond the minimal model, the observations from neutron scattering may be explained by a single domain multi-q state, but there is no further evidence for such a proposal.

The system becomes less ferromagnetic with increasing doping as the helical wave vector $k_{hel} \propto D/J$ increases. However, the effect is much stronger for doping than for pressure. k_{hel} increases by a factor of ~ 3 up to the critical concentration x_c, while under pressure the increase is only by a factor of ~ 1.3 as reported in Ref. [166].

The suppression of the magnetic order by doping can be observed in various physical properties, e.g. susceptibility, intensity of the magnetic satellites and linewidth of the chiral fluctuations as summarized in Fig. 4.25. While in pure MnSi the susceptibility exhibits a first-order peak (cf. panel (a)), this feature smears out for increasing iron concentration. The same holds for the temperature dependence of the intensity, also observing a less pronounced decay with increasing iron concentration. A smeared out decay may be understood in terms of a second-order phase transition, but can also arise from an increased disorder in the highly doped samples.

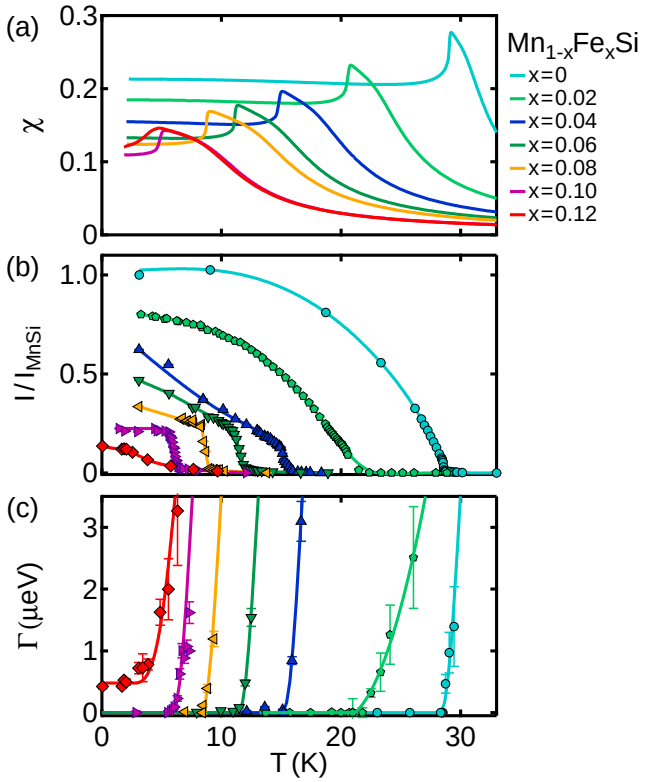

Figure 4.25.: Direct comparison of susceptibility (a), intensity of the helical Bragg peak (b) and quasielastic line width (c) measured in $Mn_{1-x}Fe_xSi$. In all quantities the suppression of the helical transition temperature T_c is visible. At an iron concentration of $x = 0.12$ line width stays finite down to 50 mK. The susceptibility is measured by A. Bauer.

For the highly doped sample with $x = 0.12$ a finite linewidth $\Gamma > 0$ is found down to 0.05 K, in contrast to all other samples under study. Hence, the ring like intensity distribution below the broad helical satellites can be explained by isotropic chiral fluctuations, rather than unaligned helical order. A similar fluctuating regime is reported in MnGe [167]. In addition, C. Franz *et al.* observed a topological Hall

signal in the same sample for temperatures $0.5\,\mathrm{K} \leq T \leq 3\,\mathrm{K}$ [45]. The combination of the topological signal with the fluctuating magnetic phase, may indicate that in this region of the phase diagram (cf. Fig. 4.24) a new type of topological non-trivial spin liquid stabilizes.

Table 4.2.: Elastic and quasi-elastic properties of the $Mn_{1-x}Fe_xSi$ and $Mn_{1-x}Co_xSi$ samples investigated in this study.

x	k_{hel} [Å^{-1}]	λ_{hel} [Å]	$\Delta\omega$ [°]	$\Delta\alpha$ [°]	T_2 [K]	T_{c} [K]	T_{QENS} [K]	anisotropy
Iron doping								
0 %	0.036(3)	173	1.3(8)	2.7(4)	30.55(5)	28.5(1)	28.3(1)	⟨111⟩
2 %	0.043(3)	146	2.2(9)	3.5(8)	23.98(5)	20.6(1)	21.9(1)	⟨111⟩
4 %	0.052(9)	128	8.9(4)	14.5(1)	19.21(5)	15.2(1)	15.6(1)	⟨111⟩
6 %	0.060(2)	105	9.2(2)	10.6(1)	15.97(5)	11.4(1)	11.7(1)	⟨110⟩
8 %	0.068(1)	92	13.7(3)	14.4(1)	13.61(5)	8.5(1)	8.3(1)	⟨111⟩
10 %	0.071(2)	88	11.9(1)	11.7(8)	10.80(5)	6.0(1)	6.0(1)	⟨110⟩
12 %	0.072(9)	89	N/A	N/A	9.06(5)	N/A	0	⟨111⟩
16 %	0.08(8)	71	N/A	N/A	5.10(5)	N/A	N/A	⟨100⟩
Cobalt doping								
2 %	0.055(2)	114	3.09(3)	4.75(11)	17.64(5)	15.1(1)	15.2(1)	⟨111⟩
4 %	0.068(2)	92	N/A	N/A	10.89(5)	N/A	N/A	⟨111⟩

Conclusion and Outlook

This thesis describes the advancements of the neutron spin echo spectrometer RESEDA towards a larger dynamic range, lower small angle scattering background and improvements for a better applicability of the Larmor precession techniques with samples under extreme conditions. The main focus is on the paramagnetic to ferromagnetic transition in iron and the evolution of the paramagnetic to helimagnetic transition with magnetic field and substitutional doping in the cubic helimagnet MnSi. Both systems were studied by means of SANS and neutron spin echo measurements.

In Chapter 2 I summarize the experimental methods used in this thesis and their improvements to realize the studies on iron and MnSi. The new generation MiniMuPAD has one order of magnitude less background compared to the first version, an increased transmission and allows a precise sample alignment between the precession elements. First test experiments with the new longitudinal NRSE setup increased the maximum resolution at RESEDA by one order of magnitude and at the same time enhanced the dynamic range to at least 10^6. The small angle scattering background is significantly reduced and the neutron flux increased by using uncoated rf-coils, a well defined collimation and vacuum flight tubes in the primary and secondary spectrometer arm. We have for the first time realized MIEZE measurements under very strong magnetic fields up to 17 T without reduction of resolution proving the feasibility to combine spin echo resolution with extreme sample environments [41].

In Chapter 3 I report a comprehensive MIEZE study of the dynamics at the paramagnetic to ferromagnetic transition in iron for both $T > T_C$ and $T < T_C$ performed at the beamline RESEDA. Above the Curie temperature the critical fluctuations can be explained by a Heisenberg model additionally considering the dipolar interaction between the fluctuations. The increased flux and reduced background at RESEDA allowed us to access very small scattering angles, hence, probing large distances in real space where weak but long-range interactions, like the dipolar interaction, become

important. Our results confirm the scaling theory developed by Schwabl and Frey [91, 93, 94] for dipolar ferromagnets. Nevertheless, the precise strength of the dipolar interaction can not be explained in this model, illustrating the influence of itinerant electrons. The large dynamic range, easily tunable with longitudinal MIEZE, enabled us to study the well defined excitations, i.e. magnons, below T_C. Our results support previous studies [104] and are in good agreement with standard magnon theory [105, 106].

In Chapter 4 I address the paramagnetic to helimagnetic transition in MnSi under three aspects. First, the chirality of the system at the zero field transition in MnSi, second, the evolution of the chiral fluctuations under the influence of a magnetic field and, third, the suppression of the magnetic order by substitutional doping of iron and cobalt atoms. The MiniMuPAD enabled us to investigate the zero field transition from paramagnetism to helimagnetism in MnSi using polarization analysis [15]. Our study confirms that in agreement with previous unpolarized studies [14] the critical spin flip scattering is very well described by the minimal model of a fluctuation-induced first-order transition in a Brazovskii scenario. The chirality of the system, characterized by the chiral fraction η, decreases above T_c as predicted within this minimal model and there is no need for a more complex model as that recently proposed in Refs. [137–139], predicting a skyrmion formation in bulk chiral magnets at zero magnetic field. Our combined SANS and MIEZE study following the evolution of the paramagnetic to helimagnetic transition in MnSi with magnetic field confirm the change from a first to a second-order transition at the tricritical point H^{TCP}. The SANS patterns vividly show that with increasing field the phase space volume populated by the chiral fluctuations is reduced, from an isotropic sphere to spots on the magnetic satellites. Approaching the tricritical point the number of degrees of freedom of the chiral fluctuations is reduced until the Brazovskii scenario breaks down and the transition becomes second-order. The inverse correlation length parallel $\kappa_{\parallel}$ and perpendicular $\kappa_{\perp}$ to the magnetic field characterizing the fluctuations can be directly calculated by means of the Brazovskii theory. Our fits to the scattering patterns confirm the change of slope of $\kappa_{\parallel}$ at the tricritical point and prove the increasing separation between $\kappa_{\parallel}$ and $\kappa_{\perp}$, both as predicted by the Brazovskii theory. The temperature dependence of Γ resembles the small decrease of T_c when approaching H^{TCP} and shows clear evidence for a change from a first to second-order phase transition. Finally, we can show that substitutional doping of iron and cobalt atoms into MnSi suppresses the magnetic order and induces the emergence of a topologically fluctuating phase. T_c is suppressed, accompanied by an increase of the helical wave vector as observed in our diffraction data. The quasielastic linewidth allows to determine the characteristic temperature T_{QENS} at which the magnetic structure becomes static. By combining our results with susceptibility data [159] and measurements of the topological Hall effect [45] we are able to draw a magnetic phase diagram as function of doping and temperature that shows how the isotropic chiral Brazovskii fluctuations at zero doping evolve to a regime that may be identified as a new form of a topological spin liquid.

Furthermore, while suppressing T_c we observe unconventional anisotropies pointing in the crystalline $\langle 110 \rangle$ direction, similar to the partial magnetic order in MnSi under hydrostatic pressure [144].

The results presented in this thesis show the great potential of combining SANS and spin echo techniques. Novel magnetic systems, like Skyrmions or other magnetic vortices, order on large length scales being perfectly accessible with SANS instruments. At the same time the dynamics of these magnetic systems is very important for their fundamental understanding, making spin echo the perfect choice. The possibility to combine depolarizing samples and sample environments with spin echo resolution using the MIEZE technique is ideally suited to study field induced QPTs for instance in $CoNb_2O_6$ [42] or QPTs at the border to ferromagnetism as for example in UGe_2 [21]. Yet another fascinating field is the study of melting and reorientation transitions in the flux line lattice of superconductors. First proof of principle experiments at RESEDA show the feasibility of such studies, but also the importance to increase the resolution. A better control of the B_0 fields and rf-coils that allow spin flips up to 4 MHz will make an effective field integral of $\approx 500\,\mathrm{mT\,m}$ available, being comparable to that applied at world leading spin echo spectrometers. The large effective field integral does not only allow to study at ultra large spin echo times using long wavelength, but also to perform measurements with medium resolution at the wavelength of maximum flux. An increased flux is very important for the study of diffuse processes as for example at continuous phase transitions where critical scattering from the fluctuations of the order parameter are observed. Longitudinal NRSE has the unique opportunity to easily implement well established focusing neutron guides in the precession region and hence to increase the neutron flux at the sample. Meanwhile, the MIEZE method can be further improved for inelastic studies and better statistics by fixing the phase of the MIEZE echo. A constant phase will allow to follow changes of the phase due to inelastic excitations in the sample and to measure their evolution towards critical fluctuations when approaching a phase transition. For the investigation of chiral helimagnets the precise understanding of the partial magnetic order - the holy grail of MnSi - remains unsettled. A combined SANS and MIEZE study addressing the suppression of the magnetic order by hydrostatic pressure may give the important hint to solve this problem.

In conclusion, within this thesis we have proven that the combination of small angle scattering and high resolution spin echo measurements is a powerful tool to investigate the nature and stability of magnetic order. The systems studied in this thesis are very good examples where fluctuations fundamentally change the properties of the system and give rise to new unexpected physical phenomena.

Publications

1. **Static and Quasi-Elastic Properties of the Spiral Magnet $Ba_2CuGe_2O_7$ Studied by Neutron Resonance Spin Echo Spectroscopy and Neutron Larmor Labeling**
   S. Mühlbauer, J. Kindervater and W. Häußler, submitted to Phys. Rev. B (2015)

2. **Neutron spin echo spectroscopy under 17 T magnetic field at RESEDA**
   J. Kindervater, N. Martin, W. Häußler, M. Krautloher, C. Fuchs, S. Mühlbauer, J. A. Lim, E. Blackburn, P. Böni, and C. Pfleiderer, EPJ Web of Conferences **83**, 03008 (2015)

3. **Critical spin-flip scattering at the helimagnetic transition of MnSi**
   J. Kindervater, W. Häußler, M. Janoschek, C. Pfleiderer, P. Böni, and M. Garst, Phys. Rev. B **89**, 180408(R) (2014) (editors suggestions)

4. **Unwinding of a Skyrmion Lattice by Magnetic Monopoles**
   P. Milde, D. Köhler, J. Seidel, L. M. Eng, A. Bauer, A. Chacon, J. Kindervater, S. Mühlbauer, C. Pfleiderer, S. Buhrandt, C. Schütte, and A. Rosch, Science **340**, 1076-1080 (2013)

5. **Polyoxometalate-stabilized, water dispersible Fe2Pt magnetic nanoparticles**
   K. M. Seemann, A. Bauer, J. Kindervater, M. Meyer, C. Besson, M. Luysberg, P. Durkin, W. Pyckhout-Hintzen, N. Budisa, R. Georgii, C. M. Schneider, and P. Kögerler, Nanoscale **5**, 2511-2519 (2013)

6. **Neutron-spin-echo from polarizing samples**
   J Kindervater, W Häußler, A Tischendorf, and P Böni, J. Phys.: Conf. Ser. **340** 012030 (2012)

7. **Detection of high frequency intensity oscillations at RESEDA using the CASCADE detector**
   W. Häußler, P. Böni, M. Klein, C. J. Schmidt, U. Schmidt, F. Groitl, and J. Kindervater, Rev. Sci. Instrum. **82**, 045101 (2011)

8. **Using polarized Neutrons for elastic and dynamic studies on protein systems**
   W. Häußler and J. Kindervater, AIP Conf. Proc. **1255**, 246 (2010)

Acknowledgements

An dieser Stelle danke ich allen, die mich während meiner Doktorarbeit unterstützt haben. Im Besonderen möchte ich mich bei folgenden Personen bedanken:

Allen voran möchte ich mich bei Prof. Peter Böni bedanken, dass ich in den letzten drei Jahren diese Arbeit bei Dir durchführen konnte. Besonderer Dank gilt natürlich auch Prof. Christian Pfleiderer. Meine Dissertation war genau zwischen euren beiden Lehrstühlen angelegt, sodass ich das Glück hatte, durch eure unterschiedliche Herangehensweise an die Physik verschiedene Blickwinkel auf die Fragestellungen zu bekommen und immer zwei Türen offen standen. Danke für die zahlreichen anregenden Diskussionen, die riesigen Freiheiten und eure Begeisterung, die mir auf meinem Weg durch die Dissertation sehr geholfen haben. Das super Arbeitsklima am E21/E51 ist nicht zuletzt euer Verdienst und war einer der Grundsteine meiner Motivation. Es hat Spaß mit euch gemacht!

Bei Wolfgang Häußler möchte ich mich für die langjährige Zusammenarbeit und die Einführung in die Geheimnisse des Spin Echos in all seinen Formen bedanken, aber auch für viele Diskussionen, die über die Physik hinausgingen. Darüber hinaus danke ich Nicolas Martin. Merci beaucoup pour le soutien extraordinaire pendant de longues périodes de mesurage. Je me suis rendu compte qu'une collaboration franco-allemande mène à un succès sans précédent.

Markus Garst danke ich für die theoretische Unterstützung bei meinen Projekten. Durch Dein Verständnis nicht nur für die Theorie sondern auch das Experiment konnten wir in vielen Telefonkonferenzen ein umfassendes Bild entwickeln.

Dem gesamten RESEDA Team: Steffen Säubert, Christian Franz, Thorsten Schröder, Franz Haslbeck, Christian Fuchs und Stefan Ernst für die gute Zusammenarbeit und neuen Schwung in einer nicht ganz einfachen Phase am Instrument.

Acknowledgements

Bei allen Kollegen am FRM II möchte ich mich bedanken: Dem SANS-1 Team, Sebastian Mühlbauer und Andre Heinemann dafür, dass ich euer Instrument als erster offizieller User einweihen durfte und ihr so fröhlich Kryostaten und Magneten mit mir getauscht habt. Das Gleiche gilt für das MIRA Team Robert Georgii, Georg Brandl, Reinhard Schwikowski und Andreas Mantwill für die Hilfe bei Hardware Ausfällen, schnellen Änderungen und spontanen Lösungen. Bei Thomas Keller für ein offenes Ohr bei Spin Echo Fragen. Ganz besonders möchte ich mich auch bei der Probenumgebung Jürgen Peters, Heinrich Kolb, Peter Biber und Milan Antic für die super Zusammenarbeit bedanken.

Bei Marc Janoschek möchte ich mich dafür bedanken, dass er mir neben physikalischen Fragen gerade auch auf die nicht physikalischen Fragen im Berufsleben eines Wissenschaftlers immer eine Antwort gibt.

Bei allen E21gern respektive E51gern: Felix Rucker, Andreas Bauer, Christoph Schnarr, Georg Benka, Stefan Giemsa, Tommy Reimann, Michael Schulz, Tim Adams, Alfonso Chacón, Robert Ritz, Marco Halder, Alexander Regnat, Philipp Schmakat, Christopher Duvinage, Michael Wagner, ... für gemeinsame Büro Essen, die E21 Bike Gang, die Kaffeerunden, das Grillen in Garching, die gemeinsamen Konferenzbesuche, die Weihnachtsfeiern und all die Dinge, die Zeit in Garching unvergesslich gemacht haben!

Bei meinen Freunden: Jonas, Sulya, Philip, Konny, Ruth, Max, Frauke, Dominik, Ingrid, Moritz, Michi, Tanja, Felix und Leonie. Ihr seid einmalig und ohne euch wären die letzten drei Jahre nur halb so lustig gewesen!

Ganz besonderer Dank gilt meiner Familie: Maria, Hans-Werner, Kathrin, Christian, Tobias, Ulrike, Elias, David und Regina. Danke für eure Unterstützung und euren Rückhalt sowie die gemeinsame Zeit, die einfach Spaß macht. Ihr seid nicht nur Familie sondern auch Freunde!

Lea, bei Dir möchte ich mich bedanken, weil ich ohne Dich nicht im Ansatz so entspannt durch die letzten drei Jahre gekommen wäre. Ich danke Dir, dass Du mir immer zur Seite stehst und ich mit Dir alles besprechen kann. Mit Dir zusammen freue ich mich riesig auf unsere zukünftigen Herausforderungen.

APPENDIX A

Appendix: Critical fluctuations at the Curie point of iron

In Tab. A.1 all parameters employed in the study on iron and the corresponding references are summarized. Fig. A.1 shows additional MIEZE data measured above the Curie point at $T_C + 30\,\mathrm{K}$ (a), $T_C + 2\,\mathrm{K}$ (b) and $T_C + 1\,\mathrm{K}$ (c). The data are treated in the same way as discussed in Ch. 3.

Table A.1.: Characteristic parameters of iron used in this chapter.

	T_C	a	κ_0	ν	A	q_D
Fe	1043 K[98]	2.87 Å[98]	1.22 Å[95]	0.69	140 meVÅ$^{5/2}$[100]	0.033 Å^{-1}[101]

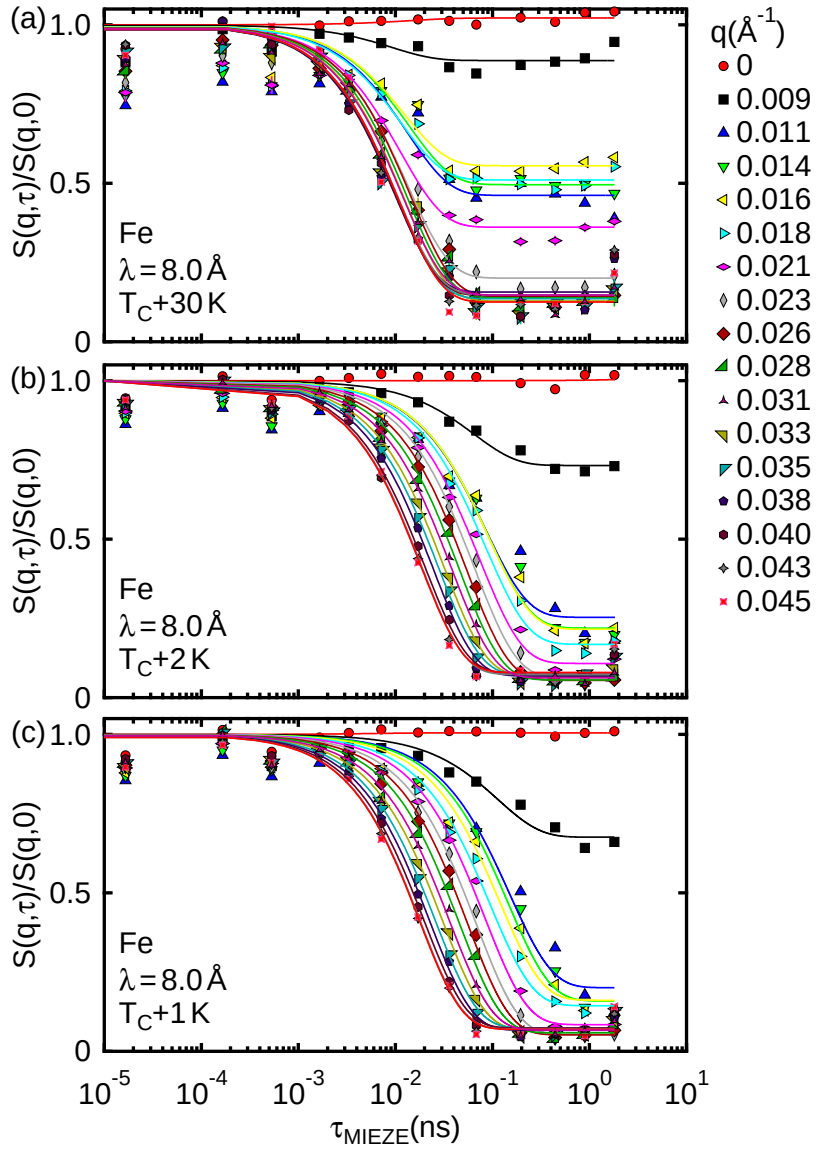

Figure A.1.: Normalized MIEZE contrast measured at $T_C + 30\,K$ (a), $T_C + 2\,K$ (b) and $T_C + 1\,K$ (c). The data were recorded using neutrons with a mean wavelength $\lambda = 8.0\,Å$.

APPENDIX B

Appendix: Cubic chiral Dzyaloshinskii-Moriya helimagnets

In this appendix the generalized scattering cross section for chiral magnets and a description of how to calculate the correlation length $\kappa_\perp$ and $\kappa_\parallel$ within the Brazovskii theory are given. Additional results for the MIEZE measurements on MnSi and the NRSE measurements on $Mn_{1-x}Fe_xSi$ and $Mn_{1-x}Co_xSi$ are shown.

B.1. Scattering cross section for chiral magnets

Equation B.2 and B.3 combine in equation B.1 to the generalized scattering cross-section σ for chiral helimagnets as introduced in Sec. 4.1.3. σ includes the dependence on an external magnetic field along the crystalline $\langle 111 \rangle$ direction of the sample. The length of the scattering vector is given by $q = \sqrt{q_1^2 + q_2^2 + q_3^2}$, the length of the helical wave vector by k_{hel}, the strength of the dipolar interaction by χ_{int} and the strength of the cubic anisotropy by α_{cub}, respectively. $\kappa_\parallel$ describes the inverse correlation length along and $\kappa_\perp$ perpendicular to the magnetic field.

$$\sigma = Ak_BT\frac{nominator}{denominator} \tag{B.1}$$

The generalized expression was calculated by M. Garst and then evaluated for $B \parallel \langle 111 \rangle$ using Mathematica [168], to resemble the field geometry in our SANS study.

$$
\begin{aligned}
&nominator = \\
&(-9q^6 - 12q_1^4 {k_{\mathrm{hel}}}^2 - 12q_2^4 {k_{\mathrm{hel}}}^2 - 24q_2^2 q_3^2 {k_{\mathrm{hel}}}^2 - 12q_3^4 {k_{\mathrm{hel}}}^2 + 3q_2^2 {k_{\mathrm{hel}}}^4 + 3q_3^2 {k_{\mathrm{hel}}}^4 + \\
&6q_2^2 q_3^2 {k_{\mathrm{hel}}}^2 \alpha_{cub} + 2q_2^2 {k_{\mathrm{hel}}}^2 {\kappa_\parallel}^2 - 2q_2 q_3 {k_{\mathrm{hel}}}^2 {\kappa_\parallel}^2 + 2q_3^2 {k_{\mathrm{hel}}}^2 {\kappa_\parallel}^2 + 2q_2^2 q_3^2 \alpha_{cub} {\kappa_\parallel}^2 + 4q_2^2 {k_{\mathrm{hel}}}^2 {\kappa_\perp}^2 \\
&+2q_2 q_3 {k_{\mathrm{hel}}}^2 {\kappa_\perp}^2 + 4q_3^2 {k_{\mathrm{hel}}}^2 {\kappa_\perp}^2 + 4q_2^2 q_3^2 \alpha_{cub} {\kappa_\perp}^2 + 2q_2^2 {\kappa_\parallel}^2 {\kappa_\perp}^2 - 2q_2 q_3 {\kappa_\parallel}^2 {\kappa_\perp}^2 \\
&+2q_3^2 {\kappa_\parallel}^2 {\kappa_\perp}^2 + q_2^2 \kappa_\perp^4 + 2q_2 q_3 \kappa_\perp^4 + q_3^2 \kappa_\perp^4 - 3q^4 (q_1^2 (-1 + 2\alpha_{cub}) \\
&+q_2^2 (-1 + 2\alpha_{cub}) + q_3^2 (-1 + 2\alpha_{cub}) + 2(3{k_{\mathrm{hel}}}^2 + {\kappa_\parallel}^2 + 2{\kappa_\perp}^2)) - 2q_1 (q_2 + q_3)(\kappa_\parallel - \kappa_\perp) \\
&(\kappa_\parallel + \kappa_\perp)(q_2 q_3 \alpha_{cub} + {\kappa_\perp}^2 - {k_{\mathrm{hel}}}^2 (-1 + \chi_{int})) - 2{k_{\mathrm{hel}}}^2 (q_2 q_3 (-{\kappa_\parallel}^2 + {\kappa_\perp}^2) \\
&+q_3^2 (3{k_{\mathrm{hel}}}^2 + {\kappa_\parallel}^2 + 2{\kappa_\perp}^2) + q_2^2 (3{k_{\mathrm{hel}}}^2 + 3q_3^2 \alpha_{cub} + {\kappa_\parallel}^2 + 2{\kappa_\perp}^2)) \chi_{int} \\
&-q^2 (-18q_3^2 {k_{\mathrm{hel}}}^2 + 9{k_{\mathrm{hel}}}^4 + 6q_3^2 {k_{\mathrm{hel}}}^2 \alpha_{cub} - 2q_3^2 {\kappa_\parallel}^2 + 6{k_{\mathrm{hel}}}^2 {\kappa_\parallel}^2 + 2q_3^2 \alpha_{cub} {\kappa_\parallel}^2 - 4q_3^2 {\kappa_\perp}^2 \\
&+12{k_{\mathrm{hel}}}^2 {\kappa_\perp}^2 + 4q_3^2 \alpha_{cub} {\kappa_\perp}^2 + 6{\kappa_\parallel}^2 {\kappa_\perp}^2 + 3\kappa_\perp^4 + 2q_2 q_3 (\kappa_\parallel - \kappa_\perp)(\kappa_\parallel + \kappa_\perp) \\
&+2q_1 (q_2 + q_3)(\kappa_\parallel - \kappa_\perp)(\kappa_\parallel + \kappa_\perp) + 6q_3^2 {k_{\mathrm{hel}}}^2 \chi_{int} + q_2^2 (3q_3^2 (-2 + \alpha_{cub}) \alpha_{cub} \\
&+2(-1 + \alpha_{cub})({\kappa_\parallel}^2 + 2{\kappa_\perp}^2) + 6{k_{\mathrm{hel}}}^2 (-3 + \alpha_{cub} + \chi_{int})) + q_1^2 (-2({\kappa_\parallel}^2 + 2{\kappa_\perp}^2) \\
&+\alpha_{cub} (3q_2^2 (-2 + \alpha_{cub}) + 3q_3^2 (-2 + \alpha_{cub}) + 2({\kappa_\parallel}^2 + 2{\kappa_\perp}^2)) + 6{k_{\mathrm{hel}}}^2 (-3 + \alpha_{cub} + \chi_{int}))) \\
&+q_1^2 (2q_2 q_3 \alpha_{cub} (-{\kappa_\parallel}^2 + {\kappa_\perp}^2) + ({k_{\mathrm{hel}}}^2 + {\kappa_\perp}^2)(3{k_{\mathrm{hel}}}^2 + 2{\kappa_\parallel}^2 + {\kappa_\perp}^2) - \alpha_{cub} \chi_{int})) \\
&-2{k_{\mathrm{hel}}}^2 (3{k_{\mathrm{hel}}}^2 + {\kappa_\parallel}^2 + 2{\kappa_\perp}^2) \chi_{int} + q_3^2 (2\alpha_{cub} ({\kappa_\parallel}^2 + 2{\kappa_\perp}^2) \\
&+6{k_{\mathrm{hel}}}^2 (-4 + \alpha_{cub} + q_2^2 (\alpha_{cub} (9q_3^2 \alpha_{cub} + 2{\kappa_\parallel}^2 + 4{\kappa_\perp}^2) + 6{k_{\mathrm{hel}}}^2 (-4 + \alpha_{cub} - \alpha_{cub} \chi_{int}))))
\end{aligned}
\tag{B.2}
$$

$$
\begin{aligned}
&\mathit{denominator} = \\
&(2(3q^8 + 3q^6(3{k_{\mathrm{hel}}}^2 + (q_1^2 + q_2^2 + q_3^2)\alpha_{cub} + {\kappa_\parallel}^2 + 2{\kappa_\perp}^2) + {k_{\mathrm{hel}}}^2(-12q_1^4{k_{\mathrm{hel}}}^2 - 12q_2^4{k_{\mathrm{hel}}}^2 \\
&-2q_2q_3(\kappa_\parallel - \kappa_\perp)(\kappa_\parallel + \kappa_\perp)({k_{\mathrm{hel}}}^2 + {\kappa_\perp}^2) \\
&-2q_1(q_2 + q_3)(\kappa_\parallel - \kappa_\perp)(\kappa_\parallel + \kappa_\perp)({k_{\mathrm{hel}}}^2 + q_2q_3\alpha_{cub} + {\kappa_\perp}^2) \\
&+q_3^2(-12q_3^2{k_{\mathrm{hel}}}^2 + ({k_{\mathrm{hel}}}^2 + {\kappa_\perp}^2)(3{k_{\mathrm{hel}}}^2 + 2{\kappa_\parallel}^2 + {\kappa_\perp}^2)) \\
&+q_2^2(({k_{\mathrm{hel}}}^2 + {\kappa_\perp}^2)(3{k_{\mathrm{hel}}}^2 + 2{\kappa_\parallel}^2 + {\kappa_\perp}^2) \\
&+2q_3^2(3{k_{\mathrm{hel}}}^2(-4 + \alpha_{cub}) + \alpha_{cub}({\kappa_\parallel}^2 + 2{\kappa_\perp}^2))) + q_1^2(2q_2q_3\alpha_{cub}(-{\kappa_\parallel}^2 + {\kappa_\perp}^2) \\
&+({k_{\mathrm{hel}}}^2 + {\kappa_\perp}^2)(3{k_{\mathrm{hel}}}^2 + 2{\kappa_\parallel}^2 + {\kappa_\perp}^2) + 2q_3^2(3{k_{\mathrm{hel}}}^2(-4 + \alpha_{cub}) + \alpha_{cub}({\kappa_\parallel}^2 + 2{\kappa_\perp}^2)) \\
&+q_2^2(6{k_{\mathrm{hel}}}^2(-4 + \alpha_{cub}) + \alpha_{cub}(9q_3^2\alpha_{cub} + 2{\kappa_\parallel}^2 + 4{\kappa_\perp}^2))))\chi_{int} \\
&+q^4(-12q_3^2{k_{\mathrm{hel}}}^2 + 9{k_{\mathrm{hel}}}^4 + 6q_3^2{k_{\mathrm{hel}}}^2\alpha_{cub} + 6{k_{\mathrm{hel}}}^2{\kappa_\parallel}^2 + 2q_3^2\alpha_{cub}{\kappa_\parallel}^2 + 12{k_{\mathrm{hel}}}^2{\kappa_\perp}^2 + 4q_3^2\alpha_{cub}{\kappa_\perp}^2 \\
&+6{\kappa_\parallel}^2{\kappa_\perp}^2 + 3{\kappa_\perp}^4 + 3q_3^2{k_{\mathrm{hel}}}^2\chi_{int} + q_2^2(\alpha_{cub}(3q_3^2\alpha_{cub} + 2{\kappa_\parallel}^2 + 4{\kappa_\perp}^2) \\
&+3{k_{\mathrm{hel}}}^2(-4 + 2\alpha_{cub} + \chi_{int})) + q_1^2(\alpha_{cub}(3(q_2^2 + q_3^2)\alpha_{cub} + 2({\kappa_\parallel}^2 + 2{\kappa_\perp}^2)) \\
&+3{k_{\mathrm{hel}}}^2(-4 + 2\alpha_{cub} + \chi_{int}))) + q^2(-12q_3^2{k_{\mathrm{hel}}}^4 + 3{k_{\mathrm{hel}}}^6 - 12q_1^4{k_{\mathrm{hel}}}^2\alpha_{cub} - 12q_2^4{k_{\mathrm{hel}}}^2\alpha_{cub} \\
&-12q_3^4{k_{\mathrm{hel}}}^2\alpha_{cub} + 3q_3^2{k_{\mathrm{hel}}}^4\alpha_{cub} - 4q_3^2{k_{\mathrm{hel}}}^2{\kappa_\parallel}^2 + 3{k_{\mathrm{hel}}}^4{\kappa_\parallel}^2 \\
&+2q_3^2{k_{\mathrm{hel}}}^2\alpha_{cub}{\kappa_\parallel}^2 - 8q_3^2{k_{\mathrm{hel}}}^2{\kappa_\perp}^2 + 6{k_{\mathrm{hel}}}^4{\kappa_\perp}^2 + 4q_3^2{k_{\mathrm{hel}}}^2\alpha_{cub}{\kappa_\perp}^2 + 6{k_{\mathrm{hel}}}^2{\kappa_\parallel}^2{\kappa_\perp}^2 \\
&+2q_3^2\alpha_{cub}{\kappa_\parallel}^2{\kappa_\perp}^2 + 3{k_{\mathrm{hel}}}^2{\kappa_\perp}^4 + q_3^2\alpha_{cub}{\kappa_\perp}^4 + 3{\kappa_\parallel}^2{\kappa_\perp}^4 \\
&+2q_3^2{k_{\mathrm{hel}}}^2(3{k_{\mathrm{hel}}}^2 + {\kappa_\parallel}^2 + 2{\kappa_\perp}^2)\chi_{int} - 2q_2q_3{k_{\mathrm{hel}}}^2(\kappa_\parallel - \kappa_\perp)(\kappa_\parallel \\
&+\kappa_\perp)(4 + \chi_{int}) - 2q_1(q_2 + q_3){k_{\mathrm{hel}}}^2(\kappa_\parallel - \kappa_\perp)(\kappa_\parallel + \kappa_\perp)(4 + \chi_{int}) \\
&+q_2^2(\alpha_{cub}(2{\kappa_\parallel}^2{\kappa_\perp}^2 + {\kappa_\perp}^4 + q_3^2\alpha_{cub}({\kappa_\parallel}^2 + 2{\kappa_\perp}^2)) + 3{k_{\mathrm{hel}}}^4(-4 + \alpha_{cub} \\
&+2\chi_{int}) + {k_{\mathrm{hel}}}^2(2({\kappa_\parallel}^2 + 2{\kappa_\perp}^2)(-2 + \alpha_{cub} + \chi_{int}) + 3q_3^2\alpha_{cub}(\alpha_{cub} + 2\chi_{int}))) \\
&+q_1^2(\alpha_{cub}(\alpha_{cub}(3q_2^2q_3^2\alpha_{cub} + (q_2^2 + q_3^2){\kappa_\parallel}^2) + 2((q_2^2 + q_3^2)\alpha_{cub} + {\kappa_\parallel}^2){\kappa_\perp}^2 \\
&+{\kappa_\perp}^4) + 3{k_{\mathrm{hel}}}^4(-4 + \alpha_{cub} + 2\chi_{int}) + {k_{\mathrm{hel}}}^2(2({\kappa_\parallel}^2 + 2{\kappa_\perp}^2)(-2 + \alpha_{cub} + \chi_{int}) \\
&+3q_2^2\alpha_{cub}(\alpha_{cub} + 2\chi_{int}) + 3q_3^2\alpha_{cub}(\alpha_{cub} + 2\chi_{int}))))))
\end{aligned}
\tag{B.3}
$$

B.2. Brazovskii theory for chiral magnets

Here the fundamental equations from the Brazovskii theory are motivated to calculate the parallel $\kappa_\parallel$ and perpendicular $\kappa_\perp$ inverse correlation length for chiral magnets in magnetic field, following the supplement of Ref. [14] and the report [169]. Close to the transition chiral fluctuations have to be treated in a self-consistent manner. We start the discussion with Eq. (B30) and (B31) from the supplement of Ref. [14] in

the paramagnetic phase $|\Psi_{\text{hel}}| = 0$. The equations read

$$\Delta_\perp = \delta + \frac{u}{3!}\phi_0^2 + \frac{u}{3!}(2D_\perp + D_\parallel) \tag{B.4}$$

$$\Delta_\parallel = \delta + \frac{u}{3!}3\phi_0^2 + \frac{u}{3!}(D_\perp + 3D_\parallel), \tag{B.5}$$

$D_\perp$ and $D_\parallel$ are the partial derivatives of the function $D(\Delta_\perp,\Delta_\parallel)$ with respect to $\Delta_\perp$ and $\Delta_\parallel$, $D_i = \partial_{\Delta_i} D(\Delta_\perp,\Delta_\parallel)$ with $i = \perp$, $\parallel$. The function D reads

$$D(\Delta_\perp,\Delta_\parallel) = k_B T \int \frac{\mathrm{d}^3 k}{(2\pi)^3} \log(\det \chi^{-1}(k)), \tag{B.6}$$

where χ is susceptibility introduced in Eq. (B24) in the supplement of Ref. [14]. D can be separated in into a part containing the leading singularity and into a subleading part $D = D_{\text{singular}} + D_{sub}$. The singular part is given by

$$D_{\text{singular}}(\Delta_\perp,\Delta_\parallel) = \frac{Q^3 k_B T}{\sqrt{2}\pi} \sqrt{\frac{\Delta_\perp + \Delta_\parallel}{JQ^2}} \cdot y\left(\frac{\Delta_\perp - \Delta_\parallel}{\Delta_\perp + \Delta_\parallel}\right), \tag{B.7}$$

with the auxiliary function

$$y(\alpha) = \sqrt{1+\alpha} - \frac{1}{\pi}\int_{-\infty}^{\infty} \mathrm{d}s \left(1 - \sqrt{\frac{1+s^2}{\alpha}} \tan^{-1} \sqrt{\frac{\alpha}{1+s^2}}\right). \tag{B.8}$$

The function yields $y(0) = 1$ and the derivative $y'(0) = 1/6$. One can rewrite Eq. B.4 and B.5 in a dimensionless form by dividing both equations through JQ^2, with the ferromagnetic exchange constant J and the scattering vector Q. We introduce $\tilde{\kappa}_i := \frac{\kappa_i}{Q}$, $\kappa_i^2 := \frac{\Delta_i}{J}$, $\tilde{\delta} := \frac{\delta}{JQ^2}$, $\tilde{u} := \frac{u}{JQ^2}$ and $\gamma := \tilde{u}\frac{k_B Q^3}{JQ^2}$. The dimensionless equations than read

$$\tilde{\kappa}_\perp^2 = \tilde{\delta} + \frac{1}{3!}\tilde{u}\phi_0^2 + \frac{1}{3!}\tilde{u}(2D_\perp + D_\parallel) \tag{B.9}$$

$$\tilde{\kappa}_\parallel^2 = \tilde{\delta} + \frac{3}{3!}\tilde{u}\phi_0^2 + \frac{1}{3!}\tilde{u}(D_\perp + 3D_\parallel). \tag{B.10}$$

The Ansatz

$$\tilde{\delta} = \frac{T - T_{MF}}{T_0} \tag{B.11}$$

leads to

$$\tilde{\kappa}_{\perp}^2 = \frac{T - T_{MF}}{T_0} + \frac{1}{3!}\tilde{u}\phi_0^2 + \quad \text{(B.12)}$$

$$+\frac{1}{3!}\frac{1}{\sqrt{2}\pi}\gamma T\left(\frac{3}{2}\frac{1}{\sqrt{\tilde{\kappa}_{\perp}^2+\tilde{\kappa}_{\parallel}^2}}\cdot y\left(\frac{\tilde{\kappa}_{\perp}^2-\tilde{\kappa}_{\parallel}^2}{\tilde{\kappa}_{\perp}^2+\tilde{\kappa}_{\parallel}^2}\right)+\frac{4\tilde{\kappa}_{\parallel}^2-2\tilde{\kappa}_{\perp}^2}{(\tilde{\kappa}_{\perp}^2+\tilde{\kappa}_{\parallel}^2)^{2/3}}\cdot y'\left(\frac{\tilde{\kappa}_{\perp}^2-\tilde{\kappa}_{\parallel}^2}{\tilde{\kappa}_{\perp}^2+\tilde{\kappa}_{\parallel}^2}\right)\right) \quad \text{(B.13)}$$

and

$$\tilde{\kappa}_{\parallel}^2 = \frac{T - T_{MF}}{T_0} + \frac{3}{3!}\tilde{u}\phi_0^2 + \quad \text{(B.14)}$$

$$+\frac{1}{3!}\frac{1}{\sqrt{2}\pi}\gamma T\left(2\frac{1}{\sqrt{\tilde{\kappa}_{\perp}^2+\tilde{\kappa}_{\parallel}^2}}\cdot y\left(\frac{\tilde{\kappa}_{\perp}^2-\tilde{\kappa}_{\parallel}^2}{\tilde{\kappa}_{\perp}^2+\tilde{\kappa}_{\parallel}^2}\right)+\frac{2\tilde{\kappa}_{\parallel}^2-6\tilde{\kappa}_{\perp}^2}{(\tilde{\kappa}_{\perp}^2+\tilde{\kappa}_{\parallel}^2)^{2/3}}\cdot y'\left(\frac{\tilde{\kappa}_{\perp}^2-\tilde{\kappa}_{\parallel}^2}{\tilde{\kappa}_{\perp}^2+\tilde{\kappa}_{\parallel}^2}\right)\right). \quad \text{(B.15)}$$

Eq. (B.13) and (B.15) only depend on temperature T, the mean field transition temperature T_{MF} and the magnetization ϕ_0 in units of μ_{B}/f.u.. For MnSi f.u. = 24.018 Å^3. $\tilde{u}$ is a field and temperature independent fit parameter.

B.3. MIEZE measurements on MnSi

In Figure B.1 the normalized intermediate scattering function $S(q,\tau)/S(q,0)$ is shown. The data were measured on a MnSi single crystal with the transversal MIEZE setup at RESEDA.

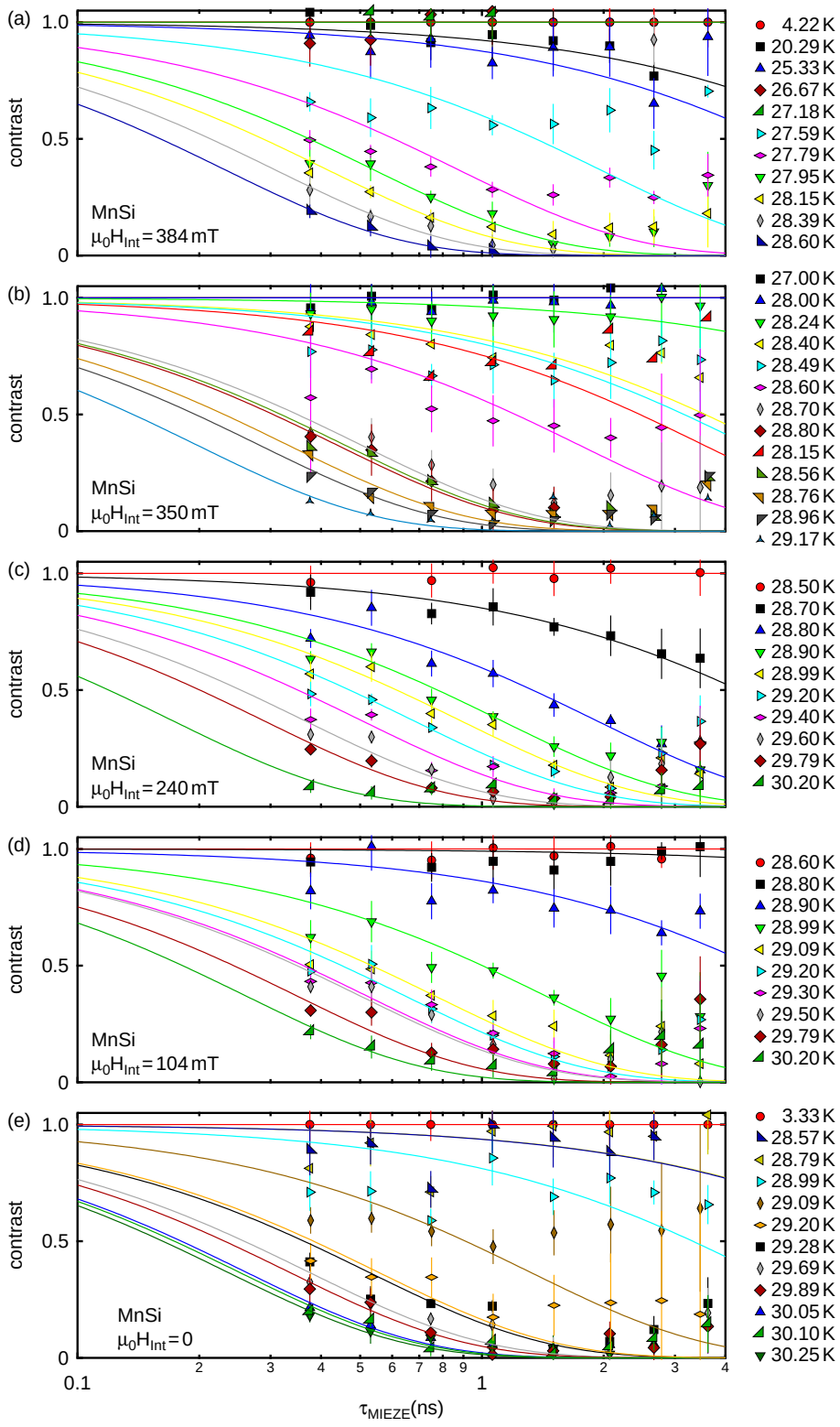

Figure B.1.: Normalized intermediate scattering function measured on the conical Bragg peak as function of temperature for different magnetic fields.

B.4. NRSE measurements from $Mn_{1-x}Fe_xSi$ and $Mn_{1-x}Co_xSi$

The following figures show the measurements using the transverse NRSE option of RESEDA. Fig B.2 and B.3 show the normalized intermediate scattering function measured on the $Mn_{1-x}Fe_xSi$ samples. Fig. B.4 shows the results as obtained from $Mn_{1-x}Co_xSi$.

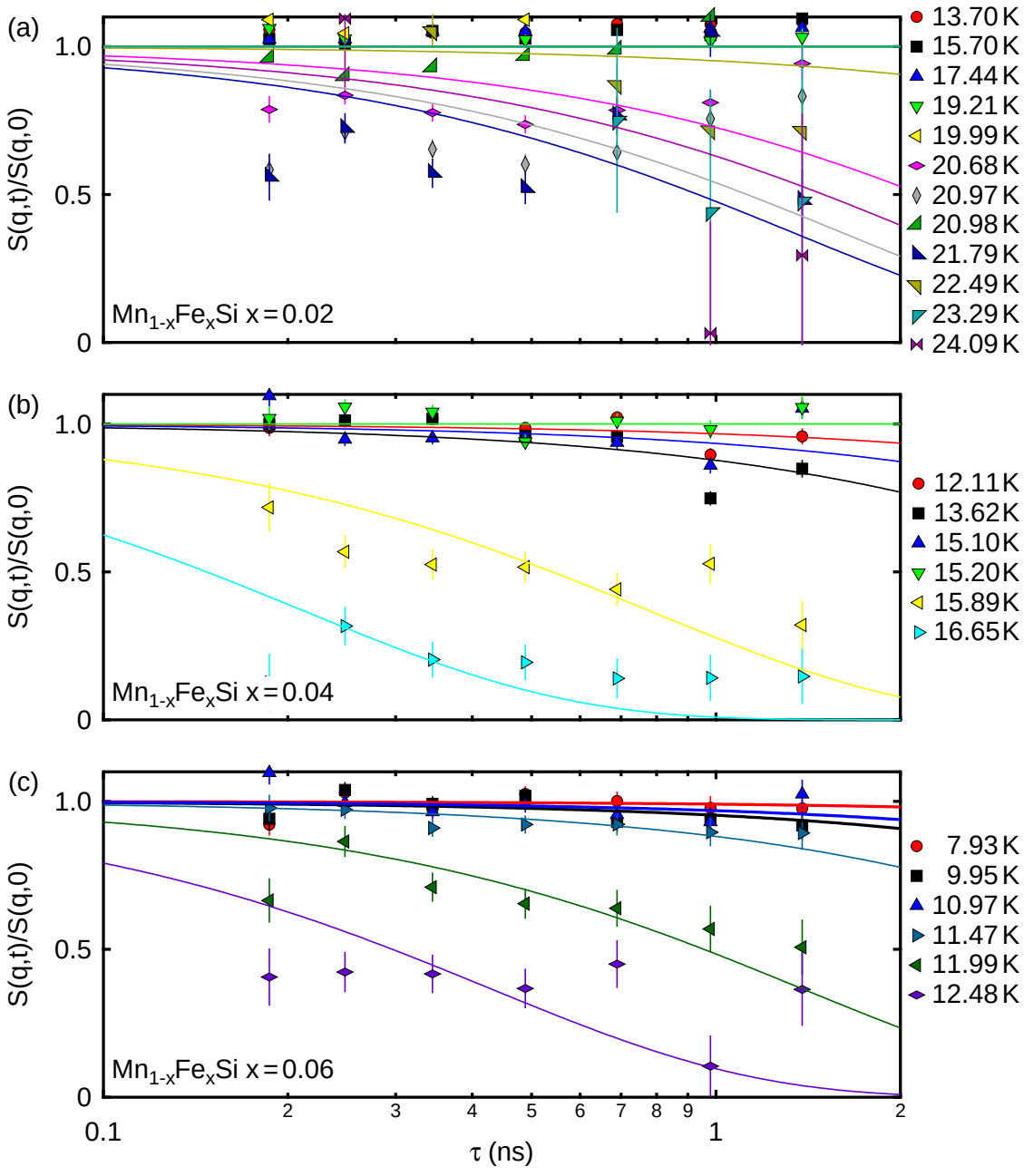

Figure B.2.: Normalized intermediate scattering function measured on the conical Bragg peak of $Mn_{1-x}Fe_xSi$ as function of temperature for different iron concentrations. (a) $x = 0.02$, (b) $x = 0.04$ and (c) $x = 0.06$.

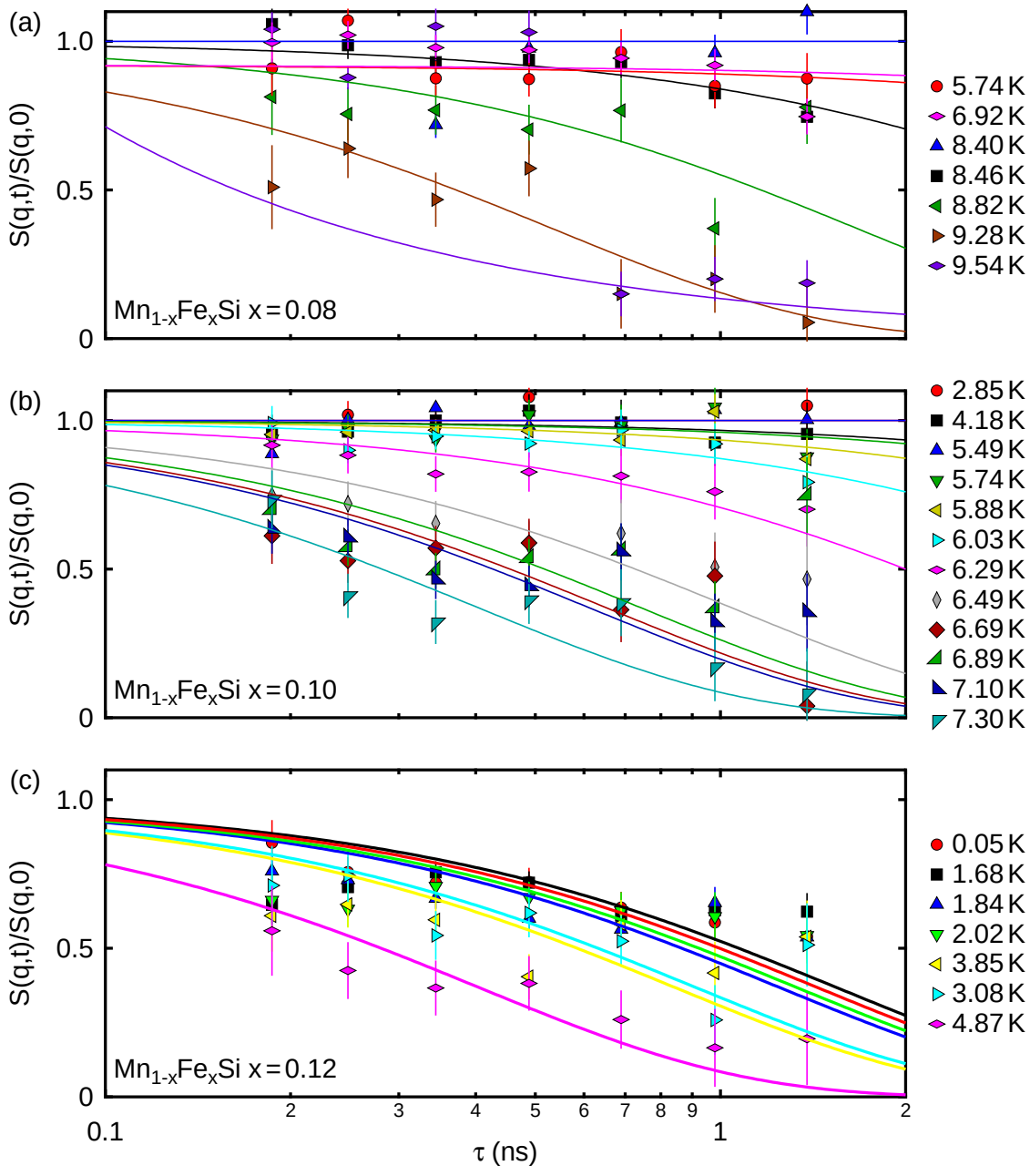

Figure B.3.: Normalized intermediate scattering function measured on the conical Bragg peak of $Mn_{1-x}Fe_xSi$ as function of temperature for different iron concentrations. (a) $x = 0.08$, (b) $x = 0.10$ and (c) $x = 0.12$.

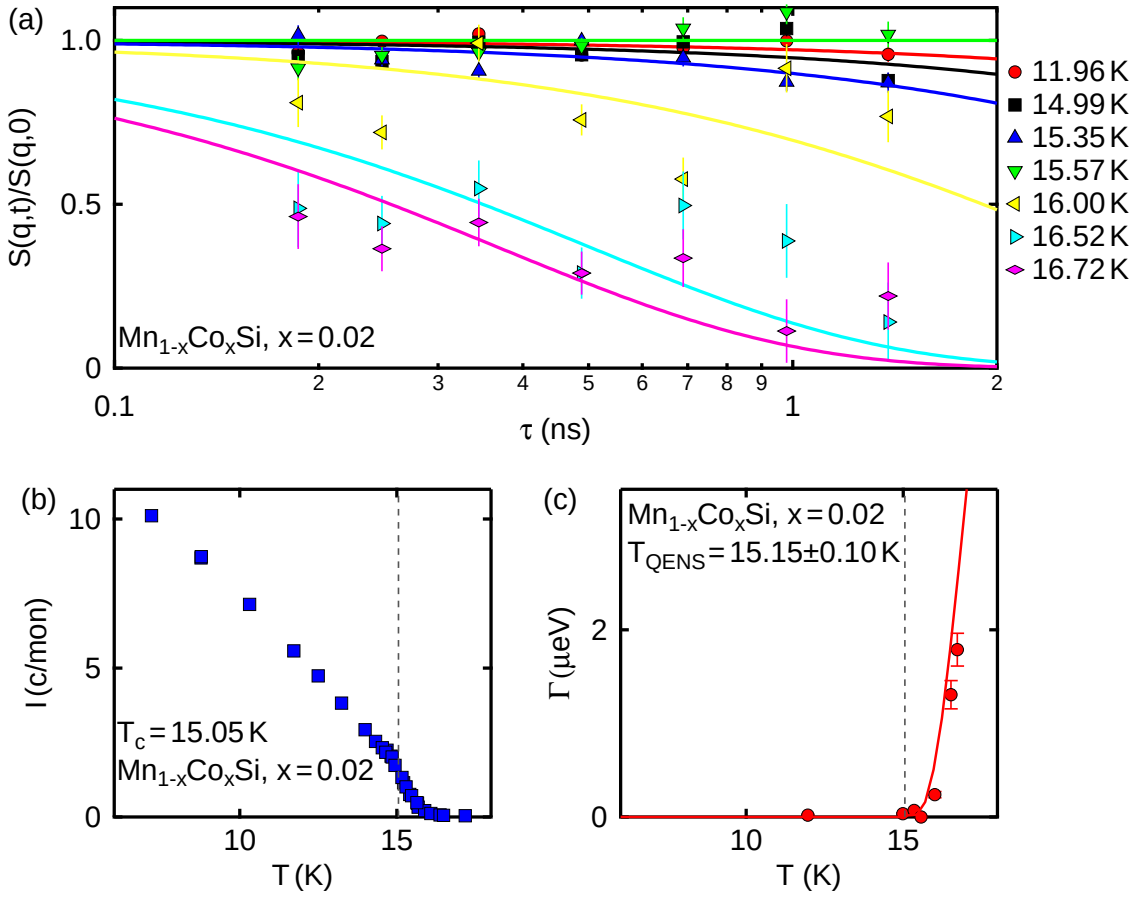

Figure B.4.: (a) Normalized intermediate scattering function measured on the conical Bragg peak of $Mn_{1-x}Co_xSi$ $x = 0.02$ as function of temperature. (b) Intensity of the helical peak as function of temperature. (c) Γ as function of temperature extracted by a single exponential fit from panel (a).

Bibliography

[1] J. G. Bednorz and K. A. Müller, Possible high T_c superconductivity in the Ba-La-Cu-O system, Z. Phys. B: Condens. Matter **64**, 189 (1986).

[2] P. A. Lee, N. Nagaosa, and X.-G. Wen, Doping a mott insulator: Physics of high-temperature superconductivity, Rev. Mod. Phys. **78**, 17 (2006).

[3] S. Mühlbauer, B. Binz, F. Jonietz, C. Pfleiderer, A. Rosch, A. Neubauer, R. Georgii, and P. Böni, Skyrmion Lattice in a Chiral Magnet, Science **323**, 915 (2009).

[4] C. Pfleiderer, S. R. Julian, and G. G. Lonzarich, Non-Fermi-liquid nature of the normal state of itinerant-electron ferromagnets, Nature **414**, 427 (2001).

[5] G. R. Stewart, Non-Fermi-liquid behavior in d- and f-electron metals, Rev. Mod. Phys. **73**, 797 (2001).

[6] H. v. Löhneysen, A. Rosch, M. Vojta, and P. Wölfle, Fermi-liquid instabilities at magnetic quantum phase transitions, Rev. Mod. Phys. **79**, 1015 (2007).

[7] K. G. Wilson, The renormalization group and critical phenomena, Rev. Mod. Phys. **55**, 583 (1983).

[8] C. Pfleiderer, Why first order quantum phase transitions are interesting, J. Phys.: Condens. Matter **17**, S987 (2005).

[9] S. A. Brazovskii, Phase transition of an isotropic system to a nonuniform state, Soviet Physics JETP **41** (1975).

[10] J. Swift, Fluctuations near the nematic-smectic-C phase transition, Phys. Rev. A **14**, 2274 (1976).

[11] A. B. Migdal, E. Saperstein, M. Troitsky, and D. N. Voskresensky, Pion degrees of freedom in nuclear matter, Physics Reports **192**, 179 (1990).

[12] T. D. Stanescu, B. Anderson, and V. Galitski, Spin-orbit coupled Bose-Einstein condensates, Phys. Rev. A **78**, 023616 (2008).

[13] J. Swift and P. C. Hohenberg, Hydrodynamic fluctuations at the convective instability, Phys. Rev. A **15**, 319 (1977).

[14] M. Janoschek, M. Garst, A. Bauer, P. Krautscheid, R. Georgii, P. Böni, and C. Pfleiderer, Fluctuation-induced first-order phase transition in Dzyaloshinskii-Moriya helimagnets, Phys. Rev. B **87**, 134407 (2013).

[15] J. Kindervater, W. Häußler, M. Janoschek, C. Pfleiderer, P. Böni, and M. Garst, Critical spin-flip scattering at the helimagnetic transition of MnSi, Phys. Rev. B **89**, 180408 (2014).

[16] M. Vojta, Quantum phase transitions, Rep. Prog. Phys. **66**, 2069 (2003).

[17] N. D. Mathur, F. Grosche, S. Julian, I. Walker, D. Freye, R. Haselwimmer, and G. Lonzarich, Magnetically mediated superconductivity in heavy fermion compounds, Nature **394**, 39 (1998).

[18] C. Pfleiderer, Superconducting phases of f-electron compounds, Rev. Mod. Phys. **81**, 1551 (2009).

[19] J. Custers, P. Gegenwart, H. Wilhelm, K. Neumaier, Y. Tokiwa, O. Trovarelli, C. Geibel, F. Steglich, C. Pepin, and P. Coleman, The break-up of heavy electrons at a quantum critical point, Nature **424**, 524 (2003).

[20] T. Vojta, Quantum phase transitions in electronic systems, Annalen der Physik **9**, 403 (2000).

[21] S. S. Saxena, P. Agarwal, K. Ahilan, F. M. Grosche, R. K. W. Haselwimmer, M. J. Steiner, E. Pugh, I. R. Walker, S. R. Julian, P. Monthoux, G. G. Lonzarich, A. Huxley, I. Sheikin, D. Braithwaite, and J. Flouquet, Superconductivity on the border of itinerant-electron ferromagnetism, Nature **406**, 587 (2000).

[22] E. Vargoz, P. Link, D. Jaccard, T. Le Bihan, and S. Heathman, Is $CeCu_2$ a pressure-induced heavy-fermion superconductor? Physica B: Condensed Matter **229**, 225 (1997).

[23] R. Movshovich, T. Graf, D. Mandrus, J. D. Thompson, J. L. Smith, and Z. Fisk, Superconductivity in heavy-fermion $CeRh_2Si_2$, Phys. Rev. B **53**, 8241 (1996).

[24] M. Brando, D. Moroni-Klementowicz, C. Albrecht, and F. M. Grosche, Quantum criticality in $NbFe_2$, *Proceedings of the International Conference on Strongly Correlated Electron Systems SCES 2005 Proceedings of the International Conference on Strongly Correlated Electron Systems*, Physica B: Condensed Matter **378–380**, 111 (2006).

[25] M. Brando, W. J. Duncan, D. Moroni-Klementowicz, C. Albrecht, D. Grüner, R. Ballou, and F. M. Grosche, Logarithmic Fermi-Liquid Breakdown in $NbFe_2$, Phys. Rev. Lett. **101**, 026401 (2008).

[26] N. Doiron-Leyraud, I. R. Walker, L. Taillefer, M. J. Steiner, S. R. Julian, and G. G. Lonzarich, Fermi-liquid breakdown in the paramagnetic phase of a pure metal, Nature **425**, 595 (2003).

[27] R. Ritz, M. Halder, M. Wagner, C. Franz, A. Bauer, and C. Pfleiderer, Formation of a topological non-Fermi liquid in MnSi, Nature **497**, 231 (2013).

[28] F. Mezei, Neutron spin echo: a new concept in polarized thermal neutron techniques, Z. Physik **255**, 146 (1972).

[29] F. Mezei, *The principles of neutron spin echo* (Springer, 1980).

[30] R. Gähler and R. Golub, A high resolution neutron spectrometer for quasielastic scattering on the basis of spin-echo and magnetic resonance, Z. Physik B **65**, 269 (1987).

[31] D. Dubbers, P. El-Muzeini, M. Kessler, and J. Last, Prototype of a zero-field neutron spin-echo spectrometer, Nucl. Instrum. Methods Phys. Res., Sect. A **275**, 294 (1989).

[32] R. Gähler, R. Golub, and T. Keller, Neutron resonance spin echo—a new tool for high resolution spectroscopy, Physica B: Condensed Matter **180**, 899 (1992).

[33] F. Mezei, 'Neutron Inelastic Scattering' 1977 (IAEA, Vienna, 1978) p. 125.

[34] F. Mezei and A. Murani, Combined three-dimensional polarization analysis and spin echo study of spin glass dynamics, J. Magn. Magn. Mater. **14**, 211 (1979).

[35] S. M. Shapiro, H. Maletta, and F. Mezei, Neutron-spin-echo study of the reentrent spin glass $Eu_xSr_{1-x}S$, J. Appl. Phys. **57**, 3485 (1985).

[36] B. V. B. Sarkissian, Cluster dynamics in Au-15%Fe alloy: neutron spin echo studies, J. Phys.: Condens. Matter **2**, 7873 (1990).

[37] C. Pappas, F. Mezei, G. Ehlers, P. Manuel, and I. A. Campbell, Dynamic scaling in spin glasses, Phys. Rev. B **68**, 054431 (2003).

[38] F. Mezei, Role of spin-nonconserving forces in the critical dynamics of fe at the curie point, Phys. Rev. Lett. **49**, 1096 (1982).

[39] W. Besenböck, R. Gähler, P. Hank, R. Kahn, M. Koppe, C.-H. De Novion, W. Petry, and J. Wuttke, First scattering experiment on MIEZE: A fourier transform time-of-flight spectrometer using resonance coils, Journal of Neutron Research **7**, 65 (1998).

[40] P. Hank, W. Besenböck, R. Gähler, and M. Koppe, Zero-field neutron spin echo techniques for incoherent scattering, Physica B: Condensed Matter **234**, 1130 (1997).

[41] J. Kindervater, N. Martin, W. Häußler, M. Krautloher, C. Fuchs, S. Mühlbauer, J. Lim, E. Blackburn, P. Böni, and C. Pfleiderer, Neutron spin echo spectroscopy under 17 T magnetic field at RESEDA, EPJ Web of Conferences **83**, 03008 (2015).

[42] R. Coldea, D. Tennant, E. Wheeler, E. Wawrzynska, D. Prabhakaran, M. Telling, K. Habicht, P. Smeibidl, and K. Kiefer, Quantum criticality in an Ising chain: experimental evidence for emergent E8 symmetry, Science **327**, 177 (2010).

[43] C. Rüegg, N. Cavadini, A. Furrer, H.-U. Güdel, K. Krämer, H. Mutka, A. Wildes, K. Habicht, and P. Vorderwisch, Bose-Einstein condensation of the triplet states in the magnetic insulator $TlCuCl_3$, Nature **423**, 62 (2003).

[44] A. Zheludev, V. O. Garlea, T. Masuda, H. Manaka, L.-P. Regnault, E. Ressouche, B. Grenier, J.-H. Chung, Y. Qiu, K. Habicht, K. Kiefer, and M. Boehm, Dynamics of quantum spin liquid and spin solid phases in IPA-$CuCl_3$ under an applied magnetic field studied with neutron scattering, Phys. Rev. B **76**, 054450 (2007).

[45] C. Franz, F. Freimuth, A. Bauer, R. Ritz, C. Schnarr, C. Duvinage, T. Adams, S. Blugel, A. Rosch, Y. Mokrousov, and C. Pfleiderer, Real-Space and Reciprocal-Space Berry Phases in the Hall Effect of $Mn_{1-x}Fe_xSi$, Phys. Rev. Lett. **112**, 186601 (2014).

[46] A. Furrer, J. Mesot, and T. Strässle, *Neutron Scattering in Condensed Matter Physics*, Vol. 4 (World Scientific Publishing Co. Pte. Ltd, 2009).

[47] G. L. Squires, *Introduction to the Theory of Thermal Neutron Scattering*, Dover books on physics (New York, 1978).

[48] S. W. Lovesey, *Theory of Neutron Scattering from Condensed Matter*, International series of monographs on physics No. Bd. 2 (1986).

[49] L. Van Hove, Correlations in space and time and Born approximation scattering in systems of interacting particles, Phys. Rev. **95**, 249 (1954).

[50] J. Kindervater, *From Heli- to Paramagnetism in MnSi: Polarization Analysis with MiniMuPAD* (Diploma Thesis, Technische Universität München (TUM), 2012).

[51] U. Fano, Description of States in Quantum Mechanics by Density Matrix and Operator Techniques, Rev. Mod. Phys. **29**, 74 (1957).

[52] Y. A. Izyumov and S. V. Maleyev, Soviet Physics JETP **14**, 1668 (1962).

[53] M. Blume, Polarization Effects in the Magnetic Elastic Scattering of Slow Neutrons, Phys. Rev. **130**, 1670 (1963).

[54] Y. A. Izyumov, Sov. Phys. Usp **16**, 359 (1963).

[55] M. Blume, Polarization Effects in Slow Neutron Scattering II. Spin-Orbit Scattering and Interference, Phys. Rev. **133**, A1366 (1964).

[56] P. J. Brown, Polarised neutrons and complex antiferromagnets: an overview, Physica B: Condensed Matter **297**, 198 (2001).

[57] M. Janoschek, S. Klimko, B. Roessli, R. Gähler, and P. Böni, Spherical neutron polarimetry with MuPAD, Physica B **397**, 125 (2007).

[58] J. S. Pedersen, D. Posselt, and K. Mortensen, Analytical treatment of the resolution function for small-angle scattering, J. Appl. Phys. **23**, 321 (1990).

[59] R. Nathans, C. Shull, G. Shirane, and A. Andresen, The use of polarized neutrons in determining the magnetic scattering by iron and nickel, J. Phys. Chem. Solids **10**, 138 (1959).

[60] R. M. Moon, T. Riste, and W. C. Koehler, Polarization Analysis of Thermal-Neutron Scattering, Phys. Rev. **181**, 920 (1969).

[61] F. Tasset, Zero field neutron polarimetry, Physica B: Condensed Matter **156**, 627 (1989).

[62] F. Tasset, P. Brown, E. Lelièvre-Berna, T. Roberts, S. Pujol, J. Allibon, and E. Bourgeat-Lami, Spherical neutron polarimetry with Cryopad-II, Physica B: Condensed Matter **267**, 69 (1999).

[63] E. Lelièvre-Berna, E. Bourgeat-Lami, P. Fouilloux, B. Geffray, Y. Gibert, K. Kakurai, N. Kernavanois, B. Longuet, F. Mantegezza, M. Nakamura, *et al.*, Advances in spherical neutron polarimetry with Cryopad, Physica B: Condensed Matter **356**, 131 (2005).

[64] M. Janoschek, *MuPAD 3D Polarization Analysis in Magnetic Neutron Scattering* (Diploma Thesis, Technische Universität München (TUM), 2004).

[65] T. Keller, R. Golub, and R. Gähler, Neutron Spin Echo - a Technique for high Resolution Neutron Scattering, Scattering and Inverse Scattering in Pure and Applied Science, Academic Press, San Diego, CA **1264**, 2002 (2002).

[66] G. Brandl, *First measurements of the linewidth in magnetic phases of MnSi using MIEZE* (Diploma Thesis, Technische Universität München (TUM), 2010).

[67] F. Haslbeck, *Simulation und Konstruktion eines MiniMuPAD* (Bachelor Thesis, Technische Universität München (TUM), 2013).

[68] Comsol Multiphysics GmbH, COMSOL Multiphysics®, (2015), https://www.comsol.de/ accesed at 01.05.2015.

[69] W. Häußler, B. Gohla-Neudecker, R. Schwikowski, D. Streibl, and P. Böni, RESEDA - the new resonance spin echo spectrometer using cold neutrons at the FRM-II, Physica B **397**, 112 (2007).

[70] M. Krautloher, *Implementation of a LNRSE option into RESEDA / MLZ* (Master Thesis, Ludwig-Maximilians-Universität München (LMU), 2014).

[71] W. Häußler, U. Schmidt, G. Ehlers, and F. Mezei, Neutron resonance spin echo using spin echo correction coils, Chemical physics **292**, 501 (2003).

[72] W. Häußler, G. Ehlers, and U. Schmidt, Field integral correction in neutron resonance spin echo, Physica B: Condensed Matter **350**, E807 (2004), proceedings of the Third European Conference on Neutron Scattering.

[73] W. Häußler and U. Schmidt, Effective field integral subtraction by the combination of spin echo and resonance spin echo. Journal of Physical Chemistry Chemical Physics **7**, 1245 (2005).

[74] W. Häußler, P. Böni, M. Klein, C. Schmidt, U. Schmidt, F. Groitl, and J. Kindervater, Detection of high frequency intensity oscillations at reseda using the cascade detector, Rev. Sci. Instrum. **82**, 045101 (2011).

[75] M. Klein and C. Schmidt, CASCADE, neutron detectors for highest count rates in combination with ASIC/FPGA based readout electronics, Nucl. Instrum. Methods Phys. Res., Sect. A **628**, 9 (2011).

[76] A. T. Holmes, G. R. Walsh, E. Blackburn, E. M. Forgan, and M. Savey-Bennett, A 17 T horizontal field cryomagnet with rapid sample change designed for beamline use, Rev. Sci. Instrum. **83**, 023904 (2012).

[77] J. Kindervater, W. Häußler, A. Tischendorf, and P. Böni, Neutron-spin-echo from polarizing samples, in *J. Phys. Conf. Ser.*, Vol. 340 (IOP Publishing, 2012) p. 012030.

[78] S. Mühlbauer, J. Kindervater, and W. Häußler, Static and Quasielastic Properties of the Spiral Magnet $Ba_2CuGe_2O_7$ Studied by Neutron Resonance Spin Echo Spectroscopy and Neutron Larmor Labelling, submitted to Phys. Rev. B (2015).

[79] F. Bloch and A. Siegert, Magnetic resonance for nonrotating fields, Phys. Rev. **57**, 522 (1940).

[80] B. I. Halperin and P. C. Hohenberg, Generalization of scaling laws to dynamical properties of a system near its critical point, Phys. Rev. Lett. **19**, 700 (1967).

[81] B. I. Halperin and P. Hohenberg, Scaling laws for dynamic critical phenomena, Phys. Rev. **177**, 952 (1969).

[82] M. Fixman, Ultrasonic attenuation in the critical region, J. Chem. Phys. **33**, 1363 (1960).

[83] M. Fixman, Absorption and Dispersion of Sound in Critical Mixtures, J. Chem. Phys. **36**, 1961 (1962).

[84] M. E. Fisher and A. Aharony, Dipolar interactions at ferromagnetic critical points, Phys. Rev. Lett. **30**, 559 (1973).

[85] P. C. Hohenberg and B. I. Halperin, Theory of dynamic critical phenomena, Reviews of Modern Physics **49**, 435 (1977).

[86] P. Böni, D. Görlitz, J. Kötzler, and J. Martnez, Dynamics of longitudinal and transverse fluctuations above T_c in EuS, Phys. Rev. B **43**, 8755 (1991).

[87] L. Chow, C. Hohenemser, and R. M. Suter, Observation of Crossover in the Dynamic Exponent z in Fe and Ni, Phys. Rev. Lett. **45**, 908 (1980).

[88] F. Mezei, Critical dynamics in isotropic ferromagnets, Journal of magnetism and magnetic materials **45**, 67 (1984).

[89] F. Mezei, Critical Dynamics in EuO at the Ferromagnetic Curie Point, Physica B+C **136**, 417 (1986).

[90] P. Résibois and C. Piette, Temperature Dependence of the Linewidth in Critical Spin Fluctuation, Phys. Rev. Lett. **24**, 514 (1970).

[91] E. Frey and F. Schwabl, Critical dynamics of dipolar ferromagnets, Physics Letters A , 49 (1987).

[92] E. Frey, F. Schwabl, and S. Thoma, Shape functions of dipolar ferromagnets at the Curie point, Physics Letters A **129**, 343 (1988).

[93] E. Frey and F. Schwabl, On the critical dynamics of ferromagnets, Z. Phys. B: Condens. Matter **71**, 355 (1988).

[94] E. Frey and F. Schwabl, Critical Dynamics of Magnets, arXiv preprint arXiv:cond-mat/9509141v1 (2008).

[95] J. Wicksted, P. Böni, and G. Shirane, Polarized-beam study of the paramagnetic scattering from bcc iron, Phys. Rev. B **30**, 3655 (1984).

[96] J. C. Le Guillou and J. Zinn-Justin, Critical exponents for the n-vector model in three dimensions from field theory, Phys. Rev. Lett. **39**, 95 (1977).

[97] J. C. Le Guillou and J. Zinn-Justin, Critical exponents from field theory, Phys. Rev. B **21**, 3976 (1980).

[98] C. Kittel, *Introduction to Solid State Physics* (Wiley, New York, 1995).

[99] J. Als-Nielsen, O. Dietrich, and L. Passell, Neutron scattering from the Heisenberg ferromagnets EuO and EuS. II. Static critical properties, Phys. Rev. B **14**, 4908 (1976).

[100] G. Shirane, Magnetic correlations in 3d ferromagnets above T_C, Journal of magnetism and magnetic materials **45**, 33 (1984).

[101] J. Kötzler, Critical phenomena in dipolar magnets, J. Magn. Magn. Mater. **54**, 649 (1986).

[102] P. Böni, H. A. Mook, J. L. Martínez, and G. Shirane, Comparison of the paramagnetic spin fluctuations in nickel with asymptotic renormalization-group theory, Phys. Rev. B **47**, 3171 (1993).

[103] P. Böni, Spin fluctuations in isotropic ferromagnets near T_C, Physica B: Condensed Matter **192**, 94 (1993).

[104] B. Farago and F. Mezei, Study of magnon dynamics in Fe near T_C by modified neutron spin echo techniques, Physica B+C **136**, 100 (1986).

[105] T. Holstein and H. Primakoff, Field dependence of the intrinsic domain magnetization of a ferromagnet, Phys. Rev. **58**, 1098 (1940).

[106] M. Collins, V. Minkiewicz, R. Nathans, L. Passell, and G. Shirane, Critical and spin-wave scattering of neutrons from iron, Physical Review **179**, 417 (1969).

[107] A. Bauer, *Investigation of itinerant antiferromagnets and cubic chiral helimagnets*, Ph.D. thesis, Technische Universität München (2014).

[108] L. D. Landau and E. M. Lifshitz, *Course of theoretical physics, vol. 8* (Pergamon Press, 1980).

[109] P. Bak and M. H. Jensen, Theory of helical magnetic structures and phase transitions in MnSi and FeGe, J. Phys. C **13**, L881 (1980).

[110] O. Nakanishi, A. Yanase, A. Hasegawa, and M. Kataoka, The origin of the helical spin density wave in MnSi, Solid State Communications **35**, 995 (1980).

[111] S. Mühlbauer, *Vortex Lattices in Superconducting Niobium and Skyrmion Lattices in the Chiral Magnet MnSi Investigated by Neutron Scattering*, Ph.D. thesis, Technische Universität München (TUM) (2009).

[112] K. Kadowaki, K. Okuda, and M. Date, Magnetization and Magnetoresistance of MnSi.–I, J. Phys. Soc. Jpn. **51**, 2433 (1982).

[113] T. H. R. Skyrme, Particle states of a quantized meson field, Proc. Royal Soc. Lond. A **262**, 237 (1961).

[114] T. H. R. Skyrme, A non-linear field theory, Proc. Royal Soc. Lond. A **260**, 127 (1961).

[115] T. H. R. Skyrme, A unified field theory of mesons and baryons, Nuclear Physics **31**, 556 (1962).

[116] X. W. Yu, N. Kanazawa, Y. Onose, K. Kimoto, W. Z. Zhang, S. Ishiwata, Y. Matsui, and Y. Tokura, Near room-temperature formation of a skyrmion crystal in thin-films of the helimagnet FeGe, Nature Mater. **10**, 106 (2010).

[117] X. W. Yu, Y. Onose, N. Kanazawa, J. H. Park, J. H. Han, Y. Matsui, N. Nagaosa, and Y. Tokura, Real-space observation of a two-dimensional skyrmion crystal, Nature **465**, 901 (2010).

[118] W. Münzer, A. Neubauer, T. Adams, S. Mühlbauer, C. Franz, F. Jonietz, R. Georgii, P. Böni, B. Pedersen, M. Schmidt, A. Rosch, and C. Pfleiderer, Skyrmion lattice in the doped semiconductor $Fe_{1-x}Co_xSi$, Phys. Rev. B **81**, 041203 (2010).

[119] S. Seki, X. W. Yu, S. Ishiwata, and Y. Tokura, Observation of skyrmions in a multiferroic material, Science **336**, 198 (2012).

[120] T. Adams, A. Chacon, M. Wagner, A. Bauer, G. Brandl, B. Pedersen, H. Berger, P. Lemmens, and C. Pfleiderer, Long-Wavelength Helimagnetic Order and Skyrmion Lattice Phase in Cu_2OSeO_3, Phys. Rev. Lett. **108**, 237204 (2012).

[121] S. Polesya, S. Mankovsky, S. Bornemann, D. Ködderitzsch, J. Minár, and H. Ebert, Skyrmion magnetic structure of an ordered FePt monolayer deposited on Pt (111), Phys. Rev. B **89**, 184414 (2014).

[122] T. Ogasawara, N. Iwata, Y. Murakami, H. Okamoto, and Y. Tokura, Submicron-scale spatial feature of ultrafast photoinduced magnetization reversal in TbFeCo thin film, Applied Physics Letters **94**, 162507 (2009).

[123] M. Finazzi, M. Savoini, A. R. Khorsand, A. Tsukamoto, A. Itoh, L. Duò, A. Kirilyuk, T. Rasing, and M. Ezawa, Laser-Induced Magnetic Nanostructures with Tunable Topological Properties, Phys. Rev. Lett. **110**, 177205 (2013).

[124] A. Neubauer, C. Pfleiderer, B. Binz, A. Rosch, R. Ritz, P. G. Niklowitz, and P. Böni, Topological Hall effect in the A-phase of MnSi, Phys. Rev. Lett. **102**, 186602 (2009).

[125] A. Neubauer, C. Pfleiderer, R. Ritz, P. G. Niklowitz, and P. Böni, Hall effect and magnetoresistance in MnSi, Physica B: Condensed Matter **404**, 3163 (2009).

[126] M. Lee, W. Kang, Y. Onose, Y. Tokura, and N. P. Ong, Unusual Hall effect anomaly in MnSi under pressure, Phys. Rev. Lett. **102**, 186601 (2009).

[127] F. Jonietz, S. Mühlbauer, C. Pfleiderer, A. Neubauer, W. Münzer, A. Bauer, T. Adams, R. Georgii, P. Böni, R. A. Duine, K. Everschor, M. Garst, and A. Rosch, Spin Transfer Torques in MnSi at Ultralow Current Densities, Science **330**, 1648 (2010).

[128] T. Schulz, R. Ritz, A. Bauer, M. Halder, M. Wagner, C. Franz, C. Pfleiderer, K. Everschor, M. Garst, and A. Rosch, Emergent electrodynamics of skyrmions in a chiral magnet, Nature Physics **8**, 301 (2012).

[129] A. Fert, V. Cros, and J. Sampaio, Skyrmions on the track, Nature Nanotech. **8**, 152–156 (2013).

[130] P. Milde, D. Köhler, J. Seidel, L. M. Eng, A. Bauer, A. Chacon, J. Kindervater, S. Mühlbauer, C. Pfleiderer, S. Buhrandt, C. Schütte, and A. Rosch, Unwinding of a Skyrmion Lattice by Magnetic Monopoles, Science **340**, 1076 (2013).

[131] S. V. Grigoriev, S. V. Maleyev, A. I. Okorokov, Y. O. Chetverikov, R. Georgii, P. Böni, D. Lamago, H. Eckerlebe, and K. Pranzas, Critical fluctuations in MnSi near T_C: A polarized neutron scattering study, Phys. Rev. B **72**, 134420 (2005).

[132] S. Grigoriev, S. Maleyev, E. Moskvin, V. Dyadkin, P. Fouquet, and H. Eckerlebe, Crossover behavior of critical helix fluctuations in MnSi, Phys. Rev. B **81**, 144413 (2010).

[133] S. M. Stishov, A. E. Petrova, S. Khasanov, G. K. Panova, A. A. Shikov, J. C. Lashley, D. Wu, and T. A. Lograsso, Magnetic phase transition in the itinerant helimagnet MnSi: Thermodynamic and transport properties, Phys. Rev. B **76**, 052405 (2007).

[134] S. Stishov, A. Petrova, S. Khasanov, G. K. Panova, A. Shikov, J. Lashley, D. Wu, and T. Lograsso, Heat capacity and thermal expansion of the itinerant helimagnet MnSi, J. Phys.: Condens. Matter **20**, 235222 (2008).

[135] A. Petrova and S. Stishov, Ultrasonic studies of the magnetic phase transition in MnSi, J. Phys.: Condens. Matter **21**, 196001 (2009).

[136] P. M. Chaikin and T. C. Lubensky, *Principles of condensed matter physics*, Vol. 1 (Cambridge Univ Press, 2000).

[137] U. K. Rößler, A. N. Bogdanov, and C. Pfleiderer, Spontaneous skyrmion ground states in magnetic metals, Nature **442**, 797 (2006).

[138] C. Pappas, E. Lelièvre-Berna, P. Falus, P. M. Bentley, E. Moskvin, S. Grigoriev, P. Fouquet, and B. Farago, Chiral Paramagnetic Skyrmion-like Phase in MnSi, Phys. Rev. Lett. **102**, 197202 (2009).

[139] C. Pappas, E. Lelièvre-Berna, P. Bentley, P. Falus, P. Fouquet, and B. Farago, Magnetic fluctuations and correlations in MnSi: Evidence for a chiral skyrmion spin liquid phase, Phys. Rev. B **83**, 224405 (2011).

[140] A. Bauer, M. Garst, and C. Pfleiderer, Specific Heat of the Skyrmion Lattice Phase and Field-Induced Tricritical Point in MnSi, Phys. Rev. Lett. **110**, 177207 (2013).

[141] D. Vollhardt, Characteristic crossing points in specific heat curves of correlated systems, Phys. Rev. Lett. **78**, 1307 (1997).

[142] C. Pfleiderer, P. Böni, T. Keller, U. K. Rößler, and A. Rosch, Non fermi liquid metal without quantum criticality, Science **316**, 1871 (2007).

[143] C. Pfleiderer, G. J. McMullan, S. R. Julian, and G. G. Lonzarich, Magnetic quantum phase transition in MnSi under hydrostatic pressure, Phys. Rev. B **55**, 8330 (1997).

[144] C. Pfleiderer, D. Reznik, L. Pintschovius, H. v. Löhneysen, M. Garst, and A. Rosch, Partial order in the non-Fermi-liquid phase of MnSi, Nature **427**, 227 (2004).

[145] Y. J. Uemura, T. Goko, I. M. Gat-Malureanu, J. P. Carlo, P. L. Russo, A. T. Savici, A. Aczel, G. J. MacDougall, J. A. Rodriguez, G. M. Luke, S. R. Dunsiger, A. McCollam, J. Arai, C. Pfleiderer, P. Böni, K. Yoshimura, E. Baggio-Saitovitch, M. B. Fontes, J. L. jr, Y. V. Sushko, and J. Sereni, Phase separation and suppression of critical dynamics at quantum phase transitions of MnSi and $(Sr_{1-x}Ca_x)RuO_3$, Nature Physics **3**, 29 (2007).

[146] J. D. Thompson, Z. Fisk, and G. G. Lonzarich, Perspective on heavy-electron and Kondo-lattice systems from high pressure studies, Physica B **161**, 317 (1989).

[147] C. Pfleiderer, R. H. Friend, G. G. Lonzarich, N. R. Bernhoeft, and J. Flouquet, Transition from a magnetic to a nonmagnetic state as a function of pressure in MnSi, International Journal of Modern Physics B **07**, 887 (1993).

[148] I. Lifshitz, Anomalies of electron characteristics of a metal in the high pressure region, Sov. Phys. JETP **11**, 1130 (1960).

[149] C. Thessieu, C. Pfleiderer, A. N. Stepanov, and J. Flouquet, Field dependence of the magnetic quantum phase transition in MnSi, J. Phys.: Condens. Matter **9**, 6677–6687 (1997).

[150] K. Koyama, T. Goto, T. Kanomata, and R. Note, Observation of an itinerant metamagnetic transition in MnSi under high pressure, Phys. Rev. B **62**, 986 (2000).

[151] G. G. Lonzarich and L. Taillefer, Effect of spin fluctuations on the magnetic equation of state of ferromagnetic or nearly ferromagnetic metals, J. Phys. C **18**, 4339 (1985).

[152] T. Moriya, *Spin fluctuations in itinerant electron magnetism*, Springer series in solid-state sciences (Springer-Verlag, 1985).

[153] W. Yu, F. Zamborszky, J. D. Thompson, J. L. Sarrao, M. E. Torelli, Z. Fisk, and S. E. Brown, Phase Inhomogeneity of the Itinerant Ferromagnet MnSi at High Pressures, Phys. Rev. Lett. **92**, 086403 (2004).

[154] P. Pedrazzini, D. Jaccard, G. Lapertot, J. Flouquet, Y. Inada, H. Kohara, and Y. Ōnuki, Probing the extended non-Fermi liquid regimes of MnSi and Fe, Physica B **378-380**, 165 (2006).

[155] C. Pfleiderer, Non-Fermi liquid puzzle of MnSi at high pressure, Physica B **328**, 100 (2003).

[156] M. Brian Maple, R. E. Baumbach, N. P. Butch, J. J. Hamlin, and M. Janoschek, Non-Fermi Liquid Regimes and Superconductivity in the Low Temperature Phase Diagrams of Strongly Correlated d-and f-Electron Materials, Journal of Low Temperature Physics **161**, 4 (2010).

[157] R. Ritz, M. Halder, C. Franz, A. Bauer, M. Wagner, R. Bamler, A. Rosch, and C. Pfleiderer, Giant generic topological Hall resistivity of MnSi under pressure, Phys. Rev. B **87**, 134424 (2013).

[158] S. V. Grigoriev, V. A. Dyadkin, E. V. Moskvin, D. Lamago, T. Wolf, H. Eckerlebe, and S. V. Maleyev, Helical spin structure of $Mn_{1-y}Fe_ySi$ under a magnetic field: Small angle neutron diffraction study, Phys. Rev. B **79**, 144417 (2009).

[159] A. Bauer, A. Neubauer, C. Franz, W. Münzer, M. Garst, and C. Pfleiderer, Quantum Phase Transitions in Single-Crystal $Mn_{1-x}Fe_xSi$ and $Mn_{1-x}Co_xSi$: Crystal Growth, Magnetization, AC Susceptibility and Specific Heat, Phys. Rev. B **82**, 064404 (2010).

[160] J. Teyssier, E. Giannini, V. Guritanu, R. Viennois, D. van der Marel, A. Amato, and S. N. Gvasaliya, Spin-glass ground state in $Mn_{1-x}Co_xSi$, Phys. Rev. B **82**, 064417 (2010).

[161] S. V. Grigoriev, E. V. Moskvin, V. A. Dyadkin, D. Lamago, T. Wolf, H. Eckerlebe, and S. V. Maleyev, Chiral criticality in the doped helimagnets $Mn_{1-y}Fe_ySi$, Phys. Rev. B **83**, 224411 (2011).

[162] S. Maleyev, V. Baryakhtar, and R. Suris, .. Fiz. Tverd. Tela **4**, 3461 (1962).

[163] A. Bauer, *Investigation of itinerant antiferromagnets and cubic chiral helimagnets*, Ph.D. thesis, Technische Universität München (2014), pp. 44-45.

[164] T. Adams, Skyrmionengitter und partielle Ordnung in B20 Übergangsmetallverbindungen, Diploma Thesis (2009).

[165] S. Ernst, Magnetic Phase Diagram of $Mn_{1-x}Fe_xSi$, $x = 0.12$ and $x = 0.10$, Inferred from Small Angle Neutron Scattering, Bachelor Thesis, Technische Universität München (2014).

[166] B. Fåk, R. A. Sadykov, J. Flouquet, and G. Lapertot, Pressure dependence of the magnetic structure of the itinerant electron magnet mnsi, J. Phys.: Condens. Matter **17**, 1635 (2005).

[167] M. Deutsch, P. Bonville, A. Tsvyashchenko, L. Fomicheva, F. Porcher, F. Damay, S. Petit, and I. Mirebeau, Stress-induced magnetic textures and fluctuating chiral phase in mnge chiral magnet, Phys. Rev. B **90**, 144401 (2014).

[168] Wolfram Research, Inc., Mathematica 10.0, Champaign, Illinios (2014).

[169] L. Köhler and M. Garst, Report, Insitute for Theoretical Physics, Universität zu Köln (2015).